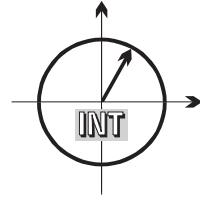


■ *Forschungsberichte aus dem  
Institut für Nachrichtentechnik  
der Universität Karlsruhe (TH)*



Sinja Brandes

# ■ **Suppression of Mutual Interference in OFDM Based Overlay Systems**

■ Band 22

Copyright: Institut für Nachrichtentechnik  
Universität Karlsruhe (TH), 2009

Druck: Uni-Druck OHG, Maisinger Weg 19  
82319 Starnberg, Tel. 08151 / 65 48 48

ISSN: 1433-3821

**Forschungsberichte aus dem Institut für Nachrichtentechnik der  
Universität Karlsruhe (TH)**

---

Herausgeber: Prof. Dr. rer. nat. Friedrich Jondral

- Band 1    Marcel Kohl  
**Simulationsmodelle für die Bewertung von Satellitenübertragungsstrecken im 20/30 GHz Bereich**
- Band 2    Christoph Delfs  
**Zeit-Frequenz-Signalanalyse: Lineare und quadratische Verfahren sowie vergleichende Untersuchungen zur Klassifikation von Klaviertönen**
- Band 3    Gunnar Wetzker  
**Maximum-Likelihood Akquisition von Direct Sequence Spread-Spectrum Signalen**
- Band 4    Anne Wiesler  
**Parametergesteuertes Software Radio für Mobilfunksysteme**
- Band 5    Karl Lütjen  
**Systeme und Verfahren für strukturelle Musteranalysen mit Produktionsnetzen**
- Band 6    Ralf Machauer  
**Multicode-Detektion im UMTS**
- Band 7    Gunther M. A. Sessler  
**Schnell konvergierender Polynomial Expansion Multiuser Detektor mit niedriger Komplexität**
- Band 8    Henrik Schober  
**Breitbandige OFDM Funkübertragung bei hohen Teilnehmergeschwindigkeiten**

**Forschungsberichte aus dem Institut für Nachrichtentechnik der  
Universität Karlsruhe (TH)**

---

Herausgeber: Prof. Dr. rer. nat. Friedrich Jondral

- Band 9     Arnd-Ragnar Rhiemeier  
**Modulares Software Defined Radio**
- Band 10    Mustafa Mengüç Öner  
**Air Interface Identification for Software Radio Systems**
- Band 11    Fatih Çapar  
**Dynamische Spektrumverwaltung und elektronische Echtzeitver-  
marktung von Funkspektren in Hotspotnetzen**
- Band 12    Ihan Martoyo  
**Frequency Domain Equalization in CDMA Detection**
- Band 13    Timo Weiß  
**OFDM-basiertes Spectrum Pooling**
- Band 14    Wojciech Kuropatwiński-Kaiser  
**Messung von MIMO-Kapazitäten mit einem auf GSM-  
Komponenten basierenden Demonstrator**
- Band 15    Piotr Rykaczewski  
**Kompensierung hochfrequenzbedingter I/Q-Fehler in Software  
Defined Radio**
- Band 16    Michael Eisenacher  
**Kompensierung der stochastischen Eigenschaften von Ultra-  
Wideband-Signalen**
- Band 17    Clemens Klöck  
**Auction-based Medium Access Control**



**Forschungsberichte aus dem Institut für Nachrichtentechnik der  
Universität Karlsruhe (TH)**

---

Herausgeber: Prof. Dr. rer. nat. Friedrich Jondral

- Band 18    Martin Henkel  
**Architektur eines DRM-Empfängers und Basisbandalgorithmen  
zur Frequenzakquisition und Kanalschätzung**
- Band 19    Stefan Edinger  
**Mehrträgerverfahren mit dynamisch-adaptiver Modulation zur  
unterbrechungsfreien Datenübertragung in Störfällen**
- Band 20    Volker Blaschke  
**Multiband Cognitive Radio-Systeme**
- Band 21    Ulrich Berthold  
**Dynamic Spectrum Access Using OFDM-based Overlay Systems**
- Band 22    Sinja Brandes  
**Suppression of Mutual Interference in OFDM Based Overlay  
Systems**



# Vorwort des Herausgebers

In den letzten Jahren durchgeführte Messkampagnen haben offen gelegt, dass selbst in relativ stark belegten Bändern des elektromagnetischen Spektrums weniger als 15 bis 20 Prozent der verfügbaren Übertragungsressource wirklich genutzt werden. Um zu einer deutlich erhöhten Effizienz in der Spektrumsnutzung zu gelangen, werden einerseits Underlaysysteme, die nach dem Ultra Wideband (UWB) Verfahren arbeiten, eingesetzt. Andererseits werden Overlaysysteme, die auch als Sekundärnutzer (*Secondary User*, SU) Systeme bezeichnet werden, untersucht. Das dabei betrachtete Band wird eigentlich von einem lizenzierten System, das hier als Primärnutzer (*Primary User*, PU) System bezeichnet wird, belegt. Setzt das PU System FDMA oder TDMA als Zugriffsmethode ein, erzeugen nicht genutzte Ressourcen über der Zeit-Frequenz-Ebene „weiße Flecken“, die dem SU System zur Übertragung dienen.

Als Übertragungsverfahren bietet sich in Szenarien der geschilderten Art, insbesondere wegen seiner hohen Anpassbarkeit, OFDM an. Die Idee dabei ist, das SU System auf OFDM-Basis arbeiten zu lassen und die Unterträger, die frequenzmäßig mit Sendungen im PU System zusammenfallen, abzuschalten. Der Einsatz OFDM-basierter Overlaysysteme ist damit einfach zu beschreiben. Die Schwierigkeiten liegen, wie in solchen Fällen häufig zu beobachten ist, im Detail. SU Systeme dürfen natürlich, um überhaupt Akzeptanz zu finden, die lizenzierten Systeme nicht stören. Anders herum sorgen Störungen vom PU System auf SU Systeme dort für einen empfindlichen Effizienzverlust.

Die vorliegende Arbeit nimmt sich der Unterdrückung von Störungen, die im Zusammenhang mit OFDM-basierten Overlaysystemen auftreten, an. Dabei werden sowohl Störungen vom SU System auf das PU System als auch Störungen in der entgegen gesetzten Richtung untersucht. Die Arbeit behandelt die Unterdrückung von Störungen auf der physikalischen (PHY) Schicht. Maßnahmen, die der Untersuchung von Medium Access Control (MAC) Layer Aspekten gewidmet sind, finden sich in der Dissertation von Ulrich Berthold<sup>1</sup>.

---

<sup>1</sup>Ulrich Berthold: *Dynamic Spectrum Access Using OFDM-based Overlay Systems*. Forschungsberichte aus dem Institut für Nachrichtentechnik der Universität Karlsruhe (TH), Band 21, Karlsruhe 2009

Beide Dissertationen sind in Kooperationsprojekten zwischen dem Institut für Nachrichtentechnik der Universität Karlsruhe (TH) und dem Institut für Kommunikation und Navigation des Deutschen Zentrums für Luft- und Raumfahrt e.V. (DLR) in Oberpfaffenhofen, die im Rahmen des Schwerpunktprogramms 1163 *TakeOFDM* der Deutschen Forschungsgemeinschaft (DFG) gefördert wurden, entstanden.

Die Dissertation *Suppression of Mutual Interference in OFDM Based Overlay Systems* von Sinja Brandes diskutiert erstmalig in ausführlicher Form die Unterdrückung von Störern beim Einsatz von OFDM-basierten Overlayssystemen auf der physikalischen Schicht. Schon darin ist ein eigenständiger Beitrag zum Fortschritt von Technik und Wissenschaft zu sehen. Folgende Themenbereiche werden eingehend behandelt:

- Die Kombination verschiedener Verfahren zur Verminderung von Außenbandstrahlung in OFDM-Sendern
- Die Kombination von Zeit- und Frequenzbereichsmethoden bei der Unterdrückung von Schmalbandstörern in OFDM-Empfängern
- Die ausführliche Charakterisierung von pulsförmigen Störern und deren Unterdrückung in OFDM-Empfängern

Karlsruhe, im Mai 2009

Friedrich Jondral

# Suppression of Mutual Interference in OFDM Based Overlay Systems

Zur Erlangung des akademischen Grades eines

DOKTOR-INGENIEURS

der Fakultät für  
Elektrotechnik und Informationstechnik  
der Universität Fridericiana Karlsruhe

genehmigte

DISSERTATION

von

Dipl.-Ing. Sinja Brandes

aus

Dortmund

Tag der mündlichen Prüfung:

05.05.2009

Hauptreferent:

Prof. Dr. rer. nat. Friedrich Jondral

Korreferent:

Prof. Dr.-Ing. Dr.-Ing. E.h. Norbert Fliege



# Danksagung

Die vorliegende Dissertation entstand im Rahmen meiner Tätigkeit als wissenschaftliche Mitarbeiterin am Institut für Kommunikation und Navigation des Deutschen Zentrums für Luft- und Raumfahrt e.V. (DLR) in Oberpfaffenhofen. Die dieser Dissertation zu Grunde liegenden Arbeiten wurden teilweise im Rahmen der Projekte TAKOKO im Schwerpunktprogramm TakeOFDM und OOS durch die Deutsche Forschungsgemeinschaft (DFG) gefördert. Darüber hinaus hatte ich am DLR die Möglichkeit an weiteren Projekten mitzuarbeiten, die mir einen Einblick in das interessante Gebiet der aeronautischen Kommunikation gewährt und eine realistische Grundlage und Anwendungsmöglichkeiten für die Untersuchungen in meiner Arbeit gegeben haben.

Bei Herrn Prof. Dr. rer. nat. Friedrich Jondral, Leiter des Instituts für Nachrichtentechnik (INT) der Universität Karlsruhe (TH), bedanke ich mich für die gute Kooperation im Rahmen der Projekte TAKOKO und OOS sowie für die Betreuung der Arbeit und die schnelle Abwicklung des Promotionsverfahrens. Mein Dank gilt ebenfalls Herrn Prof. Dr.-Ing. Dr.-Ing. E.h. Norbert Fliege, Leiter des Instituts für Technische Informatik der Universität Mannheim, für sein Interesse an meiner Arbeit und die zügige Erstellung des Zweitgutachtens.

Ulrich Berthold, der zeitlich parallel am INT promoviert hat und damit quasi ein „Leidensgenosse“ war, danke ich für die Unterstützung und die gute Zusammenarbeit in den DFG-Projekten. Die Ergebnisse der Zusammenarbeit mit Johannes Schwarz und die Beiträge von Laëtitia Falconetti im Bereich schmalbandiger Störungen sind in das vierte Kapitel dieser Arbeit eingeflossen - vielen Dank dafür. Weiterhin möchte ich mich bei meinen Kollegen am DLR für ein angenehmes und motivierendes Arbeitsklima und viele interessante Diskussionen bedanken, die zum Gelingen der Arbeit beigetragen haben. Mein besonderer Dank gilt Herrn Dr.-Ing. Michael Schnell für die Unterstützung, die vielen fachlichen Anregungen und Diskussionen und schließlich für das Korrekturlesen dieser Arbeit.

„Last but not least“ bedanke ich mich bei meiner Familie und meinen Freunden, die für die notwendige Abwechslung und Ablenkung gesorgt und mir damit - bewußt oder unbewußt - immer wieder neue Energie für die Arbeit gegeben haben.

Gilching, im Mai 2009  
Sinja Brandes





# Zusammenfassung

Die Anforderungen moderner Kommunikationssysteme an höhere Datenraten und mehr Bandbreite sind auf Grund von Frequenzknappheit und starrer Frequenzzuweisung immer schwieriger zu erfüllen. Das Konzept der „Cognitive Radios“ sieht vor, dieses Problem durch eine Steigerung der spektralen Effizienz zu lösen. Ein vielversprechender Realisierungsansatz hierfür sind Overlay-Systeme, die ein Frequenzband mit bereits bestehenden Systemen teilen, indem sie die von den lizenzierten Systemen gelassenen spektralen Lücken nutzen. Die Nutzung von orthogonalem Frequenz-Multiplex (OFDM) als Modulationsverfahren bietet die Flexibilität, das Overlay-System durch einfaches An- und Abschalten einzelner Subträger an die sich dynamisch ändernde Spektrumsbelegung anzupassen. Um eine erfolgreiche Koexistenz zu ermöglichen, müssen die wechselseitigen Interferenzen zwischen dem Overlay- und den lizenzierten Systemen unterdrückt werden, was Thema dieser Arbeit ist.

Ein Nachteil von OFDM ist eine hohe Außerbandstrahlung, die eine Unterdrückung der Nebenaussendungen am Sender des Overlay-Systems erfordert. Da existierende Methoden keine ausreichenden Ergebnisse liefern, werden in dieser Arbeit drei neue Methoden zur Reduzierung der Nebenaussendungen präsentiert, die alle darauf zielen, die Sendesequenz so zu verändern, dass sie geringere Nebenaussendungen erzeugt. Bei der Methode der Subträgergewichtung wird dies durch Multiplikation der einzelnen Subträger mit reellen Gewichtungsfaktoren realisiert, die so optimiert sind, dass sich die Nebenaussendungen der Subträgersignale gegenseitig auslöschen. Der Ansatz der Multiple-Choice Sequenzen generiert mehrere Sendesequenzen, die alle dieselbe Information repräsentieren, und wählt die Sequenz mit den niedrigsten Nebenaussendungen für die Übertragung aus. Alternativ werden so genannte Cancellation Carrier an den Rändern des Spektrums eingefügt und so mit komplexen Gewichtungsfaktoren moduliert, dass sie die Nebenaussendungen der für die Datenübertragung genutzten Subträger auslöschen. Cancellation Carrier liefern die besten Ergebnisse, die durch zusätzliche Fensterung oder durch Kombination mit Subträgergewichtung oder Multiple-Choice Sequenzen noch weiter verbessert werden können. Mit den vorgeschlagenen Kombinationen können die Nebenaussendungen auf Kosten von geringen Einbußen in der Leistungsfähigkeit erheblich reduziert werden.

Interferenz von lizenzierten Systemen beeinträchtigt die Leistungsfähigkeit des

Empfängers des Overlay-Systems erheblich und muss reduziert werden. Bei schmalbandigen Störungen treten bei der diskreten Fourier-Transformation (DFT) im Empfänger spektrale Leckeffekte auf, die dazu führen, dass alle Subträger von der Störung betroffen sind. Als Gegenmaßnahme wird das Empfangssignal im Zeitbereich gefenstert, um die spektrale Selektivität der DFT zu verbessern. Da die problematische Spitze im Interferenzsignal jedoch bestehen bleibt, werden zusätzliche Methoden im Frequenzbereich angewandt. Der Einfluss der Interferenz wird durch Subtraktion eines geschätzten Interferenzsignals oder durch Kompensation des Leckeffekts entsprechend eines den mittleren quadratischen Fehler auf jedem Subträger minimierenden Optimierungskriteriums reduziert. Für beide Ansätze ist eine Schätzung des Störsignals erforderlich, die entweder aus einer Rekonstruktion des Trägersignals basierend auf Messungen auf wenigen Beobachtungsträgern oder a priori Wissen über die spektrale Leistungsdichte des Störsignals abgeleitet werden kann. Die Interferenzleistung wird durch Subtraktion oder Kompensation des Leckeffekts basierend auf einer Schätzung des Trägers im Bereich des Trägers und durch Kompensation des Leckeffekts basierend auf a priori Wissen über die spektrale Leistungsdichte in den äußeren Bereichen des Spektrums erheblich reduziert. Diese Ergebnisse legen es nahe, beide Schätzansätze zu kombinieren und sie jeweils auf verschiedene Typen von Störern anzuwenden, so dass insgesamt der Störeinfluss beträchtlich verringert wird. Weitere Verbesserungen werden erzielt, wenn die Methoden zur Interferenzreduzierung im Frequenzbereich mit einer Fensterung im Zeitbereich kombiniert werden. In diesem Fall kann der Einfluss der Interferenz fast vollständig eliminiert werden.

Pulsförmige Interferenz tritt zwar nur sehr kurzzeitig auf, beeinträchtigt das Overlay-System aber erheblich, da sie durch große Bandbreite, hohe Leistung und große Auftrittswahrscheinlichkeit charakterisiert ist. Der Störeinfluss kann bereits durch geschickte Signalverarbeitung im Overlay-Empfänger mittels Überabtastung und Filterung gering gehalten werden. Um den Störeinfluss weiter zu reduzieren, werden konventionelle Ansätze wie Pulsauslöschung oder -amplitudenbegrenzung angewandt. Damit werden jedoch nur moderate Gewinne erzielt, da das gewünschte OFDM-Signal signifikant beeinflusst wird. Eine Analyse des Einflusses der Pulsauslöschung zeigt, dass die Pulsauslöschung zu Interferenzen zwischen den einzelnen Subträgern führt. Es wird vorgeschlagen, die deterministisch eingebrachte Störung basierend auf einer Rekonstruktion der Subträgerspektren und einer Schätzung der auf den einzelnen Subträgern übertragenen Datensymbole zu kompensieren. Auf diese Weise wird die Leistungsfähigkeit erheblich verbessert,

da der Einfluss der Pulsauslöschung auf einen Verlust im Signal-zu-Rausch-Verhältnis reduziert wird, der durch Auslöschung eines bestimmten Anteils der Signalenergie entsteht. Des Weiteren ermöglicht die Kompensation des Einflusses der Pulsauslöschung eine effizientere Anwendung der Pulsauslöschung, so dass die Interferenzleistung ohne relevante Einbußen in der Leistungsfähigkeit weiter reduziert werden kann.

Zahlreiche Simulationen anhand zweier realistischer Systeme zeigen das Potential der vorgeschlagenen Verfahren zur Reduzierung der Nebenaussendungen und zur Minimierung des Störeinflusses. Die wechselseitigen Interferenzen werden so weit unterdrückt, dass eine Koexistenz zweier Systeme im selben Frequenzband möglich wird.



# Abstract

The demands of modern communication systems for higher data rates and more bandwidth are harder and harder to meet due to scarce spectral resources and rigid spectrum management. The concept of cognitive radios envisages to overcome this problem by increasing spectral efficiency. One promising realisation of this concept are overlay systems, that share a frequency band with already existing licensed systems by using the spectral gaps left by the licensed systems. Employing orthogonal frequency-division multiplexing (OFDM) as modulation technique provides the flexibility to adapt the overlay system to the dynamically changing spectrum allocation by simply turning on and off individual subcarriers. To enable a successful co-existence, mutual interference between the overlay and the licensed system has to be suppressed which is the topic of this thesis.

OFDM suffers from high out-of-band radiation, hence requiring the suppression of sidelobes at the transmitter (Tx) of the overlay system. Given that existing methods do not provide satisfactory results, in this thesis, three advanced methods for sidelobe power reduction are presented all aiming at modifying the Tx sequence in a beneficial way such as to exhibit lower sidelobes. With the subcarrier weighting method, this is realised by multiplying the subcarriers with real-valued weighting factors which are optimised such that the sidelobes of the individual subcarrier signals cancel each other. The multiple-choice sequences approach generates several Tx sequences all representing the same information and selects the one with the smallest sidelobe power for transmission. Alternatively, cancellation carriers are inserted at the edges of the spectrum and modulated with complex weighting factors such that they cancel the sidelobes of the data bearing subcarriers. Cancellation carriers provide the best performance which can be further improved by additional Tx windowing or by the combination with subcarrier weighting or multiple-choice sequences. With the proposed combinations, sidelobe power can be reduced significantly at the cost of small performance losses.

At the overlay system receiver (Rx), interference from the licensed systems degrades performance significantly and hence has to be mitigated. When exposed to narrow-band interference (NBI), spectral leakage occurs after the discrete Fourier transform (DFT) applied at Rx resulting in all subcarriers being affected by NBI. As a countermeasure, Rx windowing applied in the time domain aims at improving the spectral selectivity of the DFT. However, since the problematic peak of

the interference signal remains, additional methods are applied in the frequency domain. Interference is mitigated by subtracting an estimation of the interference signal or by compensating the leakage effect according to an optimisation criterion that minimises the mean square error on each subcarrier. Both approaches require an estimation of the NBI signal which is either gathered from a reconstruction of the carrier signal based on measurements on a few observation subcarriers or from a priori knowledge of the power spectral density of the interference signal. Interference power is reduced significantly close to the carrier frequency with subtraction or leakage compensation based on the carrier estimation and at larger frequency offsets for the PSD based estimation and leakage compensation. These results suggest a combination of both estimation approaches and the application to different types of interferers, thus reducing the impact of NBI on the overlay system considerably. Further improvements are achieved with a combination with windowing in the time domain which eliminates the impact of NBI almost completely.

Though pulsed interference occurs only for a short time, it substantially affects the OFDM system, since the interference signal is also characterised by large bandwidth, high power, and high duty cycle. The impact on the OFDM signal can already be kept at a minimum by appropriate signal processing at Rx including over-sampling and filtering. To further mitigate the impact of pulsed interference, conventional approaches such as pulse blanking and clipping are applied. However, only moderate improvements are achieved since the desired OFDM signal is deteriorated significantly. An analysis of the impact of pulse blanking shows that pulse blanking leads to inter-carrier interference. It is proposed to compensate the deterministically induced disturbance based on a reconstruction of the subcarrier spectra and an estimation of the symbols transmitted on each subcarrier. That way, performance is improved considerably as the pulse blanking impact is reduced to a loss in signal-to-noise ratio resulting from erasing a certain fraction of received signal power. Furthermore, the compensation of the impact of pulse blanking allows for applying pulse blanking more efficiently such as to further reduce interference power without further sacrificing performance.

Numerous simulations at hand of two realistic systems show the potential of the proposed sidelobe suppression and interference mitigation techniques. Mutual interference is suppressed such that a co-existence of two systems in the same frequency band becomes feasible.

# Contents

- 1 Introduction** **1**
  
- 2 OFDM based Overlay Systems** **5**
  - 2.1 The Principle of OFDM . . . . . 6
  - 2.2 OFDM for Overlay Systems . . . . . 10
    - 2.2.1 Principle . . . . . 11
    - 2.2.2 Design Challenges . . . . . 13
  - 2.3 Considered Overlay Scenarios . . . . . 16
    - 2.3.1 Overlay System in the VHF-Band . . . . . 17
    - 2.3.2 Inlay System in the L-Band . . . . . 20
  
- 3 Suppression of Out-of-Band Radiation** **23**
  - 3.1 Conventional Techniques . . . . . 24
    - 3.1.1 Windowing . . . . . 24
    - 3.1.2 Guard Bands . . . . . 25
  - 3.2 Advanced Techniques . . . . . 27
    - 3.2.1 OFDM Tx Spectrum . . . . . 28
    - 3.2.2 Subcarrier Weighting . . . . . 30
    - 3.2.3 Multiple-Choice Sequences . . . . . 34
    - 3.2.4 Cancellation Carriers . . . . . 36
  - 3.3 Combination of Different Techniques . . . . . 41
    - 3.3.1 Combination of Advanced Techniques with Tx Windowing 41
    - 3.3.2 Combination of Advanced Techniques . . . . . 43
  - 3.4 Performance Evaluation . . . . . 44
    - 3.4.1 Simulated Scenario . . . . . 44
    - 3.4.2 Subcarrier Weighting . . . . . 44
    - 3.4.3 Multiple-Choice Sequences . . . . . 46

3.4.4	Cancellation Carriers . . . . .	46
3.4.5	Combination of Advanced Techniques . . . . .	50
3.4.6	Comparison of Different Techniques . . . . .	54
<b>4</b>	<b>Mitigation of Narrow-Band Interference</b>	<b>57</b>
4.1	Origin of Leakage Effect . . . . .	58
4.1.1	Complex Exponential Sequence . . . . .	60
4.1.2	DSB-AM Signal with Sidebands . . . . .	62
4.2	NBI Mitigation in the Time Domain . . . . .	64
4.2.1	Principle of Rx Windowing . . . . .	66
4.2.2	Impact on the Desired OFDM Signal . . . . .	69
4.2.3	Different Window Types . . . . .	71
4.3	NBI Mitigation in the Frequency Domain . . . . .	74
4.3.1	Subtraction . . . . .	74
4.3.2	Leakage Compensation . . . . .	75
4.4	Estimation of NBI . . . . .	80
4.4.1	Available A Priori Knowledge and Means of Observation . . . . .	80
4.4.2	Detection of Active Interferers . . . . .	81
4.4.3	Estimation of Carrier Signal . . . . .	82
4.4.4	Estimation based on PSD . . . . .	85
4.4.5	Comparison of Different NBI Estimation and Mitigation Techniques . . . . .	88
4.5	Combination of Time and Frequency Domain Techniques . . . . .	99
4.5.1	Principle . . . . .	99
4.5.2	Adaptation of Estimation Algorithms . . . . .	101
4.5.3	Comparison of Different Combinations . . . . .	103
4.6	Performance Evaluation . . . . .	104
4.6.1	Considered Interference Scenario . . . . .	104
4.6.2	Simulation Parameters . . . . .	106
4.6.3	Simulation Results . . . . .	107



<b>5</b>	<b>Mitigation of Pulsed Interference</b>	<b>113</b>
5.1	Characterisation of Interference . . . . .	114
5.1.1	Sources of Interference . . . . .	114
5.1.2	Description of Interference Signal . . . . .	115
5.1.3	Modelling of Interference . . . . .	116
5.2	Mitigation by Appropriate Signal Processing . . . . .	119
5.2.1	Over-sampling . . . . .	119
5.2.2	Anti-Aliasing Filtering . . . . .	121
5.3	Mitigation by Clipping and Pulse Blanking . . . . .	123
5.3.1	Clipping . . . . .	124
5.3.2	Pulse Blanking . . . . .	134
5.4	Compensation of Pulse Blanking Impact . . . . .	138
5.4.1	Impact of Pulse Blanking . . . . .	138
5.4.2	Reduction of ICI . . . . .	143
5.4.3	Reconsideration of Threshold for Pulse Blanking . . . . .	149
5.5	Performance Evaluation . . . . .	152
5.5.1	Considered Interference Scenario . . . . .	152
5.5.2	Simulation Parameters . . . . .	153
5.5.3	Simulation Results . . . . .	153
<b>6</b>	<b>Conclusions</b>	<b>159</b>
6.1	Suppression of Out-of-Band Radiation . . . . .	159
6.2	Mitigation of Narrow-Band Interference . . . . .	161
6.3	Mitigation of Pulsed Interference . . . . .	162
6.4	Conclusions and Outlook . . . . .	164
<b>A</b>	<b>Derivation of Subcarrier Spectrum</b>	<b>165</b>
A.1	Subcarrier Spectrum after Rectangular Tx Windowing . . . . .	167
A.2	Subcarrier Spectrum after Tx Windowing . . . . .	168

<b>B Derivation of Leakage Effect</b>	<b>171</b>
<b>C Derivation of MMSE Approach for NBI Mitigation</b>	<b>173</b>
<b>Abbreviations and Definitions</b>	<b>175</b>
<b>Bibliography</b>	<b>184</b>
<b>Förderung</b>	<b>193</b>
<b>Curriculum Vitae</b>	<b>195</b>

# 1 Introduction

The environment of today's and future wireless communications is characterised by the ever-growing demand for higher data rates and more bandwidth on the one hand and apparently scarce and expensive spectral resources on the other hand. The frequency charts of the regulatory bodies in the US [1] or worldwide show multiple allocations over all frequency bands which underlines the difficulty to find prime spectrum for accommodating new services as well as for the expansion of existing ones. In contrast, spectrum measurements at different times and in different parts of the world [2–5] provide evidence that wide frequency ranges are actually utilised to a limited extent only. From this situation basically two conclusions can be drawn:

1. There is an urgent need for a completely new and more flexible way of spectrum allocation.
2. New technologies are required, that are flexible and use spectral resources efficiently.

As to the first point, a large variety of new concepts for a more adequate radio resource management can be found in the literature. Different proposals comprise dynamic or random channel allocation for different users operating in a single assigned frequency range [6], free spectrum access for everybody instead of fixed frequency assignments [7], or spectrum auctioning which dynamically allocates spectral resources for a limited time to the most bidding user [8]. All approaches have in common the demand for a dynamic rather than a fixed assignment of spectral resources. This is in-line with recent developments of spectrum policy. Regulatory bodies start rethinking the rigid spectrum allocation and head towards dynamic spectrum access [9].

Concerning the second point, in 1999, the idea of cognitive radios has been presented by Joseph Mitola III and Gerald Q. Maguire as a means to promote the efficient use of the spectrum by exploiting the existence of spectral gaps and sharing frequency bands with other users on a non-interfering basis [10, 11]. The concept of cognitive radio has gained increasing interest in the last few years and has repeatedly been picked up in the literature, e.g. [12]. Among the multiple general and theoretical considerations on cognitive radio, few concrete system concepts taking into account the physical as well as the medium access layer have been addressed.

One approach presented in [5] builds up on spectrum pooling which has first been mentioned by Mitola in [11]. Spectrum pooling enables public access to already licensed frequency bands that are organised in a pool comprising frequency bands from different spectrum owners such as military or trunked radio. When the licensed system is idle, a second system may temporarily access the spectral resources. The primary proposition is that the licensed system does not need to be changed and does not even notice the existence of the second system. In [5], the second system is envisaged to employ orthogonal frequency-division multiplexing (OFDM) according to widely-used standards such as IEEE 802.11 for wireless local area networks (WLAN) [13, 14].

Using OFDM as modulation technique offers several advantages. First, OFDM itself already provides a high spectral efficiency. Second, in the past few years, OFDM has become a sophisticated technology which is applied in several commercially used systems such as WLAN or terrestrial digital video broadcasting (DVB-T) [15]. In the context of spectrum sharing, OFDM enables a flexible adaptation of the transmit signal to the current spectrum allocation. As depicted in Fig. 1.1, the OFDM system bandwidth spans a frequency band subdivided into several channels assigned to a licensed system. Dependent on the actual utilisation of the spectrum, the OFDM system adapts its transmit signal by simply turning off the subcarriers in the channels used by the licensed system. When the spectrum allocation changes, the OFDM system is dynamically adjusted by switching on and off different subcarriers.

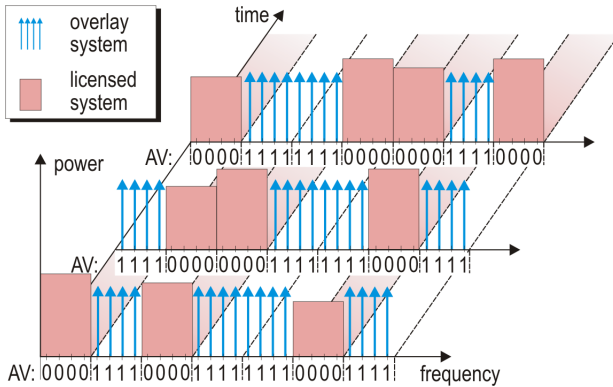


**Figure 1.1** Utilisation of spectral gaps by an OFDM based overlay system.

In this thesis, the OFDM system co-existing with a licensed system is referred to as OFDM based overlay system. In contrast to spectrum pooling, but without loss of generality, only one frequency range assigned to one licensed system rather than a pool of multiple frequency ranges is considered. Although OFDM based overlay systems are a promising approach for overcoming the problem of spectral scarcity, the feasibility of the co-existence of two systems in the same frequency band still has to be proven. A key enabler of a successful co-existence will be the virtually independent operation of the two systems without harmful interference. This also is the main concern of the regulatory bodies that has to be resolved before the strict frequency assignment will be loosened. The objective of this thesis is to provide methods that are capable of suppressing mutual interference between licensed systems and the OFDM based overlay system such as to realise a successful co-existence in the same frequency band. Therefore, on the one hand, out-of-band radiation of the OFDM transmit signal has to be kept at a minimum in order to not interfere with the licensed systems. On the other hand, out-of-band radiation from licensed systems causes interference at the OFDM based overlay system and has to be mitigated to enable the operation of the OFDM based overlay system.

The remainder of this thesis is organised as follows.

After a brief introduction to the OFDM transmission technique, the OFDM system model is extended to an OFDM based overlay system in Chapter 2. For OFDM based overlay systems, the basic structure of the OFDM system is retained while requiring only a few additional blocks and/or modifications of existing blocks that are studied in this thesis. As a realistic basis for the investigations, two exemplary overlay systems are defined.

In Chapter 3, the reduction of interference towards licensed systems is addressed. Since conventional approaches do not provide satisfactory results, three advanced methods are proposed all aiming at modifying the transmit sequence in a beneficial way such that the resulting transmit sequence produces minimal out-of-band radiation. For all three approaches, namely subcarrier weighting, multiple-choice sequences, and cancellation carriers, the principle, the optimisation problem, and the impact on the performance of the OFDM system are studied. For further performance improvements, the combination with conventional techniques as well as the combination of the advanced methods with each other is proposed. The achieved sidelobe suppression is demonstrated at hand of a worst case scenario in an exemplary overlay system.

Chapters 4 and 5 deal with the mitigation of the strong impact of interference from licensed systems onto the overlay system. In Chapter 4, narrow-band interference (NBI) lying within the bandwidth of the overlay system is considered. Due to spectral leakage which is an inherent property of the discrete Fourier transform (DFT) performed at the OFDM receiver, interference is spread over the entire OFDM bandwidth and all subcarriers are affected. For mitigating NBI, receiver windowing is applied in the time domain in order to improve the spectral selectivity of the DFT. Alternatively, the interference signal can be estimated and reconstructed in the frequency domain based on measurements on a few unused subcarriers. This estimation is either simply subtracted from the received signal or exploited for compensating the leakage effect according to an optimisation criterion that minimises the error on each subcarrier. The time and the frequency domain approach are combined to join the benefits of both methods. The achievable reduction of the interference impact for all proposed methods is shown in worst case interference conditions.

In Chapter 5, the mitigation of pulsed interference originating from interferers at small frequency offsets to the OFDM system is addressed. Although only a few samples in the time domain OFDM signal are affected by the short interference pulses, pulsed interference degrades the performance of the OFDM system considerably. With conventional approaches such as clipping and pulse blanking interference can be mitigated only moderately, since they suffer from the strong impact on the desired OFDM signal. For pulse blanking, the impairment of the OFDM signal is reasoned by inter-carrier interference that can be reconstructed based on the number and position of blanked samples as well as on an estimation of the transmit sequence. Since inter-carrier interference induced by pulse blanking can be compensated with the proposed method, even more samples can be blanked hence further reducing the remaining interference power. The performance of the OFDM system applying the proposed methods for interference mitigation is demonstrated by means of simulations in realistic interference conditions.

In Chapter 6, the main results of each chapter are summarised and an outlook with respect to the work in this thesis as well as with respect to future activities in the field of cognitive radio is given.

## 2 OFDM based Overlay Systems

The concept of OFDM is already known since the 1960s [16, 17]. When the DFT has been proposed for modulation and demodulation by Weinstein and Ebert in 1971 [18], computational complexity could be reduced considerably. Although being of continuing interest ever since, OFDM has gained increased interest in the early 1990s as it has been a promising approach to meet the growing demand for high-speed data transmission [19]. In the last years, OFDM has become a well-understood and mature technology that has already been successfully implemented in several standards for wireline and wireless communication systems such as asymmetric digital subscriber line (ADSL) [20] and WLAN according to IEEE 802.11a/g [13, 14]. OFDM is still considered for future communication systems and is planned to be implemented in the fourth generation of mobile communications systems for example.

Another application of OFDM are overlay systems, that have drawn increasing attention in the past few years, as they are a promising approach for increasing spectral efficiency and overcoming the problem of spectral scarcity. The motivation for realising overlay systems based on OFDM are two-fold. First, OFDM provides high data rates while using the available bandwidth efficiently. Second, due to its flexibility OFDM enables a simple implementation of an overlay system in frequency bands already in use by licensed systems. For use as an overlay system, the basic structure of an conventional OFDM system does not need to be modified significantly. However, parameters have to be adapted to the structure predetermined by the licensed system. In addition, the dynamic adaptation of the OFDM transmit signal and the reduction of mutual interference, both required for enabling a successful co-existence between the two systems in the same frequency range, pose special challenges for the design of an OFDM based overlay system.

The remainder of this chapter is structured as follows. After briefly recapitulating the OFDM modulation technique, in Section 2.2, the OFDM system is extended to an OFDM based overlay system and the key design parameters are identified. Finally, two examples of OFDM based overlay systems are presented that serve as realistic basis for the investigations and simulations carried out in this thesis.

## 2.1 The Principle of OFDM

The basic principle of OFDM is to split up a serial high-rate data stream into a number of lower rate parallel streams that are transmitted simultaneously over a number of subcarriers. In order to avoid inter-carrier interference (ICI) while abandoning spectrally inefficient guard bands between the subcarriers, subcarriers have to be orthogonal.

In general, two complex signals  $f_n(t)$  and  $f_m(t)$  are orthogonal if

$$\int_{-\infty}^{\infty} f_n(t)f_m^*(t)dt = \begin{cases} 0 & n \neq m \\ C & n = m, \end{cases} \quad (2.1)$$

where  $C$  denotes a constant.

Assuming equidistant subcarriers, the carrier frequency of the  $\nu$ th of a total of  $N$  subcarriers writes

$$f_\nu = \nu \cdot \Delta f + f_{\text{offset}}, \quad \nu = 0, \dots, N - 1, \quad (2.2)$$

with  $\Delta f = \text{const.}$  denoting the subcarrier spacing. For reasons of simplicity, the OFDM system is considered in the baseband meaning that the centre frequency of the OFDM system is equal to 0 Hz. A frequency offset  $f_{\text{offset}}$  is introduced to set the subcarrier frequencies such that  $f_0 = 0$ . The time domain signal  $s_\nu(t)$  transmitted on the  $\nu$ th subcarrier is obtained by loading the subcarrier with a complex data symbol  $d_\nu$  and windowing the carrier signal with  $w(t)$  yielding

$$s_\nu(t) = w(t) \cdot d_\nu \cdot e^{j2\pi f_\nu t}, \quad (2.3)$$

where  $w(t)$  is a rectangular pulse with duration corresponding to the duration of one OFDM symbol denoted by  $T_0$

$$w(t) = \text{rect}(t) = \begin{cases} 1 & 0 \leq t < T_0 \\ 0 & \text{otherwise.} \end{cases} \quad (2.4)$$

With that the orthogonality condition from (2.1) can be rewritten as

$$\int_0^{T_0} e^{j2\pi f_\kappa t} \cdot e^{-j2\pi f_\nu t} dt \stackrel{!}{=} 0, \quad \nu \neq \kappa. \quad (2.5)$$



Obviously, (2.5) is fulfilled when the subcarrier spacing is an integer multiple of the inverse OFDM symbol duration. In order to exploit the available bandwidth efficiently, the subcarrier spacing is chosen as small as possible, i.e.

$$\Delta f = 1/T_0. \quad (2.6)$$

Transmitting a complex data symbol  $d_\nu$  on each subcarrier, where  $d_\nu, \nu = 0, \dots, N - 1$ , forms one OFDM symbol, the OFDM signal transmitted on all subcarriers writes

$$x(t) = \frac{1}{N} \sum_{\nu=0}^{N-1} s_\nu(t) = \frac{1}{N} \sum_{\nu=0}^{N-1} d_\nu e^{j2\pi f_\nu t}, \quad 0 \leq t < T_0. \quad (2.7)$$

When sampling the time domain OFDM signal from (2.7) with sampling frequency  $f_s = N/T_0$  and replacing the subcarrier frequencies by their discrete equivalents according to (2.2), the samples are

$$x[k] = x(k/f_s) = \frac{1}{N} \sum_{\nu=0}^{N-1} d_\nu e^{j2\pi k\nu/N}, \quad k = 0, \dots, N - 1. \quad (2.8)$$

In the discrete domain, the length of  $N$  samples corresponds to the duration  $T_0$  of one OFDM symbol. The sampled sequence  $x[k], k = 0, \dots, N - 1$ , is the inverse discrete Fourier transform (IDFT) of the symbol sequence  $d_\nu, \nu = 0, \dots, N - 1$ , that is more generally represented by  $X[n], n = 0, \dots, N - 1$ , with frequency domain index  $n$ , i.e.

$$x[k] = \text{IDFT}\{X[n]\} = \frac{1}{N} \sum_{n=0}^{N-1} X[n] e^{j2\pi kn/N}, \quad k = 0, \dots, N - 1. \quad (2.9)$$

This is a key advantage of OFDM that allows for implementing OFDM modulation in the discrete domain by using an IDFT, or a more computationally efficient inverse fast Fourier transform (IFFT).

During transmission over the radio channel often characterised by several delayed paths, inter-symbol interference (ISI) between subsequent OFDM symbols occurs. In OFDM, ISI can be avoided completely, when a guard interval (GI) of duration

$$T_{\text{GI}} \geq \tau_{\text{max}} \quad (2.10)$$

exceeding the maximum delay  $\tau_{\max}$  of the multi-path channel precedes each OFDM symbol. The GI is a cyclic extension of each OFDM symbol and extends the duration of one OFDM symbol to

$$T_S = T_O + T_{\text{GI}}. \quad (2.11)$$

That way, subcarrier orthogonality is maintained which also avoids ICI.

The equivalent length of the GI in the discrete domain has to be

$$N_{\text{GI}} \geq \left\lceil \frac{\tau_{\max} N}{T_O} \right\rceil, \quad (2.12)$$

where  $\lceil \cdot \rceil$  denotes the ceiling operation which returns the least integer greater than or equal to the argument. With that, the time domain OFDM signal extended by a GI becomes

$$x[k] = \frac{1}{N} \sum_{\nu=0}^{N-1} d_{\nu} e^{j2\pi k \nu / N}, \quad k = -N_{\text{GI}}, \dots, N-1. \quad (2.13)$$

In the further transmitter (Tx) processing, this sequence is passed through a digital-to-analogue (D/A) converter, that ideally outputs the signal  $x(t)$  from (2.7) with increased symbol duration  $T_S$ . After up-conversion to the radio frequency (RF) the RF signal is transmitted through the multi-path channel.

At the receiver (Rx), after RF down-conversion, the Rx signal is passed through an analogue-to-digital (A/D) converter giving the Rx sequence  $r[k], k = 0, \dots, N + N_{\text{GI}} - 1$ , sampled with sampling rate  $f_s$ . The time domain Rx signal is composed of the transmitted OFDM signal  $x[k]$  affected by the multi-path channel and additive white Gaussian noise (AWGN) denoted by  $n[k], k = 0, \dots, N + N_{\text{GI}} - 1$ . The multi-path channel is modelled as a tapped delay line with  $N_D$  delayed paths with maximum delay  $\tau'_{\max} = \lceil \tau_{\max} N / T_O \rceil$  normalised to the sampling frequency of the OFDM system. With channel impulse response  $h[k]$ , the Rx sequence still including GI is given by

$$\begin{aligned} r[k] &= h[k] * x[k] + n[k] \\ &= \sum_{d=0}^{N_D-1} h[\tau_d] x[k - \tau_d] + n[k], \quad k = 0, \dots, N + N_{\text{GI}} - 1, \end{aligned} \quad (2.14)$$

where  $*$  denotes linear convolution and  $\tau_d$  represents the discrete delay of the  $d$ th path.

After removing the GI by simply discarding the first  $N_{\text{GI}}$  samples of the Rx sequence, the DFT or fast Fourier transform (FFT) can be used for demodulation, respectively. The output of the DFT is the sequence  $R[n], n = 0, \dots, N - 1$ , consisting of  $N$  complex-valued symbols

$$R[n] = \text{DFT}\{r[k]\} = \sum_{k=0}^{N-1} r[k] e^{-j2\pi kn/N}. \quad (2.15)$$

Since ICI and ISI have been avoided by the correct choice of the GI, each sub-channel can be considered isolated and an estimation of the symbol  $d_\nu$  transmitted on the  $\nu$ th subcarrier can be derived from  $R[n]$  when  $n = \nu$ . Note, the frequency index  $n$  corresponds to the subcarrier index  $\nu$  for  $n = \nu$ .

The fading on each subcarrier can be considered flat which is assured by correctly adjusting the subcarrier spacing to the coherence time and bandwidth of the channel [21]. Then, the frequency domain representation of (2.14) is

$$R[n] = H[n] \cdot X[n] + N[n], \quad n = 0, \dots, N - 1, \quad (2.16)$$

where  $H[n]$  are fading coefficients for each subcarrier retrieved from the channel transfer function, which is the equivalent representation of the channel impulse response used in the time domain. The samples  $X[n]$  represent the Tx symbols and  $N[n]$  AWGN on the  $n$ th subcarrier. Summarising the useful part of the Rx signal to  $Y[n]$ , (2.16) can be rewritten as

$$R[n] = Y[n] + N[n] \quad \text{with} \quad Y[n] = H[n] \cdot X[n], \quad n = 0, \dots, N - 1. \quad (2.17)$$

A block diagram of an OFDM system in the baseband is depicted in Fig. 2.1. For reasons of simplicity, the transmission of only one OFDM symbol is considered. Usually,  $P$  OFDM symbols are grouped to one OFDM frame in the frame composer and are transmitted frame-wise. Apart from data symbols, the frame contains synchronisation symbols at the beginning of the frame and pilot symbols for channel estimation. For distinguishing different OFDM symbols within one frame independent of their functionality, the index  $p, p = 0, \dots, P - 1$ , is introduced. The time domain Tx signal of the  $p$ th OFDM symbol of a frame is represented by  $x_p[k], k = 0, \dots, N - 1$ , for example. The duration of such an OFDM frame is  $P \cdot T_S$  or  $P \cdot (N + N_{\text{GI}})$  samples in the discrete domain.

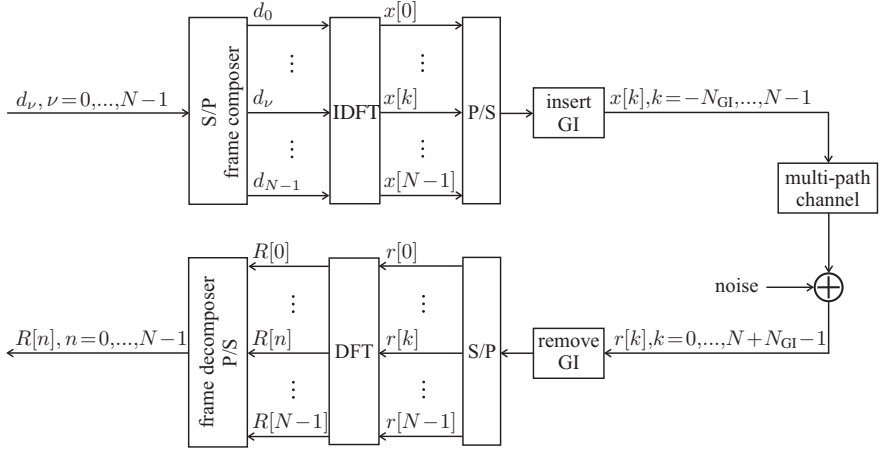


**Figure 2.1** Simplified block diagram of basic OFDM system.

### Notation

The mathematical notation introduced in the previous section is maintained throughout this thesis. Time and frequency domain variables are distinguished by small and capital letters, respectively. In the continuous domain, the time variable  $t$  is put in parentheses. For describing a variable in the discrete time domain, index  $k$  is used and put in brackets. Analogously, in the frequency domain, frequency variable  $f$  and frequency index  $n$  are used. As depending on the sampling rate,  $n$  does not necessarily correspond to the subcarrier index, the subcarrier indices are denoted by  $\nu$ .

Furthermore, vectors and matrices are written in boldface; for their elements standard letters as described above are used.

## 2.2 OFDM for Overlay Systems

Due to overlapping subcarriers, OFDM offers high spectral efficiency and allows for high-rate data transmission. In the context of overlay systems, OFDM has another advantage since it offers the flexibility for adapting the Tx spectrum to the changing spectrum allocation by simply turning on and off individual subcarriers.

For that reason, it has been considered as modulation technique for spectrum sharing systems e.g. in [12, 22, 23].

### 2.2.1 Principle

Before transmitting, the overlay system has to identify available gaps in the spectrum allocation of the licensed system and adapt its Tx signal accordingly. As it cannot be assumed that the licensed and the overlay system exchange any information, the overlay system has to monitor the licensed system's allocation autonomously. This can easily be realised when the licensed system operates on a frequency- and/or time-division multiple-access (FDMA/TDMA) basis. When the overlay system does not transmit, only the signal of the licensed system is received at the overlay system Rx. In that silent phase, the output of the DFT/FFT operation, that is available in each OFDM Rx anyway, indicates whether or not the licensed system currently uses a channel corresponding to a set of subcarriers of the overlay system [24]. Accuracy of these measurements can be increased by performing several DFT/FFT cycles and averaging the results. In addition, spatial diversity is introduced when multiple stations of the overlay system perform measurements at different locations and exchange the results to agree on a common view of the spectrum allocation of the licensed system. The results of spectral measurements are collected in the binary allocation vector (AV), that indicates for each subcarrier whether or not the subcarrier can be used by the overlay system. The allocation vector has to be updated and the Tx signal has to be adapted accordingly, when the licensed system changes its spectrum allocation. The optimal rate for spectral measurements and updates of the allocation vector has been investigated e.g. in [25].

Licensed systems where channel access is realised based on carrier sensing, i.e. carrier sense multiple-access (CSMA), are not always suitable for co-existing with overlay systems, since the spectrum allocation cannot be measured appropriately. The licensed systems listen to the channel and transmit when no other transmissions occur. The overlay system would not detect the listening licensed system, would identify the corresponding channel as idle, and start a transmission. This blocks the attempt to transmit of the licensed system until the overlay system has finished its transmission. That way the overlay system would impair the licensed system significantly to the point of blocking it completely. Nevertheless, a frequency range used by a licensed system employing CSMA can be shared with an overlay system, if the channel assignment of the licensed system can be assumed to be fix. The over-

lay system has to know the actual channel assignment at a certain location and just skips all channels that are potentially used by the licensed system.

Once the useable subcarriers are identified, the overlay system has to adapt its Tx signal to the current spectrum allocation. In OFDM, this is realised by simply turning off those subcarriers that must not be used and modulating them with zero rather than with complex Tx symbols. Hence, the basic functionality of a conventional OFDM system has not to be modified to realise an OFDM based overlay system and most blocks remain unchanged as depicted in Fig. 2.2. However, some blocks need to be slightly modified and several additional blocks are required. These blocks are highlighted in Fig. 2.2. Again, for reasons of simplicity, the transmission of only one OFDM symbol is considered the index  $p$  for the number of the OFDM symbol within one frame is omitted.

At Tx, a serial stream of complex data symbols is fed into the frame composer. Based on the binary allocation vector indicating the status of each subcarrier the data symbols are assigned to the subcarriers available for data transmission and the remaining subcarriers are filled with zeros. The obtained OFDM symbol  $\mathbf{d} = [d_0, \dots, d_\nu, \dots, d_{N-1}]^T$  is modified such as to suppress sidelobes, e.g. by inserting cancellation carriers as addressed in Chapter 3. The modified OFDM symbol  $\mathbf{d}' = [d'_0, \dots, d'_\nu, \dots, d'_{N-1}]^T$  is then transformed into the time domain by the IDFT and a cyclic prefix (CP) and cyclic suffix (CS) are attached to the time domain data stream. The CP contains a GI with length exceeding the maximum delay of the multi-path channel and  $N_w + \mu$  additional samples required for windowing at Tx and Rx as explained in Chapters 3 and 4, respectively. The CS contains  $N_w$  samples for Tx windowing. Afterwards, the signal  $\mathbf{x} = [x[-N_{GI} - N_w - \mu], \dots, x[0], \dots, x[N + N_w - 1]]^T$  is multiplied with a windowing function in order to further reduce the sidelobes and the Tx signal  $\mathbf{x}^w$  is obtained.

During transmission over the multi-path channel, the OFDM signal is exposed to interference from the licensed systems modelled as an additive signal, i.e. the Rx signal from (2.14) modifies to

$$\mathbf{r} = \mathbf{h} * \mathbf{x}^w + \mathbf{n} + \mathbf{i} \quad (2.18)$$

with  $\mathbf{i}$  representing interference samples for the duration of one OFDM symbol. Samples of the Rx and noise signal are collected in the vectors  $\mathbf{r} = [r[0], \dots, r[k], \dots, r[N + N_{GI} + 2N_w + \mu - 1]]^T$  and  $\mathbf{n} = [n[0], \dots, n[k], \dots, n[N + N_{GI} + 2N_w + \mu - 1]]^T$ , respectively. Samples of the channel impulse response are summarised in  $\mathbf{h} = [h[\tau_o], \dots, h[\tau_{N_D-1}]]^T$ . Summarising the useful part of the Rx signal like in

(2.17) to  $\mathbf{y}^w$ , (2.18) simplifies to

$$\mathbf{r} = \mathbf{y}^w + \mathbf{n} + \mathbf{i} \quad \text{with} \quad \mathbf{y}^w = \mathbf{h} * \mathbf{x}^w. \quad (2.19)$$

At Rx, the part of the CP forming the GI and the  $2 \cdot N_w$  additional samples affected by Tx windowing are discarded. Interference is mitigated in the digital time domain by windowing the Rx signal. With an appropriate choice of the windowing algorithm, the  $\mu$  additional samples required for Rx windowing are removed and the output  $\mathbf{r}^w = [r^w[0], \dots, r^w[N - 1]]^T$  is transformed to the frequency domain by means of an  $N$ -point DFT yielding  $\mathbf{R}^w = [R^w[0], \dots, R^w[N - 1]]^T$ . After the DFT operation additional methods for interference mitigation are applied in the frequency domain resulting in the modified frequency domain Rx signal  $\mathbf{R}'^w = [R'^w[0], \dots, R'^w[N - 1]]^T$ . Afterwards, the Rx data symbols are extracted from the frame and further processed. The methods for sidelobe suppression at Tx and interference mitigation at Rx are presented in Chapter 3 and Chapters 4 and 5, respectively.

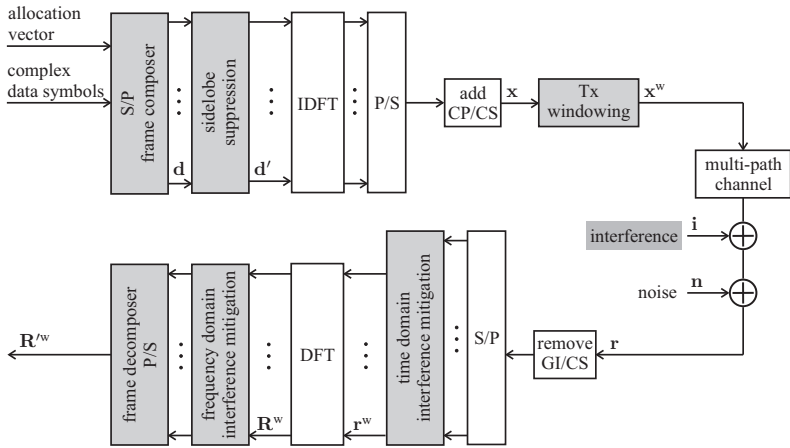


Figure 2.2 Block diagram of OFDM based overlay system.

### 2.2.2 Design Challenges

For the design of an OFDM based overlay system several constraints have to be considered in addition to design rules for conventional OFDM systems. The most

important parameter is subcarrier spacing. In conventional OFDM systems the subcarrier spacing is chosen smaller than the coherence bandwidth of the channel and the OFDM symbol duration, which is the inverse of the subcarrier spacing, has to be smaller than the coherence time of the channel [21]. With this choice of the subcarrier spacing, flat fading can be assumed per subcarrier and the channel can be considered time-invariant for the duration of one OFDM symbol. In overlay systems the subcarrier spacing is additionally determined by the licensed system. For reasons of simplicity an integer multiple of OFDM subcarriers is positioned within one channel of the licensed system. On the one hand, the number of subcarriers per channel should be as large as possible in order to achieve high throughput. On the other hand, signal propagation characteristics have to be considered like in conventional OFDM systems. From this starting point, other parameters such as the bandwidth, the DFT length, and the OFDM symbol duration are determined.

In addition to the adjustment of OFDM parameters, design constraints related to the adaptation of the spectral shape of the Tx signal and suppression of mutual interference between the licensed and the overlay system have to be taken into account as already indicated by the additional blocks in Fig. 2.2. To fulfil the special requirements of an overlay system the following main issues have to be considered for the design of the physical layer of an OFDM system [26]

- Sidelobe suppression at Tx,
- Interference mitigation at Rx,
- Time and frequency synchronisation at Rx,
- Channel estimation at Rx, and
- Detection of spectral gaps.

The suppression of interference from the overlay system towards the licensed system is especially challenging as the licensed system must not be disturbed by the overlay system and does not even notice the existence of the overlay system in the ideal case. Due to the high sidelobes of the OFDM signal, it is not sufficient to turn off the subcarriers in those channels used by the licensed system. In addition, powerful techniques for the reduction of out-of-band radiation are required that are presented in Chapter 3.

Interference from licensed systems towards the overlay system has a significant impact on the performance of the overlay system. Due to the spectral selectivity of



the DFT applied at the OFDM Rx, even narrow-band interference (NBI) degrades performance considerably [27]. Hence, interference has to be minimised in order to enable the operation of the overlay system. Depending on the characteristics of the interference signal, different countermeasures are required. In this thesis, the mitigation of narrow-band and pulsed interference is studied in Chapter 4 and 5, respectively.

Since OFDM is highly sensitive to frequency offsets, phase noise, and timing errors, accurate time and frequency synchronisation is important. In conventional OFDM systems, synchronisation is based on synchronisation symbols transmitted at the beginning of an OFDM frame. Since the synchronisation symbols have to be adapted to the spectrum allocation of the licensed system, the structure and correlation properties of synchronisation symbols are impaired or even destroyed. Moreover, synchronisation symbols are affected by interference from licensed systems which further decreases their characteristics. Hence, synchronisation has to be adapted to the environment of an overlay system. In [28], this has been investigated for the synchronisation algorithms applied in WLAN [13]. All in all, this issue has hardly been addressed in the literature and will not be studied in this thesis.

In the same way, channel estimation is affected. Due to the spectral gaps the distribution of pilot symbols for channel estimation within an OFDM frame is modified. Algorithms for channel estimation, e.g. based on linear interpolation between pilot symbols in time and frequency direction have to be adapted accordingly. Since the impact of interference is reduced after applying appropriate interference mitigation techniques, interference hardly has an impact on channel estimation performed afterwards. Hence, the performance of channel estimation is expected not to degrade significantly provided that it has been adapted to the changing structure of pilot symbols. In future work, this has to be investigated based on the achievements of interference mitigation presented in Chapter 4 and 5.

The detection of spectral gaps is another crucial issue in overlay systems, since the reliable detection first avoids collisions with the licensed system and second ensures the optimal usage of available spectral resources. On the physical layer, spectral gaps can be detected by employing the DFT as already mentioned above. However, higher layers are involved as well, because spectral measurements have to be initiated and the results have to be exchanged and coordinated within the overlay system. In this context, the efficient signalling of allocation information is important for keeping overhead at a minimum. This topic exceeds the scope of this thesis and is addressed e.g. in [29].

## 2.3 Considered Overlay Scenarios

Nowadays, air traffic management and air traffic control (ATC) still employ an analogue voice communication system based on double-sideband amplitude modulation (DSB-AM) in the very high frequency (VHF)- band. Apart from that, only a few data services such as VHF digital link (VDL) exist. However, these systems do not provide sufficient capacity and data rates. With steadily growing air traffic, the capacity limit of existing communication systems is expected to be reached around 2015-2020. Hence, new high data rate digital communication systems are urgently required. One candidate for the future aeronautical communication system is the so-called broadband VHF (B-VHF) [30, 31] system, that is designed as an OFDM based overlay system for the VHF-band. With this approach, the allocation of new spectrum is avoided which would already be difficult with respect to scarce spectral resources. In addition, the in-band transition phase from the current to the future aeronautical communication system, where both systems have to be operated in parallel, is easily realised with an overlay system.

Alternatively, the new aeronautical communication system can be deployed in the aeronautical L-band. That part of the L-band is exclusively used for aeronautical radio-navigation services, but has been assigned to aeronautical communications as well at the World Radiocommunication Conference in 2007 [32]. The allocations are subject to not causing harmful interference to, nor claiming protection from stations operating in the radio-navigation service. Since the operation of navigation systems will be continued in the future, the communication system has to use the spectral gaps. For that purpose, the broadband aeronautical multi-carrier communication (B-AMC) system [33] has been proposed. Since B-AMC uses a contiguous bandwidth within one spectral gap, this system is referred to as inlay system.

Both, the B-VHF as well as the B-AMC system, have to fulfil stringent spectral requirements to protect the licensed systems in the VHF- and the L-band, respectively. In addition, both systems are exposed to severe interference from the respective licensed systems. Hence, the two systems serve as realistic examples of OFDM based overlay systems for investigating the reduction of mutual interference in this thesis.

### 2.3.1 Overlay System in the VHF-Band

The B-VHF system has been developed in the 'Broadband VHF Aeronautical Communications System based on Multi-Carrier Technology' (B-VHF) project co-funded by the European Commission within the 6th framework programme from January 2004 to September 2006. In the project, the feasibility of a new multi-carrier based wideband communication system to support aeronautical communications while operating as an overlay system in the VHF-band has been investigated and demonstrated. B-VHF has shown good potential for satisfying the needs of future aeronautical communications providing various voice and data services for air-ground and air-air communications, high data rates, and high capacity. It has been evaluated and proposed as promising candidate for future aeronautical communications in the future communication study (FCS) [34] carried out jointly by European and US American aviation authorities, namely Eurocontrol and the Federal Aviation Administration (FAA).

Since the B-VHF system is designed as an overlay system, it has to co-exist with already deployed systems in the VHF-band as illustrated in Fig. 2.3. The VHF-band from 118.975 to 137 MHz is subdivided into 760 channels each having a bandwidth of 25 kHz. In order to increase the capacity of the DSB-AM system, some of the channels have been subdivided into three channels with 8.33 kHz bandwidth each. According to measurement flights [35] and worst case interference simulations [36] both carried out within the B-VHF project, about 35%-50% of the VHF spectrum are estimated to be available for the B-VHF system. The actual amount of re-useable spectrum depends on the level of interference the B-VHF system causes at legacy VHF systems and vice versa.

In DSB-AM, pilots and controllers on ground communicate via a common VHF channel assigned to a certain ATC sector or service. All users access this channel according to the listen before push-to-talk principle. Since a listening DSB-AM station cannot be detected by the overlay system, the spectrum allocation of the licensed system cannot be retrieved from spectral measurements. However, as channel assignment is static and the B-VHF overlay system is also employed for aeronautical communications, it can be assumed that information about the channels the B-VHF system is allowed to use in a certain area is available.

The B-VHF system is designed as a cellular system where a bandwidth of 1 MHz is assigned to each cell. This bandwidth spans 40 VHF channels with a bandwidth of 25 kHz or 120 VHF channels with a bandwidth of 8.33 kHz, respectively.

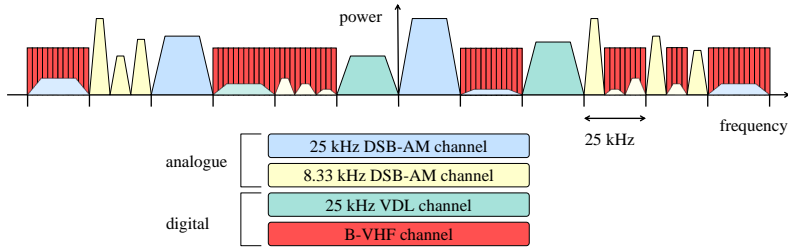


**Figure 2.3** Schematic view of VHF-band usage with B-VHF overlay system.

Each 25 kHz channel is used by 12 OFDM subcarriers, yielding subcarrier spacing  $\Delta f = 2.0833$  kHz which is sufficient with respect to expected Doppler shift and spread. This subcarrier spacing can also be applied to 8.33 kHz channels by using four subcarriers per VHF channel. In total, 480 OFDM subcarriers lie in 1 MHz bandwidth. With 16 guard subcarriers at each side of the spectrum a 512-point DFT is used for OFDM modulation. Each OFDM symbol is extended by a cyclic prefix with ten samples in order to compensate influences of multi-path propagation in the channel. With 43 OFDM symbols per frame and two synchronisation symbols at the beginning of each frame the total frame length yields approximately 22 ms.

The B-VHF frame structure is designed such as to transmit vocoder packages with a size of 96 bit with a data rate of 4.8 kbit/s. Therefore, voice samples from the vocoder output are transmitted uncoded with quadrature phase-shift keying (QPSK) modulation. For data transmission a convolutional code with variable rate from 1/2 to 3/4 and different modulation schemes ranging from QPSK to 64-quadrature amplitude modulation (QAM) are applied for providing different data rates. The packet header is encoded with two extended Golay words with rate 1/2.

In the forward link (FL), i.e. the transmission from ground station to aircraft, OFDM is combined with code-division multiple-access (CDMA) resulting in multi-carrier CDMA (MC-CDMA). In the B-VHF system spreading length 4 is intended, but different spreading lengths, e.g. 8 or 16, are also possible. In the reverse link (RL), i.e. the transmission from aircraft to ground station, orthogonal frequency-division multiple-access (OFDMA) is applied. Different users are separated by assigning different subsets of OFDM subcarriers to each user. Note, for the investigations in this thesis, pure OFDM with one user utilising all available subcarriers is assumed. FL and RL are separated by time-division duplex (TDD). Although a guard time between FL and RL slot is required, this duplex scheme has great advantages over

frequency-division duplex (FDD). Besides other drawbacks, for FDD the paired frequency bands for FL and RL would have to be separated by at least 10 MHz in order to avoid interference. Within a total bandwidth of 19 MHz this would cause difficulties building up a cellular structure. Moreover, TDD enables an easy implementation of air-to-air and party line communications, that allows all aircraft within an air traffic control sector to monitor the conversations between the ground station and all aircraft to gather situation awareness.

**Table 2.1** Basic system parameters of B-VHF overlay system

Parameter	Value
bandwidth	1 MHz
subcarrier spacing	$\Delta f = 8.33 \text{ kHz}/4 = 2.0833 \text{ kHz}$
FFT length	$N = 512$
max. number of useable subcarriers	480
IFFT/FFT Period	$T_O = 480 \mu\text{s} (= 1/\Delta f)$
length of GI	$T_{GI} = 20 \mu\text{s}, N_{GI} = 21 \text{ samples}$
OFDM symbol duration incl. GI	$T_S = 500 \mu\text{s} (= T_O + T_{GI})$
OFDM frame duration	22.5 ms
OFDM symbols per frame	$P = 45$
modulation	BPSK, QPSK, 8-PSK, 16-QAM, or 64-QAM
coding	no coding for voice convolutional code for data Golay code for header
code rate	$R_c = 1/2, 2/3, \text{ or } 3/4$
net data rate	0.312, . . . , 1.404 Mbit/s
duplex scheme	TDD

The key parameters of the B-VHF system are summarised in Tab. 2.1. Assuming that all 480 subcarriers are available for the B-VHF system and considering all overheads in an OFDM transmission frame as well as guard times in the B-VHF frame structure, the provided net data rate can be calculated. For QPSK modulation with code rate  $1/2$  a total data rate of 312 kbit/s for each direction within 1 MHz bandwidth is achieved. If channel conditions are better higher order modulation schemes such as 64-QAM with higher code rates up to  $R_c = 3/4$  is chosen and the data rate can be increased to up to 1.4 Mbit/s. In practical implementations the

useable number of subcarriers may have to be reduced due to restrictions of the Tx filter. Assuming e.g. 432 instead of 480 data subcarriers data rates of 280.8 kbit/s and 1263.6 kbit/s are still possible, respectively.

Further information on the B-VHF system can be found in the project documentation available at [30] or in [37–39].

### 2.3.2 Inlay System in the L-Band

Recent developments have shown that the future aeronautical communication system will more likely be deployed in the aeronautical L-band from 960 to 1164 MHz. For that reason, in 2007, Eurocontrol has initiated the investigation of the utilisation of the B-VHF system in the L-band. Due to significantly different propagation and interference conditions in the L-band, the B-VHF system has to be re-designed resulting in the development of the B-AMC system [33, 40, 41].

The aeronautical L-band is mainly subdivided into 1 MHz channels that are used by aeronautical navigation aids like the distance measuring equipment (DME) or the military tactical air navigation (TACAN) system. In addition, military TDMA network radio systems are operated in this frequency band. The Joint Tactical Information Distribution System (JTIDS) used by the United States armed forces and the Multi-functional Information Distribution System (MIDS) used by NATO utilise channels with a bandwidth of 3 MHz by applying frequency hopping to make the signal jam-resistant. Moreover, some parts of the L-band are allocated to Secondary Surveillance Radar (SSR) that employs two bands of 10 MHz each and Universal Access Transceiver (UAT) that uses one 1 MHz channel at 978 MHz.

The B-AMC system uses the spectral gaps between two adjacent DME channels as depicted in Fig. 2.4. In order to distinguish this deployment concept from an overlay system utilising multiple spectral gaps resulting in a non-contiguous bandwidth, this concept is referred to as inlay concept. To build up a cellular system, the B-AMC system utilises multiple spectral gaps with two channels being assigned to each cell for realising FDD. One channel lies in the frequency range 985-1009 MHz and is used for FL transmissions, the RL channel is in the 1048-1072 MHz sub-band. These frequency ranges have been selected such as to guarantee maximum separation in frequency to SSR and UAT. Moreover, co-site interference between airborne DME and B-AMC devices are intended to be kept at a minimum. Within the frequency ranges, B-AMC channels are assumed to be statically assigned to a certain cell according to frequency planning criteria aim-

ing at keeping mutual interference as small as possible. Nevertheless, the B-AMC system is exposed to severe interference from DME stations operating in the adjacent channels at only  $\pm 500$  kHz offset and JTIDS/MIDS transmissions occurring at  $\pm 0.5$ , 1.5, or 2.5 MHz offset. Due to the small separation in frequency, the B-AMC system causes interference at the licensed systems as well. The reduction of mutual interference in this scenario is addressed in Chapter 5 and Chapter 3, respectively.

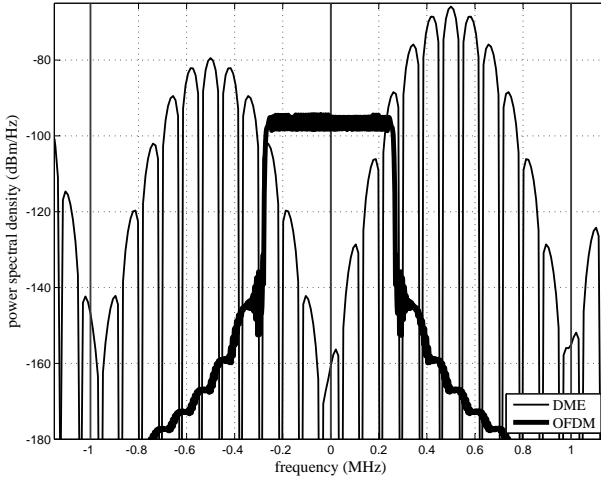


**Figure 2.4** B-AMC as inlay system between two adjacent DME channels.

In a spectral gap between two adjacent DME channels, a bandwidth of 500 kHz is assumed to be available for the B-AMC system. This bandwidth is used by 48 subcarriers with subcarrier spacing  $\Delta f = 10.416$  kHz which is chosen such as to avoid inter-carrier interference (ICI) in the expected propagation conditions. For OFDM modulation, a 64-point DFT is used with eight guard subcarriers at each side of the spectrum. This results in an OFDM symbol duration of  $96 \mu\text{s}$  that is extended by a cyclic prefix as long as  $24 \mu\text{s}$  serving as GI as well as for enabling Tx windowing for reducing out-of-band radiation. 54 OFDM symbols are organised into one OFDM frame resulting in 6.48 ms OFDM frame duration. Reserving six OFDM symbols as synchronisation symbols and pilot symbols for channel estimation, 48 OFDM symbols remain for the transmission of useful data.

B-AMC FL and RL are separated by FDD. In FL, pure OFDM is used and data is transmitted to different users on a packet-switched basis. In RL, different users are

separated by a combination of OFDMA and TDMA. Within one frame, different subcarriers or sets of subcarriers are assigned to different users. In addition, users are separated in time by assigning different subcarrier sets in different frames to different users. That way, transmission time is kept short and interference onto the DME Rx mounted on the same aircraft is restricted to short time intervals.

Modulation and coding are adapted depending on interference and channel conditions. For severe interference conditions, a convolutional code is concatenated with a Reed-Solomon code, where the Reed-Solomon code is intended to correct burst errors occurring after decoding the convolutional code due to interference from DME and JTIDS/MIDS. With modulation schemes ranging from QPSK to 64-QAM and code rates 1/2, 2/3, or 3/4 for the convolutional code and 0.89 or 1 for the Reed-Solomon code, net data rates of 272 kbit/s to 1.361 Mbit/s are achieved. Thereby, overheads in the OFDM frame as well as overheads in the OFDM framing structure are considered.

**Table 2.2** Basic system parameters of B-AMC inlay system.

Parameter	Value
bandwidth	500 kHz
subcarrier spacing	$\Delta f = 10.416$ kHz
FFT length	$N = 64$
number of used subcarriers	48
cancellation carriers	$2 \cdot 2 = 4$
IFFT/FFT Period	$T_O = 96 \mu s (= 1/\Delta f)$
OFDM symbol duration incl. CP	$T_S = 120 \mu s$
length of CP	$T_{CP} = 24 \mu s, N_{CP} = 16$ samples
composed of GI and	$T_{GI} = 12 \mu s, N_{GI} = 8$ samples
samples for Tx windowing	$T_w = 12 \mu s, N_w = 8$ samples
OFDM symbols per frame	$P = 54$
OFDM frame duration	6.48 ms
modulation	QPSK, 8-PSK, 16-QAM, or 64-QAM
coding	concatenated convolutional and Reed-Solomon code
total code rate	$R_c = 0.445, \dots, 0.75$
net data rate	0.272, ..., 1.361 Mbit/s
duplex scheme	FDD



# 3 Suppression of Out-of-Band Radiation

High out-of-band radiation is a well-known drawback of OFDM systems that restricts the efficient use of the available spectrum. The fact that OFDM sidelobes only decay with  $1/f$  [42] constitutes a problem in particular in OFDM based overlay systems. In the channels not used by the overlay system, out-of-band radiation causes interference at licensed systems and hence has to be reduced in order to enable co-existence between the two systems.

Conventional techniques for reducing out-of-band radiation such as the insertion of guard bands and pulse shaping or Tx windowing do not provide that level of sidelobe suppression required in OFDM based overlay systems. Motivated by that, advanced techniques for sidelobe suppression have been developed. These techniques aim at modifying the Tx sequence in the frequency domain in such a way that the sidelobes of the individual subcarrier spectra superimpose such as to mainly cancel each other. This is realised by means of subcarrier weighting that weights each subcarrier with a real-valued factor, where the weighting factors are determined according to an optimisation criterion that minimises the sidelobe power [43]. Alternatively, with the multiple-choice sequences method, the Tx sequence is mapped onto a set of equivalent Tx sequences all carrying the same information. For the actual transmission that sequence with the smallest sidelobe power is selected [44]. A third approach is based on the insertion of a few subcarriers referred to as cancellation carriers (CC) at both sides of the spectrum [45]. These CCs carry complex weighting factors that are optimised such that the sidelobes of the CCs cancel the sidelobes of the original Tx signal to the maximum possible extend. With these techniques or combinations of these techniques, sidelobe power can be reduced considerably at the cost of slightly increased bit error rate (BER) or reduced throughput.

The remainder of this chapter is organised as follows. In the first section, commonly used techniques for reducing out-of-band radiation in conventional OFDM systems are recapitulated briefly. The next section starts with a detailed description of the emitted OFDM Tx spectrum since this is an essential basis for all advanced techniques for sidelobe suppression presented in the following subsections. For further

improving the performance of the proposed techniques, they can be either combined with windowing or with each other. Suitable combinations are described in Section 3.3. Finally, in Section 3.4, simulation results are presented for a simple overlay system and the different techniques are compared with respect to the provided sidelobe power reduction and their impact on the performance of the OFDM system.

## 3.1 Conventional Techniques

In OFDM systems using a contiguous bandwidth, out-of-band radiation has to be reduced in order not to interfere with OFDM systems operating in adjacent channels or with other systems operating in adjacent frequency bands. For that purpose, basically two approaches exist, namely Tx windowing and the insertion of guard bands at the edges of the spectrum. Both methods are briefly described and their advantages and drawbacks in general as well as in the context of OFDM based overlay systems are analysed.

### 3.1.1 Windowing

The time domain Tx signal is multiplied with a windowing function in order to improve the spectral characteristics of the individual subcarriers, thus reducing spectral emissions of the entire OFDM signal [46]. This technique is dual to pulse shaping where the multiplication is performed in the frequency domain by multiplying the entire OFDM spectrum with a filter function that reduces out-of-band radiation.

As illustrated in Fig. 3.1, the windowing function is designed such that the useful part of the OFDM symbol including GI is not affected by the leading and trailing edges of the window. Therefore, the OFDM symbol is extended by a cyclic prefix (CP) and suffix (CS) corresponding to the roll-off factor  $\beta$  of the window. Hence, prefix and suffix contain

$$N_{\text{CP}} = N_{\text{GI}} + N_{\text{w}} \quad \text{and} \quad N_{\text{CS}} = N_{\text{w}} \quad (3.1)$$

samples with

$$N_{\text{w}} = \beta \frac{N + N_{\text{GI}}}{1 - \beta}. \quad (3.2)$$

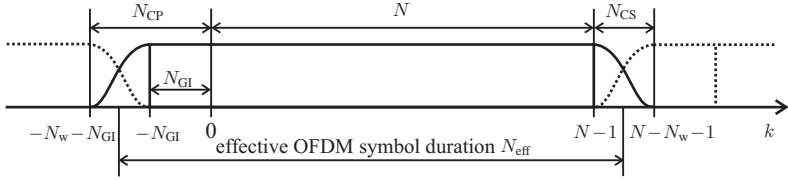


**Figure 3.1** Principle of Tx windowing.

In order to keep the throughput loss induced by the symbol extension at a minimum, consecutive OFDM symbols overlap in the roll-off region of the window such that the effective length  $N_{\text{eff}}$  of the OFDM symbol equals [46]

$$N_{\text{eff}} = N + N_{\text{GI}} + N_{\text{w}} = (N + N_{\text{GI}})/(1 - \beta). \quad (3.3)$$

In the time domain, windowing smoothes the sharp phase transitions between consecutive OFDM symbols. In the frequency domain, the spectra of individual subcarriers have lower sidelobes than the si-spectrum obtained with conventional rectangular windowing. The performance of the commonly used raised-cosine (rc) window with different roll-off factors is illustrated in Fig. 3.2 for a simple overlay system. In the outer areas of the spectrum out-of-band radiation is reduced significantly even for small roll-off factors. However, in a spectral gap spanning only 12 subcarriers, sidelobe suppression is considerably smaller. Hence, windowing does not provide the degree of sidelobe suppression required in OFDM based overlay systems. Even with improved window shapes such as the better-than raised cosine window [47] or optimised shapes [48, 49] sidelobe reduction cannot be improved significantly.

The sidelobe suppression achieved with windowing goes in with a throughput reduction due to the extended length of the OFDM symbol. The throughput loss  $D^{\text{loss}}$  corresponds to the roll-off factor of the window as

$$D^{\text{loss}} = 1 - \frac{N + N_{\text{GI}}}{N + N_{\text{GI}} + N_{\text{w}}} = \beta. \quad (3.4)$$

### 3.1.2 Guard Bands

Another commonly used approach for reducing out-of-band radiation is the insertion of guard bands at the edges of the spectrum as applied e.g. in WLAN [13]. As

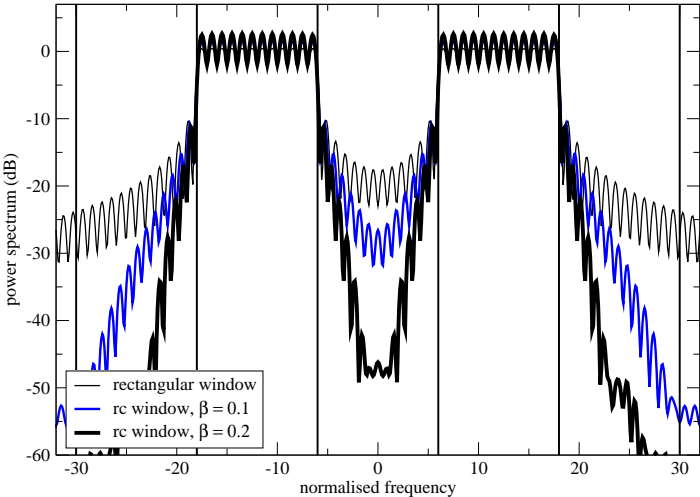


Figure 3.2 Spectra of OFDM signals after rc windowing with different roll-off factors.

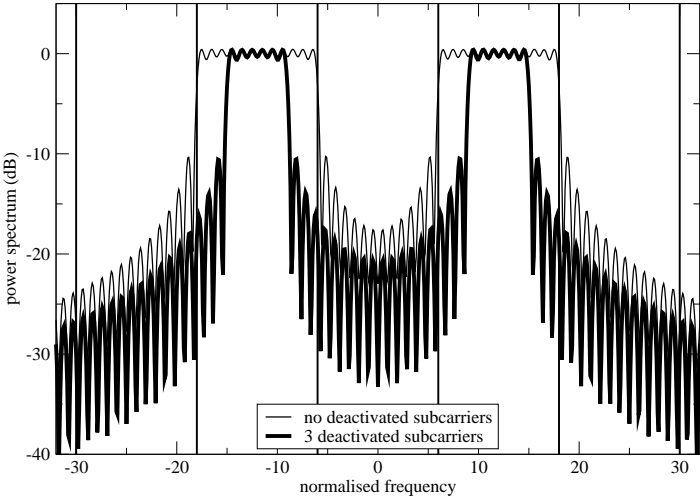
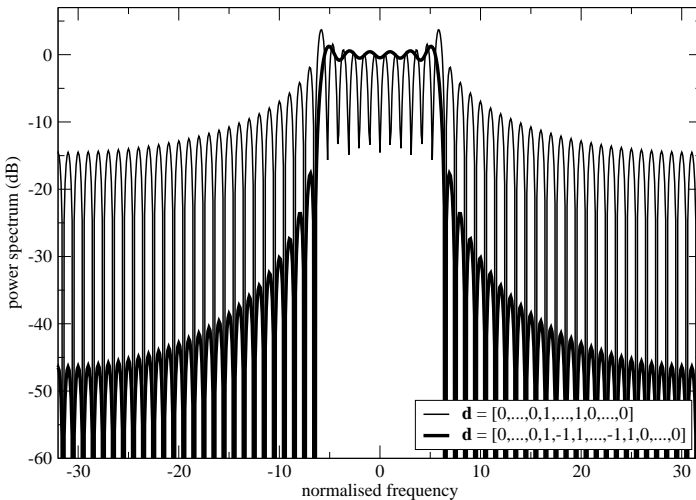


Figure 3.3 Spectra of OFDM signals with deactivation of different numbers of subcarriers.

OFDM sidelobes only decay with  $1/f$ , only a moderate reduction of out-of-band radiation is achieved. At the same time spectral efficiency is sacrificed unless the subcarriers at the edges of the spectrum cannot be used for data transmission anyway to avoid non-ideal filter flanks impairing data bearing subcarriers. As can be seen from Fig. 3.3, the insertion of guard subcarriers is not viable for overlay systems as spectral resources are wasted while achieving only moderate suppression of out-of-band radiation.

## 3.2 Advanced Techniques

In OFDM based overlay systems sidelobes do not only have to be suppressed at the outer edges of the spectrum, but also in the spectral gaps, where licensed systems are operated. The conventional techniques for sidelobe suppression presented in the previous section have been investigated for the application in OFDM based overlay systems in [50]. The reduction of out-of-band radiation with conventional techniques is related to significant throughput and bandwidth losses for the overlay system hence demanding for more powerful techniques to overcome these drawbacks.



**Figure 3.4** Spectra of OFDM signals with different Tx sequences,  $N = 64$ ,  
 $N_{\text{used}} = 12$ .

For reducing sidelobes the fact that the OFDM spectrum is different for different Tx sequences is exploited. This is illustrated in Fig. 3.4 for an OFDM system with  $N = 64$  subcarriers of which  $N_{\text{used}} = 12$  subcarriers in the centre are modulated either with '1' or with '1' and '-1' alternately. Depending on how the sidelobes of the individual subcarriers superimpose, the spectra of different Tx sequences differ considerably and about 30 dB difference in sidelobe power is observed. The advanced techniques for sidelobe suppression presented in the following all aim at modifying the Tx sequence such that the individual subcarrier spectra superimpose in a more favourable way and the resulting spectrum exhibits lower sidelobes. For determining the modified Tx sequence as well as the expected sidelobe power, the emitted Tx spectrum has to be modelled as realistically as possible. This is addressed in the next subsection before three advanced sidelobe suppression techniques are presented.

### 3.2.1 OFDM Tx Spectrum

After the IDFT at the OFDM Tx, an infinite sequence of a periodically repeated OFDM signal is obtained. To cut out a single period forming one OFDM symbol, the sequence is multiplied with a rectangular window. Its length corresponds to the length of one OFDM symbol, that in turn determines the subcarrier spacing, i.e.  $T_O = 1/\Delta f$ . In addition, a cyclic prefix forming the GI is considered and the length of the window is extended accordingly to cut out  $N + N_{\text{GI}}$  samples. In the frequency domain, this multiplication is equivalent to a convolution of the frequency domain OFDM signal and the Fourier transform of the rectangular window. Skipping the details provided in Appendix A, the Tx spectrum of the  $\nu$ th subcarrier is obtained as

$$S_\nu[n] = d_\nu \exp\left(-j\pi(n/V - \nu)\frac{N - N_{\text{GI}} - 1}{N}\right) \cdot \frac{\sin(\pi(N + N_{\text{GI}})(n/V - \nu)/N)}{\sin(\pi(n/V - \nu)/N)}, \quad n = 0, \dots, V \cdot N - 1. \quad (3.5)$$

In order to get a higher resolution of the Tx spectrum  $V$ -times over-sampling is introduced resulting in  $V \cdot N$  instead of  $N$  samples representing the spectrum of one subcarrier in the OFDM bandwidth.

As can be seen from (3.5), the subcarrier spectrum depends on the Tx symbol  $d_\nu$ . Moreover, the GI has an impact on the subcarrier spectrum when observing the

OFDM signal emitted at the Tx output. The subcarrier spacing is maintained, but the zero-crossings of the sine are shifted such that the width of the mainlobe and the sidelobes narrows by factor  $\frac{N}{N+N_{GI}}$ . As a consequence, subcarrier orthogonality is lost and the sidelobes do not superimpose in their maxima resulting in slightly lower sidelobes. This effect is illustrated in Fig. 3.5 for the spectra of two adjacent subcarriers. For comparison, in the left part, the case without GI is shown.

Note, the loss of subcarrier orthogonality is only observed in the emitted OFDM spectrum. At Rx, orthogonality is restored when removing the GI and considering segments of the OFDM signal with length coinciding with the DFT period.

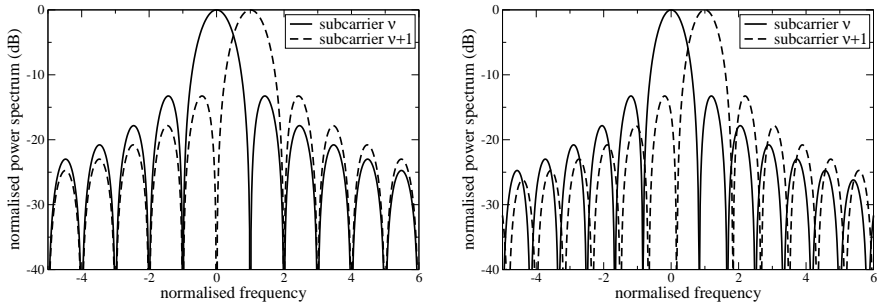


**Figure 3.5** Subcarrier spectra without GI (left) and with GI (right).

For sidelobe suppression, the spectrum is of interest in a certain optimisation range outside the used transmission bandwidth. From (3.5),  $N_K$  samples of the spectrum of the  $\nu$ th subcarrier in the optimisation range are determined and collected in the column vector

$$\mathbf{S}_\nu = [S_\nu[0], \dots, S_\nu[k], \dots, S_\nu[N_K - 1]]^T. \quad (3.6)$$

In the same way, all other subcarrier spectra are determined and summarised in the matrix

$$\mathbf{S} = [\mathbf{S}_0, \dots, \mathbf{S}_\nu, \dots, \mathbf{S}_{N-1}]. \quad (3.7)$$

Omitting the unmodulated subcarriers in (3.7),  $\mathbf{S}$  can be reduced to its  $N_{\text{used}}$  relevant columns with  $N_{\text{used}}$  denoting the number of used subcarriers

$$\mathbf{S} = [\mathbf{S}_0, \dots, \mathbf{S}_m, \dots, \mathbf{S}_{N_{\text{used}}-1}]. \quad (3.8)$$

Thereby, the subcarrier indices  $\nu$  of all subcarriers in the OFDM bandwidth are mapped onto indices  $m$  of the used subcarriers according to the allocation vector.

To keep matrix dimensions small and with that complexity of the sidelobe suppression techniques, it is sufficient to consider ten-times over-sampling of the OFDM spectrum at the maximum. Depending on the overlay system and the width of the spectral gaps, the optimisation range needs to span five to ten sidelobes at each edge of the spectrum starting with the first sidelobe outside the used bandwidth. When an OFDM signal with a large number of subcarriers in a contiguous bandwidth is considered, the OFDM spectrum can be well approximated by the spectrum of the ten outermost subcarriers while neglecting the influence of the subcarriers in the centre of the bandwidth.

All methods for sidelobe suppression aim at modifying the Tx sequence such as to reduce the sidelobe power, i.e.

$$\Psi = \sum_{k=0}^{N_k-1} \left| \sum_{\nu=0}^{N-1} S'_\nu[k] \right|^2 \rightarrow \min. \quad (3.9)$$

The subcarrier spectra  $S'_\nu$ ,  $\nu = 0, \dots, N-1$ , are generated according to (3.5), but with using the complex symbols  $d'_\nu$ ,  $\nu = 0, \dots, N-1$ , of the modified Tx sequence.

### 3.2.2 Subcarrier Weighting

In [43], subcarrier weighting (SW) has been proposed as a means for reducing out-of-band emissions of the OFDM signal.

#### Principle

All used subcarriers are multiplied with real-valued weighting factors  $g_m$ ,  $m = 0, \dots, N_{\text{used}} - 1$ , with the aim to shape the sidelobes of all subcarriers such that they cancel each other. The modified Tx symbols yield

$$d'_m = g_m d_m, \quad m = 0, \dots, N_{\text{used}} - 1. \quad (3.10)$$

The weighting factors for all used subcarriers are collected in the weighting matrix  $\mathbf{G} = \text{diag}\{g_0, \dots, g_m, \dots, g_{N_{\text{used}}-1}\}$ . Optimal weighting factors are determined by minimising the power of the weighted OFDM signal in the considered optimisation range according to

$$\mathbf{G} = \arg \min_{\mathbf{G}} \|\mathbf{S}\tilde{\mathbf{G}}\|^2, \quad (3.11)$$



where  $\tilde{\mathbf{G}}$  is a trial value of  $\mathbf{G}$ . To ensure the modified Tx sequence to consume the same power as the original Tx sequence a constraint is introduced, i.e.

$$\|\mathbf{d}'\|^2 = \|\mathbf{d}\|^2. \quad (3.12)$$

For PSK modulation, where all symbols of the modulation alphabet have the same amplitude  $|d_m| = 1$ , this constraint simplifies to

$$\sum_{m=0}^{N_{\text{used}}-1} |g_m|^2 = N_{\text{used}}. \quad (3.13)$$

In order to allow the modified Tx sequences to be detected at Rx without transmitting any side information from Tx to Rx, it has to be guaranteed that the modified symbol  $d'_m$  remains in the same decision region as the original symbol  $d_m$ . Thus, the weighting factors have to be real-valued and lie between pre-defined limits  $g_{m,\min}$  and  $g_{m,\max}$  resulting in a second constraint for the optimisation problem from (3.11)

$$0 < g_{m,\min} \leq g_m \leq g_{m,\max}, \quad g_{m,\min}, g_{m,\max}, g_m \in \mathbb{R}, \quad m = 0, \dots, N_{\text{used}} - 1. \quad (3.14)$$

For PSK modulation, the lower and upper limits are the same for all complex symbols from the modulation alphabet, i.e.  $g_{m,\min} = g_{\min}$  and  $g_{m,\max} = g_{\max} \forall m$ . However, in the more general case of QAM, where the complex symbols of the modulation alphabet have different amplitudes, the absolute values of the lower and upper bounds of the weighting factors depend on the regarded symbol. Setting the lower and upper limit for the weighting factors equally distant to the considered Tx symbol  $d_m$

$$g_{m,\min} = |d_m|^2 \left(1 - \frac{\rho - 1}{\rho + 1}\right), \quad g_{m,\max} = |d_m|^2 \left(1 + \frac{\rho - 1}{\rho + 1}\right) \quad (3.15)$$

is obtained. The ratio between the upper and the lower bound,  $\rho = g_{\max}/g_{\min}$ , is the same for all complex symbols from the modulation alphabet.

The optimisation problem given in (3.11), together with the constraints in (3.12) and (3.14), can be generalised to a nonlinear programming problem with a quadratic equality (3.12) and a linear inequality constraint (3.14). To solve such an optimisation problem many effective and reliable numerical algorithms exist, e.g. the projected Lagrangian method [51].

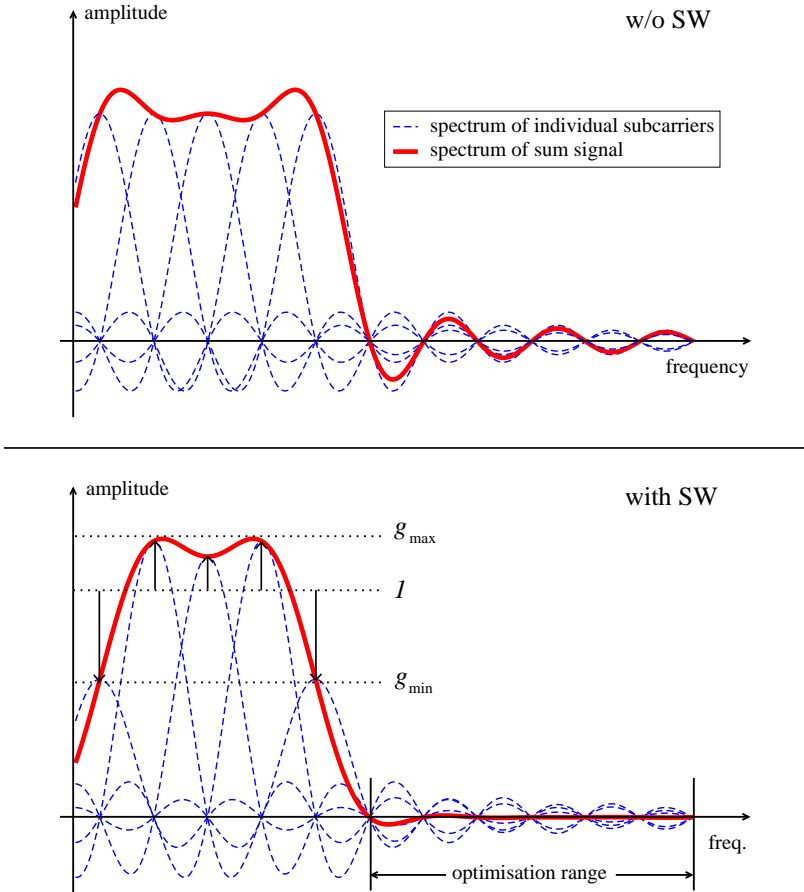


**Figure 3.6** Illustration of the SW technique: standard OFDM signal without SW and OFDM signal with SW.

The principle of SW is illustrated in Fig. 3.6 for  $N_{\text{used}} = 6$  subcarriers and Tx symbol  $\mathbf{d} = [0, \dots, 0, 1, -1, 1, -1, 1, -1, 0, \dots, 0]^T$ . The optimisation range spans six sidelobes at each side of the useful OFDM bandwidth starting with the first sidelobe outside the transmission bandwidth. Per sidelobe, ten frequency samples are considered resulting in an optimisation range comprising  $N_K = 120$  samples. Note,

for reasons of clarity, only the right part of the optimisation range is displayed. For the same reason, the phase in the subcarrier spectra as given in (3.5) is not considered in Fig. 3.6. Taking into account  $\rho = 2$ , the weighting matrix is determined as  $\mathbf{G} = \text{diag}\{0.66, 1.33, 0.66, 0.66, 1.33, 0.66\}$  with  $g_{\min} = 0.66$  and  $g_{\max} = 1.33$ . Comparing the original OFDM spectrum with the modified OFDM spectrum, it can be clearly seen that the weighting factors shape the subcarrier spectra such that the entire OFDM signal exhibits significantly lower sidelobes.

### Impact on System Performance

As the subcarriers receive unequal amounts of Tx power due to weighting, signal-to-noise ratio (SNR) varies from subcarrier to subcarrier and BER performance is affected. In general, the bit error probability  $P_b$  for a BPSK modulated signal transmitted over a channel with random attenuation factor is given as [52]

$$P_b = \int_0^{\infty} p(\gamma'_b) \cdot \text{erfc}(\gamma'_b) d\gamma'_b, \quad (3.16)$$

where  $\gamma'_b = |g|^2 \gamma_b = |g|^2 E_b/N_0$  is the SNR per bit observed after applying subcarrier weighting.  $E_b$  and  $N_0$  are the energy per bit and the noise spectral density, respectively.  $\gamma_b = E_b/N_0$  is the SNR per bit. The probability density function  $p(\gamma'_b)$  describes the influence of the channel represented by the random variable  $\gamma_b$  as well as of power fluctuations due to SW represented by the random variable  $g$ . As the two effects are independent,  $p(\gamma'_b)$  can be split up into two statistically independent probability density functions  $p^{\text{SW}}(g)$  and  $p(\gamma_b)$ . Assuming flat Rayleigh fading on each subcarrier, the channel influence is represented by a Rayleigh-distributed probability density function  $p(\gamma_b)$  that simplifies (3.16) to

$$P_b = \frac{1}{2} \int_0^{\infty} p^{\text{SW}}(g) \cdot \left( 1 - \sqrt{\frac{|g|^2 \gamma_b}{1 + |g|^2 \gamma_b}} \right) dg. \quad (3.17)$$

Since the weighting factors mainly take values close to  $g_{\min}$  and  $g_{\max}$ , respectively, the power density function of the power fluctuations caused by SW is approximated by a Dirac's delta function at  $g_{\min}$  with probability  $\epsilon \in (0,1)$  and a Dirac's delta function at  $g_{\max}$  with probability  $1 - \epsilon$

$$p^{\text{SW}}(g) = \epsilon \delta(g - g_{\min}) + (1 - \epsilon) \delta(g - g_{\max}). \quad (3.18)$$

Substituting (3.18) into (3.17), the bit error probability  $P_b$  taking into account the influences of SW can be approximated by

$$P_b = \frac{1}{2} \left( 1 - \epsilon \sqrt{\frac{|g_{\min}|^2 \gamma_b}{1 + |g_{\min}|^2 \gamma_b}} - (1 - \epsilon) \sqrt{\frac{|g_{\max}|^2 \gamma_b}{1 + |g_{\max}|^2 \gamma_b}} \right). \quad (3.19)$$

### 3.2.3 Multiple-Choice Sequences

A different approach aims at directly exploiting the fact that different Tx sequences have different spectral characteristics as shown in Fig. 3.4. This method referred to as multiple-choice sequences (MCS) maps the original Tx sequence onto another Tx sequence with lower sidelobes as proposed in [44, 53]. Similar concepts have been considered e.g. in [54, 55] for reducing the peak-to-average power ratio (PAPR).

#### Principle

From the original Tx sequence  $\mathbf{d}$ , a set of  $Q > 1$  equivalent Tx sequences  $\mathbf{d}^{(q)} = [d_0^{(q)}, \dots, d_{N-1}^{(q)}]^T$ ,  $q = 1, \dots, Q$ , of the same length is generated. This MCS set of  $Q$  sequences also contains the original Tx sequence. For each sequence, the sidelobe power  $\Psi^{(q)}$  in a certain optimisation range is calculated according to

$$\Psi^{(q)} = \sum_{k=0}^{N_K-1} \left| \sum_{m=0}^{N_{\text{used}}-1} S_m^{(q)}[k] \right|^2, \quad q = 1, \dots, Q, \quad (3.20)$$

with  $S_m^{(q)}[k]$  from (3.5) modulated with the complex data symbol  $d_m^{(q)}$ . For transmission, the sequence with the lowest sidelobe power is selected. Thus, the index  $\mathcal{Q}$  of the Tx sequence is determined by

$$\mathcal{Q} = \arg \min_q \Psi^{(q)}, \quad q = 1, \dots, Q, \quad (3.21)$$

and the sequence  $\mathbf{d} = \mathbf{d}^{(\mathcal{Q})}$  is transmitted.

At Rx, the received sequence has to be de-mapped onto the original sequence. Provided the rules for constructing the MCS set are fixed and known at both Tx and Rx, it is sufficient to signal the index of the selected Tx sequence from Tx to Rx. The index of the Tx sequence  $\mathcal{Q}$  is coded in bits, mapped onto complex symbols and sent to Rx via a separate signalling channel. For example, for an OFDM system

with  $N_{\text{used}}$  used subcarriers modulated with  $M$ -ary PSK or  $M$ -ary QAM symbols, the overhead for signalling information translates to a throughput loss

$$D^{\text{loss}} = \frac{\lceil \log_2(Q) \rceil}{\log_2(M) \cdot N_{\text{used}} + \lceil \log_2(Q) \rceil}, \quad (3.22)$$

where  $\lceil \cdot \rceil$  returns the smallest integer greater than or equal to the argument.

### MCS Algorithms

From the variety of many different possible approaches for generating the MCS set, three simple approaches from [44] are presented for illustration.

#### *Symbol Constellation Approach*

With the symbol constellation approach, a set of MCS sequences is generated such that the elements of the modified Tx sequences remain in the same modulation alphabet as the original sequence.

The elements of an  $M$ -ary PSK or  $M$ -ary QAM constellation consisting of  $M$  symbols are numbered as  $0, \dots, M - 1$ . The complex symbols of the original Tx sequence  $d_m, m = 0, \dots, N_{\text{used}} - 1$ , are equivalently described by the index  $e_m$  of the corresponding symbol in the symbol constellation. For generating the MCS set, a new index  $e_m^{(q)}$  is determined randomly by adding a random integer  $\iota_m^{(q)} \in \{0, \dots, M - 1\}$  to the original index  $e_m$  yielding

$$e_m^{(q)} = \left( (e_m + \iota_m^{(q)}) \bmod M \right), \quad m = 0, \dots, N_{\text{used}} - 1, \quad q = 1, \dots, Q. \quad (3.23)$$

The elements of the modified Tx sequences  $d_m^{(q)}$  belonging to the MCS set is determined by reassigning the indices  $e_m^{(q)}$  to symbols from the symbol constellation.

When assuming that the same random generator and the same random seed are used at both Tx and Rx, the received sequence can be re-transformed to the original sequence provided that the index  $Q$  of the selected Tx sequence has been signalled from Tx to Rx.

#### *Interleaving Approach*

In contrast to the symbol constellation approach, where complex symbols may occur in the modified Tx sequences of the MCS set, that have not been contained in the original Tx sequence, the interleaving approach is restricted to permute the complex symbols of the original Tx sequence. The MCS set is generated according

to

$$\mathbf{d}^{(q)} = \mathbf{\Pi}^{(q)} \mathbf{d}, \quad q = 1, \dots, Q, \quad (3.24)$$

where  $\mathbf{\Pi}^{(q)}$  is the  $q$ th permutation matrix stored at both Tx and Rx. The permutation matrix is generated such that interleaving is only performed among the complex symbols on the used subcarriers.

### Phase Approach

With the phase approach, random phase shifts are applied to the complex symbols of the original Tx sequence. The modified symbols contained in the MCS set are determined by

$$d_m^{(q)} = d_m \exp\left(j\varphi_m^{(q)}\right), \quad m = 0, \dots, N_{\text{used}} - 1, \quad q = 1, \dots, Q, \quad (3.25)$$

where the phase shifts  $\varphi_m^{(q)}$  lie in the interval  $[0, 2\pi)$  and can take one of  $\mathcal{P}$  discrete values. The discrete phase shifts are generated as

$$\varphi_m^{(q)} = 2\pi \left( \frac{\iota_m^{(q)}}{\mathcal{P}} \right). \quad (3.26)$$

In (3.26),  $\mathcal{P}$  is a constant integer and  $\iota_m^{(q)}$  is an integer randomly chosen from the set  $\iota_m^{(q)} \in \{0, \dots, \mathcal{P} - 1\}$ . Again, the same random seeds are used at Tx and Rx in order to allow for reconstructing the original Tx sequence at Rx. Note that assuming an  $M$ -ary PSK system and  $\mathcal{P} = M$ , this approach becomes equivalent to the corresponding symbol constellation approach.

## 3.2.4 Cancellation Carriers

Another promising approach for reducing high OFDM sidelobes is the insertion of so-called cancellation carriers (CC) at both sides of the used OFDM spectrum. These CCs are not used for data transmission but carry complex weighting factors that are optimised such that the sidelobes of the CCs compensate the sidelobes of the Tx signal [45]. In [56] and [57], a similar concept based on so-called dummy or compensation tones has been proposed. However, these subcarriers are restricted to carry weighted sums of the data transmitted on the current or on previous OFDM symbols, respectively. Moreover, this basic idea of this concept has been exploited for PAPR reduction in [58, 59]. In [60], the approaches from [45] and [59] have

been combined to optimise CCs with the aim to simultaneously reducing out-of-band radiation and PAPR. It has been shown that PAPR can be reduced in parallel with only a small loss in the achievable sidelobe power reduction.

### Principle

As depicted in Fig. 3.7, some unused subcarriers in the guard band at each side of the used spectrum are replaced by CCs. Note, to keep the illustration simple, the phase in the subcarrier spectra as given in (3.5) is not considered in Fig. 3.7. In the considered example,  $N_{CC} = 2$  CCs are inserted at each side of the spectrum directly adjacent to the  $N_{used} = 12$  data subcarriers. The complex weights  $g_c, c = 0, \dots, 2N_{CC} - 1$ , transmitted on the CCs are optimised such that the spectra of the CCs are shaped to cancel the sidelobes of the original Tx signal in a certain optimisation range. That way, the Tx sequence is extended by  $2N_{CC}$  complex values at designated positions in the OFDM symbol and the modified Tx sequence equals

$$\mathbf{d}' = \sqrt{A^{\text{norm}}} \cdot [0, \dots, 0, \underbrace{g_0, \dots, g_{N_{CC}-1}}_{\text{CCs}}, \underbrace{d_0, \dots, d_{N_{used}-1}}_{\text{data subcarriers}}, \underbrace{g_{N_{CC}}, \dots, g_{2N_{CC}-1}}_{\text{CCs}}, 0, \dots, 0]^T. \quad (3.27)$$

The normalisation factor  $0 < \sqrt{A^{\text{norm}}} \leq 1$  is introduced in order to retain the same Tx power in the case with and without CCs, i.e.

$$\|\mathbf{d}'\|^2 = \|\mathbf{d}\|^2. \quad (3.28)$$

The weighting factors for CCs are determined for each OFDM symbol individually in order to achieve an optimal sidelobe suppression. For the example from Fig. 3.7 with  $d_m = 1, m = 0, \dots, N_{used} - 1$ , the weighting factors  $g_0 = g_3^* = -1.10 + 0.04j$  and  $g_1 = g_2^* = -0.88 + 0.03j$  are determined. The power spent for CCs is limited to 25% of the total Tx power. It can be seen that the spectrum of the modified Tx signal, which is the superposition of the original Tx signal and the weighted CC spectra, exhibits significantly lower sidelobes than the original Tx signal.

### Optimisation Algorithm

For determining the weighting factors, the sidelobe power of the modified Tx signal composed of the original Tx signal and the weighted CCs has to be minimised in the optimisation range. The spectrum of the original Tx signal is the sum of all

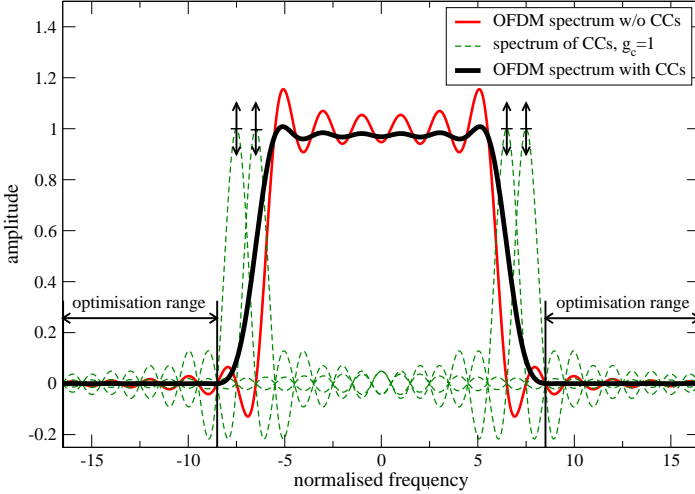


**Figure 3.7** Principle of insertion of cancellation carriers,  $N_{\text{used}} = 12$ ,  $d_m = 1$ ,  $m = 0, \dots, N_{\text{used}} - 1$ ,  $N_{\text{CC}} = 2$ ,  $g_0 = g_3^* = -1.10 + 0.04j$ ,  $g_1 = g_2^* = -0.88 + 0.03j$ .

subcarrier spectra given in (3.5). The  $N_K$  samples in the optimisation range are collected in the vector

$$\mathbf{S}^{\text{sum}} = \left[ \sum_{m=0}^{N_{\text{used}}-1} S_m[0], \dots, \sum_{m=0}^{N_{\text{used}}-1} S_m[N_K - 1] \right]^T. \quad (3.29)$$

With samples of the CC spectra summarised in the  $(N_K \times 2N_{\text{CC}})$ -dimensional matrix  $\mathbf{C}$  and the weighting factors collected in the column vector  $\mathbf{g} = [g_0, \dots, g_c, \dots, g_{2N_{\text{CC}}-1}]^T$ , the optimisation problem can be formulated as

$$\min_{\mathbf{g}} \|\mathbf{S}^{\text{sum}} + \mathbf{C} \cdot \mathbf{g}\|^2 \quad \text{subject to} \quad \|\mathbf{g}\|^2 \leq \alpha. \quad (3.30)$$

The constraint in (3.30) is introduced in order to limit the amount of Tx power spent on CCs. One algorithm for solving this linear least squares problem with quadratic inequality constraint (LSQI) is based on a generalised singular value decomposition (GSVD) [61, 62]. That way, the optimisation problem can be reduced to a linear system and further simplifies due to the simple structure of the constraint.

Extending the constraint in (3.30) by the  $(2N_{\text{CC}} \times 2N_{\text{CC}})$  identity matrix  $\mathbf{B} =$



$\mathbf{E}_{2N_{CC}}$ , the optimisation problem is rewritten by means of a GSVD

$$\begin{aligned} \mathbf{U}^T \mathbf{C} \mathbf{X} &= \text{diag}(\gamma_0, \dots, \gamma_{2N_{CC}-1}) = \mathbf{D}_C, \\ \mathbf{V}^T \mathbf{B} \mathbf{X} &= \text{diag}(\beta_0, \dots, \beta_{2N_{CC}-1}) = \mathbf{D}_B, \\ \gamma_c &\geq 0, \beta_c \geq 0, c = 0, \dots, 2N_{CC} - 1, \end{aligned} \quad (3.31)$$

where  $\mathbf{U}$  and  $\mathbf{V}$  are orthogonal matrices of the dimensions  $(N_K \times N_K)$  and  $(2N_{CC} \times 2N_{CC})$ , respectively.  $\mathbf{X}$  is a  $(2N_{CC} \times 2N_{CC})$  non-singular matrix. Defining  $\tilde{\mathbf{S}} = \mathbf{U}^T \mathbf{S}^{\text{sum}}$  and  $\tilde{\mathbf{g}} = \mathbf{X}^{-1} \mathbf{g}$  the optimisation problem from (3.30) transforms to

$$\min_{\tilde{\mathbf{g}}} \left\| \tilde{\mathbf{S}} + \tilde{\mathbf{g}} \cdot \mathbf{D}_C \right\|^2 \quad \text{subject to} \quad \left\| \mathbf{D}_B \cdot \tilde{\mathbf{g}} \right\|^2 \leq \alpha. \quad (3.32)$$

When the constraint is neglected the weighting factors for CCs are easily obtained by

$$\tilde{g}_c = \begin{cases} \tilde{S}_c / \gamma_c & \gamma_c \neq 0 \\ 0 & \gamma_c = 0 \end{cases}, c = 0, \dots, 2N_{CC} - 1 \quad (3.33)$$

and transforming  $\tilde{g}_c$  to  $g_c$ .  $\tilde{S}_c$  and  $\tilde{g}_c$  denote elements of  $\tilde{\mathbf{S}} = [\tilde{S}_0, \dots, \tilde{S}_c, \dots, \tilde{S}_{2N_{CC}-1}]^T$  and  $\tilde{\mathbf{g}} = [\tilde{g}_0, \dots, \tilde{g}_c, \dots, \tilde{g}_{2N_{CC}-1}]^T$ , respectively.

If this solution does not fulfil the constraint, the constraint is integrated into the optimisation problem by using the method of Lagrange multipliers and the following function is defined

$$h(\lambda, \tilde{\mathbf{g}}) = \left\| \tilde{\mathbf{S}} + \tilde{\mathbf{g}} \cdot \mathbf{D}_C \right\|^2 + \lambda \cdot (\left\| \mathbf{D}_B \cdot \tilde{\mathbf{g}} \right\|^2 - \alpha). \quad (3.34)$$

The derivation leads to a linear system that can be solved as

$$\tilde{g}_c(\lambda) = \frac{\gamma_c \tilde{S}_c}{\gamma_c^2 + \lambda \beta_c^2} \quad (3.35)$$

under the assumption that the matrix of coefficients is non-singular. To determine the Lagrange multiplier  $\lambda$  the secular equation  $f(\lambda) \equiv \left\| \mathbf{D}_B \cdot \tilde{\mathbf{g}} \right\|^2$  is defined and a solution for  $f(\lambda) = \alpha$  has to be found. This value for  $\lambda$  is calculated by any root-finding algorithm, e.g. Newton's method. Finally, the weighting factors become  $\mathbf{g} = \mathbf{X} \cdot \tilde{\mathbf{g}}$ .

As the optimisation problem can be reduced to a linear system computationally extensive matrix inversions are avoided and the weighting factors can be determined

easily. The most complex step of the algorithm, the GSVD, is also simple as one matrix is an identity matrix. Moreover, this step has to be performed only once in the initialisation phase.

### Impact on System Performance

CCs consume a certain amount of Tx power as already indicated by the normalisation factor  $A^{\text{norm}}$  in (3.27) which has been introduced in order to keep the power of the Tx signal with CCs the same as of the Tx signal without CCs. Assuming the power of each complex symbol to be normalised to  $|d_m|^2 = 1$ ,  $m = 0, \dots, N_{\text{used}} - 1$ , (3.28) can be rewritten and the normalisation factor becomes

$$A^{\text{norm}}(N_{\text{used}} + \|\mathbf{g}\|^2) = N_{\text{used}} \quad \Leftrightarrow \quad A^{\text{norm}} = \frac{N_{\text{used}}}{N_{\text{used}} + \|\mathbf{g}\|^2} \leq 1. \quad (3.36)$$

As due to the redistribution of power less power is available on the data bearing subcarriers, SNR on these subcarriers is reduced resulting in a decreased BER performance. The resulting SNR loss writes

$$\text{SNR}^{\text{loss}} = 10 \cdot \log_{10}(1/A^{\text{norm}}). \quad (3.37)$$

Since the optimisation of the CC weights is performed for each Tx sequence individually, the normalisation factor differs from Tx sequence to Tx sequence. The upper bound is determined by the minimum normalisation factor which in turn is controlled by the constraint  $\alpha$  in (3.30). Replacing  $\|\mathbf{g}\|^2$  by  $\alpha$  in (3.36) and substituting (3.36) in (3.37), maximum SNR loss is obtained as

$$\text{SNR}_{\text{max}}^{\text{loss}} = 10 \cdot \log_{10} \left( \frac{N_{\text{used}} + \alpha}{N_{\text{used}}} \right). \quad (3.38)$$

In most cases the actual SNR loss remains below the upper limit as the constraint is not active for all symbol sequences.

In addition, the PAPR is influenced by CCs. In general, the PAPR of an OFDM signal is defined as [21]

$$\text{PAPR} = \frac{\max_k |x_p[k]|^2}{1/N \sum_{k=0}^{N-1} |x_p[k]|^2}, \quad k = 0, \dots, N-1, \quad (3.39)$$

where  $x_p[k]$ ,  $k = 0, \dots, N-1$ ,  $p = 0, \dots, P-1$ , and  $x'_p[k]$ ,  $k = 0, \dots, N-1$ ,  $p = 0, \dots, P-1$ , are time samples of the  $p$ th OFDM symbol at the output of the IDFT

operation without and with CCs, respectively. Due to the power normalisation, the average Tx power is the same for the OFDM signal with and without CCs. The maximum PAPR is obtained when all subcarrier amplitudes superimpose constructively, i.e.

$$\text{PAPR}_{\max} = \frac{\|\mathbf{d}\|^2}{1/N \sum_{k=0}^{N-1} |x_p[k]|^2} = \frac{\|\mathbf{d}'\|^2}{1/N \sum_{k=0}^{N-1} |x'_p[k]|^2}. \quad (3.40)$$

Due to the constraint introduced by (3.28), the maximum PAPR is the same in the case with and without CCs. However, the average peak power of the OFDM signal increases when CCs are inserted. Reasons for that are the increased number of used subcarriers and the weighting factors for the CCs that may exceed the amplitudes of the data subcarriers. Since the amplitudes of the weighting factors are different for each Tx sequence, no analytical solution for the PAPR growth can be given. Numerical results are derived from Monte-Carlo simulations in Section 3.4.

### 3.3 Combination of Different Techniques

For further enhancing performance the proposed sidelobe suppression techniques are combined with standard sidelobe suppression techniques such as windowing. Alternatively and/or additionally, the advanced techniques can be applied subsequently.

#### 3.3.1 Combination of Advanced Techniques with Tx Windowing

In Fig. 3.2, it has been shown that windowing is capable of considerably reducing the sidelobes in wide areas of the spectrum except for the area close to the used bandwidth. Hence, it is straightforward to combine windowing with the advanced sidelobe suppression techniques that mainly reduce out-of-band radiation close to the used bandwidth. That way the benefits of both approaches can be combined [63].

The windowing operation can be performed after the IDFT independently of any other sidelobe suppression technique that has been applied before the IDFT. However, since windowing shapes the subcarrier spectra, the windowing operation has

to be considered in advance when sidelobe suppression techniques are applied. With windowing, the subcarrier spectra are determined by the Fourier transform of the applied window rather than by the Fourier transform of the rectangular window that is applied implicitly else. As an example, the subcarrier spectrum after rc windowing is derived in Appendix A. For the sidelobe suppression techniques presented in the previous section, the subcarrier spectrum from (A.16) is used instead of the subcarrier spectrum given in (3.5).

The influence of windowing onto the subcarrier spectra is two-fold. First, the subcarrier spectra exhibit lower sidelobes than the subcarrier spectra obtained from rectangular windowing. Second, the increased length of the OFDM symbol results in a smaller mainlobe and smaller sidelobes. Since at the same time, the subcarrier spacing is maintained, subcarrier orthogonality is lost. This is the same effect that has already been observed in Fig. 3.5 when the impact of the GI on the subcarrier spectra has been investigated. As a consequence, the maxima of the individual subcarrier spectra cannot superimpose constructively, hence resulting in a further reduction of the sidelobes of the entire OFDM signal. The loss of orthogonality only occurs when regarding the Tx spectrum. At Rx, orthogonality is restored when processing segments of the Rx data stream with length corresponding to the original length of an OFDM symbol. Both effects can be observed when comparing the spectra of two adjacent subcarriers with rectangular and rc windowing as shown in Fig. 3.8. For regarding the effect of Tx windowing isolatedly, the GI has been omitted. Taking into account the GI as well as windowing, the width of the mainlobe of each subcarrier spectrum is even smaller and the sidelobes of the entire OFDM signal are slightly lower.

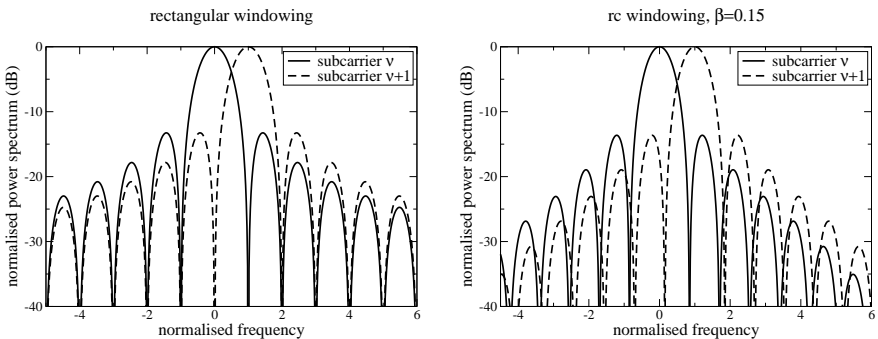


**Figure 3.8** Subcarrier spectra after rectangular and rc windowing, GI not considered.

### 3.3.2 Combination of Advanced Techniques

In order to improve sidelobe suppression the benefits of the proposed techniques are exploited by applying them jointly. However, not all combinations and orders are possible or reasonable. For example, CCs always have to be applied in the last step as CCs are optimised for a certain symbol sequence that must not be modified afterwards. Beforehand, either SW or MCS can be applied. For these reasons, only three out of six theoretically possible combinations are presented in the following, namely MCS/SW, SW/CCs, and MCS/CCs [64].

**Combination of MCS and SW** For applying the MCS and the SW technique jointly, the symbol vector is processed with the MCS algorithm followed by SW. With the reverse order of the two steps, sidelobe suppression could not be improved since the weighting factors determined for SW are already optimised for the considered symbol vector. When applying MCS followed by SW, the suppressions achieved with each of the two methods applied separately are added up at the expense of a throughput reduction due to signalling information and an increased BER caused by SW.

**Combination of SW and CCs** At first, the spectral characteristics of the Tx symbol vectors are improved by SW. Afterwards, CCs are inserted and weighting factors are optimised for the symbol vectors modified by SW. Both steps are performed independently without modifying the algorithms. With SW a large additional sidelobe reduction is expected since CCs are applied to symbol vectors with good spectral characteristics only for which the potential sidelobe suppression of CCs is very high [65]. This gain goes in with an increased BER due to the unequal distribution of Tx power on the individual subcarriers and due to the portion of Tx power spent on CCs.

**Combination of MCS and CCs** When MCS and CCs are combined the symbol vector is modified with the MCS algorithm followed by the insertion of CCs, where the weighting factors are optimised for the symbol vectors modified by the MCS technique. As for the combination of SW and CCs, only symbol vectors with relatively low sidelobe power are fed into the unit for inserting CCs resulting in a high suppression potential. The drawbacks of both methods, i.e. signalling overhead for MCS and SNR loss caused by CCs, are summed up as well.

## 3.4 Performance Evaluation

To demonstrate the potential of the proposed sidelobe suppression techniques, all techniques are investigated in an overlay scenario with only a small spectral gap. For all techniques, the same parameters are used to allow for a fair comparison.

### 3.4.1 Simulated Scenario

From the B-VHF system presented in Section 2.3.1 five DSB-AM channels in the centre of the B-VHF bandwidth are considered. Two of these channels may be used by the overlay system. Between and to the left and to the right, there are three channels that must not be used and the corresponding subcarriers are switched off. This part of the B-VHF bandwidth represents worst case conditions with respect to sidelobe suppression requirements as the spectral gap has a width of only one DSB-AM channel. Apart from that, the B-VHF system parameters given in Tab. 2.1 are used, i.e. DFT length  $N = 512$  and guard length  $N_{GI} = 21$ . With 12 subcarriers per DSB-AM channel, the maximum number of useable subcarriers is  $N_{used} = 24$ . All data are QPSK modulated. The optimisation range used for all sidelobe suppression techniques spans eight sidelobes to the left of the left used channel, eight sidelobes to the right of the right used channel as well as all sidelobes in the unused channel in the centre of the spectrum. Using ten samples per sidelobe to obtain an accurate representation of the subcarrier spectra, the optimisation range comprises  $N_K = 200$  samples in total. Sidelobe suppression is investigated only in the spectral gap in the centre of the B-VHF bandwidth to give an upper bound for the achievable sidelobe power reduction in worst case conditions.

### 3.4.2 Subcarrier Weighting

In Fig. 3.9, the spectrum of the OFDM signal averaged over 10,000 QPSK modulated OFDM symbols before and after SW is shown. For the spectrum of the OFDM signal without SW, the sidelobe power is as high as -16.4 dB averaged over all data sequences and all sidelobes in the spectral gap in the centre of the B-VHF bandwidth. With SW, the average sidelobe power is reduced by 5.2 dB when the constraint in (3.14) is set to  $\rho = \sqrt{6}$ .

As shown in Tab. 3.1, the achieved sidelobe power reduction increases with increasing  $\rho$ . This is due to the fact that the constraint in (3.14) becomes looser hence

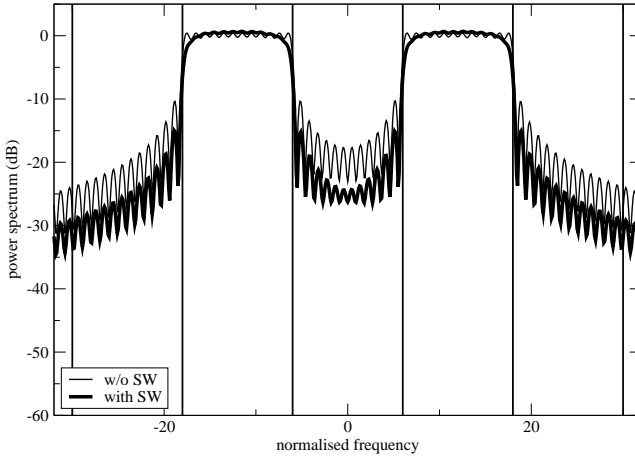


**Figure 3.9** Average OFDM spectrum without and with SW,  $\rho = \sqrt{6}$ .

allowing more degrees of freedom for finding a solution to the optimisation problem from (3.11). The corresponding SNR loss is evaluated by transmitting uncoded BPSK symbols over a Rayleigh fading channel. At Rx, zero-forcing is applied for detection assuming perfect channel knowledge. Note, in contrast to other simulations, BPSK modulation is used in order to allow for a comparison with the theoretically derived bit error probability from (3.19).

**Table 3.1** Average sidelobe suppression in gap, QPSK, and SNR loss for SW with different  $\rho$ , BPSK, no coding, Rayleigh fading channel

$\rho$	$\sqrt{2}$	$\sqrt{4}$	$\sqrt{6}$	$\sqrt{8}$
suppression	1.9 dB	4.1 dB	5.2 dB	6.1 dB
SNR loss, approx.	0.5 dB	1.1 dB	1.6 dB	1.9 dB
$\epsilon$	0.55	0.43	0.39	0.35
SNR loss, simulated	0.4 dB	1.1 dB	1.5 dB	1.8 dB

According to Tab. 3.1, the achieved sidelobe power reduction with  $\rho = \sqrt{6}$  induces an SNR loss of 1.5 dB. When loosening the constraint, SNR degradation increases. The parameter  $\epsilon$  denoting the probability that the weighting factor takes the minimum value is determined in simulations and also given in Tab. 3.1. With increasing

$\rho$ ,  $\epsilon$  decreases. Simulations have shown that the probability that the weighing factor takes the maximum value is approximately the same or slightly higher than the probability that the minimum value is used. The remaining weighting factors lie in between the lower and the upper limit. Thus, the assumption that the power density function of the weighting factors exhibits only two peaks at the upper and lower bound becomes more and more inaccurate with increasing  $\rho$ . Nevertheless, the simulated and the SNR loss theoretically determined from (3.19) show a good agreement in the considered range of  $\rho$ .

### 3.4.3 Multiple-Choice Sequences

The spectrum of the OFDM signal before and after the application of the MCS algorithm using the symbol constellation approach with set size  $Q = 16$  is shown in Fig. 3.10. Again, 10,000 QPSK modulated Tx sequences have been generated randomly and the spectra have been averaged over all these sequences. Compared to the original OFDM signal, the average sidelobe power in the gap is reduced by 4.7 dB to -21.1 dB. Simulation results for different MCS algorithms and different set sizes are listed in Tab. 3.2. As expected, the achieved sidelobe power reduction increases with increasing set size. The symbol constellation and the phase approach with  $\mathcal{P} = 32$  discrete phase steps provide a similar degree of sidelobe power reduction. Both approaches outperform the interleaving approach as with the interleaving approach the modified Tx sequence is restricted to carry the same data as the original sequence. The symbol constellation and the phase approach allow for more degrees of freedom as they may also change the phase of the complex symbols contained in the considered Tx sequence. The overhead required for signalling side information on the selected MCS sequence is also given in Tab. 3.2. According to (3.22), set size  $Q = 16$  invokes an overhead of 7.7% for the parameters considered in this example.

### 3.4.4 Cancellation Carriers

In the considered overlay scenario, CCs have to be inserted at the edges of both channels used by the overlay system. In case one or two CCs are inserted at each edge, the number of useable subcarriers reduces to  $N_{\text{used}} = 20$  or  $N_{\text{used}} = 16$ , respectively. In Fig. 3.11 and Fig. 3.12, the resulting spectra averaged over 10,000 random QPSK modulated Tx sequences are shown. In contrast to the two sidelobe



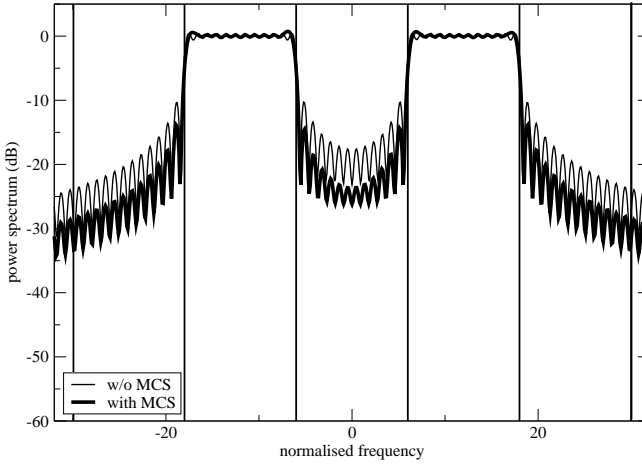


**Figure 3.10** Average spectrum without and with MCS, symbol constellation approach,  $Q = 16$ .

**Table 3.2** Average sidelobe suppression in gap and throughput loss for different sizes of MCS set

size of MCS set $Q$	2	4	8	16	32
suppression for					
- symbol constellation appr.	1.5 dB	2.7 dB	3.7 dB	4.7 dB	5.6 dB
- interleaving approach	0.9 dB	1.7 dB	2.3 dB	2.8 dB	3.3 dB
- phase approach, $\mathcal{P} = 32$	1.4 dB	2.7 dB	3.7 dB	4.7 dB	5.3 dB
overhead $D^{\text{loss}}$	2.0%	4.0%	5.9%	7.7%	9.4%

suppression techniques presented before, the OFDM spectra with one or two guard subcarriers at each edge are given as reference for allowing for a fair comparison of the achieved sidelobe power reduction based on the same amount of used subcarriers. With one or two guard subcarriers at each edge of the spectrum, the average sidelobe power in the gap is already reduced by 2 dB or 3.9 dB, respectively. The suppression achieved with CCs is determined from these already reduced sidelobe power values. Limiting the power spent on CCs to 25% of the total Tx power, with one CC at each edge, sidelobe power in the gap is reduced by 10.4 dB to -29.0 dB.

For two CCs at each edge sidelobe power reduction is as high as 14.2 dB.

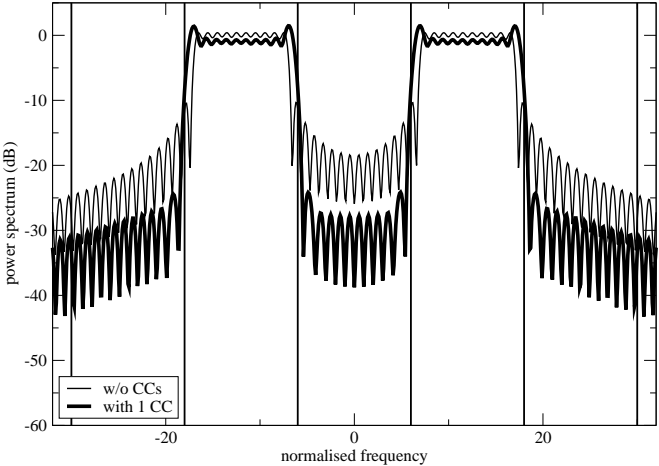


**Figure 3.11** Average OFDM spectrum with one guard subcarrier and one CC at each edge,  $N_{CC} = 2 \cdot 1$ ,  $\alpha \hat{=} 25\%$  of total Tx power.

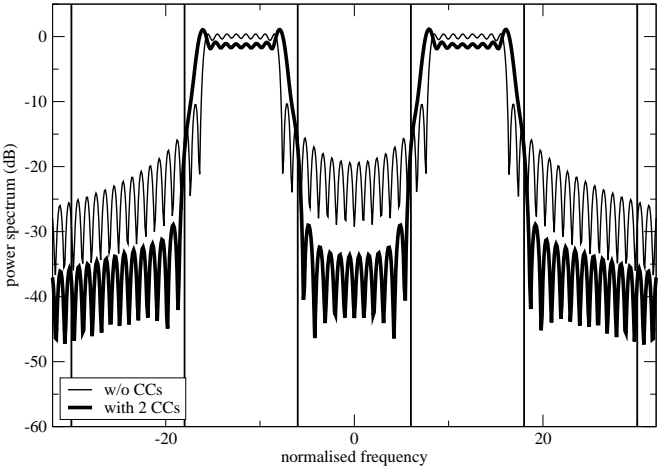


**Figure 3.12** Average OFDM spectrum with two guard subcarriers and two CCs at each edge,  $N_{CC} = 2 \cdot 2$ ,  $\alpha \hat{=} 25\%$  of total Tx power.

In Tab. 3.3, the achieved sidelobe power reduction is listed for different numbers of CCs and for different values of the constraint in (3.30) that steers the fraction of Tx power invested in CCs. With two CCs at each edge, sidelobe power reduction is significantly better than with only one CC at each edge. With more than two CCs, CCs do not have to suppress only the sidelobes of the original OFDM signal, but also the sidelobes of other CCs. Hence, the sidelobe suppression improves only moderately not justifying the additional computational complexity as well as the additionally sacrificed bandwidth. Note, two CCs at each edge of the spectrum are still sufficient when a system with more subcarriers in a contiguous bandwidth is considered. Similar results are obtained for different modulation schemes. Hence, the concept of CCs is applicable to PSK modulation as well as to QAM [66].

Sidelobe suppression improves with increasing amount of Tx power spent on CCs. However, as can be seen in Fig. 3.11 and Fig. 3.12, this goes in with increasing ripples in the spectral shape of the modified OFDM signal at those positions where CCs are inserted. These ripples may require a reduction of the overall Tx power in order to meet the requirements of the spectral mask. Alternatively, the ripples can be reduced by further restricting the power spent on CCs at the cost of reduced sidelobe suppression.

In addition, in Tab. 3.3, SNR loss induced by the insertion of two CCs at each edge of the spectrum is determined theoretically and by simulating the transmission of uncoded data over a frequency-selective Rayleigh fading channel. At Rx, zero-forcing detection is performed assuming perfect channel knowledge. As high order modulation schemes are more sensitive to SNR losses, 64-QAM is used to simulate a strong impact on BER performance. Furthermore, at Rx, ideal knowledge of the normalisation factor  $A^{\text{norm}}$  from (3.36) is assumed, as the power loss on the data subcarriers is compensated by Rx mechanisms such as automatic gain control. Inserting two CCs at each edge of the spectrum and limiting the power invested into CCs to 25% of the total Rx power, SNR is reduced by 1.24 dB. SNR loss increases with increasing amount of Tx power spent on CCs as less power is available for the transmission of useful data. The simulated values are slightly lower than the maximum SNR loss theoretically determined according to (3.38). The small difference can be explained as the CCs do not consume the maximum available amount of Tx power for all Tx sequences.

In addition, PAPR growth is given in Tab. 3.3 for the insertion of two CCs and different power constraints. PAPR obtained with  $N_{\text{used}} = 16$  at clipping rate  $10^{-2}$  serves as reference. When all  $N_{\text{used}} = 24$  subcarriers are used for data transmission,

PAPR already increases by 0.34 dB due to the larger number of used subcarriers. The additional PAPR growth of e.g. 0.27 dB for the 25% power constraint is explained by the high amplitudes of the CCs. All in all, CCs cause only a small PAPR growth that is justified by the high sidelobe suppression.

**Table 3.3** Reduction of average sidelobe power in gap with CCs for different  $\alpha$ , QPSK, and corresponding SNR loss and PAPR growth for two CCs at each edge, SNR loss simulated with 64-QAM, no coding, Rayleigh fading channel

power for CCs limited to:	10%	15%	20%	25%	30%
sidelobe suppression					
- for 1 CC	6.5 dB	8.4 dB	9.6 dB	10.4 dB	10.7 dB
- for 2 CCs	9.1 dB	11.3 dB	12.9 dB	14.2 dB	15.4 dB
SNR loss, theoretical	0.46 dB	0.71 dB	0.97 dB	1.25 dB	1.55 dB
SNR loss, simulated	0.45 dB	0.69 dB	0.97 dB	1.24 dB	1.53 dB
PAPR growth at clipping rate $10^{-2}$	0.40 dB	0.47 dB	0.57 dB	0.61 dB	0.69 dB

### 3.4.5 Combination of Advanced Techniques

In order to improve the performance of the advanced techniques, the combination with windowing as well as combinations of the different advanced techniques as proposed in Section 3.3 are investigated.

#### Combination with Windowing

After modifying the OFDM Tx sequences by means of SW, MCS or CCs, respectively, the obtained Tx sequences are Fourier transformed to the time domain and multiplied with an rc window with different roll-off factors. The resulting average sidelobe power in the gap averaged over 10,000 random QPSK modulated Tx sequences is listed in Tab. 3.4. The average sidelobe power without windowing, i.e. for  $\beta = 0$ , is given as reference.

For SW with  $\rho = \sqrt{6}$ , sidelobe power reduction only can be slightly improved with windowing. The additional suppression of 3.8 dB achieved with  $\beta = 0.2$  does not

counterbalance the throughput loss of 20% related to that roll-off factor. Similar results are obtained for the combination of MCS with windowing.

For CCs, significant improvements are achieved with roll-off factors  $\beta = 0.15$  and  $\beta = 0.2$ . For these parameters, the average sidelobe power is reduced by another 12.4 dB and 13.9 dB, respectively. For  $\beta = 0.1$ , only small improvements are observed compared to the case with CCs but without windowing. However, taking windowing with  $\beta = 0.1$  as reference, the insertion of CCs still reduces the average sidelobe power in the gap by about 10 dB.

All in all, the combination of CCs with windowing with  $\beta > 0.1$  seems to be reasonable. For SW and MCS, the improvements do not justify the throughput loss induced by windowing.

**Table 3.4** Average sidelobe power in gap achieved by combining advanced techniques with rc windowing with different  $\beta$

roll-off factor	$\beta = 0$	$\beta = 0.10$	$\beta = 0.15$	$\beta = 0.20$
SW, $\rho = \sqrt{6}$	-21.8 dB	-22.4 dB	-24.2 dB	-25.6 dB
MCS, $Q = 16$	-21.1 dB	-22.2 dB	-23.0 dB	-23.6 dB
CC, $N_{CC} = 2 \cdot 2$ , $\alpha \hat{=} 25\%$	-34.5 dB	-36.1 dB	-46.9 dB	-48.4 dB

### Combination of Advanced Techniques

**Combination of MCS and SW:** In Fig. 3.13, the OFDM spectrum after the subsequent application of MCS and SW averaged over 10,000 random QPSK modulated symbol vectors is shown. With MCS using the symbol constellation approach and set size  $Q = 16$ , the sidelobe power in the gap is reduced to -21.1 dB. An additional reduction of 6.4 dB is achieved with SW and  $\rho = \sqrt{6}$  resulting in a sidelobe power of -27.5 dB. Compared to both methods applied separately, the total suppression is slightly better because the potential of the SW algorithm for Tx sequences with already relatively low sidelobes is slightly higher.

**Combination of SW and CCs:** After applying SW with constraint  $\rho = \sqrt{6}$  to the overlay system with two guard subcarriers at each edge, the guard subcarriers are replaced by CCs that are determined with limiting  $\alpha$  to 25% of the total Tx power. The resulting spectrum averaged over 10,000 random QPSK modulated OFDM

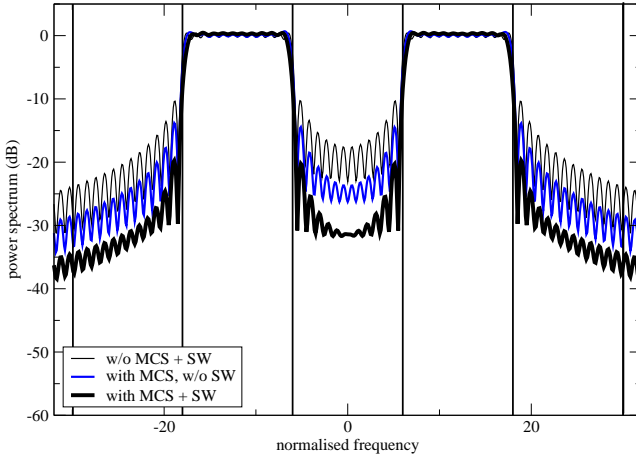


**Figure 3.13** MCS + SW,  $Q = 16$ , symbol constellation approach, SW with  $\rho = \sqrt{6}$ .

symbols is shown in Fig. 3.14. The average sidelobe power in the gap is reduced from -20.3 dB to -42.1 dB meaning an additional suppression of 7.6 dB compared to CCs applied separately. With SW applied separately, sidelobe suppression is as low as 5.5 dB. Hence, the suppression achieved with the combination is larger than the sum of the results obtained with each technique applied separately. This is due to the fact, that CCs are applied to Tx sequences with already improved spectral characteristics, which is addressed at the end of this section. Moreover, in Fig. 3.14, it is observed that the problematic ripples at the edges of the spectrum are reduced considerably compared to the case when CCs are applied separately.

Further simulations have shown that on the average, CCs consume more power and the constraint is active for more Tx sequences when SW is applied before. As a consequence, SNR loss and computational effort are slightly increased in combination with SW.

So far, the sidelobe power reduction achieved with the insertion of CCs has been averaged over all simulated Tx sequences. In Fig. 3.15, the sidelobe power with and without insertion of CCs is given separately for each of the 10,000 random QPSK modulated symbol vectors. The average sidelobe power in the gap is sorted to obtain decreasing values for the sidelobe power without CCs. The corresponding values obtained after the insertion of CCs are sorted accordingly. For OFDM symbol vectors with poor spectral characteristics, sidelobe power is reduced by

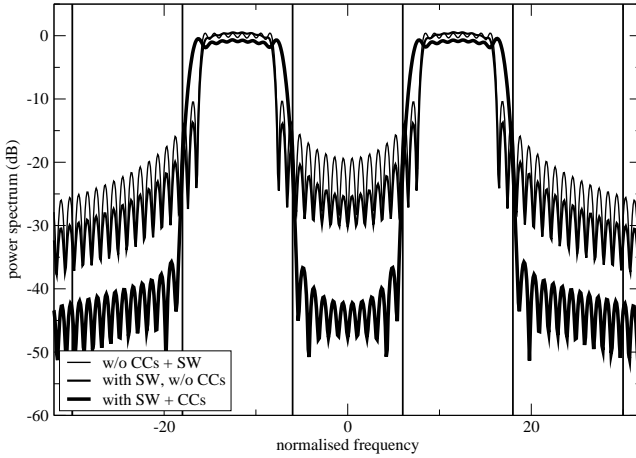


**Figure 3.14** SW + CCs,  $\rho = \sqrt{6}$ ,  $N_{CC} = 2 \cdot 2$ ,  $\alpha \hat{=} 25\%$  of total Tx power.

10-15 dB when two CCs are inserted at each edge of the spectrum. Significantly better results can be obtained when the original Tx sequence already exhibits low sidelobe power. In that case, sidelobe power reduction grows as high as 37.6 dB. When considering e.g. the 5,000 symbol vectors with low sidelobe power, the average reduction of sidelobe power is as high as 16 dB. Taking into account all symbol vectors, the average sidelobe suppression is about 2 dB smaller. This indicates the higher suppression potential of CCs for Tx sequences with already improved spectral characteristics and explains why the total suppression achieved with the combination of SW and CCs is higher than the suppression achieved with both methods applied separately.

**Combination of MCS and CCs:** The OFDM spectrum after the subsequent application of MCS and CCs averaged over 10,000 random QPSK modulated symbol vectors is shown in Fig. 3.16. When applying the MCS algorithm on  $N_{\text{used}} = 16$  data subcarriers using the symbol constellation approach with  $Q = 16$  the sidelobe power in the gap is reduced by 5.9 dB. Afterwards, two CCs are inserted at each edge of the spectrum and  $\alpha$  is limited to 25% of the total Tx power. That way the average sidelobe power in the gap is reduced by another 20.5 dB to -46.7 dB. As expected the total reduction of 26.4 dB is larger than the sum of the suppression achieved with both methods applied separately. As shown in Fig. 3.15, this is

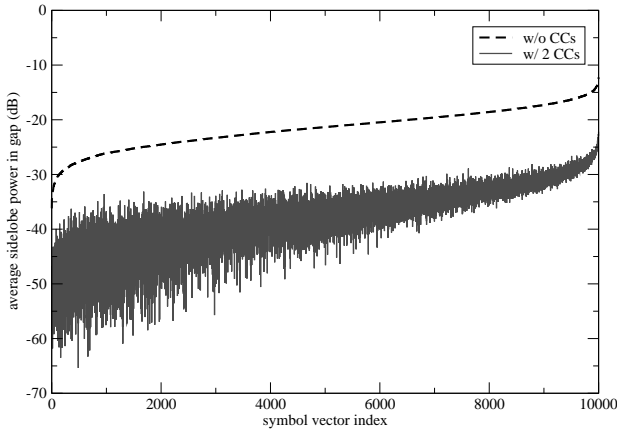


**Figure 3.15** Average sidelobe power in gap with and without CCs,  $N_{CC} = 2 \cdot 2$ ,  $\alpha \hat{=} 25\%$  of total Tx power.

due to the fact that CCs are applied to symbol vectors with already relatively good spectral characteristics having an above-average suppression potential as shown in Fig. 3.15. Moreover, additional simulations have shown that CCs consume the maximum amount of Tx power in only about 50% of the cases, hence causing a slightly smaller SNR loss and reducing computational complexity. Same as for the combination of SW and CCs, the ripples at the edges of the spectrum are reduced such that the OFDM spectrum now meets the requirements of a spectral mask that limits the normalised in-band power level to 0 dB.

### 3.4.6 Comparison of Different Techniques

In Fig. 3.17, the cumulative distribution function (CDF) of the sidelobe power in the gap is plotted for some selected methods and combinations of them. For each method, parameters are chosen according to the results from the previous sections such as to give a good trade-off between suppression and performance loss. The threshold of tolerable sidelobe power is assumed to be as low as -50 dB, i.e. 50 dB below the power level of the in-band OFDM signal. The actual threshold is expected to be in the same order of magnitude, but depends on the level of interference power the considered licensed system can tolerate without performance degradations and differs from licensed system to licensed system.



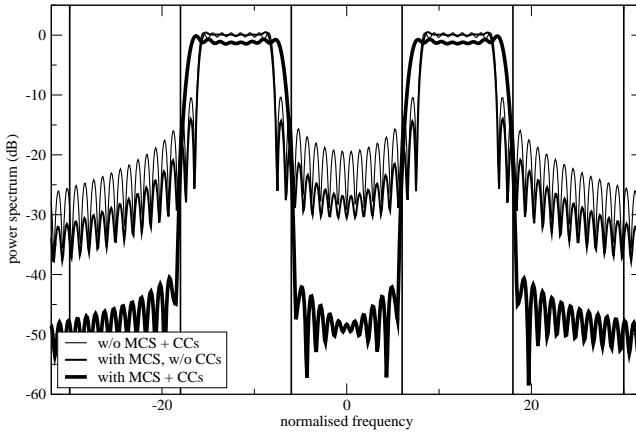


**Figure 3.16** MCS + 2 CCs,  $Q = 16$ , symbol constellation approach,  $N_{CC} = 2 \cdot 2$ ,  $\alpha \hat{=} 25\%$  of total Tx power.

For SW with constraint  $\rho = \sqrt{6}$  and MCS using the symbol constellation approach with set size  $Q = 16$ , the average sidelobe power in the gap is far above the threshold. When combining both techniques sidelobe suppression is improved, but still is above the threshold. Inserting two CCs at each edge of the spectrum and limiting their power to 25% of the total Tx power, the average sidelobe power goes below the threshold for 5% of the Tx sequences. In combination with rc windowing with roll-off factor  $\beta = 0.15$ , this is the case for 10% of the Tx sequences. With windowing the maximum sidelobe power is reduced from -22 dB to -40 dB. The minimum sidelobe power is higher without windowing and the case without windowing outperforms the case with windowing for a few symbol sequences. Nevertheless, in total, sidelobe power reduction is significantly improved due to windowing.

The probability, that the average sidelobe power is below the threshold, is further increased when CCs are combined with SW or MCS. Despite the better average suppression achieved with the combination of MCS and CCs, the probability that the sidelobe power is below the threshold is higher for the combination of SW and CCs, i.e. 32% for the combination of MCS and CCs and 50% for the combination of SW and CCs.

The best suppression results are achieved when combining CCs either with SW or with MCS. The good suppression goes in with an SNR loss of less than 3 dB

for the combination of SW and CCs and an SNR loss of about 1.25 dB and 7.7% throughput loss for the combination of MCS and SW.

With the proposed combinations sidelobe power and with that interference towards licensed systems are reduced considerably. In this section, this has been demonstrated for the B-VHF system presented in Section 2.3.1. With respect to out-of-band radiation, the worst case with a gap of only one VHF channel has been investigated. Even better results are expected for larger gaps and for sidelobes in the guard bands outside the actual transmission bandwidth of the OFDM system. The latter applies to the B-AMC inlay system as presented in Section 2.3.2. In this system two CCs are inserted at both edges of the spectrum and rc windowing is applied in order to suppress interference towards other L-band systems operating at only 500 kHz offset from the B-AMC system. If required, a slightly better sidelobe suppression can be achieved with the combination of CCs with MCS or SW, respectively.

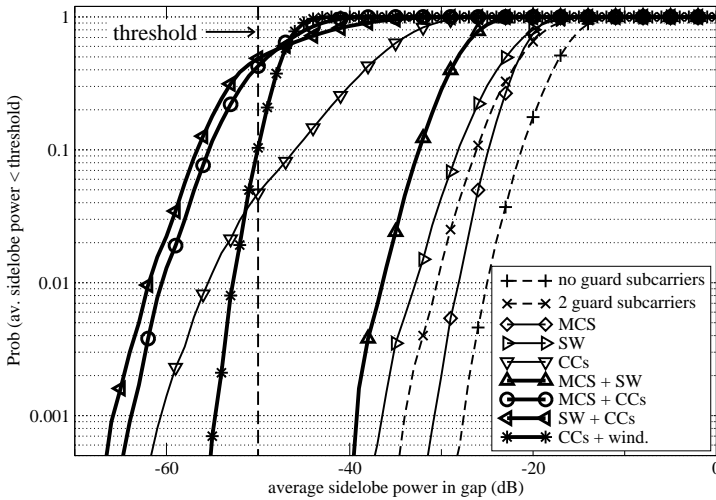


**Figure 3.17** CDF of average sidelobe power in gap after application of different sidelobe suppression techniques.

# 4 Mitigation of Narrow-Band Interference

At the overlay system Rx, the desired signal is superimposed by interference signals from licensed systems operating in the same frequency band. Due to the spectral selectivity of OFDM, even narrow-band interference (NBI) signals spanning only a few OFDM subcarriers are spread over the entire system bandwidth. Hence, all subcarriers are affected regardless of if the corresponding channel of the licensed system is used by the overlay system or not. In order to enable a successful operation of the overlay system in presence of interference, the impact of NBI has to be mitigated.

The problem of NBI has frequently been mentioned in the context of wireline systems such as asymmetric digital subscriber line (ADSL) or very-high-speed digital subscriber line (VDSL) both employing OFDM as modulation technique. Amateur radios use small frequency bands in the spectrum of broadband DSL systems and severely affect DSL transmissions. In [27, 67], several approaches for mitigating the impact of NBI are presented. The proposed methods are grouped into time and frequency domain techniques depending on if they are applied before or after the DFT operation at the OFDM Rx.

Already available techniques for mitigating almost static NBI in conventional OFDM systems can be applied to overlay systems only to a limited extent as the interference situation varies considerably due to the changing spectrum allocation of the licensed system. In this thesis, time and frequency domain techniques are adapted and redesigned such as to mitigate the impact of NBI in OFDM based overlay systems. Special emphasis is put on the estimation of a varying interference signal since this is the key enabler for dynamically adapting NBI mitigation to changing interference conditions.

The remainder of this chapter is organised as follows. In the first section, the DSB-AM signal, that is considered as an exemplary NBI signal here, is described. Furthermore, spectral leakage of the DSB-AM carrier as well as the contribution of sidebands are derived. In Section 4.2, Rx windowing is addressed as a means of NBI mitigation in the time domain. In the frequency domain, NBI is mitigated by subtracting an estimated NBI signal from the Rx signal as described in Section 4.3.

Different techniques for estimating NBI are presented in Section 4.4. In order to combine the benefits of both approaches, the joint application of NBI mitigation in the time and frequency domain is addressed in Section 4.5. The performance of all proposed methods is assessed at hand of BER vs. SNR simulations of an overlay system in the VHF-band taking into account realistic worst case interference conditions.

## 4.1 Origin of Leakage Effect

As a realistic basis for the investigations in this chapter, a DSB-AM voice signal is considered. Nowadays, DSB-AM is still in use in aeronautical communications for air traffic control and air traffic management and is the main source of interference in the overlay scenario in the VHF-band as described in Chapter 2. Note, this restriction to one type of NBI signal is not related to a loss of generality as the methods for estimating and mitigating interference signals can be applied to any kind of NBI signal.

The DSB-AM signal is composed of a carrier and sidebands. In the continuous time domain, the DSB-AM signal  $i(t)$  is given by

$$i(t) = A(t) \left( 1 + \eta \frac{b^{\text{voice}}(t)}{\max |b^{\text{voice}}(t)|} \right) \exp(j2\pi f_c t + j\vartheta_0), \quad (4.1)$$

where  $A(t)$  denotes the time-variant carrier amplitude,  $0 \leq \eta < 1$  the modulation index,  $f_c$  the carrier frequency in baseband, and  $\vartheta_0$  the phase;  $t$  is the continuous time variable. The signal  $b^{\text{voice}}(t)$  forming the sidebands is the filtered, bandlimited voice signal which is normalised to have a maximum amplitude equal to 1. For modelling the voice signal, artificial voice is generated according to [68]. Due to filtering,  $b^{\text{voice}}(t)$  is limited to a frequency range between 0.3 kHz and 2.7 kHz. For illustration, the sideband signal  $b^{\text{voice}}(t)$  can be represented by a sum of  $N_H$  simple audio tones with frequency  $f_h^{\text{sb}}$ ,  $h = 0, \dots, N_H - 1$ , varying between 0.3 kHz and 2.7 kHz yielding

$$\begin{aligned} b^{\text{voice}}(t) &= \sum_{h=0}^{N_H-1} A_h^{\text{voice}} \cos(2\pi f_h^{\text{sb}} t + j\varphi_h^{\text{sb}}) \\ &= \sum_{h=0}^{N_H-1} A_h^{\text{voice}} \frac{1}{2} \left( \exp(j2\pi f_h^{\text{sb}} t + j\varphi_h^{\text{sb}}) + \exp(-j2\pi f_h^{\text{sb}} t - j\varphi_h^{\text{sb}}) \right). \end{aligned} \quad (4.2)$$

The amplitude of the  $h$ th audio tone contributing to the sideband signal is denoted by  $A_h^{\text{voice}}$  and  $\left| \sum_{h=0}^{N_H-1} A_h^{\text{voice}} \right|^2$  is normalised to 1. Frequency  $f_h^{\text{sb}}$  and phase  $\varphi_h^{\text{sb}}$ ,  $h = 0, \dots, N_H-1$ , of the tones contained in the sideband signal are labelled with  $(\cdot)^{\text{sb}}$  in order to distinguish them from the corresponding variables of the DSB-AM carrier signal. With the simplification from (4.2), the DSB-AM signal with sidebands from (4.1) can be rewritten as

$$\begin{aligned} i(t) &= A(t) \exp(j2\pi f_c t + j\vartheta_0) \\ &+ A(t) \frac{\eta}{2} \sum_{h=0}^{N_H-1} A_h^{\text{voice}} \left( \exp(j2\pi(f_c + f_h^{\text{sb}})t + j(\vartheta_0 + \varphi_h^{\text{sb}})) \right. \\ &\quad \left. + \exp(j2\pi(f_c - f_h^{\text{sb}})t + j(\vartheta_0 - \varphi_h^{\text{sb}})) \right). \end{aligned} \quad (4.3)$$

When investigating the impact of this NBI signal onto the OFDM system, the basic signal processing at the OFDM Rx, including sampling, windowing, and the DFT operation, has to be reproduced. Thereby, segments of the interference signal corresponding to the duration of one OFDM frame are considered since Rx processing is performed OFDM frame-wise as well.

After sampling at the OFDM Rx with sampling frequency  $f_s$ , the DSB-AM signal in the discrete time domain is given by

$$\begin{aligned} i[k] &= i(k/f_s) = A[k] \exp\left(jk \frac{2\pi n_c}{N} + j\vartheta_0\right) \\ &+ A[k] \frac{\eta}{2} \sum_{h=0}^{N_H-1} A_h^{\text{voice}} \left( \exp\left(jk \frac{2\pi(n_c + n_h^{\text{sb}})}{N} + j(\vartheta_0 + \varphi_h^{\text{sb}})\right) \right. \\ &\quad \left. + \exp\left(jk \frac{2\pi(n_c - n_h^{\text{sb}})}{N} + j(\vartheta_0 - \varphi_h^{\text{sb}})\right) \right), \\ &k = 0, \dots, P \cdot (N + N_{\text{GI}}) - 1. \end{aligned} \quad (4.4)$$

The interference signal  $i[k]$  is considered for the duration of one OFDM frame consisting of  $P$  OFDM symbols resulting in  $P \cdot (N + N_{\text{GI}})$  samples contained in the sequence  $i[k]$ . The discrete carrier frequency  $n_c$  is derived from the carrier frequency in continuous domain by  $n_c = f_c/f_s \cdot N$ . Accordingly, the discrete frequencies of the tones contained in the sideband signal are determined as  $n_h^{\text{sb}} = f_h^{\text{sb}}/f_s \cdot N$  with  $h = 0, \dots, N_H - 1$ .

In the following two subsections, the carrier and the sidebands of the DSB-AM signal are considered separately. At first, the DSB-AM sidebands are neglected in Section 4.1.1, i.e. only the carrier is considered which is represented by a complex exponential sequence. In Section 4.1.2, the sidebands are regarded and the carrier and sideband signal are composed such as to give the entire DSB-AM signal.

### 4.1.1 Complex Exponential Sequence

The discrete time domain DSB-AM carrier signal  $i^{\text{carrier}}[k]$  without sidebands is obtained when setting  $\eta = 0$  in (4.4) resulting in

$$i^{\text{carrier}}[k] = A[k] \cdot \exp\left(jk \frac{2\pi n_c}{N} + j\vartheta_0\right), \quad k = 0, \dots, P \cdot (N + N_{\text{GI}}) - 1. \quad (4.5)$$

When discarding the GI at the OFDM Rx, the Rx signal is multiplied with a rectangular window of length  $N$  defined as

$$\text{rect}[k] = \begin{cases} 1 & k = 0, \dots, N - 1 \\ 0 & \text{otherwise.} \end{cases} \quad (4.6)$$

Hence, the interference signal on the  $p$ th OFDM symbol,  $p = 0, \dots, P - 1$ , within an OFDM frame consisting of  $P$  OFDM symbols is given by

$$\begin{aligned} i_p^{\text{carrier}}[k] &= \text{rect}[k] \cdot i^{\text{carrier}}[k + N_{\text{GI}} + p(N + N_{\text{GI}})] \\ &= A_p[k] \cdot \exp\left(jk \frac{2\pi n_c}{N} + j\varphi_p\right), \quad k = 0, \dots, N - 1, \end{aligned} \quad (4.7)$$

with phase

$$\varphi_p = \vartheta_0 + (p + 1) \frac{2\pi N_{\text{GI}} n_c}{N}. \quad (4.8)$$

The amplitude  $A_p[k]$  of the interference signal is assumed to be constant for the duration of one OFDM symbol, i.e.  $A_p[k] = A_p = \text{const.}$ , since the bandwidth of the DSB-AM signal is small compared to the bandwidth of the OFDM signal. As can be seen from (4.8), the GI removal causes a phase shift in the interference signals on consecutive OFDM symbols. The phase shift depends on the carrier frequency  $n_c$  of the currently considered interferer and hence cannot be easily compensated when more than one interferer is present.

After GI removal, the Rx signal is transformed from the time to the frequency domain by means of an  $N$ -point DFT as defined in (2.15). On the  $p$ th OFDM symbol within an OFDM frame the resulting interference signal  $I_p^{\text{carrier}}[n]$  after the  $N$ -point DFT yields

$$I_p^{\text{carrier}}[n] = A_p \cdot \exp\left(-j\pi(n-n_c)\frac{N-1}{N} + j\varphi_p\right) \cdot \frac{\sin(\pi(n-n_c))}{\sin(\pi/N(n-n_c))} \quad (4.9)$$

with frequency domain index  $n = 0, \dots, N-1$ . For a detailed derivation of the frequency domain representation of the interference signal please refer to Appendix B. The interference signal from (4.9) results from convolving the carrier signal which is a complex exponential sequence with the Fourier transform of the rectangular window which is an si-function. If the carrier frequency  $n_c$  coincides with a subcarrier frequency, i.e.  $n - n_c$  is an integer, (4.9) simplifies to

$$I_p^{\text{carrier}}[n] \Big|_{n-n_c \in \mathbb{N}} = \begin{cases} A_p & n = n_c \\ 0 & n \neq n_c. \end{cases} \quad (4.10)$$

In that case, the si-function is sampled in the maximum and all zero-crossings. Hence, the OFDM Rx experiences the interference signal as a single pulse only affecting the subcarrier coinciding with the carrier frequency. However, due to the Doppler effect and inaccuracies in the carrier frequency, in general, it cannot be assumed that  $n_c$  coincides with a subcarrier frequency. When  $n - n_c$  is not an integer, the si-function is shifted relative to the OFDM subcarrier grid and is sampled at its non-zero values resulting in spectral leakage.

The leakage effect is illustrated in Fig. 4.1 by means of a complex exponential sequence which is transformed to the frequency domain by an 512-point DFT. The carrier frequency is set to  $n_c = 262, 262.5, \text{ or } 262.75$ , respectively. Maximum leakage occurs, when the carrier frequency of the NBI signal is exactly in the middle between two adjacent OFDM subcarriers, e.g. at  $n_c = 262.5$ . Spectral leakage on different subcarriers is correlated, because the interference signal is narrow-band compared to the broadband OFDM signal. Moreover, the leakage effect is a deterministic property of the DFT and hence can be reconstructed. These properties are exploited when estimating the NBI signal as presented in Section 4.4.

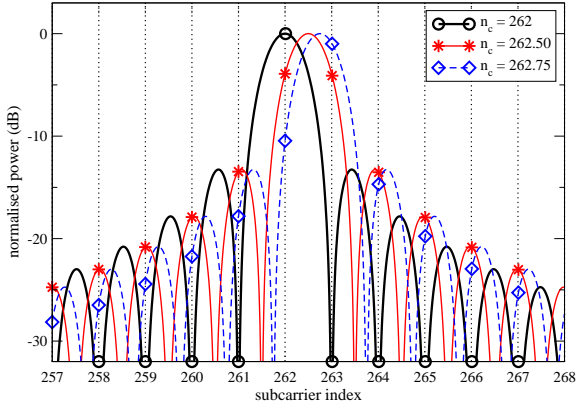


**Figure 4.1** Illustration of leakage effect originating from sampling a shifted si-function,  $N = 512$ ,  $n_c = 262, 262.50$ , or  $262.75$ .

## 4.1.2 DSB-AM Signal with Sidebands

The sideband signal in the discrete time domain is represented by the second term in (4.4). To extract the contribution on the  $p$ th OFDM symbol a rectangular window as defined in (4.6) is applied resulting in

$$i_p^{\text{sb}}[k] = A_p \eta \sum_{h=0}^{2N_H-1} A_h^{\text{voice}} \exp(j2\pi k (n_c + n_h^{\text{sb}})/N + j(\varphi_p + \varphi_h^{\text{sb}})) \quad (4.11)$$

$$k = 0, \dots, N-1.$$

Since the sidebands are symmetric, the  $2N_H$  tones contained in the left and the right sidebands can be represented by one instead of two separate terms as in (4.4). Then, the discrete frequencies  $n_h^{\text{sb}}, h = 0, \dots, 2N_H - 1$ , of the audio tones are equally distributed in the sidebands, i.e.

$$n_h^{\text{sb}} \in [-\max(f_h^{\text{sb}}/f_s N), -\min(f_h^{\text{sb}}/f_s N)], [\min(f_h^{\text{sb}}/f_s N), \max(f_h^{\text{sb}}/f_s N)], \quad (4.12)$$

where  $\min(n_h^{\text{sb}}) = 0.3 \text{ kHz}/f_s N$  and  $\max(n_h^{\text{sb}}) = 2.7 \text{ kHz}/f_s N$  in the considered example, respectively. The phase  $\varphi_h^{\text{sb}}$  is assumed to be equally distributed in the interval  $[-2\pi, 2\pi]$ .



Fourier transforming  $i_p^{\text{sb}}[k]$  to the frequency domain, one obtains

$$I_p^{\text{sb}}[n] = A_p \eta \sum_{h=0}^{2N_H-1} A_h^{\text{voice}} \cdot \left( e^{-j\pi(n-n_c+n_h^{\text{sb}})\frac{N-1}{N}+j(\varphi_p+\varphi_h^{\text{sb}})} \frac{\sin(\pi(n-n_c-n_h^{\text{sb}}))}{\sin(\pi/N(n-n_c-n_h^{\text{sb}}))} \right) \quad (4.13)$$

$$n = 0, \dots, N-1.$$

From (4.11), it can be seen that the sidebands are composed of  $2N_H$  complex exponential sequences that differ from the carrier signal just in amplitude, phase, and carrier frequency which is  $n_c+n_h^{\text{sb}}$  instead of  $n_c$ . Hence, the spectral shapes of the carrier signal given by (4.9) and the sidebands given by (4.13) are similar. Due to the smaller power contained in the sidebands, the sidebands are expected to only slightly influence the carrier signal. This becomes even more obvious when rewriting (4.13) such that the contributions of the carrier and the sidebands are separated. Using addition theorems and approximating the sine of small values by the value itself, the sideband signal from (4.13) simplifies to

$$I_p^{\text{sb}}[n] = A_p \eta \sum_{h=0}^{2N_H-1} A_h^{\text{voice}} e^{-j\pi(n-n_c)\frac{N-1}{N}+j\varphi_p} \cdot e^{-j\pi n_h^{\text{sb}}\frac{N-1}{N}+j\varphi_h^{\text{sb}}} \quad (4.14)$$

$$\cdot \frac{\sin(\pi(n-n_c)) \cdot \cos(\pi n_h^{\text{sb}})}{\sin(\pi/N(n-n_c))}$$

$$= \eta I_p^{\text{carrier}}[n] \sum_{h=0}^{2N_H-1} A_h^{\text{voice}} e^{-j\pi n_h^{\text{sb}}\frac{N-1}{N}+j\varphi_h^{\text{sb}}} \cos(\pi n_h^{\text{sb}})$$

with  $I_p^{\text{carrier}}[n]$ ,  $n = 0, \dots, N-1$ , denoting the carrier signal from (4.9). Assuming an equal distribution of  $n_h^{\text{sb}}$  and  $\varphi_h^{\text{sb}}$ , the expectation value of  $I_p^{\text{sb}}[n]$  becomes very small such that, on the average, the sidebands are negligible.

The complete DSB-AM signal is composed of the carrier from (4.5) or (4.9) and the sidebands from (4.11) or (4.13), respectively. The DSB-AM signal in the time domain writes

$$i_p[k] = i_p^{\text{carrier}}[k] + i_p^{\text{sb}}[k], \quad k = 0, \dots, N-1, \quad (4.15)$$

and analogously in the frequency domain

$$I_p[n] = I_p^{\text{carrier}}[n] + I_p^{\text{sb}}[n] \quad (4.16)$$

$$= I_p^{\text{carrier}}[n] \left( 1 + \eta \sum_{h=0}^{N_H-1} A_h^{\text{voice}} e^{-j\pi n n_h^{\text{sb}} \frac{N-1}{N} + j\varphi_h^{\text{sb}}} \cos(\pi n n_h^{\text{sb}}) \right),$$

$$n = 0, \dots, N - 1.$$

In Fig. 4.2, the spectrum of 1,000 randomly generated DSB-AM signals with sidebands is shown as observed after a 512-point DFT. In contrast to Fig. 4.1, the entire bandwidth rather than a zoom into the bandwidth around the interference peak is depicted. Moreover, in Fig. 4.2, the resolution of the interference spectrum is adjusted to the resolution of the OFDM system and only the values observed on OFDM subcarriers are drawn. Again, the carrier frequency  $n_c$  of the DSB-AM signal is chosen to lie midway between two subcarriers such as to produce maximum leakage, i.e.  $n_c = 262.5$ . For subcarrier spacing and OFDM symbol duration, parameters of the B-VHF system given in Tab. 2.1 have been assumed. In addition, the spectrum averaged over all 1,000 trials is drawn. As the expectation value of the sidebands is negligible according to (4.14), the average spectrum corresponds to the spectrum of the carrier signal without sidebands as given by (4.9). Hence, the carrier signal is dominant and the sidebands only slightly modify the spectrum. First, this can be explained by the fraction of power contained in the sidebands which is always smaller than the power of the carrier since  $\eta < 1$ . Depending on the modulation index, the sidebands cause variations at subcarriers with 30 or more subcarrier spacings offset to the carrier, i.e. the larger  $\eta$  the larger the variation around the average interference spectrum. Second, the bandwidth of the sidebands is small compared to the bandwidth of the OFDM system. In the considered example, both sidebands having a total bandwidth of 5.4 kHz span only three subcarriers and thus have an impact on the spectrum of the carrier close to the peak.

## 4.2 NBI Mitigation in the Time Domain

As shown in the previous section, NBI has a strong impact on system performance as nearly every OFDM subcarrier is affected by spectral leakage. In the literature, basically two different approaches exist for mitigating the impact of NBI in the time domain. One method applies bandstop filters to notch the interferers at their respective positions within the spectrum. This can be realised either in analogue domain [67] before A/D conversion or in digital domain [69]. However, notch filters suffer from several drawbacks. Sharp filter edges cause significant inter-symbol and inter-carrier interference, hence increasing the complexity of equalisation. The

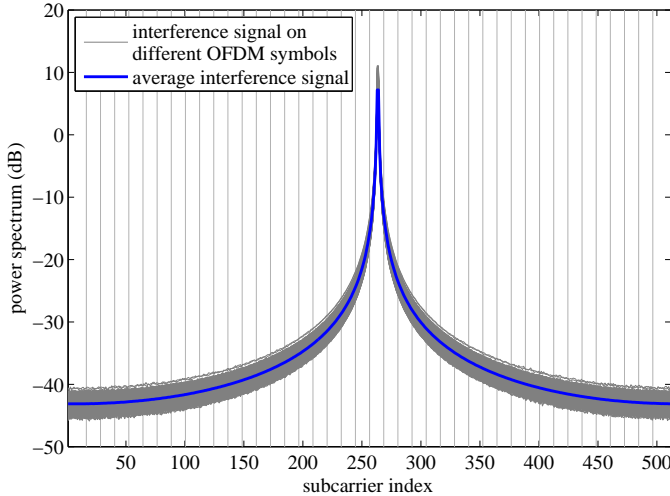


**Figure 4.2** DSB-AM signal with sidebands after DFT for 1000 OFDM symbols,  $\eta = 0.85$ ,  $N = 512$ ,  $n_c = 262.5$ .

realisation of narrow bandstop filters is complex and becomes even more complex when adaptive notches are required in OFDM based overlay systems with dynamically changing interference. Thus, in OFDM based overlay systems notch filters are typically applied only to a very limited number of interferers, if a saturation of the A/D converter by very strong interferers cannot be avoided otherwise.

Another well-known technique for mitigating the impact of NBI in the time domain is Rx windowing. Rx windowing is applied in the time domain before the DFT operation and aims at improving the spectral selectivity of the DFT. For that purpose, the Rx signal is multiplied with a window differing from the normally applied rectangular window. The shape of the window is selected such that the Fourier transform of the window exhibits lower sidelobes than the si-function corresponding to a rectangular window.

Most Rx windowing methods apply windows with a length exceeding the DFT size. Limiting the window length to the DFT size would reduce the effective OFDM symbol duration hence inevitably leading to the loss of orthogonality between the subcarriers that would result in inter-carrier interference. For enabling the application of the extended length window each OFDM symbol needs to be extended either

by an additional cyclic prefix [70] or by an additional cyclic prefix and suffix [71]. Since both variants require the same amount of additional samples and provide the same performance, only the method with an enlarged cyclic prefix according to [70] is considered in the following.

### 4.2.1 Principle of Rx Windowing

As depicted in Fig. 4.3, a cyclic prefix precedes each OFDM symbol. In contrast to conventional OFDM systems applying rectangular windowing this cyclic prefix comprises  $N_{GI}$  samples for the GI as well as  $\mu$  additional samples for windowing. The size of  $\mu$  is chosen in accordance to the roll-off factor of the window.

At Rx, at first that part of the cyclic prefix containing the GI is removed. The GI is assumed to be sufficiently large to exceed the maximum delay spread of the multi-path channel. The remaining  $N + \mu$  samples are multiplied with a window of the same length. The window is designed such that only the first and the last  $\mu$  samples lie in its roll-off region. Assuming a Nyquist window and given the facts that the first  $\mu$  samples of the OFDM Tx signal are a cyclic repetition of the last  $\mu$  samples and that the first  $\mu$  samples are not affected by multi-path effects, the first and the last  $\mu$  samples can be summed. That way, the last  $\mu$  samples of the OFDM symbol affected by windowing are restored. The first  $\mu$  samples can be discarded hence reducing the time domain signal to  $N$  samples that can still be processed with an  $N$ -point DFT. In Section 4.2.2, it is shown that the windowing operation does not impair the information bearing part of the signal when the windowing function is chosen adequately.

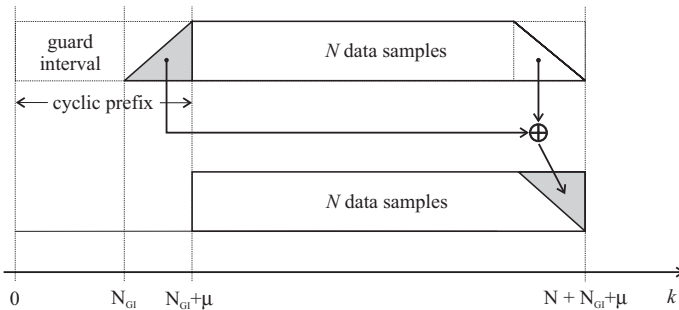


Figure 4.3 Principle of Rx windowing.

At the OFDM Rx,  $N + N_{\text{GI}} + \mu$  samples  $r_p[k]$  are received for the  $p$ th OFDM symbol of an OFDM frame. The Rx signal can be decomposed as

$$\begin{aligned} r_p[k] &= h_p[k] * x_p[k] + n_p[k] + i'_p[k] \\ &= \sum_{d=0}^{N_{\text{D}}-1} h_p[\tau_d] x_p[k - \tau_d] + n_p[k] + i'_p[k], \\ &k = 0, \dots, N + N_{\text{GI}} + \mu - 1, \end{aligned} \quad (4.17)$$

where  $x_p[k]$  denote samples of the transmitted OFDM signal. The multi-path channel  $h_p[k]$  is modelled as a tapped delay line with  $N_{\text{D}}$  delayed paths. The path delays  $\tau_d$  are normalised to the sampling frequency of the OFDM system. The samples  $n_p[k]$  represent AWGN. Note, the NBI signal as described in Section 4.1 now contains  $N + N_{\text{GI}} + \mu$  samples instead of  $N + N_{\text{GI}}$  samples per OFDM symbol. Considering only the carrier of the interference signal for illustration, the slightly modified interference signal  $i'_p[k]$  yields

$$i'_p[k] = A_p \cdot \exp\left(jk \frac{2\pi n_c}{N} + j\varphi'_p\right), \quad k = 0, \dots, N + N_{\text{GI}} + \mu - 1. \quad (4.18)$$

Due to the cyclic prefix containing the GI as well as  $\mu$  samples for windowing a phase shift of

$$\varphi'_p = \vartheta_0 + (p + 1) \frac{2\pi(N_{\text{GI}} + \mu)n_c}{N} \quad (4.19)$$

is induced between the interference signals on consecutive OFDM symbols.

The window  $w[k]$  is derived from a basic Nyquist pulse  $\bar{w}[k]$ , which is e.g. a raised-cosine pulse with a width of  $2\mu$  samples. The  $\mu$  samples of the left and the right slope of the basic pulse form the left and the right flank of the window, respectively. Hence, the windowing function writes

$$w[k] = \begin{cases} \bar{w}[k - N_{\text{GI}}] & k = N_{\text{GI}}, \dots, N_{\text{GI}} + \mu - 1 \\ 1 & k = N_{\text{GI}} + \mu, \dots, N + N_{\text{GI}} - 1 \\ 1 - \bar{w}[k - N - N_{\text{GI}}] & k = N + N_{\text{GI}}, \dots, N + N_{\text{GI}} + \mu - 1 \\ 0 & \text{otherwise,} \end{cases} \quad (4.20)$$

where the starting point of the window is already shifted such as to coincide with the  $N_{\text{GI}}$ th sample of the OFDM Rx signal. Due to the symmetry of the basic pulse

$\bar{w}[k]$  forming the window  $w[k]$  the flanks of the window are symmetric as well, i.e.

$$w[k + N_{\text{GI}} + \mu] = 1 - w[k - N + N_{\text{GI}} + \mu], k = N - \mu, \dots, N - 1. \quad (4.21)$$

The windowing operation can be written as a simple multiplication of  $w[k]$  and  $r_p[k]$ . After GI removal, windowing, and summing up the first and last  $\mu$  samples as shown in Fig. 4.3, the modified Rx signal  $r_p^{\text{w}}[k]$  yields

$$r_p^{\text{w}}[k] = \begin{cases} r_p[k + N_{\text{GI}} + \mu] & k = 0, \dots, N - \mu - 1 \\ w[k + N_{\text{GI}} + \mu]r_p[k + N_{\text{GI}} + \mu] \\ \quad + w[k - N + N_{\text{GI}} + \mu]r_p[k - N + N_{\text{GI}} + \mu]. & k = N - \mu, \dots, N - 1 \end{cases} \quad (4.22)$$

Exploiting the symmetry of the window given in (4.21), the modified Rx signal  $r_p^{\text{w}}[k]$  simplifies to

$$\begin{aligned} r_p^{\text{w}}[k] &= r_p[k + N_{\text{GI}} + \mu] \\ &\quad + w[k - N + N_{\text{GI}} + \mu](r_p[k - N + N_{\text{GI}} + \mu] - r_p[k + N_{\text{GI}} + \mu]), \\ &k = 0, \dots, N - 1. \end{aligned} \quad (4.23)$$

Note, for  $\mu = 0$ , (4.23) reduces to  $r_p^{\text{w}}[k] = r_p[k + N_{\text{GI}}]$ ,  $k = 0, \dots, N - 1$ , which is equivalent to conventional rectangular windowing with cyclic prefix removal.

Analogously to (4.23), the interference signal  $i'_p[k]$  contained in  $r_p[k]$  from (4.17) is modified by windowing to

$$\begin{aligned} i_p^{\text{w}}[k] &= i'_p[k + N_{\text{GI}} + \mu] \\ &\quad + w[k - N + N_{\text{GI}} + \mu](i'_p[k - N + N_{\text{GI}} + \mu] - i'_p[k + N_{\text{GI}} + \mu]), \\ &k = 0, \dots, N - 1. \end{aligned} \quad (4.24)$$

It can be seen that windowing only impairs the first and last  $\mu$  samples of the interference signal, whereas the rest of the interference signal remains unaffected. That way the sharp phase transitions at the beginning and at the end of the OFDM symbol are smoothed. This results in improved spectral characteristics as the sidelobes decay faster compared to the sidelobes of the si-function corresponding to a rectangular window. However, the basic oscillation with frequency corresponding to the centre frequency of the interference signal is not affected by windowing. Hence,

the spectral peak of the interference signal is expected to persist. This is shown for some selected window shapes in Section 4.2.3.

## 4.2.2 Impact on the Desired OFDM Signal

For investigating the impact of windowing on each OFDM subcarrier the Rx signal from (4.23) is Fourier transformed to the frequency domain. After the DFT, the windowed Rx signal writes

$$\begin{aligned}
 R_p^w[n] &= \text{DFT}\{r_p^w[k]\} & (4.25) \\
 &= \sum_{k=0}^{N-1} r_p[k + N_{\text{GI}} + \mu] e^{-j \frac{2\pi kn}{N}} \\
 &\quad + \sum_{k=N-\mu}^{N-1} w[k - N + N_{\text{GI}} + \mu] \\
 &\quad \cdot (r_p[k - N + N_{\text{GI}} + \mu] - r_p[k + N_{\text{GI}} + \mu]) e^{-j \frac{2\pi kn}{N}}, \\
 &\quad n = 0, \dots, N - 1.
 \end{aligned}$$

Substituting  $r_p[k]$  by (4.17) and summarising the distorted part of the OFDM Rx signal containing AWGN and interference to

$$v_p[k] = n_p[k] + i'_p[k], \quad (4.26)$$

one obtains

$$\begin{aligned}
 R_p^w[n] &= H_p[n] X_p[n] + \sum_{k=0}^{N-1} v_p[k + N_{\text{GI}} + \mu] e^{-j \frac{2\pi kn}{N}} & (4.27) \\
 &\quad + \sum_{k=N-\mu}^{N-1} w[k - N + N_{\text{GI}} + \mu] \\
 &\quad \cdot \left( \sum_{d=0}^{N_D-1} h_p[\tau_d] (x_p[k - N + N_{\text{GI}} + \mu - \tau_d] - x_p[k + N_{\text{GI}} + \mu - \tau_d]) \right. \\
 &\quad \left. + (v_p[k - N + N_{\text{GI}} + \mu] - v_p[k + N_{\text{GI}} + \mu]) \right) e^{-j \frac{2\pi kn}{N}}, \\
 &\quad n = 0, \dots, N - 1,
 \end{aligned}$$

where  $H_p[n]$  represent channel coefficients on the  $n$ th subcarrier obtained by transforming  $h_p[k]$ ,  $k = 0, \dots, N-1$ , to the frequency domain. (4.27) can be simplified by first exploiting the fact that the first  $N_{\text{GI}} + \mu$  samples of the transmitted OFDM signal are a cyclic repetition of the last  $N_{\text{GI}} + \mu$  samples, i.e.

$$x_p[k] = x_p[k + N], \quad k = 0, \dots, N_{\text{GI}} + \mu. \quad (4.28)$$

Second, the GI is assumed to be sufficiently large such that the last  $\mu$  samples of the cyclic extension are not affected by channel influences yielding

$$\begin{aligned} x_p[k - N + N_{\text{GI}} + \mu - \tau_d] &= x_p[k + N_{\text{GI}} + \mu - \tau_d], \\ k &= N - \mu, \dots, N - 1, \quad d = 0, \dots, N_{\text{D}} - 1. \end{aligned} \quad (4.29)$$

With that, the third line in (4.27) vanishes and (4.27) simplifies to

$$\begin{aligned} R_p^w[n] &= H_p[n]X_p[n] + \sum_{k=0}^{N-1} v_p[k + N_{\text{GI}} + \mu] e^{-j \frac{2\pi k n}{N}} \\ &+ \sum_{k=N-\mu}^{N-1} w[k - N + N_{\text{GI}} + \mu] \\ &\cdot (v_p[k - N + N_{\text{GI}} + \mu] - v_p[k + N_{\text{GI}} + \mu]) e^{-j \frac{2\pi k n}{N}}, \\ &n = 0, \dots, N - 1. \end{aligned} \quad (4.30)$$

From (4.30), it can be seen that Rx windowing only has an impact on noise and interference. The desired OFDM signal  $X_p[k]$  is not affected by windowing at all.

Considering a noise sample  $k \in \{N - \mu, \dots, N - 1\}$  the windowed noise  $n_p^w[k]$  is given by

$$\begin{aligned} n_p^w[k] &= w[k - N + N_{\text{GI}} + \mu] n_p[k + N_{\text{GI}} + \mu - N] \\ &+ (1 - w[k - N + N_{\text{GI}} + \mu]) n_p[k + N_{\text{GI}} + \mu], \\ &k = N - \mu, \dots, N - 1. \end{aligned} \quad (4.31)$$

For the noise variance  $\sigma_n^2 = \text{E}\{n_p[k]^2\}$  it has been shown in [70] that

$$\text{E}\{n_p^w[k]^2\} = \text{E}\{n_p[k]^2\} = \sigma_n^2. \quad (4.32)$$

It can be concluded that windowing influences the noise process, but does not impair the noise variance.



Nevertheless, the overall performance of the OFDM system is slightly degraded by windowing. The impact of the extension of the cyclic prefix required for windowing is two-fold. First, assuming that the same amount of Tx power is available in the case with and without windowing, less Tx power is spend on the transmission of useful data when windowing is performed. The corresponding reduction in SNR equals

$$\text{SNR}^{\text{loss}} = 10 \log_{10} \left( \frac{N + N_{\text{GI}} + \mu}{N + N_{\text{GI}}} \right). \quad (4.33)$$

However, with a reasonable choice of the roll-off factor  $\mu$  of the window, the SNR loss is kept small, e.g. 0.4 dB for a roll-off factor of 10%,  $N = 512$ , and  $N_{\text{GI}} = 21$  as used in the B-VHF system presented in Section 2.3.1. Second, the elongation of the cyclic prefix is related to a throughput loss. Denoting the throughput without windowing by  $D$  and the throughput with windowing by  $D^{\text{w}}$ , the throughput loss can be written as

$$D^{\text{loss}} = 1 - \frac{D^{\text{w}}}{D} = 1 - \frac{\frac{Z}{(N+N_{\text{GI}}+\mu)/f_s}}{\frac{Z}{(N+N_{\text{GI}})/f_s}} = \frac{\mu}{N + N_{\text{GI}} + \mu} \quad (4.34)$$

with  $Z$  representing the number of transmitted bits per OFDM symbol. In the considered example, throughput is reduced by 8.9%.

### 4.2.3 Different Window Types

For generating the window function according to (4.20) it has been assumed that the slopes of the basic pulse  $\bar{w}[k]$  forming the window are symmetric to the y-axis running through the maximum of the pulse. In order to allow for a summation of the first and last  $\mu$  samples affected by windowing and thus to guarantee data not being affected by windowing the pulse also has to fulfill the property

$$\bar{w}[k] + \bar{w}[\mu - k] = 1, k = 0, \dots, \mu - 1, \quad (4.35)$$

i.e. the slopes of the pulse have to be point-symmetric to the centre of the slope. Commonly used pulses fulfilling both properties are Nyquist pulses, such as a raised-cosine also known as Hann pulse or a triangular pulse also known as Barlett pulse [72]. The Hann pulse is defined as

$$\bar{w}[k] = \begin{cases} 0.5 \left( 1 - \cos \left( \frac{\pi k}{\mu} \right) \right) & k = 0, \dots, 2\mu - 1 \\ 0 & \text{otherwise.} \end{cases} \quad (4.36)$$

The amplitude of the first sidelobe of the spectrum of a Hann pulse is reduced by 31 dB relative to the peak. Compared to the si-spectrum of a rectangular spectrum the first sidelobe of a Hann pulse is 18 dB smaller.

A triangular pulse is defined as

$$\bar{w}[k] = \begin{cases} \frac{k}{\mu} & k = 0, \dots, \mu - 1 \\ 1 - \frac{k}{\mu} & k = \mu, \dots, 2\mu - 1 \\ 0 & \text{otherwise.} \end{cases} \quad (4.37)$$

According to [72], the first sidelobe of the spectrum of a triangular pulse exhibits a relative sidelobe amplitude of -25 dB meaning that it is reduced by 12 dB compared to the first sidelobe of the si-spectrum. Other well known pulses such as Blackman and Hamming pulses exhibit even lower sidelobes. However, as they do not fulfil the required properties, they are not appropriate for Rx windowing.

In the literature, approaches for optimising window shapes can be found, e.g. in [73] for mitigating the impact of non-orthogonal interference or in [74] for reducing the impact of inter-carrier interference due to frequency offsets. However, optimised window shapes do not give significant improvements compared to the Hann window. For that reason, only the Hann and the triangular window are considered in this thesis.

To demonstrate the potential of Rx windowing the spectrum of one DSB-AM interferer without sidebands after applying different windows is shown in Fig. 4.4. The centre frequency of the DSB-AM interferer is kept fix at  $n_c = 262.5$ , i.e. midway between two subcarriers in order to produce maximum leakage. At Rx, a 512-point DFT is applied and the size of the applied windows is  $\mu = 52$ , i.e. the roll-off factor is approximately 10%. Compared to the rectangular window, with the triangular window the overall power of the interference signal is reduced by 13.2 dB averaged over all subcarriers and 10,000 OFDM symbols. For the Hann window a reduction as high as 8.9 dB is achieved. Both windows have in common that at large offsets to the centre frequency a very high reduction of interference power is achieved. However, as expected, the peak of the interference signal round the centre frequency is preserved which significantly limits the achieved average interference power reduction. As the width of the remaining peak is smaller for the triangular window, the average interference power reduction is higher than for the Hann window although with the Hann window better interference mitigation is achieved at larger offsets to the centre frequency.

In Fig. 4.5, interference spectra after applying a triangular window with different window sizes ranging from  $\mu = 5$  corresponding to 1% roll-off to  $\mu = 77$  corresponding to 15% roll-off are shown. The achieved reduction of interference power increases with increasing windowing size, i.e. from 0.9 dB for  $\mu = 5$  to 18.5 dB for  $\mu = 77$ . At the same time, the width of the mainlobe, that is determined by the windowing length, decreases. Window size  $\mu = 52$  seems to be a reasonable trade-off between the achieved interference power reduction of 13.2 dB and the losses in SNR and throughput which are 0.4 dB and 8.9% in the considered example, respectively.

All in all, a considerable interference power reduction is achieved at the cost of small losses in throughput and SNR. Other advantages of Rx windowing are the low computational effort and the fact that no information about the interference signal is required at all. Moreover, with the proposed method, the FFT length can be retained. However, the spectral peak of the interference signal cannot be reduced and several subcarriers close to the centre frequency of the interferer are still affected significantly. Hence, additional or alternative methods for NBI mitigation are required.

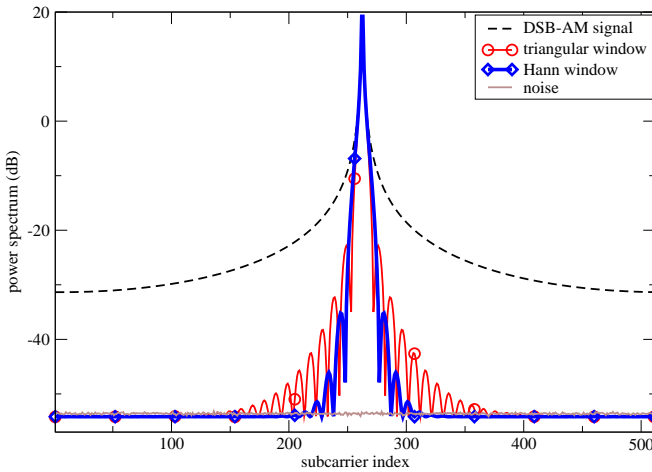


**Figure 4.4** Average interference spectrum of one DSB-AM interferer at  $n_c = 262.5$  after applying different windows,  $N = 512$ ,  $\mu = 52$ .

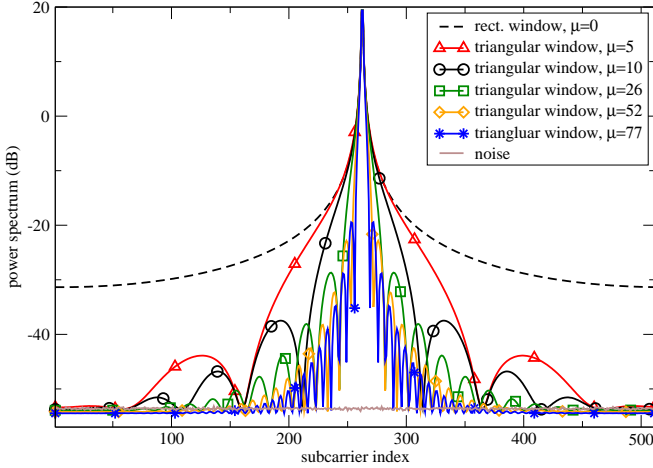


**Figure 4.5** Average interference spectrum of one DSB-AM interferer at  $n_c = 262.5$  after applying a triangular window with different window sizes,  $N = 512$ .

### 4.3 NBI Mitigation in the Frequency Domain

Techniques for mitigating the impact of NBI in the frequency domain after the DFT are mostly based on subtracting an estimation of the interference signal from the Rx signal. Different approaches are distinguished depending on if they simply try to estimate and subtract the interference signal or if they aim at reconstructing and compensating the leakage effect occurring during the DFT operation at Rx. The first method is referred to as subtraction whereas the latter is denoted as leakage compensation. In the following, both approaches are presented and appropriate estimation algorithms are proposed. Both methods are evaluated for different estimation algorithms in terms of estimation error, robustness towards estimation errors, and achieved interference power reduction.

#### 4.3.1 Subtraction

Analogously to (4.17), the frequency domain signal  $R_p[n]$  received on the  $p$ th OFDM symbol,  $p = 0, \dots, P - 1$ , and the  $n$ th subcarrier,  $n = 0, \dots, N - 1$ , is given by

$$R_p[n] = H_p[n]X_p[n] + N_p[n] + I_p[n], \quad (4.38)$$

with  $X_p[n]$  denoting transmitted complex data symbols,  $N_p[n]$  AWGN, and  $I_p[n]$  DSB-AM interference as described in Section 4.1.

A straightforward approach for NBI mitigation is the subtraction of the estimated NBI signal from the Rx signal according to

$$R'_p[n] = R_p[n] - \hat{I}_p[n], \quad n = 0, \dots, N - 1, \quad (4.39)$$

where  $\hat{I}_p[n]$  is the estimation of the NBI signal on the  $n$ th subcarrier and the  $p$ th OFDM symbol. Since the Rx signal normally is processed frame-wise at the OFDM Rx, the subtraction of the estimated interference signal is rewritten for an entire OFDM frame by

$$\mathbf{R}' = \mathbf{R} - \hat{\mathbf{I}}, \quad (4.40)$$

where  $\mathbf{R}'$  denotes the OFDM frame after frequency domain NBI mitigation containing the modified Rx values  $R'_p[n]$  of all  $N$  subcarriers and all  $P$  OFDM symbols. The values  $R_p[n]$  received on the  $n$ th subcarrier and  $p$ th OFDM symbol are collected in the vector  $\mathbf{R}_p = [R_p[0], \dots, R_p[n], \dots, R_p[N - 1]]^T$  and all  $P$  Rx vectors are combined into the matrix  $\mathbf{R} = [\mathbf{R}_0, \dots, \mathbf{R}_p, \dots, \mathbf{R}_{P-1}]$ . The matrix  $\hat{\mathbf{I}}$  represents frequency domain samples of the estimated interference signal on one OFDM frame, i.e.  $\hat{\mathbf{I}} = [\hat{\mathbf{I}}_0, \dots, \hat{\mathbf{I}}_p, \dots, \hat{\mathbf{I}}_{P-1}]$ . Interference samples belonging to the  $p$ th OFDM symbol are collected in the column vector  $\hat{\mathbf{I}}_p = [\hat{I}_p[0], \dots, \hat{I}_p[n], \dots, \hat{I}_p[N - 1]]^T$ .

A short overview of the various existing techniques for estimating NBI is given in Section 4.4. Furthermore, a very simple and efficient method for estimating the interference signal in the frequency domain is presented.

### 4.3.2 Leakage Compensation

The impact of NBI can be mitigated more efficiently by exploiting the correlation between interference contributions on adjacent subcarriers induced by the DFT operation. As the leakage effect described in Section 4.1 is a deterministic property of the DFT, the NBI signal can be reconstructed completely, when it is measured on only a few unused subcarriers referred to as observation subcarriers in the following. The NBI signal is mitigated by subtracting measurements on observation subcarriers weighted by certain coefficients from all used subcarriers. This idea has first been mentioned in [56] in the context of interference in wireline transmission systems such as DSL affected by interference originating from amateur

radios. In [56], interference has been simply modelled as a deterministic sinusoid signal with known frequency. The idea has been further refined for application to stochastic NBI signals with unknown bandwidth, power spectrum, and/or carrier frequency [75–77]. In [75, 76], the NBI signal is parameterised and only maximum Likelihood estimates of the model parameters are determined. In [77], the NBI signal is estimated according to an minimum mean square error (MMSE) criterion by exploiting coarse a priori knowledge about the power spectrum of the NBI signal.

MMSE based leakage compensation has been applied to DSB-AM signals in [78, 79]. In this thesis, the algorithm is refined and adapted to the dynamically changing interference situation which has not been considered so far. Special emphasis is put on the estimation of the NBI signal presented in Section 4.4.

### Algorithm

For mitigating the impact of NBI, a compensation matrix  $\mathbf{C}_{\text{NBI}}$  is generated that reconstructs the interference signal based on measurements on observation subcarriers collected in  $\mathbf{I}_o$ . The compensation of the interference signal can be written as

$$\mathbf{R}' = \mathbf{R} - \mathbf{C}_{\text{NBI}} \cdot \mathbf{I}_o. \quad (4.41)$$

From (4.41), it becomes obvious, that leakage compensation performs a subtraction of the estimated interference signal as well. However, in contrast to the simple subtraction presented above, the interference signal is reconstructed according to an MMSE criterion. That way an MMSE estimate of the interference signal is obtained that is defined as

$$\hat{\mathbf{I}}^{\text{MMSE}} := \mathbf{C}_{\text{NBI}} \cdot \mathbf{I}_o. \quad (4.42)$$

For reconstructing the interference signal,  $\mathbf{R}$  has to contain  $N_L$  observation subcarriers not used for data transmission. These interference measurements for the entire OFDM frame are summarised in  $\mathbf{I}_o = [\mathbf{I}_{o,0}, \dots, \mathbf{I}_{o,p}, \dots, \mathbf{I}_{o,P-1}]$  giving an  $N_L$ -by- $P$  matrix with column vectors  $\mathbf{I}_{o,p} = [R_p[o_0], \dots, R_p[o_l], \dots, R_p[o_{N_L-1}]]^T$ . The positions of the observation subcarriers are denoted by  $o_l$  with  $l = 0, \dots, N_L - 1$ .

The compensation matrix  $\mathbf{C}_{\text{NBI}}$  is generated from the interference signal observed on observation subcarriers with the aim to minimise the mean square error  $e^{\text{MSE}}$  between the actual and the estimated interference signal on each subcarrier and

each OFDM symbol within an OFDM frame

$$E\{\mathbf{e}^{\text{MSE}}\} = E\{\|\mathbf{I} - \hat{\mathbf{I}}^{\text{MMSE}}\|^2\} = E\{\|\mathbf{I} - \mathbf{C}_{\text{NBI}} \cdot \mathbf{I}_o\|^2\} \rightarrow \min. \quad (4.43)$$

Since the interference signal cannot be measured perfectly on the observation subcarriers as observation subcarriers are affected by channel noise, channel noise is taken into account when optimising  $\mathbf{C}_{\text{NBI}}$  with respect to the MMSE criterion [80]. After several manipulations which are given in detail in Appendix C, the compensation matrix is obtained as

$$\mathbf{C}_{\text{NBI}} = \mathcal{R}_{\text{II}_o} \cdot \underbrace{(\mathcal{R}_{\text{I}_o\text{I}_o} + \sigma_n^2 \mathbf{E}_{N_L})^{-1}}_{\mathcal{R}'_{\text{I}_o\text{I}_o}}, \quad (4.44)$$

where  $\mathbf{E}_{N_L}$  denotes an  $(N_L \times N_L)$ -dimensional identity matrix. Autocorrelation properties of the observation subcarriers are collected in the  $(N_L \times N_L)$ -dimensional correlation matrix  $\mathcal{R}_{\text{I}_o\text{I}_o}$  with elements in the  $l'$ th row and  $l$ th column

$$\mathcal{R}_{\text{I}_o\text{I}_o}[l', l] = E\{\mathbf{I}_o[l'] \mathbf{I}_o^H[l]\} = E\left\{\sum_{p=0}^{P-1} I_{o,p}[l'] I_{o,p}^*[l]\right\}. \quad (4.45)$$

The correlation between observation subcarriers and the interference signal is represented by the  $(N \times N_L)$ -dimensional covariance matrix  $\mathcal{R}_{\text{II}_o} = E\{\mathbf{I} \mathbf{I}_o^H\}$ . In the  $n$ th row and  $l$ th column it has the elements

$$\mathcal{R}_{\text{II}_o}[n, l] = E\{\mathbf{I}[n] \mathbf{I}_o^H[l]\} = E\left\{\sum_{p=0}^{P-1} I_p[n] I_{o,p}^*[l]\right\}. \quad (4.46)$$

The autocorrelation matrix  $\mathcal{R}_{\text{I}_o\text{I}_o}$  can easily be determined from measurements on observation subcarriers according to (4.45). For determining  $\mathcal{R}_{\text{II}_o}$ , the interference signal  $\mathbf{I}$  needs to be estimated. As presented in the next section, this can either be done by reconstructing the NBI signal based on estimates of amplitude, phase, and carrier frequency or based on a priori knowledge of the PSD of the disturbance signal.

Regarding the MMSE estimate of the interference signal from (4.42) on the  $n$ th subcarrier and  $p$ th OFDM symbol, it can be clearly seen that  $\hat{I}_p^{\text{MMSE}}[n]$  is a linear combination of measurements on all observation subcarriers of the considered

OFDM symbol

$$\hat{I}_p^{\text{MMSE}}[n] = \sum_{l=0}^{N_L-1} \mathbf{C}_{\text{NBI}}[n,l] I_{o,p}[l], \quad (4.47)$$

where elements of the compensation matrix are given by

$$\mathbf{C}_{\text{NBI}}[n,l] = \sum_{l'=0}^{N_L-1} \mathcal{R}_{\Pi_o}[n,l'] \mathcal{R}'_{I_o I_o}[l',l]. \quad (4.48)$$

### Example

The functionality of leakage compensation is demonstrated at hand of a simple example with  $N_L = 2$  and  $P = 2$ . Substituting (4.48), (4.45), and (4.46) in (4.47) and using the above parameters the MMSE estimate of the interference signal on the  $n$ th subcarrier in the 0th OFDM symbol can be expressed as

$$\begin{aligned} \hat{I}_0^{\text{MMSE}}[n] &= I_0[n] \frac{|I_{o,0}[0]I_{o,1}[1] - I_{o,0}[1]I_{o,1}[0]|^2}{\det(\mathcal{R}'_{I_o I_o})} \\ &+ I_0[n] \frac{\sigma_n^2 (|I_{o,0}[0]|^2 + |I_{o,0}[1]|^2)}{\det(\mathcal{R}'_{I_o I_o})} \\ &+ I_1[n] \frac{\sigma_n^2 (I_{o,1}^*[0]I_{o,0}[0] + I_{o,1}^*[1]I_{o,0}[1])}{\det(\mathcal{R}'_{I_o I_o})} \end{aligned} \quad (4.49)$$

with  $\mathcal{R}'_{I_o I_o}$  from (4.44). The determinant of  $\mathcal{R}'_{I_o I_o}$  equals

$$\begin{aligned} \det(\mathcal{R}'_{I_o I_o}) &= |I_{o,0}[0]I_{o,1}[1] - I_{o,0}[1]I_{o,1}[0]|^2 \\ &+ \sigma_n^2 (|I_{o,0}[0]|^2 + |I_{o,0}[1]|^2 + |I_{o,1}[0]|^2 + |I_{o,1}[1]|^2). \end{aligned} \quad (4.50)$$

Accordingly, the MMSE estimate of the interference signal on the  $n$ th subcarrier in the 1st OFDM symbol is

$$\begin{aligned} \hat{I}_1^{\text{MMSE}}[n] &= I_0[n] \frac{\sigma_n^2 (I_{o,0}^*[0]I_{o,1}[0] + I_{o,0}^*[1]I_{o,1}[1])}{\det(\mathcal{R}'_{I_o I_o})} \\ &+ I_1[n] \frac{|I_{o,0}[0]I_{o,1}[1] - I_{o,0}[1]I_{o,1}[0]|^2}{\det(\mathcal{R}'_{I_o I_o})} \\ &+ I_1[n] \frac{\sigma_n^2 (|I_{o,1}[0]|^2 + |I_{o,1}[1]|^2)}{\det(\mathcal{R}'_{I_o I_o})}. \end{aligned} \quad (4.51)$$



For the noise free case, i.e. for  $\sigma_n^2 = 0$ , leakage compensation reduces to a simple subtraction of the disturbance signal as presented in Section 4.3.1.

When only one OFDM symbol is considered, i.e.  $P = 1$ , the noise terms in (4.49) vanish. Hence, the interference signal is just subtracted and the same performance as for a simple subtraction is achieved. When more than one OFDM symbol is considered, i.e.  $P > 1$ , the noise variance of the channel is taken into account and averaging over interference signals on all considered OFDM symbols is performed. On the one hand that way noise influences distorting interference measurements on observation subcarriers are diminished. On the other hand, the interference signal varies from OFDM symbol to OFDM symbol. When determining the compensation matrix, the average of these variations is taken, leading to suboptimal results even when the interference signal is perfectly known. However, when the interference signal has to be estimated, this again is advantageous as estimation errors are diminished by averaging over the interference signals on several OFDM symbols and the method becomes robust to estimation errors.

The performance of leakage compensation strongly depends on the position and number of observation subcarriers. Theoretically, observation subcarriers can be located at arbitrary positions to reconstruct the disturbance signal from the respective measurements. However, observation subcarriers close to the peak are advantageous as there, they are hardly affected by noise and other interferers. The choice of the number of observation subcarriers appropriate for the application to DSB-AM signals is addressed in the context of NBI estimation.

### Computational Complexity

Comparing the simple subtraction and leakage compensation in terms of their complexity it is clearly seen that leakage compensation requires higher efforts when both methods base on the same NBI estimation. Despite several matrix operations, the complexity of leakage compensation is still moderate. Even the most complex operation, namely the inversion of  $(\mathcal{R}_{I_o, I_o} + \sigma_n^2 \mathbf{E}_{N_L})$  in (4.44), is related to an acceptable complexity as the matrix to be inverted is small and its dimension only depends on the number of observation subcarriers.

If required, the complexity of the MMSE estimator can be reduced significantly at the cost of slight performance losses. In [77], a low-rank approximation by means of singular value decomposition has been proposed for that purpose.

## 4.4 Estimation of NBI

For mitigating the impact of NBI in the frequency domain either with subtraction or leakage compensation, the NBI signal needs to be estimated. Estimation can be performed either in the time or in the frequency domain. In [81], an estimator has been proposed that averages samples of the time domain Rx signal by means of a sliding window acting as low-pass filter. In [82], only the amplitude is estimated via the sliding window technique whereas the frequency is estimated in the frequency domain. The phase of the NBI signal is not considered at all.

Frequency, amplitude, and phase of a single-tone sinusoid affected by noise can also be estimated using subspace-based methods [83]. Performance can be increased by exploiting the redundancy contained in the GI in order to remove the information bearing part of the OFDM signal prior to NBI estimation. However, this method is complex and requires a very long GI that reduces throughput.

In this thesis, a different approach for estimating the NBI signal in the frequency domain based on a few observation subcarriers is used [84]. Given the fact that the spectral shape of the NBI signal is known a priori since spectral leakage is a deterministic property of the DFT, frequency, amplitude, and phase of the NBI signal can be observed on a few unmodulated subcarriers. Then, the NBI signal is reconstructed by simply adapting the expected interference signal to the actually received interference measurements. As that way only the carrier of the DSB-AM signal is considered, a second algorithm is investigated that takes into account the DSB-AM sidebands by exploiting a priori knowledge about the power spectral density (PSD) [77].

### 4.4.1 Available A Priori Knowledge and Means of Observation

For estimation and mitigation of NBI as discussed in this thesis, the interference signal needs to be measured on observation subcarriers. These subcarriers may not be used for data transmission in order to allow for measuring the uncorrupted interference signal. In case an interferer occurs in a channel that cannot be used for data transmission anyway, all subcarriers within the respective channel of the licensed system may serve for observation purposes without sacrificing transmission bandwidth. In order to be able to measure interference in channels used by the overlay system, a few subcarriers must not be used for data transmission, but serve as observation subcarriers instead. In particular with respect to these channels, the number

of observation subcarriers has to be kept at a minimum.

Due to the fixed channel assignment used in many licensed systems, the maximum number and centre frequencies of interferers occurring within the transmission bandwidth of the overlay system are assumed to be known a priori. Consequently, observation subcarriers need to be inserted in channels potentially used by the licensed system, hence reducing the number of subcarriers that cannot be used for data transmission. Variations of the centre frequencies due to Doppler effects and inaccuracies in the Tx of the licensed system are limited to one subcarrier spacing such that it can be assumed to be known between which two adjacent subcarriers the centre frequency of the interferer lies. The required observation subcarriers are positioned such as to measure the interference signal as efficiently as possible, i.e. close to the interference peak. The resulting structure of the OFDM frame including observation subcarriers is illustrated in Fig. 4.6.

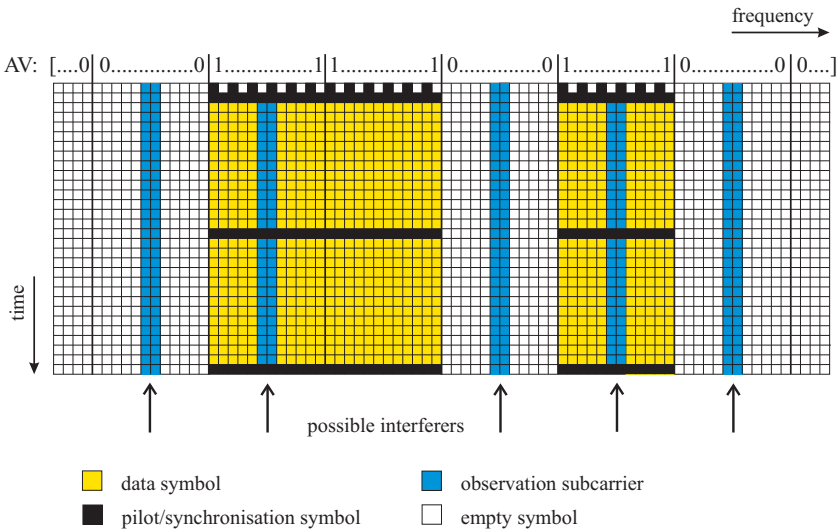


Figure 4.6 OFDM frame with observation subcarriers.

### 4.4.2 Detection of Active Interferers

In a first step, actual active interferers are detected. This is easily realised by measuring interference power on observation subcarriers. An interferer is detected to be

active when its power averaged over all observation subcarriers in the corresponding channel of the licensed system is above a certain threshold which is slightly above the noise level. With respect to a subtraction of the estimated NBI signal this decision can be taken for each individual OFDM symbol within the frame as the subtraction of the estimated NBI signal is performed for each OFDM symbol separately. However, with respect to leakage compensation which is applied to a complete OFDM frame one decision per OFDM frame is required. Hence, if an interferer is detected to be active in one OFDM symbol, it is assumed to be active for the complete OFDM frame duration.

If no interferer is detected in a channel of the licensed system, the corresponding observation subcarriers are not used for the subsequently applied estimation and mitigation algorithms. Firstly, this reduces the number of interferers to be estimated. Secondly, matrix dimensions for the leakage compensation algorithm are kept small. Hence, this detection step precedes the estimation and mitigation mainly with the aim to reduce complexity.

Even if an interferer is wrongly detected to be active, this does not have an impact on the performance of NBI estimation and mitigation. When estimating and subtracting the NBI signal, the amplitude of the interferer is estimated to be very small such that this interferer is negligible in any case. When applying leakage compensation, the entries in  $\mathcal{R}_{I_o, I_o}$  from (4.44) corresponding to the falsely detected interferer are very small such that this interferer is not considered actually.

### 4.4.3 Estimation of Carrier Signal

Given the fact that the carrier of any NBI signal substantially contributes to the leakage effect, the impact of interference can already be reduced significantly by only estimating and mitigating the carrier signal. Recalling the frequency domain representation of the interference signal given in (4.9), the carrier of the NBI signal can be reconstructed if centre frequency, amplitude, and phase are known [84]. For reasons of simplicity, at first, the estimation of one interferer is addressed and generalised to the estimation of multiple interferers later on.

In contrast to the relatively complex estimation of the carrier frequency in the time domain, the centre frequency can easily be determined at hand of two observation subcarriers directly adjacent to the presumed centre frequency  $\tilde{n}_c$ . The position of the observation subcarrier to the left of the carrier is denoted  $o_1 = \lfloor \tilde{n}_c \rfloor$ ; the position of the observation subcarrier to the right  $o_2 = \lceil \tilde{n}_c \rceil$ . The centre frequency measured

on the  $p$ th OFDM symbol can be derived from the ratio  $C_p$  of the amplitudes on the two observation subcarriers

$$C_p := \frac{|R_p[o_1]|}{|R_p[o_2]|}. \quad (4.52)$$

As shown in Fig. 4.1, both observation subcarriers have the same amplitude when the centre frequency is exactly in the middle between the two adjacent subcarriers, i.e.  $C_p = 1$ . If the amplitude of the observation subcarrier to the left is larger than the one of the observation subcarrier to the right, the centre frequency lies between  $o_1$  and  $o_1 + 0.5$  and  $C_p > 1$ . For the reverse case, the centre frequency lies between  $o_2 - 0.5$  and  $o_2$  and  $C_p < 1$ . Thus, an estimation of the carrier frequency can directly be derived from  $C_p$  given in (4.52). After substituting (4.9) into (4.52) and some simplifications the estimation of the carrier frequency  $\hat{n}_{c,p}$  for the  $p$ th OFDM symbol yields

$$\hat{n}_{c,p} = \frac{C_p \cdot o_1 + o_2}{C_p + 1}. \quad (4.53)$$

With (4.53), the carrier frequency of the NBI signal can be estimated accurately with low complexity. Prerequisites are at least two observation subcarriers and the assumption that the centre frequency varies only within one subcarrier spacing.

Once an estimate  $\hat{n}_{c,p}$  of the carrier frequency is available a preliminary estimation  $\tilde{\mathbf{I}}_p = [\tilde{I}_p[0], \dots, \tilde{I}_p[n], \dots, \tilde{I}_p[N-1]]^T$  of the interference signal on all subcarriers of the  $p$ th OFDM symbol is generated assuming  $\hat{A}_p = 1$  and  $\hat{\varphi}_p = 0$ . Using the general representation of the carrier of the interference signal from (4.9), the preliminary estimation is adjusted to the actually measured interference signal yielding

$$\begin{aligned} \hat{\mathbf{I}}_p &= \hat{A}_p \cdot \exp(j\hat{\varphi}_p) \cdot \tilde{\mathbf{I}}_p \\ &= \hat{A}_p \cdot \exp(j\hat{\varphi}_p) \cdot \exp\left(-j\pi(n - \hat{n}_{c,p})\frac{N-1}{N}\right) \cdot \frac{\sin(\pi(n - \hat{n}_{c,p}))}{\sin(\pi/N(n - \hat{n}_{c,p}))}. \end{aligned} \quad (4.54)$$

Estimations of amplitude and phase are obtained by comparing Rx values on all  $N_L$  observation subcarriers and the corresponding values on the preliminary interference signal  $\tilde{\mathbf{I}}_p$

$$\hat{A}_p = \frac{1}{N_L} \sum_{l=0}^{N_L-1} \frac{|R_p[o_l]|}{|\tilde{I}_p[o_l]|}, \quad \hat{\varphi}_p = \frac{1}{N_L} \sum_{l=0}^{N_L-1} \arg\{R_p[o_l]\} - \arg\{\tilde{I}_p[o_l]\} \quad (4.55)$$

with  $\arg\{\cdot\}$  denoting the argument of a complex number. In order to reduce the impact of noise, interference measurements are averaged over all observation subcarriers. Hence, estimation accuracy is expected to improve with increasing number of observation subcarriers.

The amplitude is estimated for each OFDM symbol separately, since that way interferers appearing and disappearing within one OFDM frame can be tracked. The phase also needs to be estimated for each OFDM symbol due to the phase shifts between interference signals on consecutive OFDM symbols induced by removing the CP. The phase shifts given by (4.8) depend on the centre frequency  $n_{c,p}$  of the interferer and thus are different for each interferer. When multiple interferers are present within the bandwidth of the overlay system, it is not possible to compensate phase shifts jointly for all interferers hence requiring an individual phase estimation each interferer in each OFDM symbol.

Theoretically, with this algorithm amplitude and phase of an NBI signal can be estimated based on an arbitrary number and position of observation subcarriers. However, observation subcarriers close to the peak of the interference signal are advantageous as there, they are hardly affected by noise, other interferers and sidebands. Moreover, the subcarriers directly adjacent to the peak are required in any case for estimating the carrier frequency.

The estimated interference signal is used for NBI mitigation algorithms described in Sections 4.3.1 and 4.3.2. For subtraction,  $\hat{\mathbf{I}}_p$  from (4.54) is just subtracted. For MMSE based leakage compensation,  $\mathcal{R}_{\text{II}_o}$  in (4.46) is derived from  $\hat{\mathbf{I}}_p$  given by (4.54). Hence, the elements of  $\mathcal{R}_{\text{II}_o}$  become

$$\mathcal{R}_{\text{II}_o}[n,l] = \text{E}\{\hat{\mathbf{I}}[n] \mathbf{I}_o^H[l]\} = \text{E}\left\{\sum_{p=0}^{P-1} \hat{I}_p[n] I_{o,p}^*[l]\right\} \quad (4.56)$$

and the compensation matrix  $\mathbf{C}_{\text{NBI}}$  is generated according to (4.44). As only the carrier signal is estimated and sidebands are neglected, only suboptimal results can be obtained with both algorithms for NBI mitigation, even if the carrier signal is estimated and reconstructed perfectly.

Neglecting mutual influences of the carrier signals of multiple interferers with different carrier frequencies occurring within the bandwidth of the OFDM based overlay system, different interferers can be estimated independently. The estimations of all carrier signals are summed up and are either subtracted or serve as input for generating a compensation matrix that jointly compensates spectral leakage of all

interferers. Instead of estimating all interferers in parallel, interferers could be estimated iteratively starting with the strongest interferer. Once the strongest interferer is estimated, the estimated signal is subtracted from the Rx signal and the second strongest interferer is estimated. When all interferers are estimated, the overall NBI estimation is generated by summing up all individually estimated signals. That way, estimation accuracy is improved as influences of other interferers are reduced that may distort the estimation of the currently considered interferer. However, as additional complexity is induced this approach is not further considered in this thesis.

#### 4.4.4 Estimation based on PSD

For generating the compensation matrix according to (4.44) the interference signal does not need to be estimated in detail. Alternatively, the correlation matrices  $\mathcal{R}_{\text{II}_o}$  and  $\mathcal{R}_{\text{I}_o\text{I}_o}$  both required for leakage compensation are constructed based on a priori knowledge about the PSD of the NBI signal [77]. For that algorithm, information on the bandwidth is sufficient whereas the actual shape of the PSD has a minor impact. Hence, the PSD of the sidebands of the DSB-AM signal can be approximated to be constant within the interval  $[-B, \dots, B]$ , where  $B$  denotes the bandwidth of the DSB-AM signal. In addition, the carrier of the DSB-AM signal is considered as a dirac impulse  $\delta(f)$  yielding the PSD  $P_I(f)$  of the complete DSB-AM signal

$$P_I(f) = \begin{cases} \delta(f) + 1/(2B) & -B, \dots, B \\ 0 & \text{otherwise.} \end{cases} \quad (4.57)$$

The actual and the approximated PSD of the sidebands are shown in Fig. 4.7. Note, for reasons of simplicity, the carrier has been omitted in this illustration. The bandwidth of the DSB-AM signal is mainly determined by the bandwidth of the filter applied at the DSB-AM transmitter which limits the bandwidth of the signal to approximately  $B = 2.7$  kHz. As the filter characteristics are known it can easily be presumed that this kind of a priori knowledge is generally available.

The covariance matrix  $\mathcal{R}_{\text{II}_o}$  from (4.46) can be rewritten to its equivalent time domain representation by

$$\mathcal{R}_{\text{II}_o}[n, l] = \text{E} \left\{ \sum_{p=0}^{P-1} I_p[n] I_{o,p}^*[l] \right\} = \text{E} \left\{ \sum_{p=0}^{P-1} I_p[n] I_p^*[o_l] \right\} \quad (4.58)$$

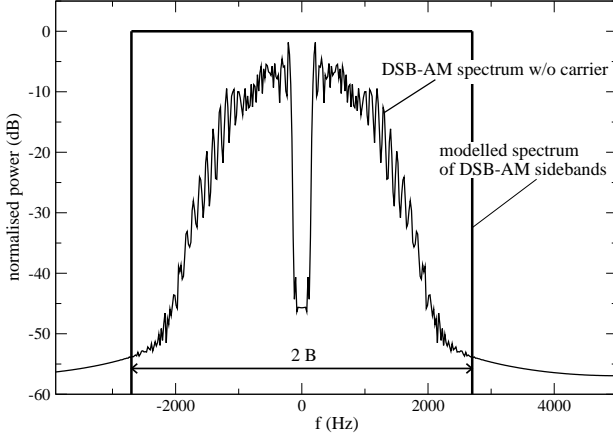


**Figure 4.7** Actual and modelled PSD of sidebands of baseband DSB-AM signal.

$$\begin{aligned}
 &= \mathbb{E} \left\{ \sum_{p=0}^{P-1} \text{DFT}\{i_p[u]\} \cdot \text{DFT}\{i_p^*[v]\} \right\} \\
 &= \mathbb{E} \left\{ \sum_{p=0}^{P-1} \sum_{u=0}^{N-1} i_p[u] e^{-j2\pi un/N} \sum_{v=0}^{N-1} i_p^*[v] e^{j2\pi v o_l/N} \right\} \\
 &= \sum_{p=0}^{P-1} \sum_{u=0}^{N-1} \sum_{v=0}^{N-1} \mathbb{E}\{i_p[u] i_p^*[v]\} e^{-j2\pi(un - v o_l)/N}.
 \end{aligned}$$

The term  $\mathbb{E}\{i_p[u] i_p^*[v]\}$  is the autocorrelation function (ACF) of the time domain interference signal  $i_p[u]$ ,  $u = 0, \dots, N - 1$ , denoted by

$$r_{ii}[u - v] := \mathbb{E}\{i_p[u] i_p^*[v]\}. \quad (4.59)$$

According to the Wiener-Khinchin theorem [85] the Fourier transform of the ACF yields the PSD. Hence, the autocorrelation function of  $i_p[u]$ ,  $u = 0, \dots, N - 1$ , writes

$$r_{ii}[u - v] = \int_{-\infty}^{\infty} P_I(f - f_c) e^{j2\pi f(u-v)/f_s} df. \quad (4.60)$$



With the PSD from (4.57), the ACF from (4.60) becomes

$$\begin{aligned} r_{ii}[u-v] &= \int_{-B+f_c}^{B+f_c} \left( \delta(f-f_c) + \frac{1}{2B} \right) e^{j2\pi f(u-v)/f_s} df \\ &= e^{j2\pi f_c(u-v)/f_s} \left( 1 + \frac{\sin(2\pi B(u-v)/f_s)}{2\pi B(u-v)/f_s} \right). \end{aligned} \quad (4.61)$$

Substituting (4.61) into (4.58), the covariance matrix can finally be rewritten as

$$\begin{aligned} \mathcal{R}_{\text{II}_o}[n,l] &= P \sum_{u=0}^{N-1} \sum_{v=0}^{N-1} \left( \left( 1 + \frac{\sin(2\pi B(u-v)/f_s)}{2\pi B(u-v)/f_s} \right) \right. \\ &\quad \left. \cdot e^{j2\pi f_c(u-v)/f_s} \cdot e^{-j2\pi(un-vo)/N} \right). \end{aligned} \quad (4.62)$$

As the bandwidth  $B$  is fixed and known,  $\mathcal{R}_{\text{II}_o}$  can be determined a priori. Analogously,  $\mathcal{R}_{\text{I}_o\text{I}_o}$  is calculated a priori hence enabling the determination of the complete compensation matrix  $\mathbf{C}_{\text{NBI}}$  according to (4.44). As the compensation matrix has to be determined only once rather than for each transmitted OFDM frame, computational complexity of the leakage compensation algorithm is reduced significantly when the PSD based estimation is applied.

If multiple interferers with different carrier frequencies occur within the bandwidth of the OFDM based overlay system, the PSD model from (4.57) has to be considered for each interferer. For determining the ACF  $r_{ii}[u-v]$  according to (4.60), for each interferer, the PSD is shifted to the respective centre frequency denoted by  $f_{c,i}$  and the resulting ACFs of the  $N_I$  different interferers sum up, i.e.

$$r_{ii}[u-v] = \sum_{i=0}^{N_I-1} e^{j2\pi f_{c,i}(u-v)/f_s} \left( 1 + \frac{\sin(2\pi B(u-v)/f_s)}{2\pi B(u-v)/f_s} \right). \quad (4.63)$$

With (4.63), the autocorrelation matrices  $\mathcal{R}_{\text{II}_o}$  and  $\mathcal{R}_{\text{I}_o\text{I}_o}$  are determined such as to represent all  $N_I$  interferers. As a prerequisite, possible positions of all interferers in the spectrum have to be known a priori in order to keep the number of observation subcarriers as well as matrix dimensions small. The MMSE estimate of the actual interference is produced by multiplying the compensation matrix  $\mathbf{C}_{\text{NBI}}$  with values  $\mathbf{I}_o$  currently measured on observation subcarriers. That way, it is ensured that only active interferers are compensated. The values on observation subcarriers of inactive interferers are at noise level such that the corresponding MMSE estimates

become negligible.

#### 4.4.5 Comparison of Different NBI Estimation and Mitigation Techniques

The potential of both estimation algorithms is demonstrated by applying them to the frequency domain NBI mitigation techniques as presented in Sections 4.3.1 and 4.3.2. The estimation of the carrier signal can be applied to both the simple subtraction as well as to leakage compensation, whereas the PSD based estimation of the interference signal is only feasible for leakage compensation. This results in three combinations, i.e.

- Subtraction of estimated carrier signal,
- Carrier based leakage compensation,
- PSD based leakage compensation.

For reasons of simplicity, only one DSB-AM interferer with centre frequency  $n_c = 262.5$  is considered in the following.

In general, the estimation error  $e^{\text{MSE}}$  is defined by the covariance matrix of the difference between the actual and estimated interference signal [80]. The estimation error averaged over all subcarriers and all OFDM symbols within an OFDM frame is obtained by forming the trace of the covariance matrix, i.e.

$$e^{\text{MSE}} = \frac{1}{N} \text{tr} \{ \text{E} \{ e^{\text{MSE}} \} \} = \frac{1}{N} \text{tr} \left\{ \text{E} \{ \| \mathbf{I} - \hat{\mathbf{I}} \|^2 \} \right\}, \quad (4.64)$$

where  $\text{tr}\{\cdot\}$  denotes the trace of a matrix.

##### Subtraction of Estimated Carrier Signal

For subtraction, the carrier of the NBI signal is estimated and subtracted from the Rx signal. Taking into account that the interference signal is composed of a carrier and sidebands and splitting up the covariance matrix into its components, the

resulting estimation error is obtained

$$\begin{aligned}
 e^{\text{MSE}} &= \frac{1}{N} \text{tr}\{\mathbf{E}\{\|\mathbf{I}^{\text{carrier}} + \mathbf{I}^{\text{sb}} - \hat{\mathbf{I}}\|^2\}\} \\
 &= \frac{1}{N} \text{tr}\{\mathcal{R}_{\mathbf{I}^{\text{carrier}}\mathbf{I}^{\text{carrier}}} - 2\text{Re}\{\mathcal{R}_{\hat{\mathbf{I}}\mathbf{I}^{\text{carrier}}}\} + \mathcal{R}_{\hat{\mathbf{I}}\hat{\mathbf{I}}} \\
 &\quad + 2\text{Re}\{\mathcal{R}_{\mathbf{I}^{\text{carrier}}\mathbf{I}^{\text{sb}}}\} - 2\text{Re}\{\mathcal{R}_{\mathbf{I}^{\text{sb}}\hat{\mathbf{I}}}\} + \mathcal{R}_{\mathbf{I}^{\text{sb}}\mathbf{I}^{\text{sb}}}\}.
 \end{aligned} \tag{4.65}$$

The matrices  $\mathcal{R}_{\mathbf{I}^{\text{carrier}}\mathbf{I}^{\text{carrier}}}$ ,  $\mathcal{R}_{\hat{\mathbf{I}}\mathbf{I}^{\text{carrier}}}$ , and  $\mathcal{R}_{\hat{\mathbf{I}}\hat{\mathbf{I}}}$  denote the covariance matrices already known from (4.44). The correlation between the carrier or the estimated carrier and the DSB-AM sidebands are represented by  $\mathcal{R}_{\mathbf{I}^{\text{carrier}}\mathbf{I}^{\text{sb}}}$  or  $\mathcal{R}_{\mathbf{I}^{\text{sb}}\hat{\mathbf{I}}}$ , respectively. The matrix  $\mathcal{R}_{\mathbf{I}^{\text{sb}}\mathbf{I}^{\text{sb}}}$  denotes the autocorrelation of the sidebands.  $\text{Re}\{\cdot\}$  refers to the real part of a complex matrix.

The estimation error in (4.65) is determined by the mismatch between the actual interference signal consisting of a carrier and sidebands and the assumed interference model, which is the carrier only. In addition, inaccuracies in the estimation of the carrier contribute to the estimation error. The estimation error related to inaccuracies of carrier estimation is evaluated by regarding the carrier signal isolatedly, i.e.  $\eta = 0$  in (4.1). The resulting contribution to the total estimation error equals

$$e_{\text{carrier}}^{\text{MSE}} = \frac{1}{N} \text{tr}\{\mathcal{R}_{\mathbf{I}^{\text{carrier}}\mathbf{I}^{\text{carrier}}} - 2\text{Re}\{\mathcal{R}_{\hat{\mathbf{I}}\mathbf{I}^{\text{carrier}}}\} + \mathcal{R}_{\hat{\mathbf{I}}\hat{\mathbf{I}}}\}. \tag{4.66}$$

The estimation error  $e_{\text{carrier}}^{\text{MSE}}$  for the carrier signal as well as the total estimation error  $e^{\text{MSE}}$  are simulated for different numbers and positions of observation subcarriers. For the simulations, the parameters of the B-VHF system as listed in Tab. 2.1 have been used. DSB-AM interference signals have been generated for 100,000 OFDM frames each having a length corresponding to  $P = 45$  OFDM symbols. One DSB-AM interferer with  $n_c = 262.5$  has been considered and its carrier frequency has been kept fix in order to focus the investigations on the estimation of amplitude and phase of the NBI signal. The average power of the DSB-AM signal is normalised to 1. The estimation errors given in Tab. 4.1 are averaged over all OFDM frames, all OFDM symbols, and all subcarriers except for those in the channel where the interferer is present, i.e. subcarriers with index  $n = 0, \dots, 511 \setminus \{257, \dots, 268\}$  have been considered.

The small estimation error  $e_{\text{carrier}}^{\text{MSE}}$  occurring when estimating the carrier of the DSB-AM signal without sidebands can be explained by noise impairments on the observation subcarriers. As can be seen from Tab. 4.1, it is advantageous to consider only

**Table 4.1** Estimation error for one interferer and different numbers and positions of observation subcarriers

observation subcarriers	subtraction of estimated carrier signal	
	with sidebands $e^{\text{MSE}}$	without sidebands $e_{\text{carrier}}^{\text{MSE}}$
$N_L = 2, o_l = 262,263$	$1.15 \cdot 10^{-3}$	$1.47 \cdot 10^{-9}$
$N_L = 2, o_l = 261,264$	$1.20 \cdot 10^{-4}$	$1.33 \cdot 10^{-8}$
$N_L = 2, o_l = 257,268$	$1.82 \cdot 10^{-6}$	$2.03 \cdot 10^{-7}$
$N_L = 4, o_l = 261, \dots, 264$	$5.49 \cdot 10^{-4}$	$3.67 \cdot 10^{-9}$
$N_L = 12, o_l = 257, \dots, 268$	$7.12 \cdot 10^{-5}$	$4.50 \cdot 10^{-8}$

a few number of observation subcarriers close to the peak of the interferer rather than averaging over a larger number of subcarriers that are farther away from the peak, e.g.  $N_L = 12$  with  $o_l = 257, \dots, 268$ , or employing observation subcarriers at the edges of the occupied DSB-AM channel, i.e.  $N_L = 2$  at  $o_l = 257, 268$ . This can be explained by the interference-to-noise ratio (INR) that is substantially smaller on the subcarriers at the edges of the DSB-AM channel than on subcarriers close to the peak and hence distorts interference measurements significantly.

In general, the estimation error  $e^{\text{MSE}}$  is significantly larger when the DSB-AM signal with sidebands is estimated indicating the major contribution of the model mismatch between the actual interference signal and the assumed interference model to the overall estimation error. Nevertheless, an estimation of the carrier only is accurate enough to provide a considerable reduction of interference power when subtracting the estimated carrier signal from the Rx OFDM signal.

The spectra of the interference signal after subtraction of the estimated interference signal are shown in Fig. 4.8 for different numbers and positions of observation subcarriers. As already indicated by the decreasing estimation error given in Tab. 4.1, the achieved reduction of interference power increases with increasing number of observation subcarriers when observation subcarriers directly adjacent to the peak are used. On the average, the power of the DSB-AM signal is reduced by 14.5 dB for  $N_L = 2$  observation subcarriers at  $o_l = 262, 263$  and by up to 24.4 dB for  $N_L = 12$  observation subcarriers at  $o_l = 257, \dots, 268$ . When  $N_L = 2$  observation subcarriers are employed but positioned at  $o_l = 261, 264$ , interference power is reduced by 21.2 dB which is close to the performance with  $N_L = 12$  observation subcarriers. Even better performance is achieved when positioning observation

subcarriers at  $o_l = 257, 268$ , i.e. at the edges of the 25 kHz DSB-AM channel. In that case interference power is reduced to the noise level on most subcarriers resulting in an average interference power reduction of 34.5 dB. This high interference power reduction is explained by the fact that parts of the sidebands are taken into account when estimating the NBI signal by means of observation subcarriers at relatively large frequency offset to the interference peak. The carrier itself is neither estimated nor mitigated accurately as can be seen from the large estimation error without sidebands in Tab. 4.1 and the strong remaining interference peak in Fig. 4.8. Hence, performance will degrade drastically for interferers with smaller power when INR on the observation subcarriers is too small to enable an accurate estimation of the DSB-AM signal including sidebands.

All in all, the achieved interference power reduction is consistent with the estimation error given in Tab. 4.1. The choice of observation subcarriers is addressed in more detail in the next but one subsection.

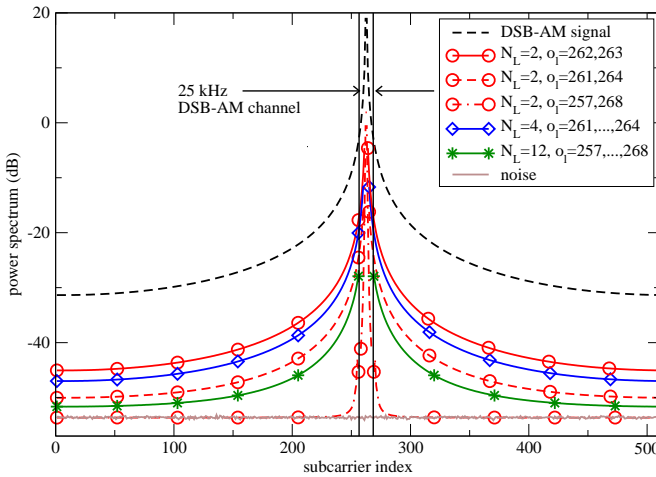


**Figure 4.8** Average interference spectrum after subtraction of estimated interference signal for different numbers and positions of observation subcarriers,  $n_c = 262.5$ ,  $N = 512$ .

### Leakage Compensation based on Estimated Carrier Signal or PSD

Employing the algorithm for leakage compensation as described in Section 4.3.2, an MMSE estimate of the interference signal for the entire OFDM frame is determined by  $\hat{\mathbf{I}}^{\text{MMSE}} = \mathbf{C}_{\text{NBI}} \cdot \mathbf{I}_o$ . Hence, the estimation error is given by

$$e^{\text{MSE}} = \frac{1}{N} \text{tr} \left\{ \mathbb{E} \left\{ \|\mathbf{I} - \mathbf{C}_{\text{NBI}} \cdot \mathbf{I}_o\|^2 \right\} \right\}. \quad (4.67)$$

Same as for the estimation error occurring when subtracting the estimated NBI signal, the estimation error occurring with leakage compensation can be split up into two contributions. First, noise impairs the measurements on observation subcarriers. Second, the mismatch between the actual interference signal and the assumed model, which is either the carrier or the PSD of the DSB-AM signal, induces estimation errors. For both estimation approaches, the estimation error  $e^{\text{MSE}}$  is simulated with the same parameters as for the subtraction of the estimated carrier. The obtained estimation errors are given in Tab. 4.2 for different numbers and positions of observation subcarriers.

As already observed for the subtraction of the estimated carrier the estimation error decreases with increasing number of observation subcarriers when subcarriers directly adjacent to the interference peak are considered. Again,  $N_L = 2$  observation subcarriers at  $o_l = 261,264$  or at  $o_l = 257,268$  are an exception as nearly the same or even smaller estimation error as with  $N_L = 12$  observation subcarriers is achieved. Again, the smallest estimation error is observed for  $N_L = 2$  at  $o_l = 257,268$  and  $N_L = 12$  observation subcarriers as on these observation subcarriers parts of the sidebands are measured which allows for partly compensating the mismatch between the actual and the assumed interference model.

As shown in the example in Section 4.3.2, for  $P = 1$ , subtraction and carrier based leakage compensation have the same performance as leakage compensation does not take advantage of averaging the measurements on multiple OFDM symbols. When the MMSE estimate is generated for the entire OFDM frame with  $P = 45$  OFDM symbols, carrier based leakage compensation outperforms the simple subtraction. Although employing the same estimation of the interference signal, the estimation error is reduced by up to one order of magnitude due to the MMSE optimisation of the estimated NBI signal. For  $N_L = 4$  and  $N_L = 12$  only slight improvements and for  $N_L = 2$  observation subcarriers at  $o_l = 257,268$ , no improvements are observed for carrier based leakage compensation. On these subcarriers, parts of the sidebands are measured that vary from OFDM symbol to OFDM

symbol. Carrier based leakage compensation averages out the variances in the sidebands resulting in a more accurate estimation of the carrier but without taking into account the sidebands at all.

For PSD based leakage compensation, in most cases, the estimation error is larger than for carrier based leakage compensation. This is due to the fact that the compensation matrix is determined a priori and the MMSE estimate only is adapted to actual interference conditions by means of the interference signal measured on observation subcarriers. As expected, the same estimation error is obtained for the case when PSD based leakage compensation is applied to the complete OFDM frame with  $P = 45$  OFDM symbols or to each OFDM symbol separately.

Since PSD based leakage compensation aims at considering the DSB-AM sidebands, observation subcarriers close to the peak are not suitable as indicated by the high estimation error for  $N_L = 2$  observation subcarriers at  $o_l = 262,263$  given in Tab. 4.2. In contrast to leakage compensation or subtraction based on carrier estimation, observation subcarriers far from the peak of the interference signal are advantageous.

**Table 4.2** Estimation error for one interferer and different numbers and positions of observation subcarriers

observation subcarriers		leakage compensation	
		based on carrier	based on PSD
$N_L = 2, o_l = 262,263$	$P = 45$	$4.26 \cdot 10^{-4}$	$4.10 \cdot 10^{-3}$
	$P = 1$	$1.15 \cdot 10^{-3}$	$4.13 \cdot 10^{-3}$
$N_L = 2, o_l = 261,264$	$P = 45$	$4.44 \cdot 10^{-5}$	$4.42 \cdot 10^{-3}$
	$P = 1$	$1.20 \cdot 10^{-4}$	$4.33 \cdot 10^{-3}$
$N_L = 2, o_l = 257,268$	$P = 45$	$1.81 \cdot 10^{-6}$	$4.50 \cdot 10^{-6}$
	$P = 1$	$1.82 \cdot 10^{-6}$	$3.56 \cdot 10^{-6}$
$N_L = 4, o_l = 261, \dots, 264$	$P = 45$	$2.10 \cdot 10^{-4}$	$2.94 \cdot 10^{-4}$
	$P = 1$	$5.49 \cdot 10^{-4}$	$2.91 \cdot 10^{-4}$
$N_L = 12, o_l = 257, \dots, 268$	$P = 45$	$3.88 \cdot 10^{-5}$	$1.12 \cdot 10^{-6}$
	$P = 1$	$7.12 \cdot 10^{-5}$	$2.92 \cdot 10^{-6}$

Similar observations are made when regarding the reduction of interference power for different number and positions of observation subcarriers. The corresponding spectra of the interference signal after carrier or PSD based leakage compensation are shown in Fig. 4.9 or Fig. 4.10, respectively. Leakage compensation is applied

to the complete OFDM frame with  $P = 45$  OFDM symbols.

As can be seen from Fig. 4.9, for carrier based leakage compensation based with  $N_L = 2$  observation subcarriers positioned at  $o_l = 262, 263$ , interference power is reduced by 20.8 dB averaged over all OFDM frames, all OFDM symbols, and all subcarriers expect for those in the channel where the interferer is present. When all subcarriers in the occupied DSB-AM channel are used for observation, i.e.  $N_L = 12$  and  $o_l = 257, \dots, 268$ , an interference power reduction of 29.6 dB is achieved. The same or even better performance is achieved for only two observation subcarriers positioned at  $o_l = 261, 264$  or at the edges of the DSB-AM channel, i.e. at  $o_l = 257, 268$ . For the latter choice of observation subcarriers interference power is diminished by 34.6 dB which is approximately the same interference power reduction as achieved with the simple subtraction of the estimated carrier.

However, in general, with carrier based leakage compensation interference power is further reduced by 5.2 dB to 8.6 dB compared to the simple subtraction of the estimated carrier signal although both methods employ the same estimation. Consequently, leakage compensation is more robust to estimation errors than the simple subtraction of the estimated carrier signal.

As shown in Fig. 4.10, interference power is hardly reduced with PSD based leakage compensation using observation subcarriers close to the interference peak. For  $N_L = 2$  observation subcarriers located at the edges of the DSB-AM channel, i.e.  $o_l = 257, 268$ , performance improves considerably and interference power is reduced by 33.2 dB which is only about 1.4 dB less compared to carrier based leakage compensation with the same set of observation subcarriers. The best performance is achieved for  $N_L = 12$  observation subcarriers. In that case, interference power reduction is as high as 34.7 dB which is approximately the same as the maximum interference power reduction achieved with carrier based leakage compensation. However,  $N_L = 12$  observation subcarriers are not feasible, since a large number of observation subcarriers is related to larger matrix dimensions and higher computational efforts that partly neutralise complexity that has been saved due to the a priori determination of the compensation matrix.

Comparing carrier and PSD based leakage compensation in the channel occupied by the DSB-AM system, one observes that the PSD based leakage compensation does not reduce the interference peak at all. With respect to the fact that PSD based leakage compensation aims at mitigating the impact of sidebands, this has been expected. However, this makes PSD based leakage compensation not feasible for mitigating interferers in channels that are used by the overlay system. Moreover,



when the outermost subcarriers of the DSB-AM channel are used for observation, small side peaks appear on the subcarriers directly adjacent to the unused DSB-AM channel. Even for lower interference power, these peaks remain and are not linearly down-scaled with decreasing interference power. On these subcarriers, INR is higher than after carrier based leakage compensation resulting in performance losses.

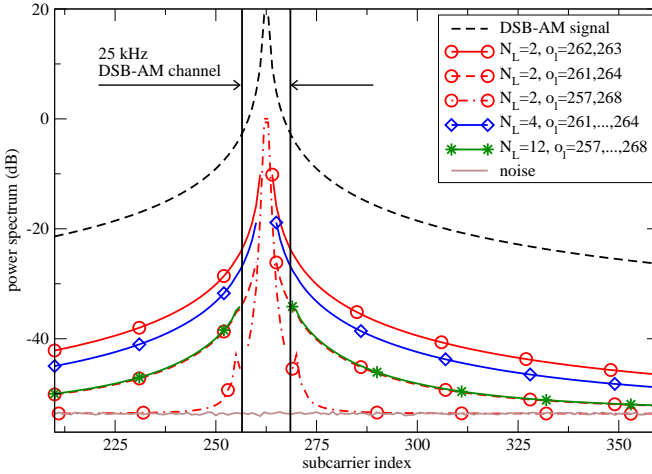


**Figure 4.9** Average interference spectrum after compensation of estimated carrier for different numbers and positions of observation subcarriers,  $n_c = 262.5$ ,  $N = 512$ ,  $P = 45$ .

### Optimal Number and Position of Observation Subcarriers

In previous work, different numbers of observation subcarriers have been employed ranging from two [76], four [75] to eleven [77]. Simulation results in the previous section show that for the estimation and mitigation techniques presented in this thesis, two observation subcarriers are sufficient. The improvements achieved with an increased number of observation subcarriers do not counterbalance increased computational efforts and a throughput reduction in channels used by the overlay system.

When using two subcarriers per interferer to estimate the carrier, it is advantageous to position them at the next but one subcarriers to the left and to the right of the

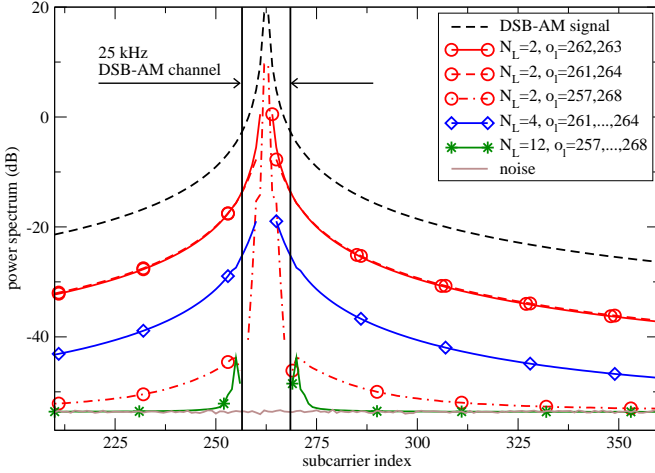


**Figure 4.10** Average interference spectrum after compensation of PSD based estimation of NBI signal for different numbers and positions of observation subcarriers,  $n_c = 262.5$ ,  $N = 512$ ,  $P = 45$ ,  $B = 2.7$  kHz.

expected carrier frequency rather than at the subcarriers directly adjacent to the expected interference carrier frequency. As can be seen from Tab. 4.1 and 4.2, for this choice of observation subcarriers the estimation error is significantly smaller than for two and even for four observation subcarriers directly adjacent to the expected carrier frequency of the interferer. This is due to the fact that the next but one subcarriers to the left and to the right of the expected carrier frequency are less affected by sidebands, hence allowing for a more accurate estimation of the carrier.

The impact of sidebands on amplitude and phase of the subcarriers close to the carrier frequency is illustrated in Fig. 4.11 for a DSB-AM interferer at  $n_c = 262.5$ . The interference signal on five subsequent OFDM symbols is considered. Although the interference power is constant, the sidebands cause variations in the amplitude. Comparing the next but one subcarriers to the left and to the right of the expected carrier frequency and the directly adjacent subcarriers, the distortions in the spectral shape of the NBI signal are less significant on subcarriers  $o_l = 261$  and  $o_l = 264$ , hence making these subcarriers more suitable for observation purposes. The advantage of subcarriers  $o_l = 261$  and  $o_l = 264$  becomes even more obvious when regarding the impact of sidebands onto the phase of the interference signal.

With two observation subcarriers at  $o_l = 257$  and  $o_l = 268$ , parts of the sidebands are estimated for the benefit of a decreased average estimation error, but at the cost of reduced accuracy in carrier estimation. These observation subcarriers may significantly be affected by noise as INR is about 20 dB smaller compared to INR on subcarriers close to the peak. In addition, other interferers in adjacent channels induce considerable estimation errors. Consequently, these observation subcarriers are not considered suitable for estimating and compensating the carrier.

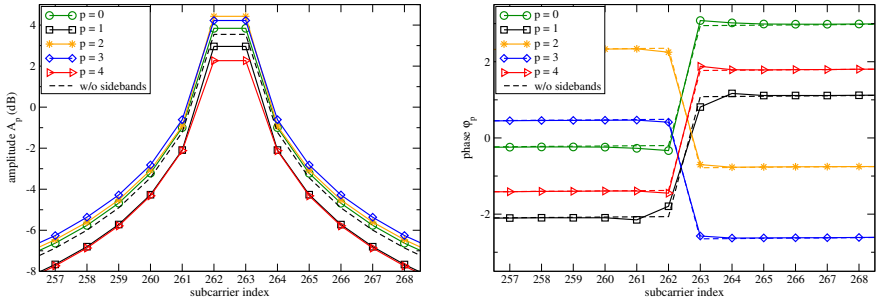


**Figure 4.11** Amplitude and phase of DSB-AM signal with sidebands close to centre frequency,  $n_c = 262.5$ .

As the PSD based leakage compensation focuses on taking into account sidebands rather than on mitigating the carrier, different positions of observation subcarriers have to be chosen. As shown in Fig. 4.11, the subcarriers at the edges of the DSB-AM channel, i.e. at  $o_l = 257$  and  $o_l = 268$ , are most suitable for measuring the impact of sidebands on the amplitude of the NBI signal. Regarding the spectrum of the DSB-AM signal over the complete bandwidth as shown in Fig. 4.2, subcarriers farther away from the interference peak would be even more appropriate for observation purposes. However, with respect to interferers operating in adjacent and other VHF channels, this is not feasible. Depending on the power of the interferer it may be even advantageous to use observation subcarriers closer to the interference peak, e.g. at  $o_l = 258$  and  $o_l = 267$ , as the higher INR on these subcarriers enables a more accurate estimation.

## Frequency Variations

So far, the frequency of the DSB-AM carrier has been kept constant in order to focus on the estimation of amplitude and phase. However, due to the Doppler effect and inaccuracies of the carrier modulation, the carrier frequency varies within one

subcarrier spacing. Limiting frequency variations to one subcarrier spacing is valid for any OFDM system as the subcarrier spacing is chosen to be a multiple of the maximum Doppler frequency. Inaccuracies of the carrier modulation usually also lie in that order of magnitude.

Considering the DSB-AM signal as an example, frequency variations of  $\pm 1$  kHz have to be taken into account for an overlay system with  $\Delta f = 2.0833$  kHz. In Figure 4.12, spectra of the interference signal after NBI mitigation are shown for an DSB-AM interferer with  $n_c = 262.5 \pm 0.5$ . For NBI estimation,  $N_L = 2$  subcarriers are employed. They are located at  $o_l = 261, 264$ , when the carrier is estimated and at  $o_l = 257, 268$ , when the NBI signal is compensated based on the PSD, respectively.

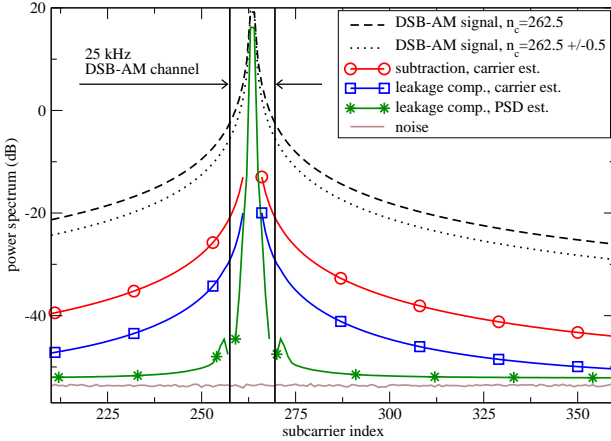


**Figure 4.12** Average interference spectrum after mitigation of estimated interference signal,  $n_c = 262.5 \pm 0.5$ ,  $N_L = 2$ .

When frequency variations are considered, the power of the DSB-AM signal averaged over all subcarriers except for those in the occupied DSB-AM channel becomes 3 dB smaller compared to the signal with carrier frequency fixed at  $n_c = 262.5$  where worst case spectral leakage occurs permanently. The estimation of the carrier slightly degrades and the resulting estimation error increases from  $1.20 \cdot 10^{-4}$  to  $7.97 \cdot 10^{-4}$ . When the estimated carrier signal is subtracted from the Rx signal, interference power is reduced by 15.3 dB. Compared to the results with constant carrier frequency, the average remaining interference power is 6.4 dB larger.

When leakage compensation is performed based on the same estimation of the carrier, interference power is suppressed by 23.3 dB on the average. As the average remaining interference power is only 3.4 dB larger than in the case with constant interference power, it can be concluded that the leakage compensation algorithm is less sensitive to estimation errors than the mere subtraction of the estimated carrier.

For the PSD based leakage compensation, the bandwidth of the assumed interference spectrum is extended from  $B = 2.7$  kHz to  $B = 3.7$  kHz in order to take into account frequency variations. Using two observation subcarriers at  $\omega_l = 257,268$ , interference power is reduced by 30.1 dB on the average resulting in an average remaining interference power which is close to noise on most subcarriers. Compared to the case with constant carrier frequency, the average remaining interference power is only 3.1 dB larger, hence revealing the robustness of PSD based leakage compensation towards variations in the carrier frequency and the estimation errors related to that.

## 4.5 Combination of Time and Frequency Domain Techniques

In order to exploit the advantages of both approaches, NBI mitigation techniques in the time and frequency domain are applied jointly. For example, this straightforward approach has also been applied in [76], where Rx windowing has been combined with a subtraction of maximum Likelihood estimates of the interference signal in the frequency domain. In this thesis, Rx windowing is applied followed either by a subtraction of a simple interference estimate or an MMSE estimate aiming at compensating the leakage effect.

### 4.5.1 Principle

Windowing in the time domain is performed as described in Section 4.2 independently of the frequency domain NBI mitigation technique applied subsequently. Inversely, Rx windowing has to be taken into account when estimating and mitigating the NBI signal in the frequency domain, because the NBI spectrum is influenced by windowing.

As shown in the block diagram in Fig. 4.13, for windowing segments of length  $N + N_{GI} + \mu$  are cut out of the Rx data stream. Considering the carrier of the DSB-

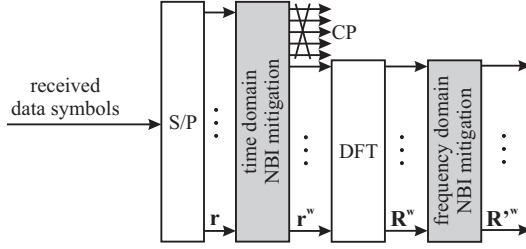


**Figure 4.13** Block diagram of OFDM Rx performing time and frequency domain NBI mitigation.

AM signal only, the time domain interference signal on the  $p$ th OFDM symbol in an OFDM frame is given by

$$i'_p[k] = A_p \cdot \exp\left(jk\frac{2\pi n_c}{N} + j\varphi'_p\right), \quad k = 0, \dots, N + N_{\text{GI}} + \mu - 1. \quad (4.68)$$

with

$$\varphi'_p = \vartheta_0 + (p + 1)\frac{2\pi(N_{\text{GI}} + \mu)n_c}{N}. \quad (4.69)$$

In the time domain, the interference signal is multiplied with the windowing function and the first  $\mu$  samples are added to the last  $\mu$  samples of the windowed signal yielding the windowed interference signal  $i_p^w[k]$  given in (4.24). Transforming (4.24) to the frequency domain, the spectrum  $I_p^w[n]$  of the windowed NBI signal is obtained as

$$\begin{aligned} I_p^w[n] &= \text{DFT}\{i_p^w[k]\} \\ &= \sum_{n=0}^{N-1} i'_p[k + N_{\text{GI}} + \mu] e^{-j\frac{2\pi kn}{N}} \\ &\quad + \sum_{k=N-\mu}^{N-1} w[k - N + N_{\text{GI}} + \mu] \\ &\quad \cdot (i'_p[k - N + N_{\text{GI}} + \mu] - i'_p[k + N_{\text{GI}} + \mu]) e^{-j\frac{2\pi kn}{N}} \\ &= e^{j(p+1)\frac{2\pi\mu n_c}{N}} I_p[n] \\ &\quad - A_p e^{j\varphi_{p+1}} (1 - e^{-j2\pi n_c}) \sum_{k=N-\mu}^{N-1} w[k - N + N_{\text{GI}} + \mu] \cdot e^{j\frac{2\pi k(n_c - n)}{N}}. \end{aligned} \quad (4.70)$$

For  $\mu = 0$ , (4.70) simplifies to (4.9) and the same spectrum as for the case without windowing is obtained. In case  $\mu > 0$ , the last equation in (4.70) reveals that the NBI signal is reduced by a sum of exponential functions weighted by windowing coefficients. For NBI estimation and mitigation in the time domain, the windowed interference spectrum from (4.70) is taken into account instead of the interference spectrum from (4.9).

The combination of windowing and frequency domain NBI mitigation techniques is advantageous in many respects. At first, the impact of NBI is expected to be reduced considerably compared to the case when each method is applied separately. In addition, the estimation of the NBI carrier improves, since the impact of sidebands close to the peak becomes smaller. At the same time the difference between the interference model and the actual interference becomes smaller in the complete bandwidth. This becomes obvious when comparing spectra of the DSB-AM signal including sidebands with windowing as shown in Fig. 4.14 and without windowing as shown in Fig. 4.2. The lower sidelobes of the NBI signal also simplify the parallel estimation of multiple interferers, as the contribution of adjacent interferers is diminished by windowing.

The drawbacks of both the time and frequency domain NBI mitigation methods are combined as well. A throughput loss is induced by windowing and due to observation subcarriers required for frequency domain NBI estimation and mitigation. In addition, computational efforts required for each of the two methods are summed up.

## 4.5.2 Adaptation of Estimation Algorithms

For reconstructing the carrier of the NBI signal, (4.70) is taken into account instead of (4.9). As the peak of the NBI signal is hardly affected by windowing, the same estimation algorithm as presented in Section 4.4 can be used for determining carrier frequency, amplitude, and phase of the interferer. The resulting estimate can be used without modifications for subtraction or for generating an MMSE estimate required for carrier based leakage compensation.

When the MMSE estimate of the interference signal is calculated based on a priori knowledge about the PSD of the NBI signal, the PSD of the windowed NBI signal has to be considered. With the windowed time domain interference signal  $i_p^w[k]$  from (4.24), the ACF  $r_{ii}[u - v]$  from (4.60) that is required for determining the covariance matrix  $\mathcal{R}_{II_o}$  according to (4.58) for the leakage compensation algorithm

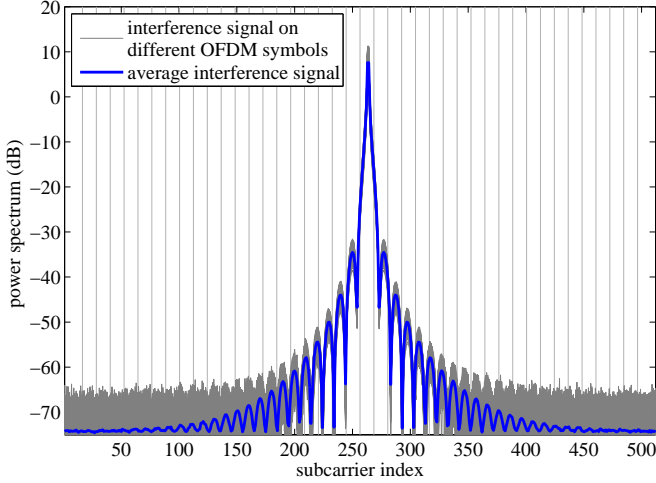


**Figure 4.14** DSB-AM signal with sidebands after triangular windowing with  $\mu = 52$  and 512-point DFT for 1000 OFDM symbols,  $\eta = 0.85$ ,  $n_c = 262.5$ .

writes

$$\begin{aligned} \mathbb{E}\{i_p^w[u]i_p^{*w}[v]\} &= \mathbb{E}\left\{(i_p'[u + N_{\text{GI}} + \mu] + w[u - N + N_{\text{GI}} + \mu] \right. & (4.71) \\ &\quad \cdot (i_p'[u - N + N_{\text{GI}} + \mu] - i_p'[u + N_{\text{GI}} + \mu])) \\ &\quad \cdot (i_p^*[v + N_{\text{GI}} + \mu] + w[v - N + N_{\text{GI}} + \mu] \\ &\quad \left. \cdot (i_p^*[v - N + N_{\text{GI}} + \mu] - i_p^*[v + N_{\text{GI}} + \mu]))\right\}. \end{aligned}$$

Since  $i_p'$  is a version of  $i_p$  extended by  $\mu$  samples required for windowing, it can easily be assumed that  $i_p$  and  $i_p'$  have the same PSD and the same ACF as given by (4.60), i.e.  $\mathbb{E}\{i_p[u]i_p^*[v]\} = \mathbb{E}\{i_p'[u]i_p'^*[v]\} = r_{\text{ii}}[u - v]$ . Hence, the corresponding terms in (4.71) can be replaced by  $r_{\text{ii}}[u - v]$  and the ACF  $r_{\text{ii}}^w[u - v]$  of the windowed interference signal can be rewritten as a function of  $r_{\text{ii}}[u - v]$  yielding

$$\begin{aligned} r_{\text{ii}}^w[u - v] &= r_{\text{ii}}[u - v] & (4.72) \\ &\quad - w[u - N + N_{\text{GI}} + \mu](r_{\text{ii}}[u - N - v] - r_{\text{ii}}[u - v]) \\ &\quad - w[v - N + N_{\text{GI}} + \mu](r_{\text{ii}}[u - v + N] - r_{\text{ii}}[u - v]) \\ &\quad + w[u - N + N_{\text{GI}} + \mu] \cdot w[v - N + N_{\text{GI}} + \mu] \\ &\quad \cdot (2r_{\text{ii}}[u - v] - r_{\text{ii}}[u - v + N] - r_{\text{ii}}[u - N - v]). \end{aligned}$$



With (4.58) and (4.72), the elements of the covariance matrix  $\mathcal{R}_{\text{II}_o}^w$  of the windowed NBI signal are obtained

$$\mathcal{R}_{\text{II}_o}^w[n, l] = P \sum_{u=0}^{N-1} \sum_{v=0}^{N-1} r_{\text{ii}}^w[u - v] e^{-j2\pi(un - v o_l)/N}. \quad (4.73)$$

Calculating  $\mathcal{R}_{\text{I}_o\text{I}_o}^w$  analogously, the compensation matrix  $\mathbf{C}_{\text{NBI}}$  can be determined a priori according to (4.44).

### 4.5.3 Comparison of Different Combinations

The performance of the combination of NBI mitigation techniques in the time and the frequency domain is demonstrated at hand of a simple example with one DSB-AM interferer at  $n_c = 262.5$ . In the time domain, triangular windowing with  $\mu = 52$ , corresponding to about 10% roll-off for DFT length  $N = 512$ , is applied. The spectra before and after NBI mitigation shown in Fig. 4.15 are averaged over the interference signals on 10,000 OFDM symbols. When the windowed NBI signal is estimated based on  $N_L = 2$  observation subcarriers at  $o_l = 261,264$  and subtracted from the windowed Rx signal, interference power is reduced by 28.1 dB averaged over all 10,000 OFDM symbols and all subcarriers except for those in the channel occupied by the DSB-AM interferer. With windowing or subtraction applied separately, interference power is only reduced by 13.2 dB or 21.2 dB, respectively. Better performance is achieved with windowing combined with carrier based leakage compensation. When employing  $N_L = 2$  observation subcarriers at  $o_l = 261,264$  for estimating the windowed interference signal, overall interference power is reduced by 32.3 dB which means 2.6 dB additional interference power reduction compared to the case without windowing. With PSD based leakage compensation the benefit from applying windowing in addition is even smaller. For  $N_L = 2$  observation subcarriers at  $o_l = 257,268$ , which is the best choice for PSD based leakage compensation, interference power is reduced by 33.7 dB on the average. Compared to the case without windowing, the average remaining interference power is only reduced by 0.5 dB, which does not justify the throughput and SNR loss related to windowing.

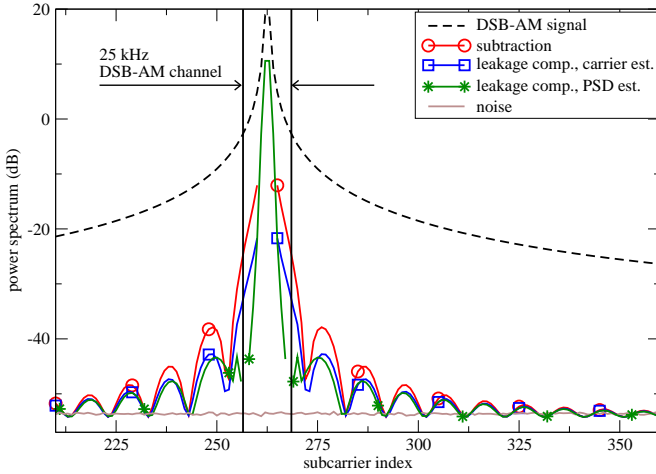


**Figure 4.15** Average interference spectrum after mitigation of estimated interference signal in the frequency domain and triangular windowing with  $\mu = 52$  in the time domain,  $n_c = 262.5$ ,  $N_L = 2$ .

## 4.6 Performance Evaluation

In the previous sections, simulations for the different NBI estimation and mitigation techniques have already shown that interference power can be reduced significantly. In this section, the impact of the remaining interference onto the performance of an overlay system operating in the VHF-band as described in Chapter 2 is investigated.

### 4.6.1 Considered Interference Scenario

Measurement flights over the United Kingdom and parts of continental Europe [35] have identified the 1 MHz band around 120.15 MHz as the band with the highest number of interferers observed from an aircraft flying at an en-route flight level in 26,000 feet altitude. In the worst case, DSB-AM interferers are measured in 13 channels yielding an occupancy of  $13/40 = 32.5\%$ . According to their average power weak and strong interferers are distinguished. Seven interferers below a threshold of  $-82$  dBm are referred to as weak interferers. The sources for interference in these channels are assumed to be sufficiently separated in space from the B-VHF overlay system. Hence, these channels can be used by the overlay sys-

tem without causing harmful interference in the DSB-AM system. In addition, six strong interferers with power exceeding  $-82$  dBm are observed. The corresponding channels must not be used by the overlay system.

The average power of strong and weak interferers has been determined to be  $-78.36$  dBm and  $-83.57$  dBm, respectively [35]. Since interference sources as well as the airborne victim Rx are moving, interference power received by the overlay system varies. In the simulations, this is taken into account by means of power probability density functions (PDF) for strong and weak interferers, respectively. From the power PDFs shown in Fig. 4.16, a new interference power value is determined for each interferer in each simulation run. In addition, it is considered that interferers are not active permanently. According to [35], the activity factors for strong and weak interferers are 25.34% and 7.57%, respectively.

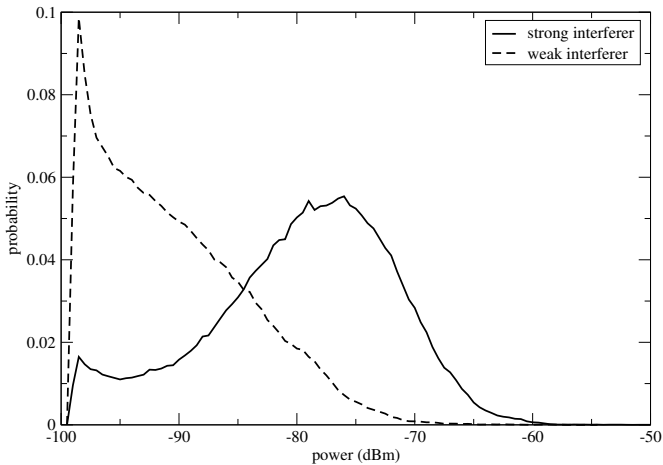


**Figure 4.16** Power PDFs of strong and weak interferers retrieved from measurement flights [35].

The resulting interference signal observed at the overlay system Rx is depicted in Fig. 4.17. Assuming a total noise power as high as  $-105$  dBm within the considered 1 MHz band, obviously interference likely affects most subcarriers depending on the SNR used in the overlay system.

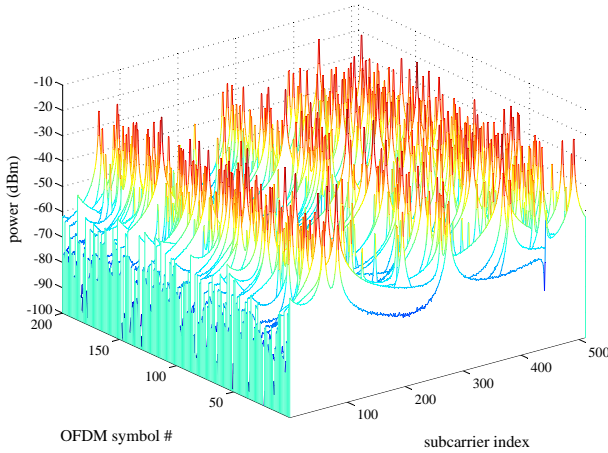


**Figure 4.17** Interference spectrum observed on 200 OFDM symbols,  $N = 512$ .

## 4.6.2 Simulation Parameters

For the overlay system, the parameters of the B-VHF system as given in Tab. 2.1 are considered. The transmission from the B-VHF ground station to an airborne flying at an en-route flight level is simulated. Among the various possibilities, the most robust transmission is selected, i.e. QPSK with a (133,171) convolutional code with code rate  $R_c = 1/2$ . Moreover, ideal synchronisation and channel estimation are assumed. Hence, all  $P = 45$  OFDM symbols within one frame can be used for data transmission.

The channel is modelled by means of a wide-sense stationary uncorrelated scattering (WSSUS) channel model. Parameters are set such as to model propagation conditions of an en-route flight. One strong line-of-sight (LOS) component with Rician factor 15 dB as well as two scattered components with maximum delay  $15 \mu\text{s}$  are taken into account. In addition, Doppler shifts up to 120 Hz are considered that reflect aircraft velocities as high as 260 m/s. Due to the strong LOS component the channel behaviour is expected to be similar to AWGN.

Interference is modelled as described in the previous section. Due to strong interferers, six DSB-AM channels corresponding to 72 subcarriers cannot be used by the overlay system. Hence, the number of useable subcarriers reduces from 480 to 408 subcarriers. Interference power is varied according to the power PDFs from

Fig. 4.16, whereas the average interference power as well as the noise level are kept constant. Hence, the average INR is fix, but the power of the desired OFDM signal is varied by varying  $E_b/N_0$ .

### 4.6.3 Simulation Results

In the simulations,  $E_b/N_0$  is varied from 0 to 30 dB, which spans the  $E_b/N_0$  range considered to be available for the B-VHF system. For each  $E_b/N_0$  point, up to 100,000 OFDM frames are transmitted in order to obtain reliable statistical results for BER.

As reference, the BER vs.  $E_b/N_0$  without interference as well as the BER performance with interference that is not mitigated at all is given.

#### Time Domain

In Fig. 4.18, the performance of the overlay system is shown after applying a Hann or a triangular window with different lengths to mitigate the impact of NBI. As expected, the impact of NBI decreases with increasing window size. Window length  $\mu = 52$  appears to be a good-trade off between performance in terms of interference power reduction and BER and the corresponding throughput loss which is about 10%. Triangular windowing outperforms Hann windowing as the width of the remaining peak is smaller than for the Hann window. Hence, after triangular windowing less subcarriers are affected by very strong interference power levels. All in all, the impact of interference is reduced moderately. At  $\text{BER} = 10^{-2}$ , the required  $E_b/N_0$  is reduced by about 10 dB for triangular windowing with  $\mu = 52$ . However,  $E_b/N_0$  required to achieve  $\text{BER} = 10^{-3}$ , is improved by only 3 dB compared to the case without any NBI mitigation. At this point, all different window types and lengths perform similarly.

To explain this effect, strong and weak interferers are considered separately in Fig. 4.19. Obviously, strong interferers dominate the performance of the overlay system. By means of windowing, their impact can be reduced significantly. At  $\text{BER} = 10^{-3}$ ,  $E_b/N_0$  is reduced by 12.5 dB for Hann and by 17 dB for triangular windowing, respectively. The impact of weak interferers is smaller, but becomes as strong as the impact of strong interferers around  $E_b/N_0 = 30$  dB. Up to  $E_b/N_0 = 15$  dB, the impact of weak interferers can be slightly reduced by means of windowing, whereas for larger  $E_b/N_0$  hardly any reduction is achieved. This

explains nearly the same performance of all window types and window lengths at  $E_b/N_0 > 24$  dB as observed in Fig. 4.18. At that point, the impact of strong interferers is mitigated to a large extent, whilst weak interferers cannot be mitigated further.

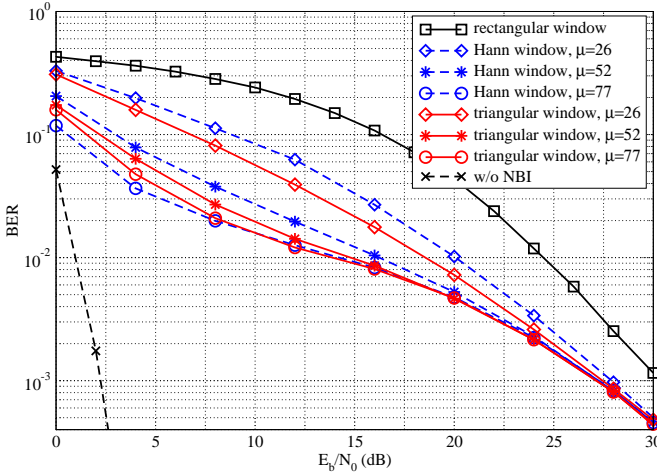


**Figure 4.18** BER performance for different window types and lengths, worst case interference scenario.

## Frequency Domain

The performance of the proposed frequency domain NBI mitigation techniques is investigated for strong and weak interferers separately in order to investigate the optimal position of observation subcarriers. The corresponding BER after subtraction of the estimated carrier signals and after carrier or PSD based leakage compensation is depicted in Fig. 4.20 and 4.21, respectively. For all methods, two observation subcarriers are applied for each channel where an interferer possibly resides, but the positions with respect to the interference peak are varied.

By subtracting the estimated carrier signal, the  $E_b/N_0$  degradation induced by strong interferers is reduced by 13.7 dB at  $\text{BER} = 10^{-3}$  when observation subcarriers directly adjacent to the interference peak are used and by 18.3 dB when the next but one subcarriers to the left and to the right of the peak are employed for observation, i.e. when subcarriers at  $o_l = \lfloor n_{c,i} \rfloor - 1, \lceil n_{c,i} \rceil + 1, l = 0, \dots, N_L - 1$ , are used for observing the  $i$ th interferer, where  $n_{c,i}$  denotes the discrete carrier fre-

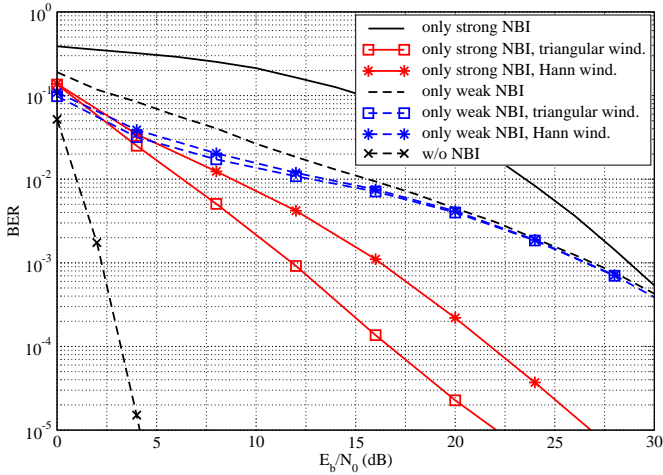


**Figure 4.19** BER performance after windowing,  $\mu = 52$ , worst case interference scenario, strong and weak interferers regarded separately.

frequency of the  $i$ th interferer. Carrier based leakage compensation outperforms the simple subtraction by about 2 dB. Same as for the simple subtraction, observation subcarriers at the next but one subcarriers to the left and to the right of the peak are advantageous as the impact of sidebands is smaller on these subcarriers as shown in Section 4.4.5. As expected from the better interference power reduction, PSD based leakage compensation outperforms carrier based leakage compensation. However, this is only observed for  $E_b/N_0 > 8$  dB. At smaller  $E_b/N_0$ , PSD based leakage compensation performs considerably worse because of side peaks in the remaining interference signal on subcarriers directly adjacent to the channel used by the DSB-AM system as shown in the interference spectra in Fig. 4.10. Even when interference power is reduced, these side peaks remain and are not linearly down-scaled with decreasing interference power. When subcarriers at  $o_l = \lfloor n_{c,i} \rfloor - 5, \lfloor n_{c,i} \rfloor + 5, l = 0, \dots, N_L - 1$ , are used for observing the  $i$ th interferer a larger fraction of these side peaks is in the bandwidth outside the unused DSB-AM channel than for the case with  $o_l = \lfloor n_{c,i} \rfloor - 4, \lfloor n_{c,i} \rfloor + 4, l = 0, \dots, N_L - 1$ , hence explaining the better performance with observation subcarriers at  $o_l = \lfloor n_{c,i} \rfloor - 4, \lfloor n_{c,i} \rfloor + 4$ . These side peaks exceed the remaining interference signal after carrier based leakage compensation resulting in worse BER performance for PSD based leakage compensation. For larger  $E_b/N_0$ , these side peaks become negligible compared to the

overall better interference suppression in most ranges of the spectrum.

Considering weak interferers only, i.e. interferers operating in channels used by the overlay system, subtracting the estimated carrier signals improves performance by 18.3 dB when the next but one subcarriers to the left and to the right of the peak are used as observation subcarriers. Other than for strong interferers only,  $E_b/N_0$  required to achieve  $\text{BER} = 10^{-3}$  is reduced by another 1.8 dB when the observation subcarriers directly adjacent to the peak are used. This is due to the fact that overall interference power is better reduced by means of the next but one subcarriers to the left and to the right of the peak, but interference on the subcarriers directly adjacent to the peak is hardly reduced. When the respective DSB-AM channel is used by the overlay system as it is the case for weak interferers, high remaining interference on the subcarriers directly adjacent to the peak reduces performance and compensates the gain achieved with additional interference reduction on all other subcarriers. The same holds true for carrier based leakage compensation. At  $\text{BER} = 10^{-3}$ ,  $E_b/N_0$  is reduced from 26.7 dB to 4.4 dB meaning a performance improvement of 22.3 dB when two observation subcarriers directly adjacent to the interference side peaks are used. For larger  $E_b/N_0$ , the gain achieved with NBI mitigation based on carrier estimation decreases, as the impact of weak interferers cannot be further reduced.

As the interference peak is hardly reduced, PSD based leakage compensation is not suitable for mitigating weak interferers. When subcarriers at  $o_l = \lfloor n_{c,i} \rfloor - 5, \lfloor n_{c,i} \rfloor + 5, l = 0, \dots, N_L - 1$ , are used for observing the  $i$ th interferer,  $E_b/N_0$  required to achieve  $\text{BER} = 10^{-3}$  is still as high as 21.7 dB which is only 5.3 dB less than in the case without any interference mitigation technique. Nearly the same results are obtained for observation subcarriers at  $o_l = \lfloor n_{c,i} \rfloor - 4, \lfloor n_{c,i} \rfloor + 4, l = 0, \dots, N_L - 1$ .

### Combined Time and Frequency Domain

In order to combine the benefits of both time and frequency domain NBI mitigation, at first a triangular window with  $\mu = 52$  is applied followed by a subtraction of the estimated carrier signals or leakage compensation, respectively. The corresponding BER vs.  $E_b/N_0$  curves are given in Fig. 4.22. Interference is modelled according to the worst case interference scenario comprising 13 strong and weak interferers in total.

In all simulations, two observation subcarriers per active interferer are used. Ac-



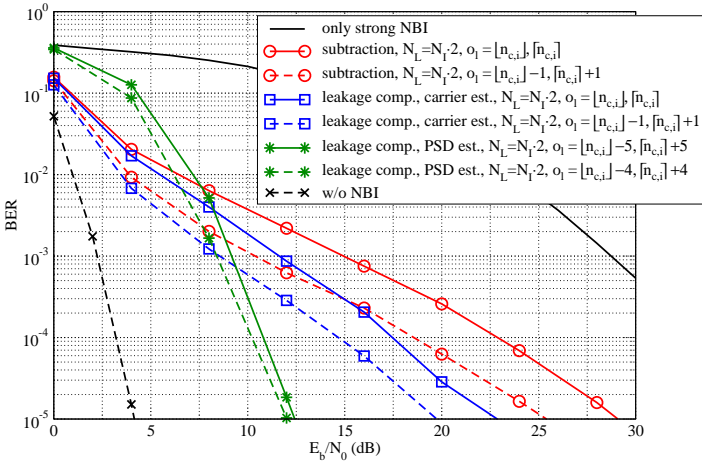


**Figure 4.20** BER performance after subtraction and leakage compensation, worst case interference scenario, strong interferers.

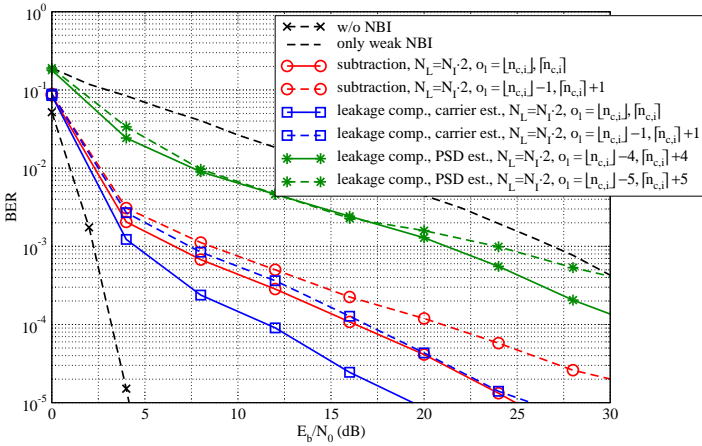


**Figure 4.21** BER performance after subtraction and leakage compensation, worst case interference scenario, weak interferers.

According to the simulation results from the previous section, for strong interferers, observation subcarriers at  $o_l = [n_{c,i}] - 1, [n_{c,i}] + 1, l = 0, \dots, N_L - 1$ , are

used, whereas for weak interferers, observation subcarriers directly adjacent to the interference peak provide the best results. With this choice of observation subcarriers, the impact of interference is reduced by 26.1 dB at BER =  $10^{-3}$  after windowing and subtraction of the estimated carrier signals. Compared to subtraction applied solely, an improvement of 8.7 dB is achieved. Slightly better results are obtained with carrier based leakage compensation. At larger  $E_b/N_0$ , the improvements achievable by means of a mitigation of the carrier signal decrease. As expected from the results for weak interferers from Fig. 4.21, this is due to the high remaining impact of weak interferers that cannot be diminished further.

Despite the good performance for strong NBI, PSD based leakage compensation performs poor when applied to weak and strong interferers jointly. Even the combination with windowing does not provide significant improvements. Again, this is explained by the fact that weak interferers are hardly reduced with PSD based leakage compensation. The best results can be obtained when applying PSD based leakage compensation to strong interferers and the carrier based compensation to weak ones. Given the significant interference reduction achieved with both methods applied separately, with that combination, the impact of interference is expected to be reduced nearly completely.

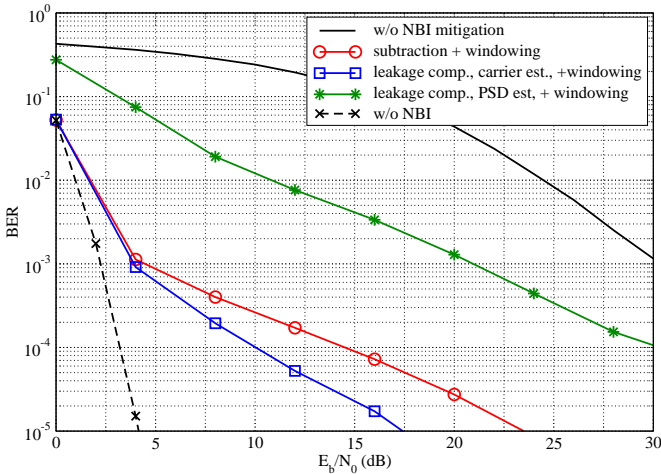


**Figure 4.22** BER performance after combined time and frequency domain NBI mitigation, worst case interference scenario,  $N_I = 2 \cdot N_T$ .

# 5 Mitigation of Pulsed Interference

Apart from NBI as addressed in the previous chapter, an OFDM system may be exposed to pulsed interference when operated in a different frequency band. As pulsed interference significantly differs from NBI with respect to its characteristics as well as to its impact on the OFDM system, different approaches for mitigating pulsed interference are required.

Interference occurs in form of pulses that are short compared to the duration of one OFDM symbol and affect only a few samples of the OFDM system. However, the spectrum of the interference signal is broadband and impairs a significant number of subcarriers depending on the frequency offset between the centre frequency of the interferer and the OFDM system. Although the impairment can already be diminished by means of appropriate signal processing at the OFDM Rx, pulsed interference still significantly deteriorates the performance of the OFDM system.

In the context of OFDM, the mitigation of impulsive noise has been addressed, whereas pulsed interference has hardly been mentioned. Techniques for mitigating the impact of pulsed interference have been well investigated for other systems such as satellite navigation systems that are also affected by pulsed interference [86]. The proposed techniques are mainly based on pulse blanking and clipping and can easily be applied to OFDM based systems. A general drawback of these approaches is their impact on the desired signal which is especially serious in OFDM systems because all subcarriers are affected when a few samples of the time domain signal are clipped or blanked. However, when applying pulse blanking, the induced inter-carrier interference (ICI) can be determined and the impact of pulse blanking on the desired part of the OFDM signal is largely compensated. Hence, the main drawback of pulse blanking is counterbalanced while still a considerable reduction of interference power is achieved.

The remainder of this chapter is organised as follows. In the first section, the interference signal is characterised taking interference from DME systems in the L-band as an example. Using the parameters of the B-AMC inlay system from Chapter 2.3.2 that is operated in the L-band at small frequency offset to the DME system, an appropriate model for this type of interference is derived taking into account signal processing at the OFDM Rx. By slightly adapting Rx processing to the interference signal, the impact of interference can already be diminished as ad-

dressed in Section 5.2. In Section 5.3, the principle of clipping and pulse blanking is presented and the required parameters are optimised. After analysing the impact of pulse blanking on the desired OFDM signal, an algorithm for compensating that impact is derived in Section 5.4. Finally, the performance of the proposed techniques is demonstrated by means of simulations of the B-AMC inlay system in Section 5.5.

## 5.1 Characterisation of Interference

After identifying sources of pulsed interference potentially affecting the B-AMC inlay system that is used as example in this thesis, the interference signal is characterised and an appropriate interference model and Rx structure are derived.

### 5.1.1 Sources of Interference

The aeronautical part of the L-band, i.e. 960 - 1164 MHz, is mainly used by the distance measuring equipment (DME) and the military tactical air navigation (TACAN) system both being used for determining the slant range between an aircraft and a ground station. An airborne interrogator sends a random sequence of pulse pairs to a ground station that responds with the same random sequence with a certain delay. By measuring the elapsed time between the interrogation and the reception of the transponder reply, the airborne facility computes the distance to the ground station. To determine its exact position, the aircraft interrogates multiple ground stations and triangulates the measurement results.

For interrogations, the frequency ranges 1041-1083 MHz and 1094-1150 MHz are used. The responses are sent at a fixed offset of  $\pm 63$  MHz to the interrogator frequency. The reply frequencies are allocated to ground stations in a 1 MHz channel grid.

As an example for an OFDM system operated in this frequency band, the B-AMC inlay system as presented in Chapter 2.3.2 is utilised. For forward link (FL) transmissions, centre frequencies in the sub-band 985-1009 MHz are selected. As this frequency range is only used by DME ground stations, only interference from DME ground stations but not from DME airborne stations is expected. The target band for the reverse link (RL) is 1048-1072 MHz or 1100-1124 MHz, respectively. Hence, RL transmissions are exposed to interference from DME facilities onboard the own

and on other aircraft as well as from a few DME ground stations in the proximity.

Other systems such as Universal Access Transceiver (UAT) and Secondary Surveillance Radar (SSR) also operating in the aeronautical L-band are not considered, as the separation in frequency between these systems and the B-AMC system can be assumed to be sufficiently large due to the proper selection of the FL and RL frequency ranges. Furthermore, military communication systems such as the Joint Tactical Information Distribution System (JTIDS) or the Multi-functional Information Distribution System (MIDS) also apply pulsed transmissions causing interference in the bandwidth used by the B-AMC system. This type of interference can be mitigated with the same methods as studied in this chapter, but is not addressed in this thesis.

### 5.1.2 Description of Interference Signal

The DME signal consists of pairs of Gaussian-shaped pulses with spacing  $\Delta t$ . One pulse pair in the baseband writes

$$b^{\text{DME}}(t) = e^{-\varepsilon/2t^2} + e^{-\varepsilon/2(t-\Delta t)^2}. \quad (5.1)$$

The parameter  $\varepsilon = 4.5 \cdot 10^{11} \text{ 1/s}^2$  is set such that the time interval between the 50% amplitude point on leading and trailing edges of the pulse envelope is  $3.5 \mu\text{s}$ . The spacing  $\Delta t$  between the two pulses depends on the DME transmission mode and is  $12 \mu\text{s}$ ,  $30 \mu\text{s}$ , or  $36 \mu\text{s}$ , respectively. These pulse pairs are modulated to carrier frequencies corresponding to the centre frequency of the channel where the regarded DME system is operated. As DME interference in the channels at small offsets to the OFDM system is investigated, the DME signal is modulated to relative carrier frequencies of the channels to the left and to the right of the OFDM system, i.e.  $\pm 500 \text{ kHz}$ ,  $\pm 1.5 \text{ MHz}$ , ..., with the centre frequency of the OFDM system being at  $0 \text{ Hz}$ . The interference signal observed at the OFDM Rx is composed of contributions from  $N_I$  DME stations operating in the same or different DME channels. The duty cycle of each DME station is considered by generating  $N_{U,i}$ ,  $i = 0, \dots, N_I - 1$ , pulse pairs in the considered time interval for the  $i$ th DME station. The starting times  $t_{i,u}$ ,  $u = 0, \dots, N_{U,i} - 1$ , of the  $N_{U,i}$  pulse pairs of the  $i$ th DME station are modelled as a Poisson process that well reflects the random character of DME pulse pairs. The phases  $\varphi_{i,u}$  are equally distributed in the interval  $[0, 2\pi]$ . The received interference power  $\Psi_i^{\text{DME}}$  is taken into account by loading each pulse pair with  $A_i^{\text{DME}} = \sqrt{\Psi_i^{\text{DME}}}$ ,  $i = 0, \dots, N_I - 1$ , where  $A_i^{\text{DME}}$  and  $\Psi_i^{\text{DME}}$  denote the peak am-

plitude and peak power of the  $i$ th DME signal. The resulting interference signal given by

$$i(t) = \sum_{i=0}^{N_1-1} \sum_{u=0}^{N_{u,i}-1} A_i^{\text{DME}} b^{\text{DME}}(t - t_{i,u}) e^{j2\pi f_{c,i}t + j\varphi_{i,u}} \quad (5.2)$$

is composed of contributions from  $N_1$  DME stations with different duty cycle, power, and relative carrier frequency. For illustrating the parameters, DME pulse pairs of the  $i$ th interferer are depicted in Fig. 5.1.

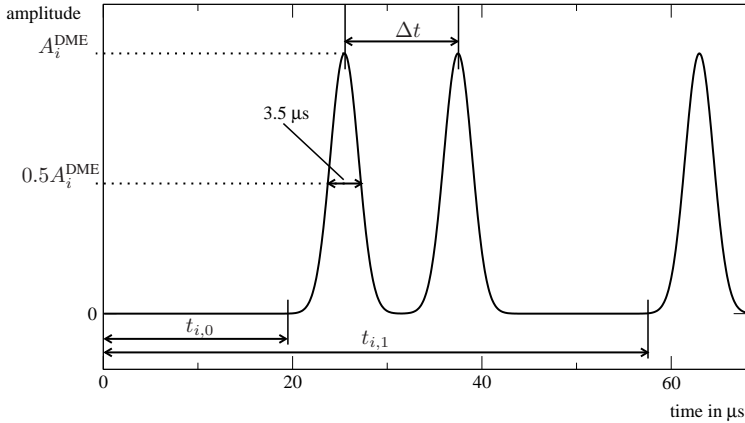


**Figure 5.1** Amplitude of  $i$ th DME interferer in the time domain.

### 5.1.3 Modelling of Interference

At the OFDM Rx, the desired OFDM signal and the interference signal superimpose and the interference signal is processed in the same way as the OFDM signal. To evaluate the impact of interference on the OFDM system, the interference signal and its Rx processing have to be modelled as realistically as possible.

As the spectrum of the interference signal partly falls into the bandwidth of the OFDM signal, filtering at the OFDM Rx affects the interference signal and hence has to be considered. Therefore, the Rx signal is first filtered by a low-pass filter to extract those parts of the Rx signal in the desired bandwidth. The frequency selectivity of the OFDM Rx is assumed to be similar to standard DME receivers. The

characteristic  $F^{\text{RF}}(f)$  of the radio frequency (RF) filter is derived from characteristics of commercially available DME equipment and down-scaled to the OFDM bandwidth, which is 666.6 kHz in the considered example [87]. With  $f^{\text{RF}}(t)$  denoting the impulse response of the filter obtained by Fourier transforming  $F^{\text{RF}}(f)$ , the filtered interference signal writes

$$i^{\text{filt}}(t) = f^{\text{RF}}(t) * i(t) \quad (5.3)$$

in the time domain and

$$I^{\text{filt}}(f) = F^{\text{RF}}(f) \cdot I(f) \quad (5.4)$$

in the frequency domain, respectively. An example of the spectrum of the resulting interference signal is shown in Fig. 5.2 for four active DME interferers at  $\pm 0.5$  MHz and  $\pm 1.5$  MHz offset to the OFDM signal. Interferers at frequency offsets  $\geq \pm 1.5$  MHz are reduced substantially. However, fractions of the interferers at  $\pm 0.5$  MHz offset fall into the OFDM bandwidth and are hardly reduced by filtering.

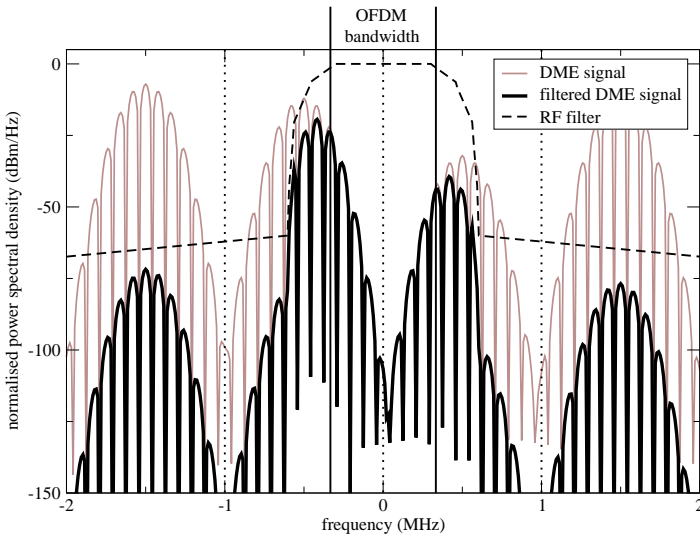


**Figure 5.2** Spectrum of filtered DME signal.

When sampling the Rx signal with the sampling period of the OFDM system, aliasing effects occur, as the Nyquist theorem is violated for the DME interference sig-

nal. To circumvent this problem, an anti-aliasing filter in combination with over-sampling is introduced. By means of over-sampling, the sampling rate is increased such that periodic repetitions of the spectra of interference signals in the channels at  $\pm 0.5$  and  $\pm 1.5$  MHz offset do not coincide with the OFDM bandwidth. To reduce the power of interference signals from channels with larger offsets falling into the OFDM bandwidth, an anti-aliasing filter is introduced in addition.

Summarising the RF filter denoted by  $(\cdot)^{\text{RF}}$  and the anti-aliasing filter denoted by  $(\cdot)^{\text{AA}}$  to one representative filter with frequency response  $F(f) = F^{\text{RF}}(f) \cdot F^{\text{AA}}(f)$ , the filtered interference signal in the time and frequency domain yield

$$i^{\text{filt}}(t) = f(t) * i(t), \quad \text{and} \quad I^{\text{filt}}(f) = F(f) \cdot I(f), \quad (5.5)$$

respectively. Sampling (5.5) with sampling frequency  $V \cdot f_s$ , the discrete time domain representation is obtained as

$$i^{\text{ov}}[k] = i^{\text{filt}}(k/V/f_s), \quad k = 0, \dots, PV(N + N_{\text{GI}}) - 1, \quad (5.6)$$

with  $V$  denoting the over-sampling factor. Same as for the NBI signal investigated in Chapter 4, the interference signal is considered for the duration of one OFDM frame consisting of  $P$  OFDM symbols with  $V(N + N_{\text{GI}})$  samples each. The interference signal on the  $p$ th OFDM symbol,  $p = 0, \dots, P - 1$ , is obtained by cutting out a segment with length corresponding to the duration of one OFDM symbol of the Rx data stream. This is realised by applying a rectangular window that selects  $VN$  samples. At the same time,  $N_{\text{GI}}$  samples belonging to the GI are removed resulting in

$$i_p^{\text{ov}}[k] = \text{rect}[k] \cdot i^{\text{ov}}[k + VN_{\text{GI}} + pV(N + N_{\text{GI}})], \quad k = 0, \dots, VN - 1, \quad (5.7)$$

with

$$\text{rect}[k] = \begin{cases} 1 & k = 0, \dots, VN - 1 \\ 0 & \text{otherwise.} \end{cases} \quad (5.8)$$

The impact of pulsed interference on the OFDM signal can already be kept at a minimum by appropriate signal processing. To further reduce interference, the pulses are mitigated in the time domain before Fourier transforming the Rx signal to the frequency domain. Both approaches for mitigating the impact of pulsed interference are integrated in the OFDM Rx block diagram shown in Fig. 5.3. Note, when processing the desired OFDM signal, filtering can be neglected as the OFDM



signal is completely in the pass-band of the filters. However, over-sampling has to be taken into account by over-sampling the time domain OFDM Rx signal as well. In accordance to (5.6), the over-sampled Rx signal on the  $p$ th OFDM symbol after GI removal is given by

$$r_p^{\text{ov}}[k] = y_p^{\text{ov}}[k] + n_p^{\text{ov}}[k] + i_p^{\text{ov}}[k], \quad k = 0, \dots, VN - 1, \quad p = 0, \dots, P - 1, \quad (5.9)$$

where the samples  $y_p^{\text{ov}}[k]$  and  $n_p^{\text{ov}}[k]$  represent the desired OFDM signal, i.e. the OFDM Tx signal affected by the transmission channel, and the over-sampled noise signal, respectively. The superimposed interference and OFDM signal are transformed to the frequency domain by means of a DFT with size increased to  $V \cdot N$  in accordance to the over-sampling factor. The relevant subcarriers are selected by ideally low-pass filtering the output of the DFT.

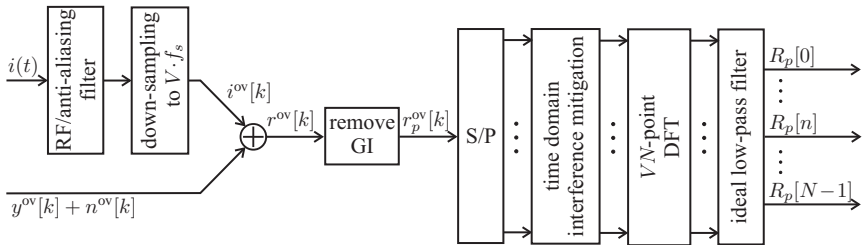


**Figure 5.3** Block diagram of OFDM Rx performing mitigation of pulsed interference.

## 5.2 Mitigation by Appropriate Signal Processing

As already briefly described in the previous section, the impact of DME interference can already be kept at a minimum by appropriate signal processing at the OFDM Rx. In the following two subsections, the reduction of aliasing by means of over-sampling and filtering is addressed.

### 5.2.1 Over-sampling

As a property of the DFT operation, the frequency domain representation of a time domain signal with a certain sampling rate exhibits a periodicity according to the sampling rate. For further processing the signal, only one period is considered. The

sampling rate is adjusted to the bandwidth of the OFDM system and hence, the output of the DFT represents exactly the values received on each subcarrier. However, the sampling frequency of the OFDM system is not adjusted to the interference signal. As the bandwidth of the interference signal is significantly larger than that of the OFDM system, the Nyquist sampling theorem is violated.

The occurring aliasing effect is illustrated in Fig. 5.4 for one DME interferer in the channel at 0.5 MHz offset to the OFDM system. After the DFT operation at the OFDM Rx periodic repetitions of the interference spectrum occur with a periodicity according to the OFDM sampling frequency, i.e.  $f_s = 666.6$  kHz in the considered example. One repetition at 500 kHz - 666.6 kHz = -166.6 kHz falls exactly into the bandwidth of the OFDM system and causes additional interference. In the same way, periodic repetitions of interferers in other channels occur in the OFDM bandwidth and increase interference on all subcarriers.

A conventional approach for reducing aliasing is increasing the sampling frequency. For example, introducing two-times over-sampling enlarges the periodicity to 1.333 MHz. That way, periodic repetitions of the interference spectra from the channels at  $\pm 0.5$  MHz are prevented from coinciding with the OFDM bandwidth. However, interferers from the channels at  $\pm 1.5$  MHz offset still fall into the OFDM bandwidth. The contributions of these interferers are already reduced by the RF filter, but are not yet negligible.

With two-times over-sampling, the sampling frequency is increased to  $f_s = 1.333$  MHz. According to the Nyquist theorem frequencies up to  $f_s/2 = 666.6$  kHz can be resolved. Since the DME signal exhibits even higher frequencies, the sampling frequency is further increased to  $f_s = 2.666$  MHz resulting in four-times over-sampling. As shown in Fig. 5.4, that way the periodicity of the periodically repeated interference spectra is enlarged such that periodic repetitions of interferers in the channels at  $\pm 0.5$  MHz and  $\pm 1.5$  MHz do not coincide with the OFDM bandwidth.

The frequency domain representation of the over-sampled Rx signal is obtained by first removing the GI and secondly transforming the over-sampled time domain Rx signal to the frequency domain by means of an  $VN$ -point DFT resulting in

$$R_p^{\text{ov}}[n] = Y_p^{\text{ov}}[n] + N_p^{\text{ov}}[n] + I_p^{\text{ov}}[n], \quad n = 0, \dots, VN - 1, \quad p = 0, \dots, P - 1. \quad (5.10)$$

Analogously to the time domain representation from (5.9),  $Y_p^{\text{ov}}[n]$ ,  $N_p^{\text{ov}}[n]$ , and  $I_p^{\text{ov}}[n]$  denote samples of the desired OFDM signal including channel influences,

the noise signal, and the interference signal, respectively. The parts outside the used OFDM bandwidth are discarded by applying an ideal low-pass (LP) filter with pass-band coinciding with the bandwidth of the OFDM system. Its frequency response  $F^{\text{LP}}[n]$  ideally fulfils

$$F^{\text{LP}}[n] = \begin{cases} 1 & n = N(V-1)/2, \dots, N(V-1)/2 + N - 1 \\ 0 & \text{otherwise.} \end{cases} \quad (5.11)$$

The Rx signal  $R_p[n]$ ,  $n = 0, \dots, N-1$ , on the relevant subcarriers is obtained from the over-sampled Rx signal  $R_p^{\text{ov}}[n]$ ,  $n = 0, \dots, VN-1$ , by

$$\begin{aligned} R_p[n] &= \frac{1}{\sqrt{V}} F^{\text{LP}}[n + N(V-1)/2] \cdot R_p^{\text{ov}}[n + N(V-1)/2] \\ &= \frac{1}{\sqrt{V}} R_p^{\text{ov}}[n + N(V-1)/2], \quad n = 0, \dots, N-1, p = 0, \dots, P-1. \end{aligned} \quad (5.12)$$

The normalisation factor  $1/\sqrt{V}$  is introduced in order to keep the signal power the same in the case with and without over-sampling.

### 5.2.2 Anti-Aliasing Filtering

Introducing four-times over-sampling, undesired contributions from interferers in the channels at  $\pm 0.5$  and  $\pm 1.5$  MHz offset to the interference signal observed in the OFDM bandwidth are prevented. However, periodic repetitions of interference signals from channels at larger offsets may still coincide with the OFDM bandwidth. The power of the corresponding interferers is already reduced considerably by the RF filter. However, this reduction of interference power is not sufficient e.g. for DME stations at small spatial separation to the OFDM Rx causing high levels of interference power. To reduce the potential impact of interferers at offsets  $\geq 2.5$  MHz to a negligible level, an additional anti-aliasing filter is introduced. As in several conventional communication systems, a raised-cosine filter is applied for this purpose. The roll-off factor is chosen like in the universal mobile telecommunication system (UMTS) and is set to 0.22.

The performance of the additional anti-aliasing filter is demonstrated in Fig. 5.5 for a DME interferer with high power operating at  $-2.5$  MHz offset to the OFDM system. The peak power of the interferer received at the OFDM Rx is set to  $\Psi_0^{\text{DME}} = -40$  dBm which represents a strong interferer with small spacial separation to the OFDM Rx. After additional anti-aliasing filtering the power of the strong interferer

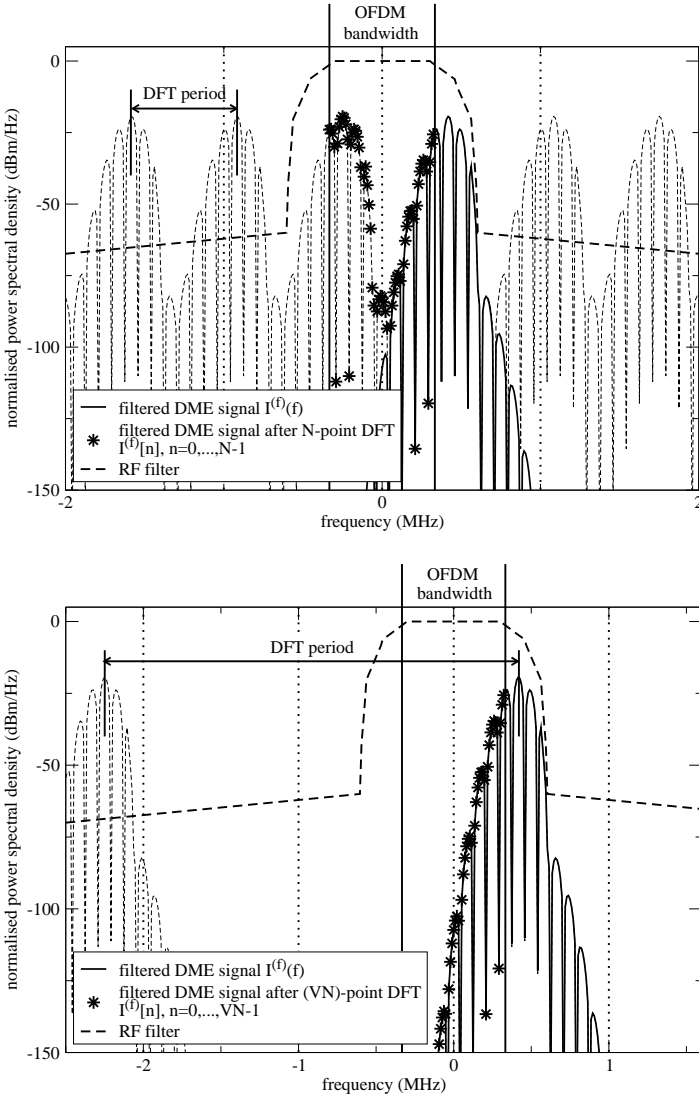


**Figure 5.4** Spectrum of received DME signal without over-sampling ( $V = 1$ ) and with over-sampling ( $V = 4$ ).

in the OFDM bandwidth is reduced to the noise floor. The noise floor is assumed to be at  $-165$  dBm/Hz, taking into account thermal noise with density  $-174$  dBm/Hz and  $9$  dB Rx noise figure which is a typical value for the noise figure of a DME Rx [88].

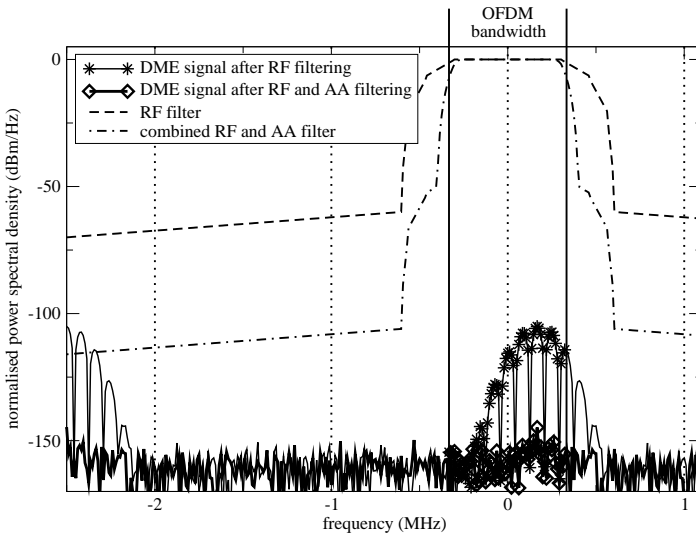


**Figure 5.5** Spectrum of interferer with high power at 2.5 MHz offset with and without anti-aliasing filter.

### 5.3 Mitigation by Clipping and Pulse Blanking

Clipping and pulse blanking are well known approaches to combat pulsed interference. As already indicated by the names, the Rx signal containing the interference signal is clipped at a certain threshold or set to zero when the Rx signal exceeds a certain threshold, respectively. Both methods have been applied to DME interference in the E5- and L5-bands at 1176.45 MHz or 1207.14 MHz used by satellite navigation systems [86] and to impulsive noise in OFDM systems [89, 90]. The combination of both approaches for mitigating impulsive noise has been proposed in [89]. Although very simple, both methods suffer from the drawback that the desired signal is clipped or blanked as well.

When applying both approaches in OFDM systems affected by pulsed interference, special characteristics of the OFDM signal as well as the structure of the DME interference signal have to be taken into account by carefully choosing the threshold and by accurately detecting interference pulses [91, 92]. The choice of the threshold as well as the detection of interference pulses is addressed in detail in the context of clipping in Section 5.3.1. In the same way, the threshold for pulse blanking is determined in Section 5.3.2.

### 5.3.1 Clipping

#### Principle

As depicted in Fig. 5.6, the amplitude of samples of the Rx signal affected by interference is reduced to a certain threshold  $T^{\text{clip}}$  when their amplitude exceeds  $T^{\text{clip}}$ . With  $r_p^{\text{ov}}[k]$  denoting the over-sampled Rx signal of the  $p$ th OFDM symbol after GI removal, the clipping operation yields the clipped Rx signal  $r_p^{\prime\text{ov}}[k]$  and writes

$$r_p^{\prime\text{ov}}[k] = \begin{cases} r_p^{\text{ov}}[k] & |r_p^{\text{ov}}[k]| < T^{\text{clip}} \\ T^{\text{clip}} \exp\{j \arg\{r_p^{\text{ov}}[k]\}\} & |r_p^{\text{ov}}[k]| \geq T^{\text{clip}} \end{cases} \quad (5.13)$$

$$k = 0, \dots, VN - 1, p = 0, \dots, P - 1.$$

Recalling from (2.18) that the Rx signal is composed of the desired OFDM signal, noise, and interference, obviously not only the interference signal but also the noise and the desired signal are affected by clipping. To keep the impact on the useful signal at an acceptable level, the threshold  $T^{\text{clip}}$  for clipping has to be optimised as a trade-off between the achieved reduction of interference power and the impact on the desired OFDM signal. In addition, the interference signal has to be detected accurately from the Rx signal in order to be able to apply clipping efficiently.

#### Determination of Threshold

The two counteracting effects induced by clipping, namely the reduction of interference power and the impairment of the desired OFDM signal, are demonstrated by means of a simple example with one DME interferer at  $f_{c,0} = -0.5$  MHz offset to the OFDM system. The peak power of the interferer is varied from  $\Psi_0^{\text{DME}} = -65$  dBm to  $\Psi_0^{\text{DME}} = -75$  dBm and the pulse rate is 10800 pulse pairs per sec-

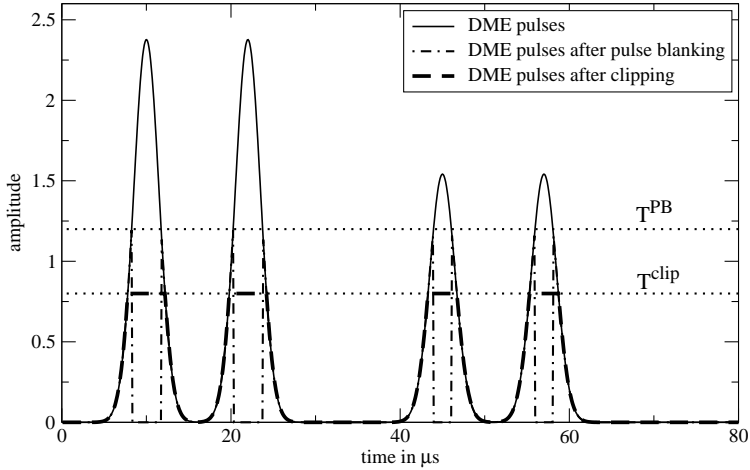


**Figure 5.6** Principle of clipping and pulse blanking.

ond (ppps) such as to represent typical interference conditions, where three DME ground stations with the same power and maximum duty cycle superimpose. The power of the interference signal is adjusted to the Rx power of the OFDM signal with the average Rx power of the OFDM signal being normalised to 1. Assuming the thermal noise density at  $N_0 = -174$  dBm/Hz resulting in a total noise power of  $-115.8$  dBm in the considered bandwidth and setting  $\text{SNR} = 5$  dB, the corresponding absolute Rx power yields  $-110.8$  dBm. After applying the RF and AA filter, this results in an average signal-to-interference and noise power ratio (SINR) ranging from  $-12.9$  dB to  $-3.5$  dB for the considered interference power values.

In Fig. 5.7, the spectrum of an interference signal with  $\Psi_0^{\text{DME}} = -70$  dBm is shown after applying clipping with different thresholds. Interference signals are randomly generated for the duration of 10,000 OFDM frames and the resulting spectra are averaged over all trials. The clipping threshold is set relative to the average amplitude of the OFDM Rx signal. When the threshold is set to the same level as the average power of the desired OFDM signal, i.e.  $T^{\text{clip}} = 1$ , interference power is nearly reduced to the noise level. As expected, when the threshold is set to the maximum amplitude of the interference signal, i.e.  $T^{\text{clip}} = 7$ , interference power is hardly reduced. Varying the threshold in between these two bounds, on the average the remaining interference power increases with increasing threshold. However, on

some subcarriers, interference power rises and is even higher than without clipping due to the sharp phase transitions in the clipped interference signal.

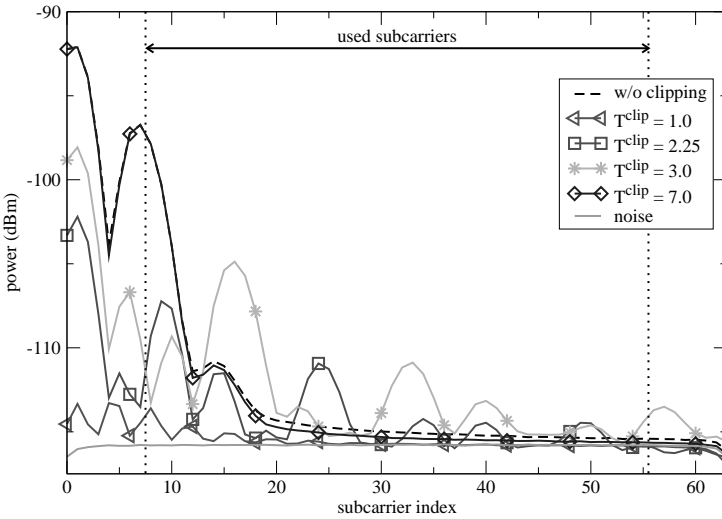


**Figure 5.7** Spectrum of DME signal after clipping with different thresholds  $T^{\text{clip}}$ ,  $f_{c,0} = -0.5$  MHz,  $\Psi_0^{\text{DME}} = -70$  dBm.

Since only interference contributions on the actually used subcarriers determine the performance of the OFDM system, the remaining interference power is calculated on these subcarriers, i.e.  $N_{\text{used}} = 48$  and  $n = 8, \dots, 55$ , for the considered B-AMC system. The remaining interference power after clipping averaged over all used subcarriers and 10,000 randomly generated interference signals is given vs. threshold  $T^{\text{clip}}$  in Fig. 5.8. Independent on the interference power, the curves in Fig. 5.8 exhibit the same shape. For small thresholds, the remaining interference power is small and reduced even below the noise level as long as  $T^{\text{clip}} < 4.5$ . The remaining interference power grows with increasing threshold until the threshold exceeds the maximum amplitude of the interference signal and no reduction of interference power is achieved. Around  $T^{\text{clip}} = 2$ , the curves for interferers with different power values diverge and exhibit discontinuities. This can be explained by the non-linear shape of the interference signal and the coarse resolution of the interference signal induced by four-times over-sampling which results in the same number of clipped OFDM samples for different threshold values. Furthermore, it is



observed that the average interference power of interferers with  $\Psi_0^{\text{DME}} = -74$  dBm and  $\Psi_0^{\text{DME}} = -75$  dBm always remains below the noise level, although the maximum amplitude exceeds the average amplitude of the OFDM signal. Hence, for these interferers, no significant benefits are expected from clipping.

In Fig. 5.9, the average number of clipped samples per OFDM symbol is given vs. threshold. As expected, for small thresholds, a significant amount of the OFDM signal is clipped. With increasing threshold, the average number of clipped samples per OFDM symbol decreases until the threshold exceeds the maximum amplitude of the interference signal. Since up to 110 of 256 samples contained in one OFDM symbol are clipped, clipping is expected to significantly derogate the desired OFDM signal. Same as for the remaining interference power, the curves for different power values are not linear and do not exhibit exactly the same shape. This is explained by the coarse resolution stemming from four-times over-sampling and the shape of the interference pulses.

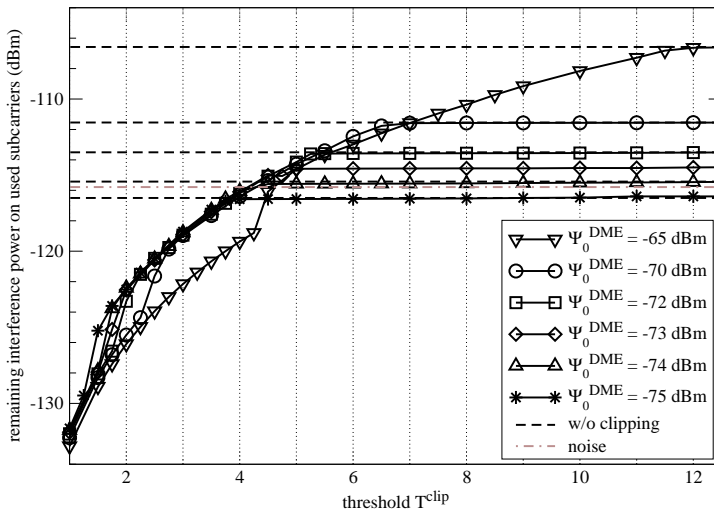


**Figure 5.8** Remaining interference power after clipping with different thresholds  $T^{\text{clip}}$ ,  $f_{c,0} = -0.5$  MHz, 10800 pps.

To determine the optimal threshold as a trade-off between the two effects described above, SINR is employed as a figure of merit for the expected performance [89]. Before clipping, SINR is defined as the ratio of the power of the desired signal and

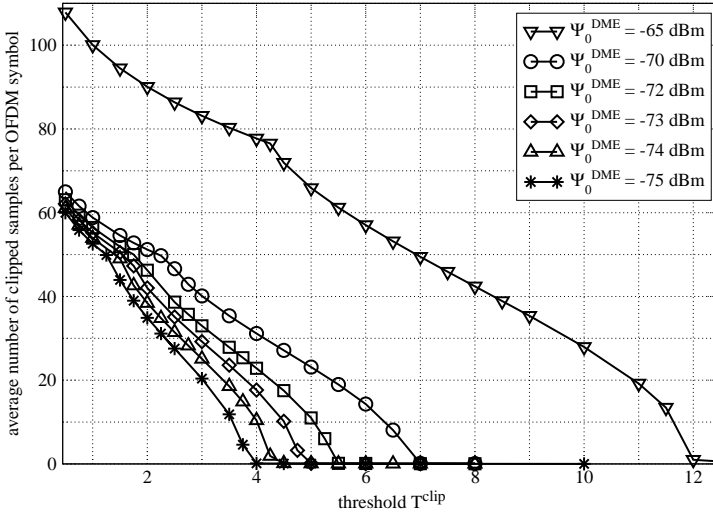


**Figure 5.9** Average number of clipped samples per OFDM symbol,  $V = 4$ ,  $f_{c,0} = -0.5$  MHz, 10800 ppps.

the noise and interference power. With uncorrelated noise and interference, SINR is given by

$$\text{SINR} = \frac{E\{|y_p^{\text{ov}}[k]|^2\}}{E\{|n_p^{\text{ov}}[k]|^2\} + E\{|i_p^{\text{ov}}[k]|^2\}}. \quad (5.14)$$

After clipping has been applied, the power of the desired signal is attenuated and interference power is reduced. In addition, a distortion representing the impact on the desired OFDM signal is induced. Since this distortion is correlated with the useful OFDM signal  $y_p^{\text{ov}}[k]$ , the SINR definition from (5.14) cannot be used. In [89, 93], the Rx signal after clipping  $r_p^{\text{ov}}[k]$  has been split up into a useful and a distorted part resulting in

$$r_p^{\text{ov}}[k] = \underbrace{\xi \cdot y_p^{\text{ov}}[k]}_{\text{useful part}} + \underbrace{v_p^{\text{ov}}[k]}_{\text{distorted part}}. \quad (5.15)$$

The distorted part of the clipped Rx signal contains AWGN, the remaining interference signal, as well as the distortion induced by clipping. The scaling factor  $\xi$  represents the attenuation of the desired OFDM signal due to clipping. In [89, 93],

$\xi$  is defined such as to achieve an uncorrelated useful and distorted part resulting in

$$\xi = \frac{E\{r_p^{\text{ov}}[k]y_p^{\text{ov}*}[k]\}}{E\{|y_p^{\text{ov}}[k]|^2\}}. \quad (5.16)$$

Since the distorted and the useful part of the clipped Rx signal are now uncorrelated, the SINR after clipping  $\text{SINR}^{\text{clip}}$  can easily be defined as

$$\text{SINR}^{\text{clip}} = \frac{E\{|\xi y_p^{\text{ov}}[k]|^2\}}{E\{|v_p^{\text{ov}}[k]|^2\}} = \frac{E\{|\xi y_p^{\text{ov}}[k]|^2\}}{E\{|r_p^{\text{ov}}[k] - \xi y_p^{\text{ov}}[k]|^2\}}. \quad (5.17)$$

To neglect interference contributions lying in the GI and to focus on the actually used subcarriers in the centre of the OFDM bandwidth, SINR is rewritten in the frequency domain by means of Parseval's theorem yielding

$$\text{SINR}^{\text{clip}} = \frac{E\{|\xi Y_p[n]|^2\}}{E\{|V_p[n]|^2\}} = \frac{E\{|\xi Y_p[n]|^2\}}{E\{|R'_p[k] - \xi Y_p[n]|^2\}}, \quad n = 8, \dots, 55, \quad (5.18)$$

with  $V_p[n]$  being the low-pass filtered Fourier transform of  $v_p^{\text{ov}}[k]$  from (5.17).

The threshold  $T^{\text{clip}}$  for which SINR becomes maximal is determined by means of simulations with one DME interferer using the same parameters as for Fig. 5.8 and 5.9. In Fig. 5.10, SINR before and after clipping are given. For small clipping thresholds, SINR after clipping is small and may be even below the SINR before clipping, since a significant fraction of the OFDM signal is impaired by clipping which is not counterbalanced by the achieved reduction of interference power. When the threshold exceeds the maximum amplitude of the interference signal, SINR reaches the SINR value without clipping, as interference power is not reduced and no samples of the desired OFDM signal are clipped. In contrast to the expectations, before SINR without clipping is approached, a minimum occurs. In this threshold region, only a few samples per OFDM symbol are clipped on the average, but receive high amplitudes and hence derogate the OFDM signal considerably while only slightly reducing interference power. The desired maximum SINR occurs for  $T^{\text{clip}} = 2.25$  or  $T^{\text{clip}} = 2.5$ . At these thresholds, the optimal trade-off between interference power reduction and impact on the desired OFDM signal is achieved. No clear maximum is observed which again can be explained by the resolution of the interference signal induced by four-times over-sampling meaning that for different threshold values the same number of OFDM samples

is clipped. Hence, the smallest threshold value is selected and the optimal threshold is set to  $T^{\text{clip}} = 2.25$ . As expected, for interferers with  $\Psi_0^{\text{DME}} = -74$  dBm and  $\Psi_0^{\text{DME}} = -75$  dBm, no SINR improvement is achieved. In contrast, SINR is worse after clipping due to the distortion of the desired OFDM signal that is not counterbalanced by any reduction of interference power.

The same observations are made for different pulse rates. Considering only one interference pulse, always the same number of samples is clipped and the same fraction of interference power remains. Hence, despite different absolute SINR obtained for different pulse rates, the trade-off between the two effects is the same independent of the pulse rate and the maximum occurs at the same threshold.

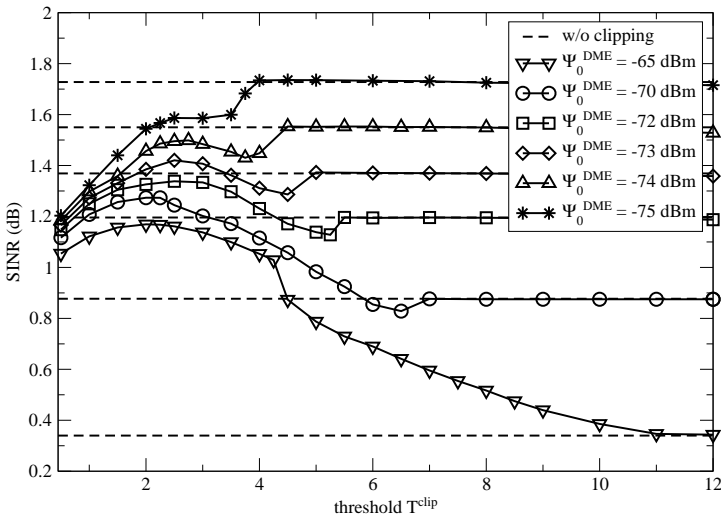


**Figure 5.10** Optimal clipping threshold  $T^{\text{clip}}$ , SNR = 5 dB,  $f_{c,0} = -0.5$  MHz, 10800 ppps.

From the results in Fig. 5.8 and Fig. 5.10, it would be straightforward to conclude that clipping is only applicable to interferers with power  $\Psi_0^{\text{DME}} \geq -73$  dBm. For interferers with smaller power, no benefits are expected from clipping. However, in the investigations above, coding and the error correcting capabilities of the decoder in particular have not been considered.

The BER performance of the transmission of QPSK modulated and convolutional coded data in an AWGN channel is shown in Fig. 5.11. As examples, one DME in-

terferer with pulse rate 10800 ppps and different power values ranging from  $\Psi_0^{\text{DME}} = -65$  dBm to  $\Psi_0^{\text{DME}} = -75$  dBm are considered. When clipping is applied, the threshold is set to  $T^{\text{clip}} = 2.25$  which is the optimal threshold according to the results from Fig. 5.10. Comparing the results without and with clipping, a performance improvement is observed for all interferers independent of their power and independent of the SNR, whereas the achieved SNR gain increases with increasing interference power. For interferers with power  $\Psi_0^{\text{DME}} \geq -73$  dBm, these results have been expected with respect to the SINR improvement obtained with clipping. For interferers with power  $\Psi_0^{\text{DME}} < -73$  dBm, BER performance improves although SINR decreases when clipping is applied. This can be explained by the applied convolutional code that is capable of partly correcting the errors in the desired OFDM signal caused by clipping. For weak interferers, the impact of clipping does not preponderate any more and is reduced such that it is counterbalanced by the achieved reduction of interference power. In Fig. 5.11, it is also observed that for high SNR and/or small interference power, performance is not improved at all with clipping. In that case, the threshold exceeds the maximum amplitude of the signal and has to be re-optimised for the considered SNR region.

Since coding is employed in all modern communication systems, it can be concluded that it is worth clipping all interferers independent of their power. The optimal clipping threshold determined based on an SINR criterion is still optimal for the coded system, as the maximal SINR is the best working point in any case.

### Detection of Pulses

So far, ideal detection based on the known interference signal has been assumed. More realistically, the interference signal and the corresponding samples to be clipped have to be detected from the Rx signal which is composed of the desired OFDM signal, noise, and interference. As the power level of the DME pulses usually exceeds the level of the desired signal, DME pulses can be detected in the time domain Rx signal. However, the detection is aggravated by the non-constant signal level with peaks which is an inherent property of the OFDM signal resulting in a high PAPR.

The PAPR is upper-bounded by the number of used subcarriers provided that all subcarriers receive equal unit energy. In the considered example,  $N_{\text{used}} = 48$  used subcarriers result in a theoretically maximum PAPR as high as  $\text{PAPR}_{\text{max}} = 48 = 16.8$  dB with the average power of the OFDM signal being normalised to 0 dB. Hence, as illustrated in Fig. 5.12, the OFDM signal exhibits peaks that are higher

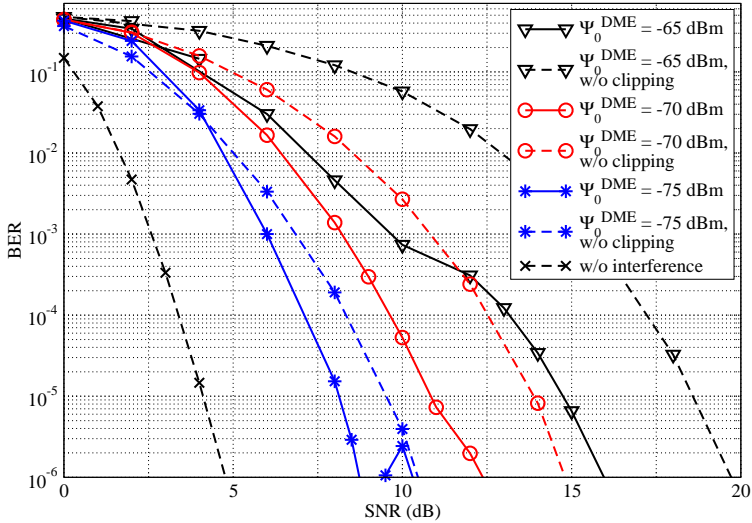


**Figure 5.11** BER performance, optimal clipping threshold  $T^{\text{clip}} = 2.25$ , QPSK, AWGN channel, convolutional coding,  $R_c = 1/2$ .

than the optimal threshold for clipping determined above. Detecting interference pulses based on a simple threshold decision, peaks in the OFDM signal would falsely be identified as pulses. Clipping the corresponding samples would lead to additional bit errors while not reducing the impact of interference at all. An analysis of the peaks in the OFDM signal including noise has shown that this effect is not negligible. In particular, for low SNR, peaks with a width of up to eight samples are observed leading to more than 5% of the samples of an OFDM symbol being falsely clipped.

To circumvent this problem, the amplitude of the interference signal is reconstructed based on the correlation of the Rx signal and a DME pulse with peak amplitude normalised to 1 [92]. The correlation of the Rx signal and a known signal is a well-known procedure for signal detection at Rx.

Prior to clipping or pulse blanking, the cross-correlation function  $r_{rp}[u-v]$  between the time domain Rx signal  $r_p[u]$  and a generic DME pulse  $p[v]$  is generated as

$$r_{rp}[u-v] = E\{r_p[u]p^*[v]\}, u = 0, \dots, VN-1, v = 0, \dots, VN-1. \quad (5.19)$$

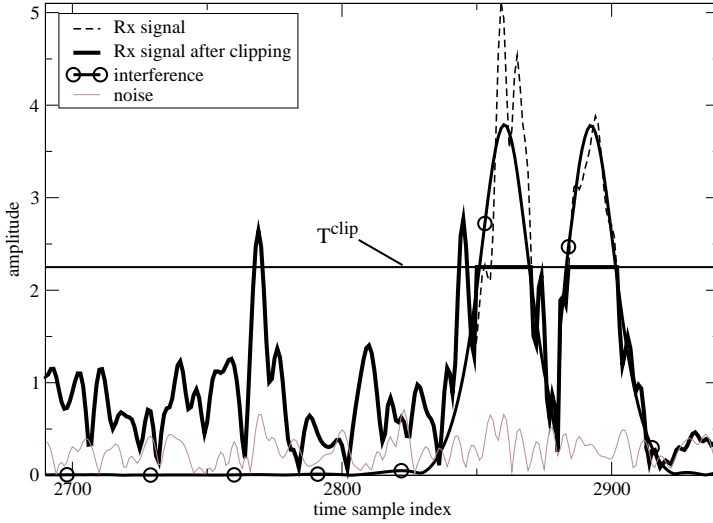


**Figure 5.12** Detection of DME pulses and peaks in the Rx signal.

The generic DME pulse is determined from (5.2) in the same way as (5.7), but using different parameters, i.e.

$$\begin{aligned}
 N_1 &= 1, \\
 N_{u,0} &= 1, \\
 A_0^{\text{DME}} &= 1, \\
 f_{c,0} &= 0, \\
 \varphi_{0,0} &= 0, \\
 t_{0,0} &= 6 \mu\text{s}, \quad \Delta t = 0 \mu\text{s}.
 \end{aligned} \tag{5.20}$$

The starting time  $t_{0,0}$  of the pulse is chosen such as to obtain an amplitude close to 0 at  $t = 0$  and to limit the infinite Gaussian shaped pulse. The pulse is not modulated to a carrier frequency to be able to detect both interferers at  $+0.5$  and  $-0.5$  MHz offset to the centre frequency of the OFDM system. The phase is set to 0 and the amplitude is set to a fixed value, e.g.  $A_0^{\text{DME}} = 1$ . With these parameters, the generic DME pulse  $p[k]$  in the discrete time domain is given by

$$p[k] = e^{-\varepsilon/2(k/V/f_s)^2}, \quad k = 0, \dots, VN - 1. \tag{5.21}$$

In Fig. 5.13, the Rx signal, the interference signal as well as the resulting cross-correlation function of the Rx signal and a generic DME pulse are given. Two interferers with different power and different centre frequency are considered. The power level of the Rx signal is set such as to give SNR = 5 dB. In the cross-correlation function, peaks are observed at the same positions as peaks occur in the actual interference signal. For deriving the amplitude of the interference signal, the amplitude of the peaks in  $r_{\text{TP}}[u - v]$  is adapted to the amplitude of the Rx signal averaged over four samples around the maximum to remove noise. Given the relatively low resolution of the interference signal induced by only four-times over-sampling, the accuracy of this estimation is sufficient for applying the threshold  $T^{\text{clip}}$  or  $T^{\text{PB}}$  to this estimation and clipping or blanking the samples in the Rx signal accordingly.

As can be seen from Fig. 5.13, the amplitude of the peaks in the cross-correlation function does not perfectly match the actual amplitude of the interference pulses when the Rx signal exhibits a large amplitude at that point, where an interference pulse occurs. However, due to the relatively low resolution induced by only four-times over-sampling, this inaccuracy can be tolerated. Compared to clipping based on the perfectly known interference signal, in most cases the same number of samples is clipped in the Rx signal. Thus, in the following, perfect pulse detection based on the actual interference signal is assumed.

## 5.3.2 Pulse Blanking

### Principle

In contrast to clipping, the samples of the Rx signal affected by interference are set to zero rather than setting their amplitudes to a certain threshold as illustrated in Fig. 5.6. When the amplitude of the over-sampled Rx signal  $r_p^{\text{ov}}[k]$  after GI removal given by (5.9) exceeds the threshold  $T^{\text{PB}}$  the corresponding samples are blanked resulting in

$$r_p^{\prime\text{ov}}[k] = \begin{cases} r_p^{\text{ov}}[k] & |r_p^{\text{ov}}[k]| \leq T^{\text{PB}} \\ 0 & |r_p^{\text{ov}}[k]| > T^{\text{PB}} \end{cases} \quad (5.22)$$

$$k = 0, \dots, VN - 1, p = 0, \dots, P - 1.$$

Same as for clipping, the samples of the Rx signal actually affected by interference cannot be detected from the Rx signal by a simple threshold decision because



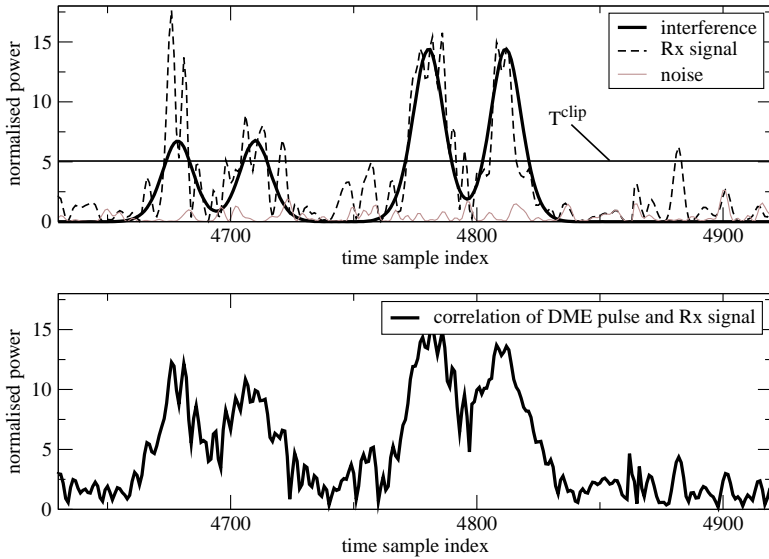


**Figure 5.13** Cross-correlation of Rx signal and generic DME pulse for detection of interference pulses,  $V = 4$ , SNR = 5 dB.

noise and peaks in the desired OFDM signal falsify the result. Therefore, the same detection algorithm as proposed for clipping in the previous section is applied.

Given that the Rx signal is composed of the desired OFDM signal, noise, and the interference signal, all parts of the Rx signal are affected by pulse blanking to the same extent. Same as for clipping, the impact on the desired part of the Rx signal can be kept at a minimum when optimising the threshold for blanking as a trade-off between the reduction of interference power and the impairment of the desired OFDM signal. Since both, the reduction of interference power as well as the impact on the desired OFDM signal differ from what is achieved with clipping, the threshold has to be determined separately for pulse blanking.

### Determination of Threshold

With respect to the desired OFDM signal, the same number of samples of the desired OFDM signal is affected with clipping as well as with pulse blanking. Hence, the average number of clipped samples shown in Fig. 5.9 is also valid for pulse

blanking. However, the resulting impact on the OFDM signal is different for clipping and pulse blanking. Furthermore, interference power reduction achieved with pulse blanking is better than with clipping since the interference signal is erased rather than reduced to a certain amplitude. The remaining interference power after applying pulse blanking with different thresholds  $T^{\text{PB}}$  is shown in Fig. 5.14. The same parameters as for Fig. 5.8 are used. In contrast to the expectations, the interference power remaining after pulse blanking is only slightly smaller than after clipping as shown in Fig. 5.8. Although with pulse blanking a larger fraction of the interference signal is erased, pulse blanking leaves sharp transitions between the reminders of the interference pulses and the blanked part of the interference signal which result in high remaining interference power on some subcarriers. In turn, this generates a high average remaining interference power that is only slightly smaller than the average interference power remaining after clipping.

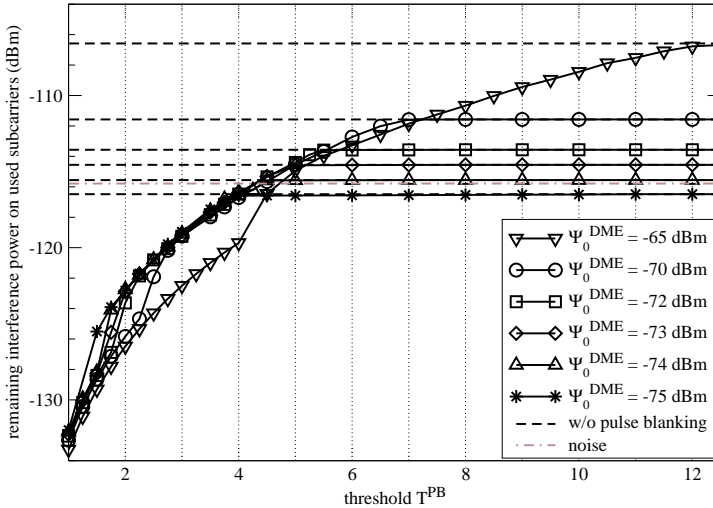


**Figure 5.14** Remaining interference power after pulse blanking with different thresholds  $T^{\text{PB}}$ ,  $f_{c,0} = -0.5$  MHz, 10800 ppps.

The optimal threshold  $T^{\text{PB}}$  for pulse blanking is derived from the SINR observed after applying pulse blanking with different thresholds. Using the SINR definition from [89, 93], SINR after pulse blanking is defined in the same way as for clipping given in (5.18). The average SINR on the used OFDM subcarriers after pulse

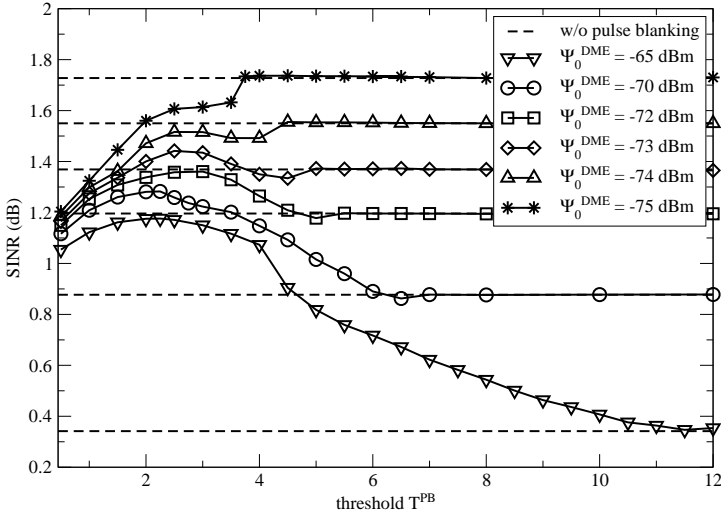


**Figure 5.15** Optimal pulse blanking threshold  $T^{\text{PB}}$ ,  $\text{SNR} = 5$  dB.

blanking yields

$$\text{SINR}^{\text{PB}} = \frac{E\{|\xi Y_p[n]|^2\}}{E\{|V_p[n]|^2\}} = \frac{E\{|\xi Y_p[n]|^2\}}{E\{|R'_p[k] - \xi Y_p[n]|^2\}}, \quad n = 8, \dots, 55. \quad (5.23)$$

Using the same parameters as for Fig. 5.10,  $\text{SINR}^{\text{PB}}$  is determined and shown in Fig. 5.15. The performance of pulse blanking is similar to clipping. For small threshold  $T^{\text{PB}}$ , SINR is very small and falls even below the SINR without pulse blanking in some cases. When the threshold exceeds the maximum amplitude of the DME pulses, obviously SINR is the same as without pulse blanking. Before the threshold approaches the maximum amplitude of the interference signal, a minimum occurs. In this threshold region, interference power is hardly reduced while still impairing some samples of the desired OFDM signal. Compared to clipping, this minimum is less distinct, since the affected samples of the OFDM signal are erased rather than set to high amplitudes that induce significant interference power. The searched maximum SINR is observed for thresholds ranging between 2.25 and 2.75. Since no clear maximum can be observed due to the small resolution induced by only four-times over-sampling, the optimal threshold is set to  $T^{\text{PB}} = 2.25$ , which is the same value as for clipping. For this threshold, SINR is increased substantially

for all interferers with power  $\Psi_0^{\text{DME}} \geq -73$  dBm independent of the duty cycle. Hence, BER performance is expected to improve as will be shown by means of simulations in Section 5.5. Same as for clipping, for interferers with  $\Psi_0^{\text{DME}} < -73$  dBm, SINR decreases after pulse blanking. However, when coding is applied, errors induced by pulse blanking are expected to be partly corrected such that all in all, pulse blanking provides performance improvements for all interferers independent of their power.

Comparing pulse blanking and clipping, a similar performance is observed with pulse blanking performing slightly better than clipping.

## 5.4 Compensation of Pulse Blanking Impact

As shown in the previous section, interference power is reduced significantly with clipping and pulse blanking. However, both approaches affect the OFDM signal such that the potential performance improvement degrades considerably. Considering pulse blanking, the impact on the OFDM signal can be determined and compensated to a wide extend. However, this is not applicable to clipping, since the Rx signal is clipped rather than simply erased.

The impact of pulse blanking on the OFDM signal can be determined exactly when representing pulse blanking as a windowing operation. The window function is a rectangular window that exhibits notches at those positions where the Rx signal is blanked. Recalling that the shape of the window determines the spectrum of the OFDM subcarriers, the subcarrier spectra can be determined and the distortion induced by pulse blanking is identified as ICI. ICI can easily be reduced by subtracting the known impact of all other subcarriers from the considered subcarrier as applied for example for reducing ICI in OFDMA induced by frequency offsets [94].

### 5.4.1 Impact of Pulse Blanking

The impact of pulse blanking on the OFDM signal is illustrated at hand of a simple example taking into account only three adjacent subcarriers and one notch in the time domain OFDM signal generated by pulse blanking. This is generalised to  $N$  OFDM subcarriers and an arbitrary number of notches in the OFDM signal later.

In Fig. 5.16, the real part of the randomly chosen 6th, 7th and, 8th subcarrier in the time domain is shown. When applying pulse blanking,  $z_b = 10$  samples are set to

zero resulting in sharp transitions in the time domain signal as shown in the lower part of Fig. 5.16.

The corresponding frequency domain representation of Fig. 5.16 is shown in Fig. 5.17. Before pulse blanking is applied, the subcarrier spectra are orthogonal and all other subcarriers are zero when the considered subcarrier is in its maximum. The output of the DFT operation corresponds to the maxima of all subcarrier spectra at Rx. Hence, the data transmitted on each subcarrier are observed isolatedly and are independent of the other subcarriers. Pulse blanking modifies the subcarrier spectra resulting in a loss of orthogonality that in turn induces ICI. Considering e.g. the 6th subcarrier, one observes that the maximal amplitude is reduced due to the power loss induced by erasing a certain fraction of the Rx signal. In addition, contributions from the 7th and 8th subcarrier occur at that point where the Rx signal is evaluated during the DFT operation at Rx.

In general, the rectangular window that represents the pulse blanking operation exhibits  $N_B \leq N - 1$  notches per OFDM symbol. Per notch,  $z_b, b = 0, \dots, N_B - 1$ , samples are notched. Summing up all notched samples, per OFDM symbol

$$z = \sum_{b=0}^{N_B-1} z_b, b = 0, \dots, N_B - 1, \quad (5.24)$$

samples are erased.

Defining the lower and the upper bound of the  $b$ th notch in the  $p$ th OFDM symbol as  $B_{p,b}^l$  and  $B_{p,b}^u$ , respectively, the pulse blanking window is defined as

$$w_p^{\text{PB}}[k] = \begin{cases} 1 & 0 \leq k \leq B_{p,0}^l, B_{p,0}^u \leq k \leq B_{p,1}^l, \dots, \\ & B_{p,N_B-1}^u \leq k \leq VN - 1, \\ 0 & \text{otherwise} \end{cases} \quad k = 0, \dots, N - 1, p = 0, \dots, P - 1. \quad (5.25)$$

As the interference signal varies from OFDM symbol to OFDM symbol, the window has to be defined for each OFDM symbol separately as indicated by the index  $p$  denoting the  $p$ th OFDM symbol within one OFDM frame. For reasons of simplicity, only one OFDM symbol is considered and  $p$  is set to 0 for illustrating the generalised shape of the pulse shaping window in Fig. 5.18. In addition, over-sampling has to be considered as pulse blanking is applied to the over-sampled Rx signal.

With (5.25), the time domain signal of the  $p$ th OFDM symbol after pulse blanking

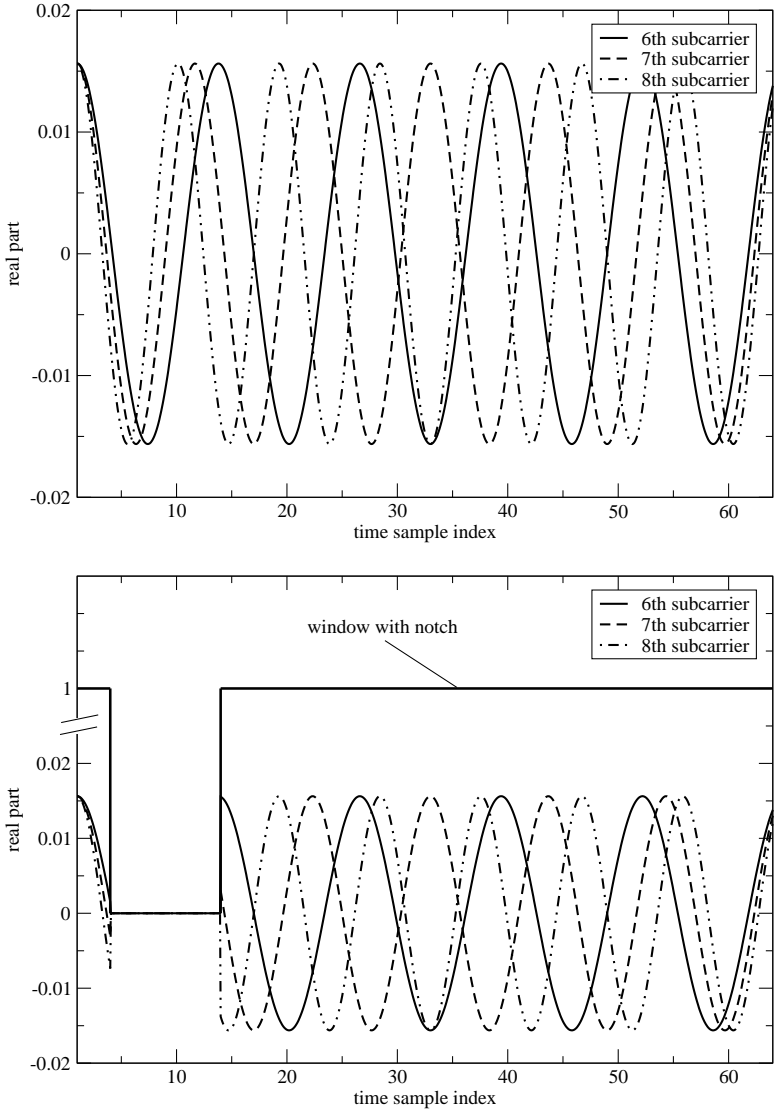
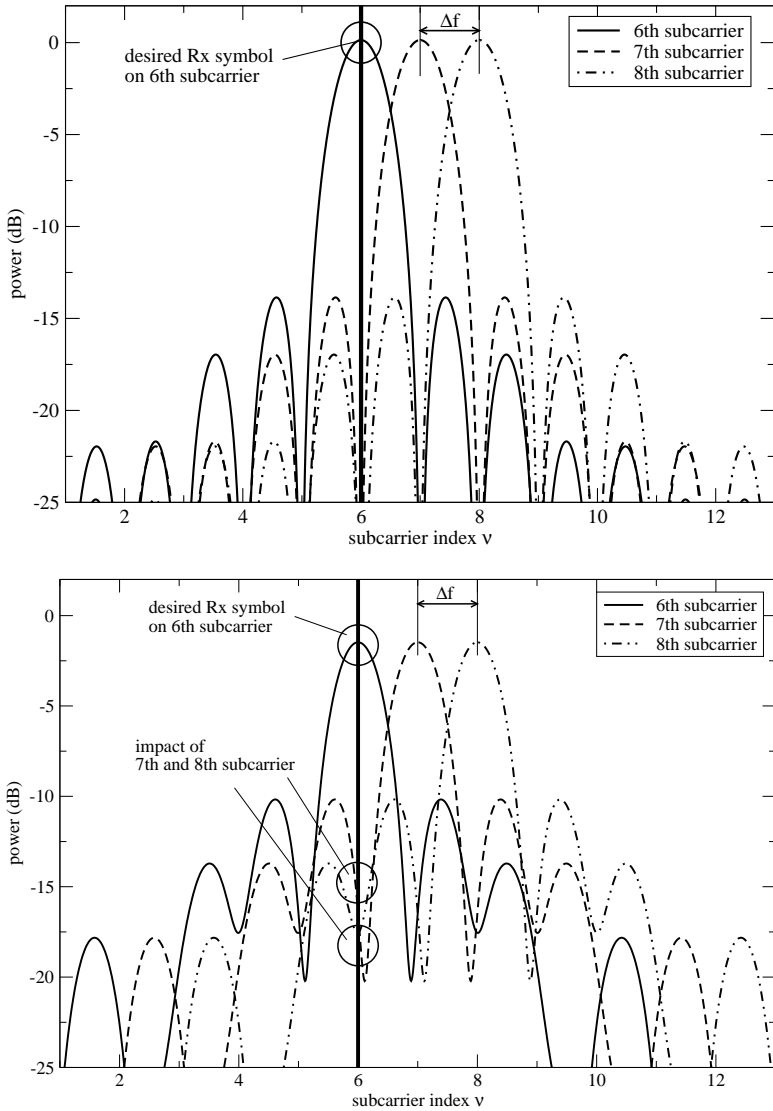


Figure 5.16 Real part of time domain OFDM signal before and after pulse blanking.



**Figure 5.17** Subcarrier spectra before and after pulse blanking.

is given by

$$r_p^{\text{ov}}[k] = w_p^{\text{PB}}[k] \cdot r_p^{\text{ov}}[k], k = 0, \dots, VN - 1, p = 0, \dots, P - 1, \quad (5.26)$$

which is equivalent to the definition of the pulse blanking operation from (5.22).

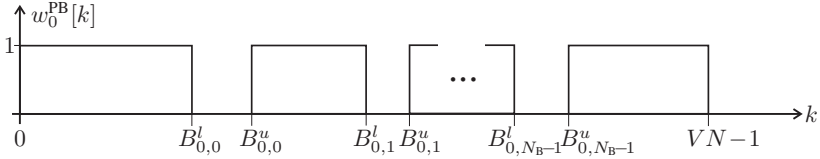


**Figure 5.18** Pulse blanking window,  $p = 0$ .

The performance degradation caused by erasing different fractions of the OFDM signal is shown in Fig. 5.19. For the simulations, it has been assumed that one pulse pair occurs per OFDM symbol, i.e. pulse rate is approximately 8333 ppps. When blanking one pulse pair,  $N_B = 2$  notches are inserted in the Rx signal. The width of the notches is varied, i.e.  $z_b = 4, 8, 12, 16, 20, 24, 28$  with  $b = 0, 1$ , such as to represent interferers with different power levels and different thresholds for pulse blanking. For example, assuming an interferer with  $\Psi_i^{\text{DME}} = -70$  dBm and threshold  $T^{\text{PB}} = 2.25$ ,  $z = 2 \cdot 12$  samples are blanked per OFDM symbol. Note, when determining the number of notched samples, over-sampling with  $V = 4$  is taken into account. To be able to consider the impact of inserting notches in the OFDM signal isolatedly, the actual interference is not added. For generating the OFDM signal, uncoded QPSK symbols are transmitted over an AWGN channel.

Blanking  $z_b = 4, b = 0, 1$  samples per OFDM symbol results in an SNR loss of 0.92 dB at  $\text{BER} = 10^{-3}$ . As expected, SNR loss grows with increasing number of erased samples. For  $N_B = 2$  and  $z_b = 12, b = 0, 1$ , SNR degrades by 7.2 dB at  $\text{BER} = 10^{-3}$ . In more realistic interference conditions with multiple interferers, more than  $N_B = 2$  notches occur per OFDM symbol resulting in even larger SNR losses. Part of the observed SNR loss can be explained by the power reduction caused by erasing a certain fraction of the Rx signal. The corresponding SNR loss is defined as

$$\text{SNR}^{\text{loss}} = 10 \log_{10} \left( \frac{VN - z}{VN} \right) \quad (5.27)$$

and yields relatively small values, e.g.  $\text{SNR}^{\text{loss}} = 0.43$  dB for  $N_B = 2$  and  $z_b =$



12,  $b = 0,1$ . The remaining SNR loss of 6.77 dB is explained by the distortion induced to the OFDM signal and is expected to be reduced by compensating ICI.

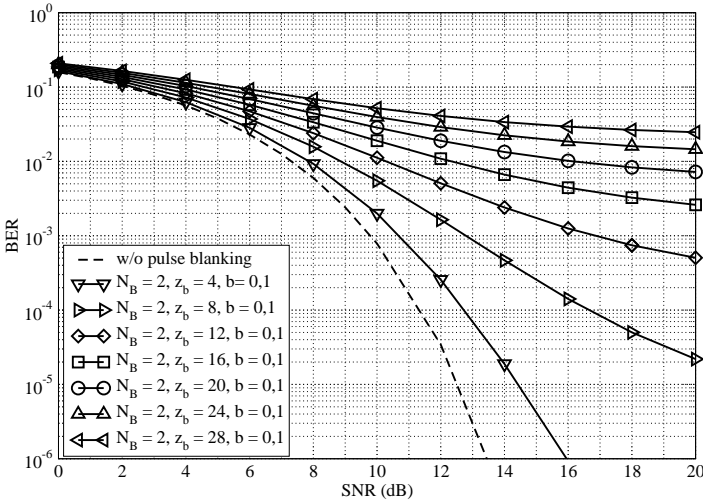


**Figure 5.19** BER after inserting different numbers of notches with different lengths in OFDM signal, QPSK, no coding, AWGN channel.

## 5.4.2 Reduction of ICI

For evaluating and compensating ICI, the spectra of the individual subcarriers after pulse blanking have to be derived. In OFDM, the subcarrier spectrum is determined by the window that extracts an OFDM symbol from the data stream. In contrast to the conventional rectangular window of length corresponding to the length of one OFDM symbol, after pulse blanking, the pulse blanking window as defined in (5.25) has to be taken into account. In the time domain, the signal  $\hat{s}_\nu[k]$  received on the  $\nu$ th subcarrier equals

$$\hat{s}_\nu[k] = w^{\text{PB}}[k] \cdot \hat{d}_\nu e^{j2\pi\nu k/V/N}, \quad k = 0, \dots, VN - 1, \quad (5.28)$$

when channel and noise influences are neglected. Since the transmitted data symbols  $d_\nu$  cannot be assumed to be perfectly known at Rx, an estimation of the transmitted data symbols  $\hat{d}_\nu$  has to be used for determining the subcarrier signal. Hence,

the subcarrier signal also is an estimation of the actual subcarrier signal as indicated by ( $\hat{\cdot}$ ). For reasons of simplicity, but without loss of generality, only one OFDM symbol of the OFDM frame is considered and the index  $p$  is omitted in the following. With these simplifications, the spectrum of the  $\nu$ th subcarrier can be calculated by Fourier transforming (5.28) to the frequency domain. Taking into account  $V$ -times over-sampling, an estimation of the  $\nu$ th subcarrier spectrum  $\hat{S}_\nu[n]$  yields

$$\begin{aligned}
\hat{S}_\nu[n] &= \text{DFT}\{\hat{s}_\nu[k]\} & (5.29) \\
&= \hat{d}_\nu \sum_{k=0}^{B_0^l} e^{-jk(\Omega-\Omega_\nu)} + \hat{d}_\nu \sum_{b=0}^{N_B-2} \sum_{k=B_b^u}^{B_{b+1}^l} e^{-jk(\Omega-\Omega_\nu)} \\
&\quad + \hat{d}_\nu \sum_{k=B_{N_B-1}^u}^{VN-1} e^{-jk(\Omega-\Omega_\nu)} \\
&= \hat{d}_\nu \left( e^{-j(\Omega-\Omega_\nu)B_0^l/2} \frac{\sin((\Omega-\Omega_\nu)B_0^l/2)}{\sin((\Omega-\Omega_\nu)/2)} \right. \\
&\quad + \sum_{b=0}^{N_B-2} e^{-j(\Omega-\Omega_\nu)(B_{b+1}^l+B_b^u)/2} \frac{\sin((\Omega-\Omega_\nu)(B_{b+1}^l-B_b^u+1)/2)}{\sin((\Omega-\Omega_\nu)/2)} \\
&\quad \left. + e^{-j(\Omega-\Omega_\nu)(VN+B_{N_B-1}^u-1)/2} \frac{\sin((\Omega-\Omega_\nu)(VN-B_{N_B-1}^u)/2)}{\sin((\Omega-\Omega_\nu)/2)} \right).
\end{aligned}$$

The frequency and the subcarrier index  $n$  and  $\nu$  are represented by  $\Omega = 2\pi n/V/N$  and  $\Omega_\nu = 2\pi\nu/V/N$ , respectively. Note, when only one notch occurs, i.e.  $N_B = 1$ , the second summand vanishes.

With the known subcarrier spectra, the impact of pulse blanking on the  $n$ th subcarrier can be compensated by subtracting the influences of all other subcarriers with index  $\nu \neq n$ . The subcarriers outside the OFDM bandwidth are loaded with zeros and can be omitted by ideally low-pass filtering the used OFDM bandwidth as in (5.12). The influence of a subcarrier is not only determined by the spectral shape and the transmitted data symbol, but also by the channel influences the subcarrier has experienced. Hence, the fading coefficients  $H[\nu]$  have to be taken into account as well. The OFDM signal  $R^{\text{comp}}[n]$  after compensating the impact of pulse blank-

ing on the  $N$  relevant subcarriers writes

$$R^{\text{comp}}[n] = R'[n] - \sum_{\substack{\nu=0 \\ \nu \neq n}}^{N-1} H[\nu] \hat{S}_\nu[n + N(V-1)/2], \quad n = 0, \dots, N-1. \quad (5.30)$$

As can be seen from (5.29) and (5.30), the compensation of pulse blanking requires knowledge about the number and position of the notches as well as of the transmitted data symbols. Information on the notches is available from pulse blanking in form of the parameters  $N_B$ ,  $B_b^1$ , and  $B_b^u$ . The transmitted data symbols cannot easily be estimated from the Rx values  $R'[n]$  on the  $N$  subcarriers as they are distorted by the channel, AWGN, and ICI, which is illustrated in the following.

The strong impact of ICI induced by pulse blanking is illustrated in Fig. 5.20 at hand of the received QPSK symbol constellation observed after pulse blanking. In the Rx signal,  $N_B = 2$  notches are inserted with each notch having a length of  $z_b = 24$ ,  $b = 0, 1$ , samples. To focus on ICI, AWGN, channel influences, and interference are not considered. Comparing the received symbol constellation to the transmitted one, it is observed that on the average the QPSK symbols receive less power as a fraction of the Rx signal is erased. Moreover, pulse blanking induces a strong distortion that even moves some QPSK symbols into the wrong decision region. Taking into account noise and channel influences in addition and/or increasing the number of blanked samples per OFDM symbol, this effect becomes even more distinctive, hence aggravating the estimation of the Tx sequence.

An estimation of the Tx sequence is derived from the Rx sequence by equalising, demodulating, and decoding the Rx signal as usual. To obtain improved estimates  $\hat{d}_\nu$ ,  $\nu = 0, \dots, N-1$ , of the Tx symbols, the decoded bits are encoded and modulated again. ICI is then reconstructed and subtracted from the Rx signal according to (5.30). In order to improve the reliability of the estimates of the Tx sequence, an iterative structure is introduced as shown in the simplified Rx block diagram in Fig. 5.21. After the first iteration, estimates of the Tx sequence are derived from the Rx signal, where the impact of ICI has already been partly compensated. With the thus obtained more accurate estimates of the Tx symbols, ICI can be further reduced. The number of required iterations depends on the actual interference conditions and the related number of blanked samples of the OFDM signal. Furthermore, coding reduces the required number of iterations as several bit errors are already corrected at the decoder.

Since channel estimation is out of the scope of this thesis, the fading coefficients



The performance of the proposed compensation of the impact of pulse blanking is illustrated at hand of a simple OFDM signal, where a fix number of notches with fixed width is inserted, i.e.  $N_B = 2$  and  $z_b = 24, b = 0,1$  or  $z_b = 12, b = 0,1$ , respectively. The actual interference signal is not taken into account. To be able to neglect the influences of the channel itself and of channel estimation, an AWGN channel is considered with channel coefficients  $H[n] = 1$  for all subcarriers and all OFDM symbols. Moreover, an uncoded system is assumed to focus the study on the improvement due to the iterative structure rather than on the error correction capabilities of the chosen code.

As shown in Fig. 5.22, the impact of pulse blanking can be reduced significantly when the Tx symbols are perfectly known. In that case, the performance without pulse blanking is reached by 0.9 dB for  $z_b = 24$ . This small remaining performance loss is explained by the SNR loss induced by erasing  $2 \cdot z_b = 48$  out of 256 samples of the OFDM symbol. According to (5.27), the resulting SNR loss yields 0.8 dB which shows a good agreement with the simulations.

As perfect knowledge of the Tx sequence cannot be assumed, the Tx sequence has to be estimated from the Rx signal. In the first iteration, the impact of pulse blanking is already reduced considerably. However, the performance is poor compared to the case with perfectly known Tx sequence. With three additional iterations, BER decreases and falls below  $10^{-3}$  which is satisfying for uncoded transmission. After five iterations no further performance improvement is observed. For all SNR, the performance of the ideal case with perfectly known Tx sequence is not reached. For  $\text{SNR} < 12$  dB, the ideal performance is approached by only 0.7 dB due to estimation errors even remaining after five iterations. For higher SNR, an error floor is observed that is mainly determined by estimation errors of the Tx sequence rather than by noise influences.

Similar observations are made for the compensation of pulse blanking with  $2 \cdot z_b = 24$  given in the lower part of Fig. 5.22. In the ideal case with perfectly known Tx sequence, the performance of the interference-free case is approached by 0.4 dB which well corresponds to the theoretical SNR loss from (5.27). When estimating the Tx sequence from the Rx signal, the same performance is achieved after only two iterations for  $\text{SNR} < 14$  dB. For higher SNR, again an error floor occurs, which, however, is significantly lower than the error floor observed for the compensation of pulse blanking with  $z_b = 24$ .

Since the accuracy of the estimation of the Tx sequence mainly determines the performance of ICI compensation, estimation errors are investigated separately. The

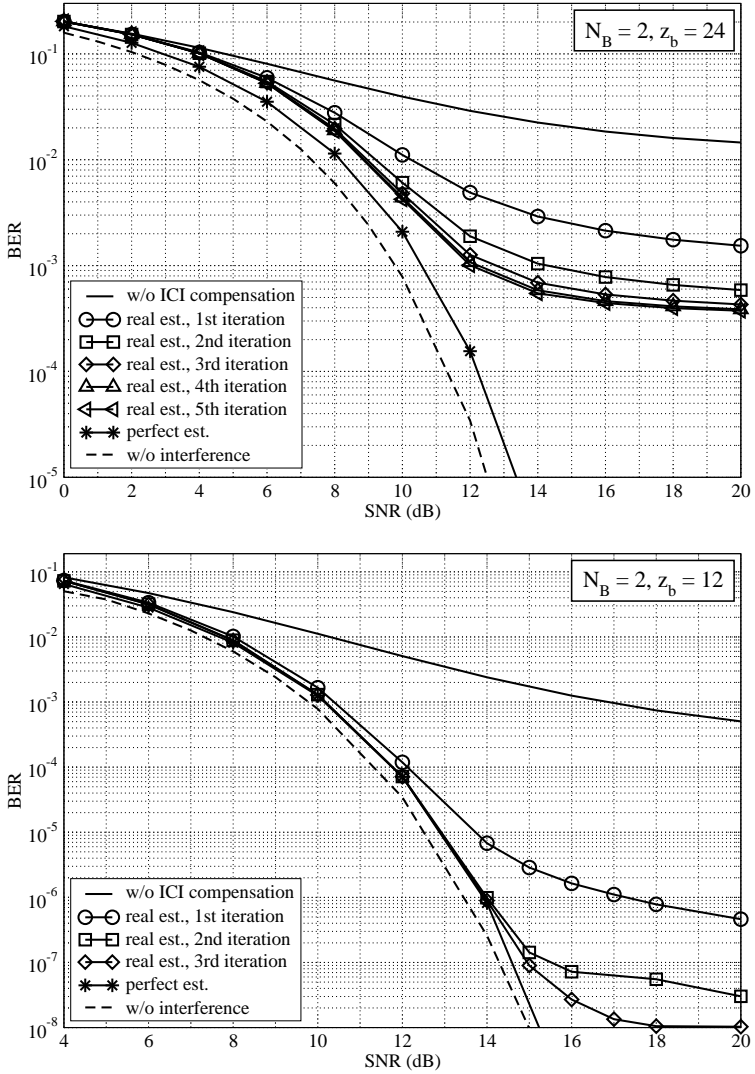


**Figure 5.22** BER performance after compensation of pulse blanking impact,  $N_B = 2$ ,  $z_b = 24$  and  $z_b = 12$ , no interference signal considered, QPSK, uncoded, AWGN channel.

mean square error (MSE) is defined as

$$e^{\text{MSE}} = \text{E} \left\{ \|\mathbf{d} - \hat{\mathbf{d}}\|^2 \right\} \quad (5.31)$$

with  $\mathbf{d}$  and  $\hat{\mathbf{d}}$  denoting the original and the estimated Tx sequence, respectively. The estimation error corresponding to the results from Fig. 5.22 is given in Fig. 5.23. As supposed from the improving BER performance, the estimation error decreases from iteration to iteration. For pulse blanking with  $z_b = 24$ , after four iterations the accuracy of the estimation is not further improved although the estimation error is still high. This can be explained as follows. In the first iteration, the estimation error is well above the noise variance independent of the SNR. As supposed by the received QPSK constellation after pulse blanking with  $z_b = 24$  shown in Fig. 5.20, a significant amount of the data symbols is moved to the wrong decision region when pulse blanking is applied. First, this results in a high estimation error in the first iteration and second, this prohibits further improvements in the following iterations, since the errors cannot be corrected without coding.

Also for pulse blanking with  $z_b = 12$ , the estimation error from Fig. 5.23 well corresponds to the BER performance shown in Fig. 5.22. Even in the first iteration, the estimation error is significantly lower than for  $z_b = 24$ . Hence, the impact of pulse blanking with  $z_b = 12$  can be reduced much better and additional improvements are possible with additional iterations. As already observed in Fig. 5.22, three iterations are sufficient to reach the performance of the case with perfectly known Tx sequence.

When coding is considered, much lower estimation errors are expected resulting in a lower error floor and a reduced number of iterations required to reach the performance of the case with perfectly known Tx sequence. Coding will be considered when evaluating the performance of pulse blanking as well as of ICI compensation in a realistic interference scenario in Section 5.5.

### 5.4.3 Reconsideration of Threshold for Pulse Blanking

Comparing the BER performance after ICI compensation for  $z_b = 12$  and  $z_b = 24$  as given in Fig. 5.22, the BER after ICI compensation is roughly the same for SNR  $< 12$  dB, although the impact of pulse blanking on the OFDM signal is significantly higher for  $z_b = 24$ . This suggests reducing the threshold  $T^{\text{PB}}$  for pulse blanking while accepting additionally blanked samples in the OFDM signal that have to be

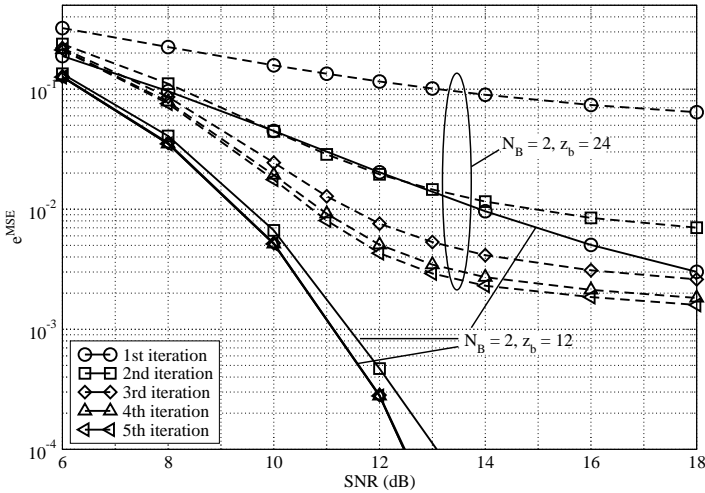


**Figure 5.23** Mean square estimation error of Tx sequence after different iterations of compensation of pulse blanking,  $N_B = 2$ ,  $z_b = 24$  and  $z_b = 12$ , no interference signal considered, QPSK, uncoded, AWGN channel.

compensated. At the same time, the remaining interference power is further reduced without substantially sacrificing BER performance.

The demand for decreasing the threshold for pulse blanking becomes more obvious when splitting the Rx signal after compensating the impact of pulse blanking into its components. Assuming that ICI is perfectly reduced, the Rx signal comprises the desired OFDM signal affected by the radio channel, AWGN  $N'[n]$  slightly modified by pulse blanking, and the interference signal  $I'[n]$  remaining after pulse blanking and writes

$$R^{\text{comp}}[n] = H[n]d_n + N'[n] + I'[n], \quad n = 0, \dots, N - 1. \tag{5.32}$$

As the spectrum of the remaining interference signal from Fig. 5.7 suggests, the remaining interference can be quite large on some subcarriers. This may impede an accurate estimation of the Tx symbols, in particular with respect to the fact that the influence of the remaining interference cannot be diminished by employing several iterations. A straightforward approach to circumvent this problem is reducing the threshold  $T^{\text{PB}}$  for pulse blanking in order to keep the remaining interference as small as possible. Again, the optimal threshold has to be determined, now as a



trade-off between the remaining interference power and the impact onto the desired OFDM signal remaining after ICI compensation. Hence, the optimisation of the threshold from Section 5.3.2 is revisited taking into account the compensation of the impact of pulse blanking. The SINR after pulse blanking and ICI compensation is determined according to (5.23), but the compensated Rx signal  $R^{\text{comp}}[n]$  is used instead of the Rx signal after pulse blanking  $R'[n]$ .

Using the same parameters as for Fig. 5.15, the SINR after pulse blanking with subsequently compensating the impact of pulse blanking is shown in Fig. 5.24 for different thresholds  $T^{\text{PB}}$ . In general, SINR is significantly higher after compensating the impact of pulse blanking than after pulse blanking applied separately as shown in Fig. 5.15. Same as for the case without compensation SINR reaches SINR without pulse blanking, when the threshold exceeds the maximum amplitude of interference signal. In contrast to the results without compensation, SINR improves for all power values, hence making the distinction between strong and weak interferers obsolete. For all interferers, a clear maximum is observed at  $T^{\text{PB}} = 1.25$ . Same as for the case without ICI compensation, the same threshold value is obtained for other parameters such as other pulse rates and other power values. As expected,  $T^{\text{PB}}$  is significantly smaller than the threshold determined for pulse blanking which

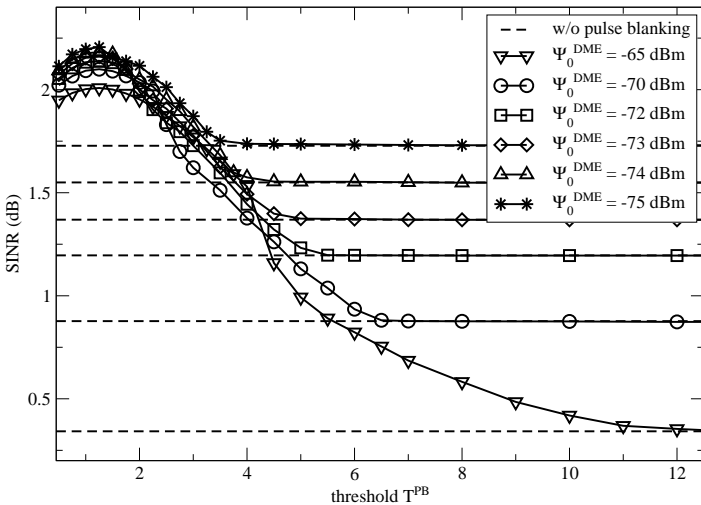


**Figure 5.24** Optimal pulse blanking threshold with compensation of pulse blanking, SNR = 5 dB.

has been  $T^{\text{PB}} = 2.25$ . With this newly determined threshold, interference power can be further reduced. This is related to a stronger impairment of the OFDM signal, but facilitates the compensation of the impact of pulse blanking hence resulting in an overall better performance.

## 5.5 Performance Evaluation

In the previous sections, a strongly simplified scenario with only one interferer has been used to illustrate the impact of interference onto the B-AMC system from Chapter 2 and to demonstrate the performance of the techniques for mitigating this impact. Using the optimal parameters for the mitigation techniques derived in the previous section, the proposed techniques for interference mitigation are evaluated in a realistic interference scenario derived from real channel assignments.

### 5.5.1 Considered Interference Scenario

As no measurement data are available, the expected interference from DME stations is derived analytically from real DME channel assignments. The real DME channel allocation is modeled with the NAVSIM tool [97] for the area around Paris as this is the area with the highest density of DME ground stations in Europe. The victim B-AMC Rx is positioned at an en-route flight level at 45,000 feet altitude in the centre of this area. Since only the FL is considered, only DME/TACAN ground stations operating in the channels in the sub-band 985 - 1009 MHz are studied. The peak interference power originating from each DME/TACAN station is determined via simple link budget calculations, taking into account free space propagation loss and antenna patterns dependent on elevation angles for both the transmitting DME/TACAN ground station and the victim airborne Rx [98]. For all DME/TACAN stations, the maximum duty cycle is assumed, i.e. 2700 ppps for DME and 3600 ppps for TACAN ground stations, respectively [88].

Severe interference conditions are observed when the B-AMC system is operated at 994.5 MHz. In the channel at 994 MHz, three interferers with power up to -72.4 dBm occur. The pulse rates of the interferers superimpose such that almost each OFDM symbol is affected by at least one pulse pair. In addition, a strong interferer occurs in the channel at 995 MHz. Simulations have shown that interferers at  $\pm 2.5$  MHz offset to the centre frequency of the B-AMC system have no impact

on the performance and hence can be neglected.

**Table 5.1** FL en-route interference scenario.

Station	Frequency	Interference power at victim Rx input	Pulse rate
TACAN	994 MHz	-72.4 dBm	3600 ppps
TACAN	994 MHz	-74.0 dBm	3600 ppps
TACAN	994 MHz	-88.2 dBm	3600 ppps
B-AMC	994.5 MHz		
TACAN	995 MHz	-67.9 dBm	3600 ppps

### 5.5.2 Simulation Parameters

For the OFDM system, the parameters of the B-AMC system as given in Tab. 2.2 are considered. The transmission from the B-AMC ground station to an aircraft flying at an en-route flight level is simulated. Due to severe interference as given in Tab. 5.1, the most robust transmission mode is selected, i.e. QPSK with a (133,171) convolutional code with code rate  $R_c = 1/2$ . The outer Reed-Solomon code is not considered. At Rx, ideal synchronisation and channel estimation are assumed.

Propagation conditions of an en-route flight are modelled with a WSSUS channel model. One strong LOS component with Rician factor 15 dB as well as two scattered components with maximum delay  $15 \mu\text{s}$  are taken into account. In addition, Doppler shifts up to 1.25 kHz are considered that reflect aircraft velocities as high as 300 m/s. Due to the strong LOS component the channel behaviour is expected to be similar to AWGN. Interference is modelled as described in the previous section.

### 5.5.3 Simulation Results

In the simulations, SNR is varied from 0 to 15 dB, which spans the SNR range considered to be available for the B-AMC system. For each SNR point, up to 500,000 OFDM frames each containing 54 OFDM symbols are transmitted in order to obtain reliable statistical results. As reference, the BER vs. SNR without interference as well as the BER performance with interference that is not mitigated at all is given.

### Pulse Blanking and Clipping

In Fig. 5.25, the performance of pulse blanking and clipping is shown. In all simulations, perfect pulse detection is assumed meaning that a threshold decision is taken based on the perfectly known interference signal. The threshold is set to the optimal value determined in Section 5.3, i.e.  $T^{\text{clip}} = 2.25$  and  $T^{\text{PB}} = 2.25$ , respectively. For pulse blanking, threshold values below and above the optimised threshold, i.e.  $T^{\text{PB}} = 1.5$  and  $T^{\text{PB}} = 3.0$ , are simulated in addition to verify the choice of the threshold. For  $\text{SNR} < 5$  dB, the performance with  $T^{\text{PB}} = 1.5$  and  $T^{\text{PB}} = 3.0$  is slightly worse than the performance with the optimal threshold. However, starting from  $\text{SNR} = 5$  dB, performance degrades and nearly reaches the performance without pulse blanking for  $T^{\text{PB}} = 3.0$ . For smaller threshold values, this occurs at higher SNR and indicates that the threshold is no more optimal for the respective SNR range as too few samples of the interference signal are blanked and a significant amount of interference power remains. However, the choice of the threshold is still feasible since the target operation point for the B-AMC system in the en-route scenario is around  $\text{SNR} = 5$  dB [33, 41].

Even for the optimally chosen threshold, pulse blanking reduces the impact of interference by only 1.7 dB at  $\text{BER} = 10^{-3}$ . The gap to the interference-free case is explained by the remaining interference power as well as by the impact on the desired OFDM signal. To regard these two influencing factors separately, the BER after applying pulse blanking to the OFDM signal but without adding the actual interference signal is given in Fig. 5.25 as well. Compared to the case with interference, performance is improved by 1.3 dB. This difference can be explained by the interference power remaining after pulse blanking as first, some pulses with high power are not blanked completely and second, the weakest interferer in the channel at -0.5 MHz is not blanked at all since its amplitude is always below the threshold. The gap to the performance of the interference-free case is as high as 2.4 dB and is caused by the distortion of the desired OFDM signal. This strong impact of pulse blanking on the OFDM signal is expected to be widely reduced by the proposed ICI compensation which is addressed in the next subsection.

For clipping, similar results are obtained when the same thresholds are used. However, the performance of pulse blanking is slightly better due to the slightly smaller remaining interference power.

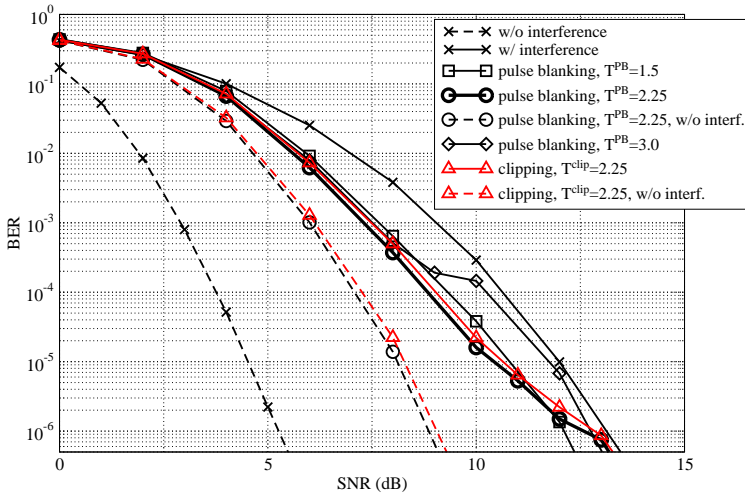


**Figure 5.25** BER performance with pulse blanking and clipping, ideal pulse detection, en-route interference scenario.

### Compensation of Pulse Blanking Impact

In Fig. 5.26, the performance of pulse blanking and the compensation of the pulse blanking impact is shown for different thresholds. Again, perfect detection of the interference pulses is assumed in order to optimally determine the samples to be blanked. For the compensation of the impact of pulse blanking, perfect channel estimation has been assumed, i.e. the channel coefficients  $H_p[n]$ ,  $n = 0, \dots, N - 1$ ,  $p = 0, \dots, P - 1$ , on all subcarriers and in all OFDM symbols are perfectly known.

At first, threshold  $T^{\text{PB}} = 2.25$  is considered that has been determined without taking into account the subsequent compensation of the impact of pulse blanking. Even with perfect ICI compensation based on perfect knowledge of the Tx sequence, the performance of the interference-free case is approached by only 2.4 dB at  $\text{BER} = 10^{-4}$ . For higher SNR values, the gap to the interference-free case even increases as an error floor occurs. The large difference to the case with perfect knowledge of the Tx sequence without interference shows that for higher SNR not enough samples of the interference signal are blanked resulting in a significant fraction of the interference signal remaining after pulse blanking.

Since the remaining interference power constitutes a problem that degrades the achievable performance, the threshold for pulse blanking has been re-determined taking into account that the impact of pulse blanking is compensated afterwards. With threshold  $T^{\text{PB}} = 1.25$ , the performance with pulse blanking degrades as too many samples of the OFDM signal are erased. However, the impact on the desired OFDM signal can be reduced considerably when the Tx sequence is known perfectly. In that case, the performance of the interference-free case is approached by 1.6 dB at  $\text{BER} = 10^{-4}$ . The comparison to the case with perfect knowledge of the Tx sequence without interference shows a difference of only 0.3 dB and indicates that only a small fraction of interference power remains. The gap to the interference-free case is as small as 1.3 dB and can be explained by the SNR loss induced by erasing a certain fraction of the OFDM signal. At the considered SNR, on the average,  $z = 60.8$  of 256 samples of the OFDM signal are blanked. According to (5.27), this results in an SNR loss of 1.2 dB which well agrees to the simulation results.

When deriving an estimation of the Tx sequence from the Rx sequence, the gap to the interference-free case is 1.9 dB at  $\text{BER} = 10^{-4}$  which is only 0.3 dB larger than in the ideal case with perfect knowledge of the Tx sequence. These results are obtained already in the first iteration, hence making further iterations obsolete and reducing computational complexity.

In Fig. 5.22, the performance of the compensation of pulse blanking and the estimation of the Tx sequence have been investigated without coding and without considering interference. Even for less erased samples per OFDM symbol, i.e.  $z = 2 \cdot 24 = 48$ , an error floor has occurred resulting in a large difference between the cases with estimated and perfectly known Tx sequence. This error floor does not occur in Fig. 5.26, because due to coding, estimation errors are corrected already in the first iteration. Although the performance of the ideal case is nearly achieved, the difference between the cases with estimated and perfectly known Tx sequence can still be further reduced by means of a more sophisticated algorithm for estimating the Tx sequence, that e.g. takes into account the correlation between the Rx values on the difference subcarriers.

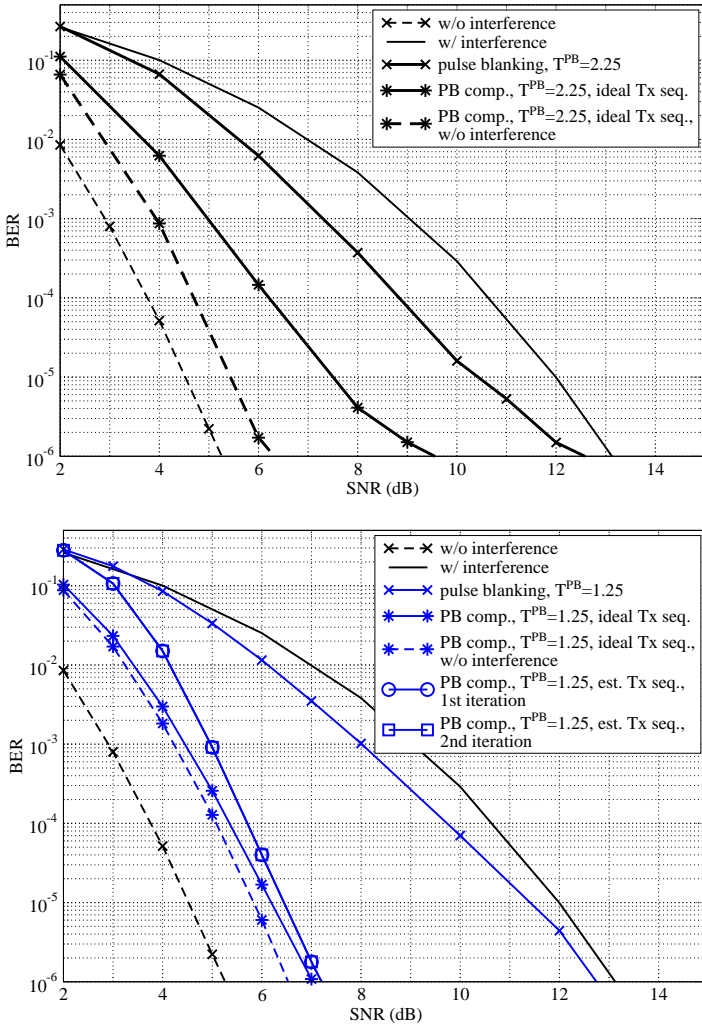


**Figure 5.26** BER after compensation of pulse blanking impact,  $T^{PB} = 2.25$  (above),  $T^{PB} = 1.25$  (below), en-route interference scenario, perfect channel estimation.





# 6 Conclusions

To overcome the contradiction of spectral scarcity on the one hand and the ever-growing demand for more bandwidth and higher data rates on the other hand, spectral efficiency has to be increased. A promising approach is the co-existence of two systems in the same frequency band which can be realised by means of OFDM based overlay systems.

For enabling such co-existence, the suppression of mutual interference between the two systems is a key issue. One goal of this thesis has been the suppression of out-of-band radiation at the OFDM Tx in order to keep interference towards already existing licensed systems at a minimum. A second goal has been the mitigation of interference from licensed systems that significantly degrades the performance of the OFDM based overlay system. The main results of this thesis can be summarised as follows.

## 6.1 Suppression of Out-of-Band Radiation

Since OFDM suffers from high out-of-band radiation, interference towards the licensed systems has to be reduced in order not to constrict the operation of the licensed systems. As the stringent requirements cannot be met with conventional techniques for sidelobe power reduction, in Chapter 3, three advanced methods have been proposed, namely subcarrier weighting (SW), multiple-choice sequences (MCS), and cancellation carriers (CCs). These advanced methods aim at modifying the Tx sequence such as to exhibit lower sidelobes. This is realised by multiplying each subcarrier with a real-valued weighting factor, by generating several Tx sequences all representing the same information and selecting the one with the smallest sidelobe power for transmission, or by inserting CCs at the edges of the spectrum that are weighted such that they cancel the sidelobes of the data bearing subcarriers, respectively. All three techniques have been investigated with respect to the achieved sidelobe power reduction and the corresponding impact on the performance of the OFDM system in terms of BER, PAPR, signalling overhead, and computational complexity. When selecting the parameters for all methods as a reasonable trade-off between performance degradation and sidelobe suppression, in the considered scenario sidelobe power reduction is as high as 5.2 dB, 4.7 dB, and

14.2 dB, for SW, MCS, and CCs, respectively.

In order to further improve performance, the three advanced techniques have been combined with windowing. For SW and MCS, the additional reduction of out-of-band radiation does not counterbalance the throughput loss induced by the increased OFDM symbol duration required for windowing. In contrast, with CCs and windowing, a considerable sidelobe suppression is achieved, whereby CCs reduce sidelobes close to the used OFDM bandwidth and windowing improves spectral characteristics in the remaining areas of the spectrum.

A different approach for further reducing out-of-band emissions is the combination of the proposed advanced techniques with each other. From the three possible and reasonable combinations, namely MCS/SW, SW/CCs, and MCS/CCs, the combination of CCs either with SW or with MCS provides significant improvements that even exceed the sum of the sidelobe power reduction of the two methods applied separately. The achieved average sidelobe power reduction of 21.8 dB or 26.4 dB for SW/CCs or MCS/CCs ensures a minimal impairment of the licensed system or an increase of the Tx power of the overlay system if the licensed system tolerates higher out-of-band radiation.

All in all, the proposed advanced techniques for sidelobe suppression and their combinations in particular are a promising approach for keeping interference towards licensed systems at a minimum. Although several Tx characteristics such as windowing and the IDFT have already been considered, the model for generating the Tx spectrum can be further refined by taking into account non-linearities of the power amplifier and possibly applied techniques for PAPR reduction. Since PAPR reduction techniques also shape the Tx spectrum, the joint optimisation of PAPR reduction and sidelobe suppression techniques is straightforward [60].

So far, out-of-band radiation has only been considered from the perspective of the overlay system. In future work, it has to be investigated how the licensed system actually experiences interference from the OFDM based overlay system. This as well as the actual degree of tolerable out-of-band radiation strongly depend on the considered licensed system and has to be investigated for each overlay scenario individually.

## 6.2 Mitigation of Narrow-Band Interference

Depending on the frequency range where the overlay system is operated, the Rx signal is deteriorated by NBI originating from licensed systems operating within the bandwidth of the overlay system. Although narrow-band, interference contributes to all OFDM subcarriers due to spectral leakage which is an inherent property of the DFT.

For mitigating the severe impact of NBI onto the OFDM system, in this thesis, two different approaches are pursued. In the time domain, before the DFT operation at the OFDM Rx, Rx windowing is applied for enhancing the spectral selectivity of the DFT. With this simple method, interference power is reduced in wide ranges of the spectrum. However, the peak of the interference signal remains, hence requiring additional and/or alternative methods for NBI mitigation. After transforming the Rx signal to the frequency domain, interference is mitigated by subtracting an estimation of the interference signal or by compensating the leakage effect according to an optimisation criterion that minimises the MSE on each subcarrier. Both approaches require an estimation and reconstruction of the interference signal. Exploiting the fact that spectral leakage is a deterministic property of the DFT, amplitude, phase, and frequency of the carrier of the interferer can be estimated based on measurements on a few observation subcarriers not used for data transmission. For compensating the leakage effect, instead of the estimated carrier, a priori knowledge about the PSD of the interference signal can be used for reconstructing the interference signal. The performance of all approaches can be improved by combining them with Rx windowing. The joint application of both the time and the frequency domain approaches is easily realised by adapting the estimation algorithms such as to take into account the preceded Rx windowing operation.

Both the subtraction as well as leakage compensation with two estimation techniques are investigated with respect to the achievable reduction of interference power and the estimation error. Thereby, the number and position of observation subcarriers has been optimised as a trade-off between performance and computational effort. At hand of a DSB-AM interference signal, it is shown that interference power can be reduced by up to 30 dB when subtracting the estimated carrier or applying carrier based leakage compensation with carrier based leakage compensation outperforming the mere subtraction by 5 dB to 8 dB. Although the carrier is estimated accurately with the proposed estimation algorithm using only two observation subcarriers per interferer, performance is not optimal as only the carrier

is mitigated whilst the sidebands are neglected. When sidebands are considered by means of the PSD based reconstruction and compensation of the interference signal, significant interference power reduction is achieved in the outer areas of the spectrum whilst the peak of the interference signal remains resulting in the same average interference power reduction as the carrier based approach.

Simulations of an overlay system in the VHF-band under realistic worst case conditions have shown, that the achieved reduction of interference power leads to a considerably improved BER performance that reduces SNR required to obtain a certain BER by up to 26 dB. The results suggest applying carrier based leakage compensation or a simple subtraction of the estimated carrier signal for reducing the peak of weak interferers lying in channels used by the overlay system. Since the channels occupied by strong interferers are not used by the overlay system, the remaining peak does not constitute a problem. Hence, strong interferers can be best mitigated by the PSD based leakage compensation. The results can be further improved when combining the proposed techniques with Rx windowing. With that approach, the impact of NBI on the OFDM system is expected to be mitigated nearly completely.

### **6.3 Mitigation of Pulsed Interference**

As a different source of interference, pulsed interference has been addressed as it occurs in the aeronautical part of the L-band for example. As the considered OFDM system is operated in a spectral gap between two adjacent channels used by licensed L-band systems, interference has a strong impact on the performance of the OFDM system and has to be mitigated. In contrast to NBI occurring in the bandwidth of the OFDM system, the impact of interference occurring at small frequency offset outside the OFDM bandwidth can already be reduced by applying over-sampling and an anti-aliasing filter. The remaining interference is mitigated by means of pulse blanking or clipping. When applying these well-known approaches to OFDM systems, first, the interference pulses have to be detected from the Rx signal. As the distinction of interference pulses and peaks in the OFDM signal is demanding, the amplitude of the interference signal is estimated and reconstructed based on a cross-correlation between the Rx signal and a generic DME pulse. Second, the thresholds for clipping or pulse blanking have to be optimised as a trade-off between the achieved reduction of interference power and the impact on the OFDM signal. In this thesis, this has been done based on an SINR criterion that maximises SINR af-

ter clipping or pulse blanking. Simulations in a realistic interference scenario show, that with clipping or pulse blanking, the impact of interference can be reduced only moderately resulting in an SNR improvement of 1.7 dB. This poor performance can be explained by the strong impact of clipping and pulse blanking on the OFDM signal, which prohibits achieving the performance of the interference-free case.

A detailed analysis of the impact of pulse blanking on the OFDM signal has shown that pulse blanking leads to ICI. Representing pulse blanking as windowing operation with a rectangular window exhibiting notches at those positions where the OFDM signal is blanked, ICI can be reconstructed and compensated. The required knowledge of the Tx sequence can be derived from decoding and re-encoding the Rx signal and improving this estimation over several iterations. There, the interference power remaining after pulse blanking constitutes a problem that first decreases performance and second aggravates the estimation of the Tx sequence required for the compensation of the impact of pulse blanking. Hence, the optimal threshold for pulse blanking is re-determined taking into account the compensation of the impact of pulse blanking. As a result, the threshold could be decreased considerably for the benefit of a reduction of the remaining interference power. The higher impairment of the desired OFDM signal going in with the decreased pulse blanking threshold could be reduced by compensating the impact of pulse blanking. Simulations have shown, that that way the impact of interference can be eliminated nearly completely. The small remaining gap of about 1.3 dB is explained by the power loss induced by erasing a certain fraction of the OFDM signal when blanking the interference signal. The contribution of an inaccurate compensation of the pulse blanking impact to the remaining gap is negligible. Already after the first iteration, the Tx sequence can be estimated nearly perfectly such that a nearly perfect compensation of the impact of pulse blanking is enabled.

The already good performance of the compensation of the pulse blanking impact can be improved by enhancing the estimation of the Tx sequence. Furthermore, channel estimation and the interaction of channel estimation and the compensation of the pulse blanking impact have to be investigated in future work. A promising approach seems to be the joint estimation of the Tx sequence and the channel coefficients according to the same principle as frequency offsets and the channel coefficients are estimated in OFDM systems [95, 96].

## 6.4 Conclusions and Outlook

All in all, the investigations in this thesis have shown, that mutual interference in OFDM based systems constitutes a design challenge. However, with the proposed methods mutual interference can be reduced considerably such that an operation of the OFDM system in such interference conditions seems to be feasible hence making OFDM based overlay systems a promising solution for increasing spectral efficiency.

OFDM based overlay systems or cognitive radio in general are emerging topics of current research activities that already result in first steps towards a realisation. For example, IEEE working group 802.22 is chartered with the development of a cognitive radio based wireless regional area network (WRAN) for use by license-exempt devices on a non-interfering basis in spectrum that is allocated to the TV broadcast service [99]. The physical layer of the WRAN, OFDM or OFDMA are envisaged due to their high spectral efficiency and flexibility. Another example is the B-AMC system which is a promising candidate for the future L-band digital aeronautical communication system (L-DACS). Before selecting one system for the L-DACS, the theoretical co-existence study has to be verified by laboratory measurements to proof the feasibility of the B-AMC inlay concept.

In parallel to the technological investigations, regulatory bodies are rethinking their strict frequency assignments such indicating that the development of overlay systems is also initiated on the regulatory and political side [9].

# A Derivation of Subcarrier Spectrum

All advanced techniques for reducing out-of-band radiation presented in Chapter 3 require a representation of the Tx spectrum that is as realistic as possible. The spectral shape of the OFDM signal is basically determined by the IDFT that induces a periodicity and by the window applied to shape individual OFDM symbols. Both influencing factors are considered when deriving the subcarrier spectra in the following. Moreover, different window shapes are considered, namely the commonly used rectangular window and the raised-cosine window used for improving the spectral characteristics of each subcarrier.

The time domain OFDM signal  $x[k]$ ,  $k = 0, \dots, N-1$ , is obtained by transforming the vector of complex symbols  $\mathbf{d} = [d_0, \dots, d_n, \dots, d_{N-1}]$  to be transmitted on the  $N$  subcarriers to the time domain by means of an  $N$ -point IDFT resulting in

$$x[k] = \text{IDFT}\{d_n\} = \frac{1}{N} \sum_{n=0}^{N-1} d_n \exp\left(j \frac{2\pi nk}{N}\right). \quad (\text{A.1})$$

Recalling that the OFDM signal is composed of  $N$  subcarrier signals denoted by  $x_n[k]$ , (A.1) can be rewritten as

$$x[k] = \frac{1}{N} \sum_{n=0}^{N-1} x_n[k] \quad (\text{A.2})$$

with the  $n$ th subcarrier signal

$$x_n[k] = d_n \exp\left(j \frac{2\pi nk}{N}\right). \quad (\text{A.3})$$

As a property of the DFT, the output of the IDFT is an unlimited periodically repeated signal with periodicity  $N$ . To cut out one OFDM symbol, a window  $w[k]$  with length corresponding to one OFDM symbol including cyclic prefix (CP) and if required cyclic suffix (CS) is applied. Afterwards, one OFDM symbol in the time domain writes

$$x'[k] = \begin{cases} w[k] \cdot x[k] & k = -N_{\text{CP}}, \dots, N + N_{\text{CS}} - 1 \\ 0 & \text{otherwise.} \end{cases} \quad (\text{A.4})$$

The spectrum is obtained by transforming the resulting OFDM signal to the frequency domain resulting in

$$X'[n] = \text{DFT}\{x'[k]\}. \quad (\text{A.5})$$

Analogously, the spectrum of the  $n$ th subcarrier is obtained by applying the window  $w[k]$  to  $x_n[k]$  and transforming the resulting subcarrier signal  $x'_n[k]$  to the frequency domain.

To obtain a higher resolution of the spectrum, the discrete-time Fourier transform (DTFT) is introduced [72, 100]. The input is a discrete time domain signal of infinite length that has been obtained by sampling a continuous time domain signal at time instances  $k/f_s$  with  $k \in \mathbb{N}$  and sampling frequency  $f_s$ . After applying the DTFT, a continuous frequency domain representation  $X(e^{j\Omega})$  of the input sequence is obtained that equals

$$X(e^{j\Omega}) = \text{DTFT}\{x[k]\} = \sum_{k=-\infty}^{\infty} x[k]e^{-j\Omega k} \quad (\text{A.6})$$

with the normalised angular frequency  $\Omega = 2\pi f/f_s$ . The continuous frequency domain signal  $X(e^{j\Omega})$  is periodic with  $\Omega$  and cycle length  $2\pi$ . Since usually the input sequence  $x[k]$  is not infinite but limited to the interval  $[0, N-1]$ , (A.6) can be simplified to

$$X(e^{j\Omega}) = \sum_{k=0}^{N-1} x[k]e^{-j\Omega k}. \quad (\text{A.7})$$

Discretising the DTFT by setting  $\Omega$  to the subcarrier frequencies, i.e.  $\Omega = 2\pi n/N$ ,  $n = 0, \dots, N-1$ , the DFT as defined in (2.15) is obtained. From that relationship between DFT and DTFT, it can be concluded that the DTFT and the DFT have the same properties, also with respect to periodicity. This makes the DTFT an appropriate means for representing the subcarrier spectra with higher resolution while maintaining their actual characteristics.

With the DTFT, the spectrum of the  $\nu$ th subcarrier is determined from the windowed time domain signal  $x'_\nu[k]$  by

$$S_\nu(e^{j\Omega}) = \text{DTFT}\{x'_\nu[k]\}. \quad (\text{A.8})$$

Since the methods for sidelobe suppression from Chap. 3 employ a discrete signal with high resolution rather than a continuous frequency domain signal, the subcarrier spectrum is discretised using  $V$ -times over-sampling. The normalised angular



frequency is discretised to  $\Omega = 2\pi n/V/N$  resulting in  $S_\nu[n]$ ,  $n = 0, \dots, VN - 1$ . Note, in order to avoid confusion of the frequency and the subcarrier index, the frequency index is denoted by  $n$  while the subcarrier index is denoted by  $\nu$ , where  $n = \nu$  for  $V = 1$ .

## A.1 Subcarrier Spectrum after Rectangular Tx Windowing

In most common OFDM systems, a rectangular window is applied to cut out one OFDM symbol of the data stream. Taking into account a CP forming the GI comprising  $N_{\text{GI}}$  samples, the window is defined as

$$w[k] = \text{rect}[k] = \begin{cases} 1 & k = -N_{\text{GI}}, \dots, N - 1 \\ 0 & \text{otherwise.} \end{cases} \quad (\text{A.9})$$

After applying the rectangular window to the time domain signal at the output of the IDFT

$$x'_\nu[k] = \begin{cases} d_\nu \exp(j2\pi\nu k/N) & k = -N_{\text{GI}}, \dots, N - 1 \\ 0 & \text{otherwise} \end{cases} \quad (\text{A.10})$$

is obtained.

The equivalent continuous frequency domain signal is obtained by using the DTFT resulting in

$$\begin{aligned} S_\nu(e^{j\Omega}) &= \text{DTFT}\{x'_\nu[k]\} \\ &= d_\nu \sum_{k=-N_{\text{GI}}}^{N-1} \exp(-jk(\Omega - \Omega_\nu)) \end{aligned} \quad (\text{A.11})$$

with the frequency of the  $\nu$ th subcarrier denoted by  $\Omega_\nu = 2\pi\nu/N$ . Since the sum in (A.11) is a geometric series, (A.11) can be rewritten and simplified to

$$\begin{aligned} S_\nu(e^{j\Omega}) &= e^{jN_{\text{GI}}(\Omega - \Omega_\nu)} \frac{1 - e^{j(\Omega - \Omega_\nu)(N + N_{\text{GI}})}}{1 - e^{j(\Omega - \Omega_\nu)}} \\ &= d_\nu \exp\left(-j(\Omega - \Omega_\nu) \frac{N - N_{\text{GI}} - 1}{2}\right) \cdot \frac{\sin\left(\frac{N + N_{\text{GI}}}{2}(\Omega - \Omega_\nu)\right)}{\sin\left(\frac{1}{2}(\Omega - \Omega_\nu)\right)}. \end{aligned} \quad (\text{A.12})$$

The discretisation of (A.12) using  $V$ -times over-sampling yields

$$S_\nu[n] = d_\nu \exp\left(-j\pi(n/V - \nu)\frac{N - N_{\text{GI}} - 1}{N}\right) \cdot \frac{\sin(\pi(N + N_{\text{GI}})(n/V - \nu)/N)}{\sin(\pi(n/V - \nu)/N)}, \quad n = 0, \dots, V \cdot N - 1. \quad (\text{A.13})$$

For  $N \rightarrow \infty$ , (A.13) becomes the well-known si-spectrum. However, to obtain a more realistic representation of the Tx spectrum, the periodicity of the DFT operation has to be considered. In that case, the subcarrier spectra also become periodic with cycle duration corresponding to the DFT length.

## A.2 Subcarrier Spectrum after Tx Windowing

To improve the spectral characteristics of the subcarrier spectra, the rectangular window is replaced by a raised-cosine (rc) window for cutting out OFDM symbols of the infinite data stream. The rc window is defined as

$$w[k] = \begin{cases} \frac{1}{2} \left(1 - \cos\left(\frac{\pi}{N_w} (k + N_{\text{GI}} + N_w)\right)\right) & k = -N_w - N_{\text{GI}}, \dots, -N_{\text{GI}} - 1 \\ 1 & k = -N_{\text{GI}}, \dots, N - 1 \\ \frac{1}{2} \left(1 - \cos\left(\frac{\pi}{N_w} (k - N - N_w + 1)\right)\right) & k = N, \dots, N + N_w - 1 \\ 0 & \text{otherwise,} \end{cases} \quad (\text{A.14})$$

where the roll-off factor of the window is chosen such that  $N_w$  samples lie in the roll-off region of the window as depicted in Fig. 3.1.

Same as for the rectangular window, the spectrum of the  $\nu$ th subcarrier is obtained by applying the DTFT to the windowed signal  $x'_\nu[k]$  of the  $\nu$ th subcarrier resulting in

$$\begin{aligned} S_\nu(e^{j\Omega}) &= \text{DTFT}\{x'_\nu[k]\} \\ &= d_\nu e^{j(\Omega - \Omega_\nu)/2} \cdot \left[ e^{-j(\Omega - \Omega_\nu)(N - N_{\text{GI}})/2} \cdot \frac{\sin((N + N_{\text{GI}})/2(\Omega - \Omega_\nu))}{\sin(1/2(\Omega - \Omega_\nu))} \right. \\ &\quad \left. + \frac{1}{2} \frac{\sin(N_w/2(\Omega - \Omega_\nu))}{\sin(1/2(\Omega - \Omega_\nu))} \right] \end{aligned} \quad (\text{A.15})$$

$$\begin{aligned}
& \cdot \left( -e^{-j(\Omega-\Omega_\nu)(N_w/2+N)} + e^{j(\Omega-\Omega_\nu)(N_w/2+N_{GI})} \right) \\
& + \frac{j \sin(N_w/2(\Omega - \Omega_\nu - \pi/N_w))}{4 \sin(1/2(\Omega - \Omega_\nu - \pi/N_w))} \\
& \cdot \left( e^{-j(\Omega-\Omega_\nu)(N_w/2+N)+j\pi/(2N_w)} - e^{j(\Omega-\Omega_\nu)(N_w/2+N_{GI})-j\pi/(2N_w)} \right) \\
& + \frac{j \sin(N_w/2(\Omega - \Omega_\nu + \pi/N_w))}{4 \sin(1/2(\Omega - \Omega_\nu + \pi/N_w))} \\
& \cdot \left( -e^{-j(\Omega-\Omega_\nu)(N_w/2+N)-j\pi/(2N_w)} + e^{j(\Omega-\Omega_\nu)(N_w/2+N_{GI})+j\pi/(2N_w)} \right) \Big]
\end{aligned}$$

After discretisation employing  $V$ -times over-sampling, the  $\nu$ th subcarrier spectrum yields

$$\begin{aligned}
S_\nu[n] &= d_\nu e^{j\pi(n/V-\nu)/N} \tag{A.16} \\
& \cdot \left[ e^{-j\pi(n/V-\nu)(N-N_{GI})/N} \cdot \frac{\sin(\pi(N+N_{GI})/N(n/V-\nu))}{\sin(\pi/N(n/V-\nu))} \right. \\
& + \frac{1 \sin(\pi N_w/N(n/V-\nu))}{2 \sin(\pi/N(n/V-\nu))} \\
& \cdot \left( -e^{-j\pi(n/V-\nu)(N_w/2+N)/N} + e^{j\pi(n/V-\nu)(N_w/2+N_{GI})/N} \right) \\
& + \frac{j \sin(\pi N_w/N(n/V-\nu-N/(2N_w)))}{4 \sin(\pi/N(n/V-\nu-N/(2N_w)))} \\
& \cdot \left( e^{-j\pi((n/V-\nu)(N_w/2+N)/N-1/(2N_w))} - e^{j\pi((n/V-\nu)(N_w/2+N_{GI})/N-1/(2N_w))} \right) \\
& + \frac{j \sin(\pi N_w/N(n/V-\nu+N/(2N_w)))}{4 \sin(\pi/N(n/V-\nu+N/(2N_w)))} \\
& \cdot \left. \left( -e^{-j\pi((n/V-\nu)(N_w/2+N)/N+1/(2N_w))} + e^{j\pi((n/V-\nu)(N_w/2+N_{GI})/N+1/(2N_w))} \right) \right].
\end{aligned}$$



# B Derivation of Leakage Effect

For reasons of simplicity a carrier signal, i.e. a complex exponential sequence, is regarded as an example of an interference signal. The interference signal in the time domain is obtained by sampling the received interference signal with the sampling frequency  $f_s$  of the OFDM system

$$i[k] = i(k/f_s) = A[k] \cdot \exp\left(jk \frac{2\pi n_c}{N} + j\vartheta_0\right), \quad (\text{B.1})$$

where  $k = 0, \dots, P \cdot (N + N_{\text{GI}}) - 1$ , when the interference signal is regarded for the duration corresponding to one OFDM frame. Of the Rx data stream fractions of  $N$  samples are cut out by means of a rectangular window of the same length. At the same time, the GI is removed by skipping the first  $N_{\text{GI}}$  samples belonging to each OFDM symbol. This operation including GI removal can be written as

$$\begin{aligned} i_p[k] &= \text{rect}[k] \cdot i[k + N_{\text{GI}}] \\ &= A_p \cdot \exp\left(jk \frac{2\pi n_c}{N} + j\varphi_p\right), \quad k = 0, \dots, N - 1, \end{aligned} \quad (\text{B.2})$$

with  $\text{rect}[k]$  denoting the rectangular window from (4.6) and phase

$$\varphi_p = \vartheta_0 + (p + 1) \frac{2\pi N_{\text{GI}} n_c}{N}. \quad (\text{B.3})$$

The phase shift  $(p + 1) \frac{2\pi N_{\text{GI}} n_c}{N}$  between consecutive OFDM symbols is introduced when removing the GI of length  $N_{\text{GI}}$ .

At the OFDM Rx, the interference signal  $i_p[k]$  coinciding with the  $p$ th OFDM symbol is transformed to the frequency domain by means of an  $N$ -point DFT as defined in (2.15). The resulting frequency domain interference signal  $I_p[n]$  equals

$$\begin{aligned} I_p[n] &= \sum_{k=0}^{N-1} i_p[k] \exp\left(-j \frac{2\pi kn}{N}\right) \\ &= \sum_{k=0}^{N-1} A_p \cdot \exp\left(j \frac{2\pi kn_c}{N} + j\varphi_p\right) \exp\left(-j \frac{2\pi kn}{N}\right) \\ &= A_p \exp(j\varphi_p) \sum_{k=0}^{N-1} \exp\left(-j \frac{2\pi k(n - n_c)}{N}\right). \end{aligned} \quad (\text{B.4})$$

The sum in (B.4) is a geometric series and hence can be rewritten as

$$\begin{aligned}
 I_p[n] &= A_p e^{j\varphi_p} \frac{1 - \exp(-j2\pi(n_c - n))}{1 - \exp(-j2\pi(n_c - n)/N)} \\
 &= A_p e^{j\varphi_p} \frac{e^{-j\pi(n_c - n)/N}}{e^{-j\pi(n_c - n)}} \frac{e^{j\pi(n_c - n)} - e^{-j\pi(n_c - n)}}{e^{j\pi(n_c - n)/N} - e^{-j\pi(n_c - n)/N}} \\
 &= A_p e^{-j\pi(n - n_c) \frac{N-1}{N} + j\varphi_p} \frac{e^{j\pi(n_c - n)} - e^{-j\pi(n_c - n)}}{e^{j\pi(n_c - n)/N} - e^{-j\pi(n_c - n)/N}}.
 \end{aligned} \tag{B.5}$$

According to Euler's formula, the fraction in (B.5) can be replaced by sines resulting in

$$I_p[n] = A_p \cdot \exp\left(-j\pi(n - n_c) \frac{N-1}{N} + j\varphi_p\right) \cdot \frac{\sin(\pi(n - n_c))}{\sin(\pi/N(n - n_c))}. \tag{B.6}$$

The frequency domain interference signal from (B.6) is a convolution of the carrier signal with an si-function which is a result of the multiplication of the time domain interference signal with a rectangular window. Spectral leakage is caused when the interference signal is sampled at positions, that are not integer multiples of the carrier frequency  $n_c$  of the interferer, i.e. when  $n - n_c \notin \mathbb{N}$ .

# C Derivation of MMSE Approach for NBI Mitigation

Frequency domain NBI mitigation techniques aim at minimising the MSE between the actual interference spectrum and the estimated interference spectrum, i.e.

$$E\{\mathbf{e}^{\text{MMSE}}\} = E\{\|\mathbf{I} - \hat{\mathbf{I}}^{\text{MMSE}}\|^2\} \rightarrow \min, \quad (\text{C.1})$$

where  $\mathbf{I}$  and  $\hat{\mathbf{I}}^{\text{MMSE}}$  represent the interference signal and the estimated interference signal on one entire OFDM frame, respectively. In contrast to the simple subtraction of an estimated interference signal, for leakage compensation an MMSE estimate of the interference signal is subtracted which is generated by multiplying a compensation matrix  $\mathbf{C}_{\text{NBI}}$  with measurements of the actual interference signal collected in  $\mathbf{I}_0$

$$\hat{\mathbf{I}}^{\text{MMSE}} = \mathbf{C}_{\text{NBI}} \cdot (\mathbf{I}_0 + \mathbf{N}). \quad (\text{C.2})$$

As the measurements on the observation subcarriers are affected by channel noise, channel noise with variance  $\sigma_n^2$  has to be taken into account. The noise samples on all  $N$  subcarriers and all  $P$  OFDM symbols of an OFDM frame are collected in the matrix  $\mathbf{N}$ . Substituting (C.2) in (C.1), dissolving the quadratic term and reorganising the estimation values, one obtains

$$\begin{aligned} E\{\mathbf{e}^{\text{MMSE}}\} &= E\{\|\mathbf{I} - \mathbf{C}_{\text{NBI}} \cdot (\mathbf{I}_0 + \mathbf{N})\|^2\} \\ &= E\{\mathbf{I}\mathbf{I}^H - \mathbf{I}\mathbf{I}_0^H \mathbf{C}_{\text{NBI}}^H - \mathbf{I}\mathbf{N}^H \mathbf{C}_{\text{NBI}}^H - \mathbf{C}_{\text{NBI}}\mathbf{I}_0\mathbf{I}^H \\ &\quad + \mathbf{C}_{\text{NBI}}\mathbf{I}_0\mathbf{I}_0^H \mathbf{C}_{\text{NBI}}^H + \mathbf{C}_{\text{NBI}}\mathbf{I}_0\mathbf{N}^H \mathbf{C}_{\text{NBI}}^H - \mathbf{C}_{\text{NBI}}\mathbf{N}\mathbf{I}^H \\ &\quad + \mathbf{C}_{\text{NBI}}\mathbf{N}\mathbf{I}_0^H \mathbf{C}_{\text{NBI}}^H + \mathbf{C}_{\text{NBI}}\mathbf{N}\mathbf{N}^H \mathbf{C}_{\text{NBI}}^H\} \\ &= E\{\mathbf{I}\mathbf{I}^H\} - E\{\mathbf{I}\mathbf{I}_0^H\} \mathbf{C}_{\text{NBI}}^H - E\{\mathbf{I}\mathbf{N}^H\} \mathbf{C}_{\text{NBI}}^H - \mathbf{C}_{\text{NBI}} E\{\mathbf{I}_0\mathbf{I}^H\} \\ &\quad + \mathbf{C}_{\text{NBI}} E\{\mathbf{I}_0\mathbf{I}_0^H\} \mathbf{C}_{\text{NBI}}^H + \mathbf{C}_{\text{NBI}} E\{\mathbf{I}_0\mathbf{N}^H\} \mathbf{C}_{\text{NBI}}^H - \mathbf{C}_{\text{NBI}} E\{\mathbf{N}\mathbf{I}^H\} \\ &\quad + \mathbf{C}_{\text{NBI}} E\{\mathbf{N}\mathbf{I}_0^H\} \mathbf{C}_{\text{NBI}}^H + \mathbf{C}_{\text{NBI}} E\{\mathbf{N}\mathbf{N}^H\} \mathbf{C}_{\text{NBI}}^H\}. \end{aligned} \quad (\text{C.3})$$

As there is no correlation between noise and the interference signal, the terms  $E\{\mathbf{I}\mathbf{N}^H\}$ ,  $E\{\mathbf{I}_0\mathbf{N}^H\}$ ,  $E\{\mathbf{N}\mathbf{I}^H\}$ , and  $E\{\mathbf{N}\mathbf{I}_0^H\}$  vanish. Defining the correlation ma-

trices

$$\mathcal{R}_{\text{II}} := \text{E}\{\mathbf{I}\mathbf{I}^H\} \quad (\text{C.4})$$

$$\mathcal{R}_{\text{I}_o\text{I}_o} := \text{E}\{\mathbf{I}_o\mathbf{I}_o^H\} \quad (\text{C.5})$$

$$\mathcal{R}_{\text{I}_o\text{I}} := \text{E}\{\mathbf{I}_o\mathbf{I}^H\} \quad (\text{C.6})$$

$$\mathcal{R}_{\text{II}_o} := \text{E}\{\mathbf{I}\mathbf{I}_o^H\} \quad (\text{C.7})$$

and

$$\text{E}\{\mathbf{N}\mathbf{N}^H\} = \sigma_n^2 \mathbf{E}_{N_L}, \quad (\text{C.8})$$

where  $\mathbf{E}_{N_L}$  denotes the  $(N_L \times N_L)$  dimensional identity matrix, (C.3) can be written as

$$\text{E}\{\mathbf{e}^{\text{MMSE}}\} = \mathcal{R}_{\text{II}} - \mathcal{R}_{\text{II}_o} \mathbf{C}_{\text{NBI}}^H - \mathbf{C}_{\text{NBI}} \mathcal{R}_{\text{I}_o\text{I}} + \mathbf{C}_{\text{NBI}} (\mathcal{R}_{\text{I}_o\text{I}_o} + \sigma_n^2 \mathbf{E}_{N_L}) \mathbf{C}_{\text{NBI}}^H. \quad (\text{C.9})$$

After completing the square one obtains

$$\begin{aligned} \text{E}\{\mathbf{e}^{\text{MMSE}}\} &= (\mathbf{C}_{\text{NBI}} (\mathcal{R}_{\text{I}_o\text{I}_o} + \sigma_n^2 \mathbf{E}_{N_L}) - \mathcal{R}_{\text{II}_o}) (\mathcal{R}_{\text{I}_o\text{I}_o} + \sigma_n^2 \mathbf{E}_{N_L})^{-1} (\text{C.10}) \\ &\quad ((\mathcal{R}_{\text{I}_o\text{I}_o} + \sigma_n^2 \mathbf{E}_{N_L}) \mathbf{C}_{\text{NBI}}^H - \mathcal{R}_{\text{I}_o\text{I}}) \\ &\quad - \mathcal{R}_{\text{II}_o} (\mathcal{R}_{\text{I}_o\text{I}_o} + \sigma_n^2 \mathbf{E}_{N_L}) \mathcal{R}_{\text{I}_o\text{I}} + \mathcal{R}_{\text{II}} \\ &\stackrel{!}{=} \mathbf{0}_N, \end{aligned}$$

where  $\mathbf{0}_N$  denotes a  $(N \times N)$  dimensional matrix containing all zeros. The error between the actual and the estimated interference signal according to (C.10) becomes minimal if the terms depending on the compensation matrix vanish, i.e.

$$\begin{aligned} \mathbf{C}_{\text{NBI}} (\mathcal{R}_{\text{I}_o\text{I}_o} + \sigma_n^2 \mathbf{E}_{N_L}) - \mathcal{R}_{\text{II}_o} &= \mathbf{0}_{N \times N_L} \quad (\text{C.11}) \\ \vee (\mathcal{R}_{\text{I}_o\text{I}_o} + \sigma_n^2 \mathbf{E}_{N_L}) \mathbf{C}_{\text{NBI}}^H - \mathcal{R}_{\text{I}_o\text{I}} &= \mathbf{0}_{N \times N_L}. \end{aligned}$$

Solving (C.11) for  $\mathbf{C}_{\text{NBI}}$ , the compensation matrix is obtained as

$$\mathbf{C}_{\text{NBI}} = \mathcal{R}_{\text{II}_o} \cdot (\mathcal{R}_{\text{I}_o\text{I}_o} + \sigma_n^2 \mathbf{E}_{N_L})^{-1}. \quad (\text{C.12})$$



# Abbreviations and Definitions

## Abbreviations

ACF	Autocorrelation Function	86
A/D	Analogue-to-Digital	8
ADSL	Asymmetric Digital Subscriber Line	5
ATC	Air Traffic Control	16
AV	Allocation Vector	11
AWGN	Additive White Gaussian Noise	8
BER	Bit Error Rate	23
B-AMC	Broadband Aeronautical Multi-Carrier Communications	16
B-VHF	Broadband VHF Aeronautical Communications System based on MC-CDMA	16
CC	Cancellation Carriers	36
CDF	Cumulative Distribution Function	54
CDMA	Code-Division Multiple-Access	18
CP	Cyclic Prefix	12
CS	Cyclic Suffix	12
CSMA	Carrier Sense Multiple-Access	11
D/A	Digital-to-Analogue	8
DFT	Discrete Fourier Transform	4
DME	Distance Measuring Equipment	20
DSB-AM	Double-Sideband Amplitude Modulation	16
DSL	Digital Subscriber Line	57
DVB-T	Digital Video Broadcasting - Terrestrial	2
DTFT	Discrete-Time Fourier Transform	166
FAA	Federal Aviation Administration	17
FDD	Frequency-Division Duplex	19
FDMA	Frequency-Division Multiple-Access	11
FFT	Fast Fourier Transform	9
FL	Forward Link	18
GI	Guard Interval	7
GSVD	Generalised Singular Value Decomposition	38
ICAO	International Civil Aviation Organization	191

ICI	Inter-Carrier Interference	6
IDFT	Inverse Discrete Fourier Transform	7
IEEE	Institute of Electrical and Electronic Engineers	2
IFFT	Inverse Fast Fourier Transform	7
INR	Interference-to-Noise Ratio	90
ISI	Inter-Symbol Interference	7
JTIDS	Joint Tactical Information Distribution System	20
L-DACS	L-band Digital Aeronautical Communication System	164
LOS	Line-of-Sight	106
LP	Low-Pass (Filter)	121
MC- CDMA	Multi-Carrier Code-Division Multiple-Access	18
MCS	Multiple-Choice Sequences	34
MIDS	Multi-functional Information Distribution System	20
MMSE	Minimum Mean Square Error	76
NBI	Narrow-Band Interference	4
OFDM	Orthogonal Frequency-Division Multiplexing	2
OFDMA	Orthogonal Frequency-Division Multiple-Access	18
PAPR	Peak-to-Average Power Ratio	34
PDF	Probability Density Function	105
ppps	pulse pairs per second	125
PSD	Power Spectral Density	80
QAM	Quadrature Amplitude Modulation	18
QPSK	Quadrature Phase-Shift Keying	18
rc	raised-cosine	25
RF	Radio Frequency	8
RFI	Radio Frequency Interference	189
RL	Reverse Link	18
Rx	Receiver	8
SINR	Signal-to-Interference-and-Noise Ratio	125
SNR	Signal-to-Noise Ratio	33
SSR	Secondary Surveillance Radar	20
SW	Subcarrier Weighting	30
TACAN	Tactical Air Navigation	20
TDD	Time-Division Duplex	18
TDMA	Time-Division Multiple-Access	11
Tx	Transmitter	8

UAT	Universal Access Transceiver	20
UMTS	Universal Mobile Telecommunication System	121
VDL	VHF Digital Link	16
VDSL	Very-high-speed Digital Subscriber Line	57
VHF	Very High Frequency	16
WLAN	Wireless Local Area Network	2
WRAN	Wireless Regional Area Network	164
WSSUS	Wide Sense Stationary Uncorrelated Scattering	106

## Notation

### Operators

$(\cdot)^*$	conjugate complex
$(\cdot)^{-1}$	inverse of a matrix
$(\cdot)^H$	Hermitian matrix
$(\cdot)^T$	transpose of a vector or a matrix
$f * g$	linear convolution of $f$ and $g$
$ \cdot $	absolute value
$\ \cdot\ $	$L^2$ -norm of a vector or matrix
$\lfloor \cdot \rfloor$	flooring operation
$\lceil \cdot \rceil$	ceiling operation
$(\cdot)$	estimation
$\arg\{\cdot\}$	argument of a complex number
$\delta(t)$	Dirac's delta function
$\det\{\cdot\}$	determinant of a matrix
$E\{\cdot\}$	expected value
$\exp(\cdot)$	exponential function
$\text{Im}\{\cdot\}$	imaginary part of a complex number
$\text{Re}\{\cdot\}$	real part of a complex number
$\text{tr}\{\cdot\}$	trace of a matrix

### Symbols

$\mathbf{0}_N$	$(N \times N)$ dimensional zero matrix
----------------	--

$A$	amplitude of interference signal
$\hat{A}$	estimated amplitude of interference signal
$A_i^{\text{DME}}$	amplitude of $i$ th DME interferer
$A_p$	amplitude of interference signal on $p$ th OFDM symbol
$A^{\text{voice}}$	amplitude of voice part of interference signal
$A^{\text{norm}}$	normalisation factor
$B$	signal bandwidth
$B_{p,b}^l$	lower bound of $b$ th notch in $p$ th OFDM symbol
$B_{p,b}^u$	upper bound of $b$ th notch in $p$ th OFDM symbol
$b$	index of notch
$b^{\text{DME}}(t)$	unmodulated DME signal
$b^{\text{voice}}(t)$	filtered, bandlimited voice signal
$C_p$	ratio of interference amplitudes on observation subcarriers in $p$ th OFDM symbol
$\mathbf{C}_{\text{NBI}}$	compensation matrix
$c$	cancellation carrier index
$D$	throughput in bit per second
$D^{\text{loss}}$	throughput loss in %
$d$	index of delayed path
$d_\nu$	complex data symbol transmitted on $\nu$ th subcarrier
$d'_\nu$	modified complex data symbol transmitted on $\nu$ th subcarrier
$\mathbf{E}_M$	$(M \times M)$ dimensional identity matrix
$e^{\text{MSE}}$	mean square error
$e_m$	index of $m$ th complex symbol in the symbol constellation
$F^{\text{AA}}(f)$	filter characteristic of anti-aliasing filter
$F^{\text{LP}}[n]$	filter characteristic of digital low-pass filter
$F^{\text{RF}}(f)$	filter characteristic of Rx filter
$f$	continuous frequency variable
$f_{c,i}$	carrier frequency of $i$ th interferer in Hz
$f_{\text{offset}}$	frequency offset in Hz
$f_s$	sampling frequency in Hz

$f_h^{\text{sb}}$	frequency of $h$ th sinusoidal tone contained in DSB-AM sidebands in Hz
$\Delta f$	subcarrier spacing in Hz
<b>G</b>	diagonal matrix with weighting factors for SW
$g_{\text{min}}$	lower bound of subcarrier weights
$g_{\text{max}}$	upper bound of subcarrier weights
<b>g</b>	weighting factors for cancellation carriers
$H_p[n]$	frequency domain channel coefficients for $n$ th subcarrier of $p$ th OFDM symbol
$h$	index of sinusoidal tone contributing to DSB-AM sidebands
$h_p[k]$	$k$ th sample of the channel impulse response affecting the $p$ th OFDM symbol
<b>I</b>	$(P \times N)$ dimensional matrix of received interference signal in the frequency domain
$\hat{\mathbf{I}}$	$(P \times N)$ dimensional matrix of estimated interference signal in the frequency domain
$\hat{\mathbf{I}}^{\text{MMSE}}$	$(P \times N_L)$ dimensional matrix of MMSE estimation of interference signal in the frequency domain
$\mathbf{I}_o$	$(P \times N_L)$ dimensional matrix containing interference signal on observation subcarriers
$I^{\text{filt}}(f)$	filtered interference signal in the frequency domain
$i$	interferer index
$i(t)$	interference signal in continuous time domain
$i^{\text{filt}}(t)$	filtered interference signal in continuous time domain
$i[k]$	samples of interference signal in the time domain
$i_p[k]$	samples of interference signal in the time domain on $p$ th OFDM symbol
$i'_p[k]$	samples of interference signal in the time domain on $p$ th OFDM symbol with extended CP
$i_p^{\text{carrier}}[k]$	samples of carrier of interference signal in the time domain on $p$ th OFDM symbol
$i_p^{\text{sb}}[k]$	samples of sidebands of interference signal in the time domain on $p$ th OFDM symbol

$j$	$= \sqrt{-1}$ , imaginary unit
$k$	index of time domain samples
$l$	observation subcarrier index
$M$	size of modulation alphabet
$m$	index of used subcarriers
$N$	number of subcarriers in DFT/FFT bandwidth
$N_B$	number of notches
$N_{CC}$	number of cancellation carriers at each edge of the spectrum
$N_{CP}$	length of cyclic prefix in samples
$N_{CS}$	length of cyclic suffix in samples
$N_D$	number of delayed paths of multi-path channel
$N_{\text{eff}}$	effective length of OFDM symbol in samples
$N_{\text{FFT}}$	FFT length
$N_{\text{GI}}$	length of guard interval in samples
$N_H$	number of sinusoidal tones contributing to DSB-AM sidebands
$N_I$	number of interferers
$N_K$	number of samples in the optimisation range
$N_L$	number of observation subcarriers per channel
$N_p[n]$	noise on $n$ th subcarrier of $p$ th OFDM symbol
$N_{U,i}$	number of pulse pairs of $i$ th interferer per time interval
$N_{\text{used}}$	number of used subcarriers
$N_w$	number of samples in roll-off region of Tx window
$n$	index of frequency domain samples
$n_c$	discrete carrier frequency
$n_{c,i}$	discrete carrier frequency of $i$ th interferer
$n_h^{\text{sb}}$	discrete frequency of $h$ th sinusoidal tone contained in DSB-AM sidebands
$n_p[k]$	time samples of AWGN on $p$ th OFDM symbol
$n_p^w[k]$	time samples of AWGN on $p$ th OFDM symbol after windowing

$n_h^{\text{sb}}$	discrete frequency of $h$ th sinusoidal tone contained in DSB-AM sidebands
$o_l$	position of $l$ th observation subcarrier
$P$	number of OFDM symbols per frame
$P_b$	bit error probability
$\mathcal{P}$	number of discrete phase shifts for MCS phase approach
$p$	index of OFDM symbol
$p[k]$	generic DME pulse in the time domain
$Q$	MCS set size
$\mathcal{Q}$	selected Tx sequence from MCS set
$q$	index of MCS sequence
$R_c$	code rate
$\mathbf{R}$	$(N \times P)$ dimensional matrix of received OFDM frame in frequency domain
$\mathbf{R}'$	$(N \times P)$ dimensional matrix of received OFDM frame after NBI mitigation in frequency domain
$\mathbf{R}_p$	$p$ th received OFDM symbol in frequency domain
$\mathbf{R}_p^{\text{comp}}$	$p$ th received OFDM symbol in the frequency domain after ICI compensation
$\mathbf{R}_p^{\text{w}}$	$p$ th received OFDM symbol in the frequency domain after Rx windowing
$\mathcal{R}_{\mathbf{I}_o \mathbf{I}_o}$	autocorrelation matrix of $\mathbf{I}_o$
$\mathcal{R}_{\mathbf{I}_o \mathbf{I}_o}$	cross-correlation matrix of $\mathbf{I}$ and $\mathbf{I}_o$
$r_p^{\text{ov}}[k]$	$k$ th time sample of $p$ th received over-sampled OFDM symbol after pulse blanking or clipping
$r_p^{\text{w}}[k]$	$k$ th time sample of $p$ th received OFDM symbol after Rx windowing
$r_{\text{ii}}[u - v]$	autocorrelation function of $i[u]$
$r_{\text{ip}}[u - v]$	cross-correlation function of $i[u]$ and $p[v]$
$S_\nu[n]$	$n$ th sample of spectrum of $\nu$ th subcarrier
$\hat{S}_\nu[n]$	estimation of $n$ th sample of spectrum of $\nu$ th subcarrier
$\mathbf{S}$	$(N_K \times N)$ matrix with $N_K$ samples of $N$ subcarrier spectra

$\mathbf{S}^{\text{sum}}$	$N_K$ -dimensional vector with samples of OFDM spectrum
$T_{\text{clip}}$	threshold for clipping
$T_{\text{GI}}$	length of guard interval in s
$T_{\text{O}}$	OFDM symbol duration in s
$T_{\text{PB}}$	threshold for pulse blanking
$T_{\text{S}}$	OFDM symbol duration incl. GI in s
$t$	continuous time variable
$\Delta t$	time interval in s
$u$	pulse pair index
$V$	over-sampling factor
$v_p[k]$	distorted part of OFDM Rx signal in the time domain containing noise and interference
$v_p^{\text{ov}}[k]$	distorted part of OFDM Rx signal in the time domain containing noise and interference, over-sampled
$w[k]$	samples of Tx or Rx window
$\bar{w}[k]$	samples of basic window shape
$w_p^{\text{PB}}[k]$	samples of pulse blanking window of $p$ th OFDM symbol
$X_p[n]$	Tx signal transmitted on $n$ th subcarrier on $p$ th OFDM symbol
$x_p[k]$	samples of Tx signal transmitted on $p$ th OFDM symbol
$Y_p^{\text{ov}}[n]$	desired part of the Rx signal on $n$ th subcarrier on $p$ th OFDM symbol
$y_p^{\text{ov}}[k]$	samples of desired part of $p$ th OFDM Rx symbol in the time domain, over-sampled
$Z$	number of bits transmitted per OFDM symbol
$z$	total number of blanked samples per OFDM symbol
$z_b$	number of blanked samples in $b$ th notch
$\alpha$	constraint for optimisation of CCs
$\beta$	roll-off factor of Tx window



$\gamma_b$	bit energy to noise density ratio $E_b/N_0$
$\gamma'_b$	bit energy to noise density ratio $E_b/N_0$ after SW
$\epsilon$	probability that subcarrier weight is at lower bound
$\varepsilon$	variance parameter for Gaussian DME pulse
$\eta$	modulation index of DSB-AM signal
$\vartheta_0$	starting phase
$\iota_m^{(q)}$	random integer used for generating $m$ th symbol in $q$ th MCS sequence
$\lambda$	Lagrange multiplier
$\mu$	number of samples in roll-off region of Rx window
$\nu$	subcarrier index
$\xi$	scaling factor representing impact of pulse blanking/clipping on the desired OFDM signal
$\mathbf{\Pi}^{(q)}$	permutation matrix of $q$ th MCS sequence
$\rho$	ratio of lower and upper bound for subcarrier weights
$\sigma_n^2$	noise variance
$\tau$	path delay of the channel in s
$\tau_d$	discrete path delay of $d$ th path
$\tau_{\max}$	maximum path delay of the channel
$\varphi$	phase variable
$\varphi_h^{\text{sb}}$	phase of $h$ th sinusoidal tone contained in DSB-AM sidebands in Hz

$\Psi$	sidelobe power in certain optimisation range
$\Psi_i^{\text{DME}}$	peak power of $i$ th DME interferer
$\Omega$	normalised angular frequency

# Bibliography

- [1] Federal Communications Commission (FCC), Office of Engineering and Technology, Policy and Rules Division, "FCC Online Table of Frequency Allocations," September 2008.
- [2] T. Erpek, K. Steadman, and D. Jones, "Dublin Ireland Spectrum Occupancy Measurements Collected On April 16-18, 2007," Tech. Rep., Shared Spectrum Company, November 2007.
- [3] T. Erpek, M. Lofquist, and K. Patton, "Spectrum Occupancy Measurements, Loring Commerce Centre Limestone, Maine, September 18-20, 2007," Tech. Rep., Shared Spectrum Company, 2007.
- [4] M.A. McHenry, D. McCloskey, D. Roberson, and J.T. MacDonald, "Spectrum Occupancy Measurements, Chicago, Illinois, November 16-18, 2005," Tech. Rep., Shared Spectrum Company, December 2005.
- [5] T. Weiss and F.K. Jondral, "Spectrum Pooling - An Innovative Strategy for the Enhancement of Spectrum Efficiency," *IEEE Communications Magazine*, vol. 42, no. 3, pp. S8–S14, March 2004.
- [6] Jens Zander, "Radio resource management in future wireless networks: requirements and limitations," *IEEE Communications Magazine*, vol. 35, no. 8, pp. 30–36, August 1997.
- [7] Eli M. Noam, "Taking the Next Step Beyond Spectrum Auctions: Open Spectrum Access," *IEEE Communications Magazine*, vol. 33, pp. 66–73, December 1995.
- [8] Shamik Sengupta and Mainak Chatterjee, "Designing Auction Mechanisms for Dynamic Spectrum Access," *Mobile Networks and Applications, Springer Netherlands*, vol. 13, no. 5, pp. 498–515, October 2008.
- [9] Federal Communications Commission (FCC) Spectrum Policy Task Force, "Report ET Docket no. 02-1935," November 2002.
- [10] J. Mitola III and G.Q. Maguire Jr., "Cognitive radio: Making software radios more personal," *IEEE Personal Communications*, vol. 6, pp. 13–18, August 1999.
- [11] J. Mitola, "Cognitive radio for flexible mobile multimedia communications," in *IEEE International Workshop on Mobile Multimedia Communications*, San Diego, CA, USA, November 1999, pp. 3–10.
- [12] Simon Haykin, "Cognitive Radio: Brain-Empowered Wireless Communications," *IEEE Journal on Selected Areas in Communications*, vol. 23, no. 2, pp. 201–220, February 2005.

- [13] IEEE, "802.11a standard, ISO/IEC 8802-11:1999/Amd 1:2000(E), High-Speed Physical Layer in the 5 GHz Band," 1999.
- [14] IEEE, "802.11g standard, Amendment 4: Further Higher Data Rate Extension in the 2.4 GHz Band," June 2003.
- [15] European Telecommunications Standards Institute (ETSI), "Digital Video Broadcasting (DVB); Framing structure, channel coding and modulation for digital terrestrial television," September 2008, EN 300 744, Version 1.6.1.
- [16] B.R. Saltzberg, "Performance of an Efficient Parallel Data Transmission System," *IEEE Transactions on Communication Technology*, vol. COM-15, pp. 805–811, December 1967.
- [17] R. W. Chang and R. A. Gibby, "A Theoretical Study of Performance of an Orthogonal Multiplexing Data Transmission Scheme," *IEEE Transactions on Communication Technology*, vol. COM-16, pp. 529–540, August 1968.
- [18] S. Weinstein and P. Ebert, "Data Transmission by Frequency-Division Multiplexing Using the Discrete Fourier Transform," *IEEE Transactions on Communications*, vol. 19, pp. 628–634, October 1971.
- [19] J.A.C. Bingham, "Multicarrier modulation for data transmission: an idea whose time has come," *IEEE Communications Magazine*, vol. 28, pp. 5–14, May 1990.
- [20] International Telecommunication Union, "Asymmetric digital subscriber line (ADSL) transceivers, ITU-T Recommendation G.992.1," June 1999.
- [21] K. Fazel and S. Kaiser, *Multi-Carrier and Spread Spectrum Systems*, John Wiley & Sons Ltd., 2003.
- [22] Danijela Cabric and Robert W. Brodersen, "Physical Layer Design Issues Unique to Cognitive Radio Systems," in *IEEE 16th International Symposium on Personal, Indoor and Mobile Radio Communications (PIMRC)*, Berlin, Germany, September 2005, pp. 759–763.
- [23] U. Berthold, S. Brandes, M. Schnell, and F.K. Jondral, "OFDM based Overlay Systems - A Promising Approach for Enhancing Spectral Efficiency," *IEEE Communications Magazine*, vol. 45, no. 12, pp. 52–58, December 2007.
- [24] Timo Weiss, Jörg Hillenbrand, and Friedrich Jondral, "A diversity approach for the detection of idle spectral resources in spectrum pooling systems," in *48th International Scientific Colloquium, TU Ilmenau*, Ilmenau, Germany, September 2003, p. CDROM.
- [25] Ulrich Berthold and Friedrich K. Jondral, "Guidelines for Designing OFDM Overlay Systems," in *Proceedings of the IEEE 1st International Symposium on New Frontiers in Dynamic Spectrum Access Networks (DySPAN '05)*, Baltimore (MD), USA, November 2005, pp. 626–629.

- [26] S. Brandes, U. Berthold, M. Schnell, and F.K. Jondral, "OFDM Based Overlay Systems - Design Challenges and Solutions," in *18th Annual IEEE International Symposium on Personal, Indoor and Mobile Radio Communications (PIMRC)*, Athens, Greece, September 2007, Invited Paper.
- [27] John A.C. Bingham, *ADSL, VDSL, and Multicarrier Modulation*, John Wiley & Sons, Inc., 2000.
- [28] T. Weiss, A. Krohn, and F. Jondral, "Synchronization Algorithms and Preamble Concepts in Spectrum Pooling Systems," in *IST Mobile and Wireless Telecommunications Summit*, Aveiro, Portugal, June 2003.
- [29] U. Berthold, *Dynamic Spectrum Access Using OFDM-based Overlay Systems*, Ph.D. thesis, Institut für Nachrichtentechnik, Universität Karlsruhe (TH), February 2008.
- [30] B-VHF project, "[www.b-vhf.org](http://www.b-vhf.org)," 2004.
- [31] Michael Schnell, Erik Haas, Christoph Rihacek, and Miodrag Sajatovic, "B-VHF - An Overlay System Concept for Future ATC Communications in the VHF Band," in *Proc. of 23th Digital Avionics Systems Conference (DASC 2004)*, Salt Lake City, UT, USA, October 2004.
- [32] Air Navigation Commission, "Report on the Results of the ITU World Radiocommunication Conference (2007) (WRC-07)," Tech. Rep., International Civil Aviation Organization (ICAO), December 2007.
- [33] M. Schnell, S. Brandes, S. Gligorevic, C.-H. Rokitansky, M. Ehammer, Th. Gräupl, C. Rihacek, and M. Sajatovic, "B-AMC - Broadband Aeronautical Multi-carrier Communications," in *8th Integrated Communications, Navigation, and Surveillance (ICNS) Conference*, Bethesda, MD, USA, May 2008.
- [34] Eurocontrol/Qinetiq, "Future Communications Infrastructure - Step 2: Technology Assessment Results, Version 1.0," Tech. Rep., October 2007.
- [35] B-VHF project, "VHF Channel Occupancy Measurements," Tech. Rep. D-12, B-VHF consortium, available at [www.b-vhf.org](http://www.b-vhf.org), February 2005.
- [36] B-VHF project, "Interference on the B-VHF Overlay System," Tech. Rep. D-09, B-VHF consortium, available at [www.b-vhf.org](http://www.b-vhf.org), October 2005.
- [37] S. Brandes, I. Cosovic, and M. Schnell, "Techniques for Ensuring Co-existence Between B-VHF and Legacy VHF Systems," in *2006 IEEE Aerospace Conference*, Big Sky, MT, USA, March 2006.
- [38] S. Brandes, M. Schnell, C.H. Rokitansky, M. Ehammer, Th. Gräupl, H. Steendam, M. Guenach, C. Rihacek, and B. Haindl, "B-VHF – Selected Simulation Results and Assessment," in *25th Digital Avionics Systems Conference (DASC 2006)*, Portland, OR, USA, October 2006.

- [39] S. Brandes, S. Gligorevic, M. Schnell, C.H. Rokitansky, M. Ehammer, Th. Gräupl, A. Schlereth, and C. Rihacek, "Final Assessment of the B-VHF Overlay Concept," in *2007 IEEE Aerospace Conference*, Big Sky, MT, USA, March 2007.
- [40] C.-H. Rokitansky, M. Ehammer, Th. Gräupl, M. Schnell, S. Brandes, S. Gligorevic, C. Rihacek, and M. Sajatovic, "B-AMC - Aeronautical Broadband Communication in the L-Band," in *First CEAS European Air and Space Conference*, Berlin, Germany, September 2007.
- [41] C.-H. Rokitansky, M. Ehammer, Th. Gräupl, M. Schnell, S. Brandes, S. Gligorevic, C. Rihacek, and M. Sajatovic, "B-AMC - A System for Future Broadband Aeronautical Multi-Carrier Communications in the L Band," in *26th Digital Avionics Systems Conference (DASC)*, Dallas, TX, USA, October 2007.
- [42] K. Panta and J. Armstrong, "Spectral Analysis of OFDM Signals and its Improvement by Polynomial Cancellation Coding," *IEEE Transactions on Consumer Electronics*, vol. 42, no. 4, pp. 939–943, November 2003.
- [43] I. Cosovic, S. Brandes, and M. Schnell, "Subcarrier Weighting - A Method for Side-lobe Suppression in OFDM Systems," *IEEE Communications Letters*, vol. 10, no. 6, pp. 444–446, June 2006.
- [44] I. Cosovic and T. Mazzoni, "Suppression of Sidelobes in OFDM Systems by Multiple-Choice Sequences," *European Transactions on Telecommunications (ETT)*, vol. 17, no. 6, pp. 623–630, June 2006.
- [45] S. Brandes, I. Cosovic, and M. Schnell, "Reduction of Out-of-Band Radiation in OFDM Systems by Insertion of Cancellation Carriers," *IEEE Communications Letters*, vol. 10, no. 6, pp. 420–422, June 2006.
- [46] R. van Nee and R. Prasad, *OFDM for Wireless Multimedia Communications*, Artech House Publishers, 2000.
- [47] P. Tan and N. C. Beaulieu, "Reduced ICI in OFDM Systems Using the "Better Than" Raised-Cosine Pulse," *IEEE Communications Letters*, vol. 8, no. 3, pp. 135–137, March 2004.
- [48] T. Magesacher, P. Ödling, and P.O. Börjesson, "Optimal intersymbol transmit windowing for multicarrier modulation," in *Proc. 7th Nordic Signal Processing Symposium (NORSIG 2006)*, Reykjavik, Iceland, June 2006, pp. 70–73.
- [49] Yuan-Pei Lin and See-May Phoong, "Window Design for DFT-Based Multicarrier Systems," *IEEE Transactions on Signal Processing*, vol. 53, no. 3, pp. 1015–1024, March 2005.
- [50] T. Weiss, J. Hillenbrand, A. Krohn, and F.K. Jondral, "Mutual interference in OFDM-based spectrum pooling systems," in *Proc. of IEEE 59th Semiannual Vehicular Technology Conference (VTC Spring '04)*, Milan, Italy, May 2004.

- [51] R. Fletcher, *Practical Methods of Optimization*, John Wiley & Sons Ltd., 2nd edition, 2000.
- [52] John G. Proakis, *Digital Communications*, McGraw-Hill, 4th edition, 2001.
- [53] I. Cosovic and V. Janardhanam, "Sidelobe Suppression in OFDM Systems," in *5th Intl. Workshop on Multi-Carrier Spread-Spectrum (MC-SS'05)*, Oberpfaffenhofen, Germany, September 2005, pp. 473–482.
- [54] R. Bäuml, R. Fischer, and J. Huber, "Reducing the Peak-to-Average Power Ratio of Multicarrier Modulation by Selected Mapping," *Electronics Letters*, vol. 32, no. 22, pp. 2056–2057, October 1996.
- [55] L.J. Cimini and N.R. Sollenberger, "Peak-to-Average Power Ratio Reduction of an OFDM Signal Using Partial Transmit Sequences," *IEEE Communications Letters*, vol. 4, no. 3, pp. 86–88, March 2000.
- [56] J.A.C. Bingham, "RFI suppression in multicarrier transmission system," in *Proc. of IEEE Global Telecommunications Conference (Globecom'96)*, London, U.K., 1996, vol. 2, pp. 1026–1030.
- [57] T. Magesacher, P. Ödling, and P.O. Börjesson, "Optimal intra-symbol spectral compensation for multicarrier modulation," in *Int. Zurich Seminar on Broadband Comm. (IZS 2006)*, Zurich, Switzerland, February 2006, pp. 138–141.
- [58] E. Lawrey and C.J. Kikkert, "Peak to Average Power Ratio Reduction of OFDM Signals using Peak Reduction Carriers," in *5th Intl. Symposium on Signal Processing and its Applications (ISSPA'99)*, Brisbane, Queensland, Australia, August 1999, pp. 737–740.
- [59] J. Tellado, *Peak to Average Power Reduction for Multicarrier Modulation*, Ph.D. thesis, Stanford University, 2000.
- [60] Matrin Senst, Markus Jordan, Meik Dörpinghaus, Michael Färber, Gerd Ascheid, and Heinrich Meyer, "Joint Reduction of Peak-to-Average Power Ratio and Out-of-Band Power in OFDM Systems," in *Proc. of IEEE Global Telecommunications Conference (Globecom'07)*, Washington, DC, USA, November 2007, pp. 3812–3816.
- [61] G.H. Golub and C.F. Van Loan, *Matrix Computations*, John Hopkins University Press, third edition, 1996.
- [62] W. Gander, "Least squares with a quadratic constraint," *Numer. Math.*, vol. 36, pp. 291–307, 1981.
- [63] S. Brandes, I. Cosovic, and M. Schnell, "Reduction of out-of-band radiation in OFDM based overlay systems," in *1st IEEE Symposium on Dynamic Spectrum Access Networks (DySPAN 2005)*, Baltimore, MD, USA, November 2005, pp. 662–665.

- [64] S. Brandes, I. Cosovic, and M. Schnell, "Techniques for Reducing Out-of-Band Radiation in OFDM Based Transmission Systems," *submitted to European Transactions on Telecommunications (ETT)*, October 2007.
- [65] S. Brandes, I. Cosovic, and M. Schnell, "Sidelobe suppression in OFDM systems by insertion of cancellation carriers," in *IEEE 62nd Semiannual Vehicular Technology Conf. (VTC Fall '05)*, Dallas, TX, USA, Sept. 2005.
- [66] S. Brandes and M. Schnell, "Sidelobe suppression with cancellation carriers for OFDM based overlay systems," in *Proc. of 10th International OFDM Workshop*, Hamburg, Germany, August 2005, pp. 235–239.
- [67] Luc de Clercq, Miguel Peeters, Sigurd Schelstraete, and Thierry Pollet, "Mitigation of Radio Interference in xDSL Transmission," *IEEE Communications Magazine*, vol. 38, no. 3, pp. 168–173, 2000.
- [68] International Telecommunication Union, "ITU-T Recommendation P.50 - Artificial Voices," June 1999.
- [69] Alan J. Coulson, "Bit Error Rate Performance of OFDM in Narrowband Interference with Excision Filtering," *IEEE Transactions on Wireless Communications*, vol. 5, no. 9, pp. 2484–2492, 2006.
- [70] A.J. Redfern, "Receiver window design for multicarrier communication systems," *IEEE Journal on Selected Areas in Communications*, vol. 20, no. 5, pp. 1029–1036, 2002.
- [71] Paul Spruyt, Peter Reusens, and Stijn Braet, "Performance of improved DMT transceiver for VDSL," April 1996, ANSI T1E1.4, Doc. 96-104.
- [72] A. V. Oppenheim, R. W. Schaffer, and J. R. Buck, *Discrete-Time Signal Processing*, Pearson Education, 1999.
- [73] Patrick Nickel, Wolfgang Gerstacker, Christof Joniety, Gerd Kilian, Albert Heuberger, and Wolfgang Koch, "Reduction of Non-Orthogonal Interference in OFDM Receivers by Optimized Windowing," in *11th International OFDM Workshop*, Hamburg, Germany, August 2006, pp. 81–85.
- [74] Stefan H. Müller-Weinfurtner, "Optimum Nyquist Windowing in OFDM Receivers," *IEEE Transactions on Communications*, vol. 49, no. 3, pp. 417–420, March 2001.
- [75] F. Sjöberg, R. Nilsson, N. Grip, P.O. Börjesson, S.K. Wilson, and P. Ödling, "Digital RFI Suppression in DMT-based VDSL Systems," in *Proc. of International Conference on Telecommunications (ICT'98)*, Chalkidiki, Greece, June 1998, vol. 2, pp. 189–193.
- [76] F. Sjöberg, R. Nilsson, P.O. Börjesson, P. Ödling, B. Wiese, and J.A.C. Bingham, "Digital RFI Suppression in DMT-based VDSL Systems," *IEEE Transactions on Circuits and Systems*, vol. 51, no. 11, pp. 2300–2312, November 2004.



- [77] R. Nilsson, F. Sjöberg, and J.P. LeBlanc, "A Rank Reduced LMMSE Canceller for Narrowband Interference Suppression in OFDM-based Systems," *IEEE Transactions on Communications*, vol. 51, no. 12, pp. 2126–2140, December 2001.
- [78] Johannes Schwarz, *Enhancing the Spectral Selectivity of Discrete Multi-Tone Modulation*, Ph.D. thesis, University of Mannheim, 2006.
- [79] J. Schwarz and S. Brandes, "Leakage Compensation in an OFDM Overlay System for DSB-AM Aircraft Radio," in *Proc. of 10th International OFDM Workshop*, Hamburg, Germany, August 2005, pp. 240–244.
- [80] Louis L. Scharf, *Statistical Signal Processing: Detection, Estimation, and Time Series Analysis*, Addison-Wesley Publishing Company, Inc., 1991.
- [81] Mohamed Marey and Heidi Steendam, "Cancellation of Digital Narrowband Interference for Multi-Carrier Systems," in *Multi-Carrier Spread Spectrum 2007*, Simon Plass et al., Ed. May 2007, pp. 127–136, Springer.
- [82] Dieter Van Welden and Heidi Steendam, "Interference Cancellation of AM Narrowband Interference Signals," in *Proc. of IEEE 65th Semiannual Vehicular Technology Conference (VTC Spring '07)*, Dublin, Ireland, April 2007, pp. 1617–1621.
- [83] Cormac de Fréin, Mark Flanagan, and Anthony Fagan, "OFDM Narrowband Interference Estimation Using Cyclic Prefix Based Algorithm," in *11th International OFDM Workshop*, Hamburg, Germany, August 2006, pp. 61–65.
- [84] S. Brandes and M. Schnell, "Mitigation of Dynamically Changing NBI in OFDM based Overlay Systems," in *Multi-Carrier Spread Spectrum 2007*, Simon Plass et al., Ed. May 2007, pp. 117–126, Springer.
- [85] John G. Proakis and Dimitris G. Manolakis, *Digital Signal Processing*, Prentice Hall, third edition, 1996.
- [86] Grace Xingxin Gao, "DME/TACAN Interference and its Mitigation in L5/E5 Bands," in *ION Institute of Navigation Global Navigation Satellite Systems Conference*, Fort Worth, TX, USA, September 2007.
- [87] B-AMC Project Deliverable D4, "B-AMC Interference Analysis and Spectrum Requirements," Tech. Rep., Eurocontrol, Issue 1.1, October 2007.
- [88] International Civil Aviation Organization (ICAO), "International Standards and Recommended Practices, Aeronautical Telecommunications, Annex 10 to the Convention on International Civil Aviation, Volume I (Radio Navigation Aids)," July 2006.
- [89] Sergey V. Zhidkov, "Analysis and Comparison of Several Simple Impulsive Noise Mitigation Schemes for OFDM Receivers," *IEEE Transactions on Communications*, vol. 56, no. 1, pp. 5–9, January 2008.

- [90] Sergey V. Zhidkov, "Performance Analysis and Optimization of OFDM Receiver With Blanking Nonlinearity in Impulsive Noise Environment," *IEEE Transactions on Vehicular Technology*, vol. 55, no. 1, pp. 234–242, January 2006.
- [91] S. Brandes and M. Schnell, "Mitigation of Pulsed Interference in OFDM Based Systems," in *13th International OFDM Workshop (InOwO '08)*, Hamburg, Germany, August 2008, pp. 193–197.
- [92] S. Brandes and M. Schnell, "Interference Mitigation for the Future Aeronautical L-Band Communication System," in *7th International Workshop on Multi-Carrier Systems & Solutions (MC-SS 2009)*, Herrsching, Germany, Simon Plass et al., Ed. May 2009, Springer.
- [93] P. Banelli and S. Cacopardi, "Theoretical analysis and performance of OFDM signals in nonlinear AWGN channels," *IEEE Transactions on Communications*, vol. 48, no. 3, pp. 430–441, March 2000.
- [94] R. Fantacci, D. Marabissi, and S. Papini, "Multiuser interference cancellation receivers for OFDMA uplink communications with carrier frequency offset," in *Proc. of IEEE Global Telecommunications Conference (Globecom'04)*, Dallas, TX, USA, November 2004, pp. 7081–7085.
- [95] Xiaoqing Ma, Hasashi Kobayashi, and Stuart C. Schwartz, "Joint Frequency Offset and Channel Estimation for OFDM," in *Proc. of IEEE Global Telecommunications Conference (Globecom'03)*, San Francisco, CA, USA, December 2003, vol. 1, pp. 15–19.
- [96] T. Cui and C. Tellambura, "Robust joint frequency offset and channel estimation for OFDM systems," in *Proc. of the 60th IEEE Vehicular Technology Conference (VTC Fall'04)*, Los Angeles, CA, USA, September 2004, pp. 603–607.
- [97] Eurocontrol, "VDL Mode 2 Capacity Analysis through Simulations, WP3.B, NAVSIM Overview and Validation Results," Tech. Rep., Edition 1.2, October 2005.
- [98] B-AMC Project Deliverable D1, "Proposed L-Band Interference Scenarios," Tech. Rep., Eurocontrol, Version 1.0, February 2008.
- [99] C. Cordeiro, K. Challapali, D. Birru, and Sai Shankar, "IEEE 802.22: the first worldwide wireless standard based on cognitive radios," in *Proc. of the 1st IEEE International Symposium on New Frontiers in Dynamic Spectrum Access Networks (DySPAN)*, Baltimore, MD, USA, November 2005, pp. 328–337.
- [100] N. Fliege, *Systemtheorie*, B.G. Teubner, 1991.

# Förderung

Die dieser Dissertation zu Grunde liegenden Arbeiten wurden teilweise im Rahmen der Projekte TAKOKO (Techniken, Algorithmen und Konzepte für COFDM Systeme zur Koexistenz mit autorisierten Systemen im selben Frequenzband, Förderkennzeichen SCHN 774/2-2) und OOS (OFDM-basierte Overlay-Systeme zur dynamischen und effizienten Nutzung des Spektrums, Förderkennzeichen SCHN 774/3-1) durch die Deutsche Forschungsgemeinschaft (DFG) gefördert. Das Projekt TAKOKO war in das Schwerpunktprogramm TakeOFDM (Techniken, Algorithmen und Konzepte für zukünftige COFDM Systeme) eingebettet.



# Curriculum Vitae

## Personal Data

Name	Sinja Brandes
Date of Birth	June 1, 1980
Place of Birth	Dortmund, Germany
Nationality	German

## School Education

1986-1990	Gemeinschaftsgrundschule Unna-Hemmerde, Germany (Primary School)
1990-1999	Privates staatliches anerkanntes Ursulinen-Gymnasium für Mädchen und Jungen, Werl, Germany (Grammar School)

## Academic Education and Work Experience

1999-2004	Technische Universität München, Germany Studies of electrical engineering and information technology with focus on communication and multimedia engineering
since 2004	Research assistant (wissenschaftliche Mitarbeiterin) at the Institute of Communications und Navigation, German Aerospace Centre (DLR), Oberpfaffenhofen, Germany